PARTICLE RESUSPENSION FROM SURFACES

Thesis by

Denis Joseph Phares

In Partial Fulfillment of the Requirements

for the Degree of

Doctor of Philosophy

California Institute of Technology

Pasadena, California

1999

(Submitted May 5, 1999)

Acknowledgements

Many people contributed to making my stay at Caltech a productive and enjoyable experience. First, I would like to thank my adviser, Rick Flagan, for his support and encouragement, and for giving me the freedom to take the project wherever I felt was necessary. I am especially indebted to Greg Smedley, who taught me how to conduct experimental research and whose enthusiasm for science in general definitely rubbed off on me. I am thankful to Paul Drayton for patiently showing me the ropes in lab early on. The contribution of Rodney Rojas to the project was critical as his handiwork was present in every experimental setup used for this thesis. He also taught me how to use the machine shop myself, saving me a lot of time and money. Suresh Guptha kept the computers running and the data intact, and was always willing to help out with all of my computer questions. Jim Morgan and Glen Cass were available for much needed career counseling and general advice. I am grateful to Fran, Linda, Andrea, Carol, Laurel, and Marta for taking care of the business side of things.

In order to keep myself relatively sane, while spending these years in a windowless lab, I became involved in many activities outside of science; and consequently, made quite a few friends, whom I would like to acknowledge. I would like to thank the Rugby Club, especially the ol' boys - Donal, James, Calum, Neil, Gavin, Lou, Chris E., Al, George, Adam, Bob, Jon, and Teflon Toth - for making it possible for me to live out my NCAA fantasy. The Env/Me soccer team kept me looking forward to Sundays; and the Env softball team kept me looking forward to summer. I will miss everyone who showed up to Wednesday afternoon basketball all those years. I have to thank Gary, Fred, and Rob for all the gigs, practices, and recording sessions. I can't wait for the reunion tour. I also had the great pleasure of making music with Tom, Bobby, Lou, Marc, Clancy, Anna, Bill, and the Monday Jazz Band. I want to thank my fellow air pollution group members - Pat, Jim, Jason, Tim, Mike, Don, and Matt

- with whom I have shared many laughs or many drinks. Rodney, Miltos, Neil, and Darren were great friends through thick and thin. Ashok and Dave made commuting not so bad. And Jay kept us all smiling when he was with us, and that's how I'll always remember him.

I have saved the best for last. I would like to thank Mom, Dad, Caroline, Pascal, Nany, and Loulou for their confidence in me, and for never letting me feel like I was alone. And I would like to thank Tanya, whose love, patience, and support kept me going through my most difficult time as a grad student - writing up. I don't know how she put up with me. I am lucky to have met such a wonderful person.

Abstract

A series of experiments were performed in order to investigate how fine particles are resuspended from a surface once they are adhered to the surface through van der Waals interactions. Model spherical particles were generated, deposited on well-characterized substrates, and exposed to various types of forces. Impulsive forces were applied to the particles using impacting particles and impinging shock waves, and steady shearing forces were applied by impinging gas jets and a laminar channel flow. In each case, the threshold conditions to resuspension were determined by optically monitoring particle removal from the substrate. Particles of various size and material properties were considered. Resuspension thresholds were reproducible and unambiguous in the model experiments.

The threshold to resuspension of the model spheres exposed to impinging gas jets was evidenced by abrupt changes in removal efficiency at specific locations. An analytical method to solve the flow field produced by an impinging jet was developed in order to calculate the shear stress experienced by the particles at the threshold locations. An inviscid model of normal jet impingement provided the free stream conditions for the ensuing boundary layer analysis. Calculated shear stress distributions using the model agree with previous measurements.

Theoretical descriptions of the resuspension mechanisms were inferred from the observed resuspension thresholds. Such an undertaking involves the combination of existing equilibrium adhesion models and the kinetics of aerodynamic or particle collisional interactions. Resuspension models based on equilibrium adhesion theories did not accurately describe the observed size dependence of threshold applied shear stress, or the effect on resuspension of force duration. A kinetic model was developed to qualitatively describe these observed trends.

The particle removal techniques were applied to a study of particle sampling from explosive fingerprint transfer deposits and fingerprint simulations. A crude sampling

system consisting of an impinging gas jet and a suction tube/filter assembly was calibrated with model composite spheres made from a mixture of polystyrene and 2,4,6-trinitrotoluene. Observed removal and collection efficiencies were related to the results of the model experiments. It was found that calibrated sampling systems could be used effectively to test the accuracy of fingerprint simulations.

Contents

List of Figures

List of Tables

Chapter 1 Introduction

Particle resuspension from surfaces is relevant to a wide range of industrial and environmental processes. In arid regions, the entrainment of coarse dust particles by wind initiates the formation of dust storms, which are fueled by the coarse particles falling back to the ground and causing fine particle resuspension through impaction. Once released from the ground, the fine dust particles can be transported through the atmosphere, affecting local sea surface temperatures and overall climate. In many cases, the removal of particulate contamination from surfaces is essential. In the semiconductor industry, the presence of contaminant particles on silicon wafers ultimately reduce product yield. Planned life detection missions to Mars will rely on the assumption that the Mars rover and surface samplers can be completely cleaned of particulate matter from earth, so as to prevent contamination of a Martian soil sample with biological molecules from earth. The main motivation of the present study is the need for an efficient particle sampler for subsequent vapor analysis. Due to the alarming number of recent terrorist attacks on civilian targets using explosives, the development of an efficient explosives detector has become a top priority throughout the world. The near inevitable transfer of explosive particulate matter through fingerprint transfer makes it possible to detect concealed explosives through the efficient sampling of particles from surfaces.

Particles adhere strongly to surfaces through a combination of molecular interactions and mechanical stresses. Descriptions of particle resuspension processes must incorporate the effect on the particle/surface system of an applied force. Disagreement between theories describing equilibrium particle adhesion to surfaces has made the incorporation of an applied force into the equilibrium theories difficult. This thesis presents an experimental and theoretical investigation of the forces associated with particle resuspension and the possible detachment mechanisms. In order to enable theoretical descriptions, experiments were performed using model particles. The generation of

the well-characterized particles is described in Chapter 2.

Chapter 3 presents an experimental study of particle resuspension induced by particle impaction through exposure of a particle laden surface to a particle laden gas jet. Threshold conditions leading to impaction induced resuspension are determined. A simple equilibrium model describing this type of resuspension is presented. Chapter 4 presents an experimental study of particle resuspension induced by impinging shock waves. Particle removal patterns indicated that shock strength decay could be described by a simple point source model.

Chapters 5 and 6 investigate particle removal under gas jets impinging the surface at normal and oblique incidence, respectively. Particle removal was found to scale with applied shear stress. The location of the threshold shear stress was evidenced by an abrupt change in particle removal efficiency. In this way monosized spheres on well-characterized surfaces could be used as shear stress sensors. In order to quantify the shear stress at the threshold locations, the shear stress distribution under an impinging jet needed to be calculated. The impinging jet flow field was, therefore, modeled as an inviscid flow coupled with a boundary layer. The inviscid flow solution is presented in Chapter 7. Solutions to the stream-vorticity equation are developed for arbitrary influx velocity profiles. The inviscid solution provides the free stream conditions necessary to solve the boundary layer equations along the impingement surface. The boundary layer analysis is presented in Chapter 8. Results are compared to previous measurements of the wall shear stress distribution under various impinging jet configurations. Experiments utilizing monosized spheres were used to extend the derived wall shear stress distribution to compressible jets.

The knowledge of the wall shear stress distribution under a jet impinging at normal incidence facilitates the direct measurement of threshold shear stress for microspheres of various size and materials, as presented in Chapter 9. It was observed that threshold shear stress is much more sensitive to particle size than predicted by equilibrium adhesion theories. Furthermore, particle resuspension was found to occur over a period of time, the duration of which is dependent on the magnitude of the applied shear stress. Therefore a kinetic model of particle detachment, based on the principles

of contact mechanics, is presented.

Chapter 10 applies the experimental techniques developed in the previous chapters to the characterization of particle resuspension from a fingerprint deposit of C4 explosive and a fingerprint simulation. The observed differences between the two deposits are explained within the context of conclusions drawn from the present study. The ability to quantify differences between fingerprints and fingerprint simulations is essential to the development and testing of efficient explosive detectors.

Chapter 2 Particle Generation

2.1 Introduction

The generation of smooth, spherical, and monosized particles is the most critical aspect of the present study. Quantification of forces associated with the resuspension of small particles from surfaces requires uniform distributions of well-characterized particles on a clean flat substrate. Since particle and substrate roughness can greatly affect adhesion [1, 2], it is important to keep the particles and surfaces as smooth as possible so that adhesion forces can be accurately calculated. Also, the ability to produce particles of varying size and material properties enables experimental determination of the effect on the resuspension threshold of parametric variation and, thus, theoretical modeling of resuspension processes. The vibrating orifice aerosol generator (VOAG) allows for satisfaction of all of these criteria, since smooth monodisperse spheres are created from solution droplets. The spheres can be made of any material that is soluble in a solvent with low enough viscosity that the solution can be forced through a microorifice. The size of the resulting spheres depends on the initial solution concentration. The solution of known concentration is forced through a small orifice - typically between 5 and 100 μm - resulting in a fine, steady jet of solution. Jet instability is induced through sinusoidal vibrations of the orifice at a constant frequency. For certain well defined frequencies, the jet will break apart into equal sized droplets of solution [3]. If these droplets are dried slowly enough, the remaining particles will be smooth and spherical. The diameter of the droplets, D_d, is given by:

$$D_d = (\frac{6Q}{\pi f})^{\frac{1}{3}}, \tag{2.1}$$

where f is the vibration frequency, and Q is the solution flow rate through the orifice. Since the volume concentration, C, of the solution is known, the final dry particle

diameter is easily calculated, e.g.,

$$D_p = D_d C^{\frac{1}{3}}. \tag{2.2}$$

2.2 Apparatus

The particle generator employed throughout the present study is a VOAG that is specially designed to work with organic solvents. The generator was constructed for a previous study [4] to synthesize and pyrolize glassy-carbon spheres, and has been slightly modified for the present study. As shown in Fig. 2.1, it consists of a droplet atomizer, a view region, a 2 meter long drying column, and a sampling port at the bottom of the column.

2.2.1 Atomizer

Equal sized droplets of a given solution are produced in the atomizer. The solution is forced through a small orifice, 50 μm in diameter, using a pressure feed system. Unlike in typical vibrating orifice aerosol generators, jet breakup is not induced by vibration of the orifice. Rather, a piezoelectric crystal/shim assembly creates the mechanical vibrations, which are subsequently transferred to the jet acoustically through the solution reservoir behind the orifice. The piezo vibrations are caused by direct application of a sinusoidal voltage with a 10 Volt amplitude across the crystal using a function generator. The piezoelectric crystal is shielded from the organic solvent by the shim, preventing damage to the crystal and the adhesives used to attach the crystal. A dispersion gas flow, applied to the jet just as it exits the orifice, helps to reduce coagulation of the droplets and should ideally minimize the presence of doublets in the final sample.

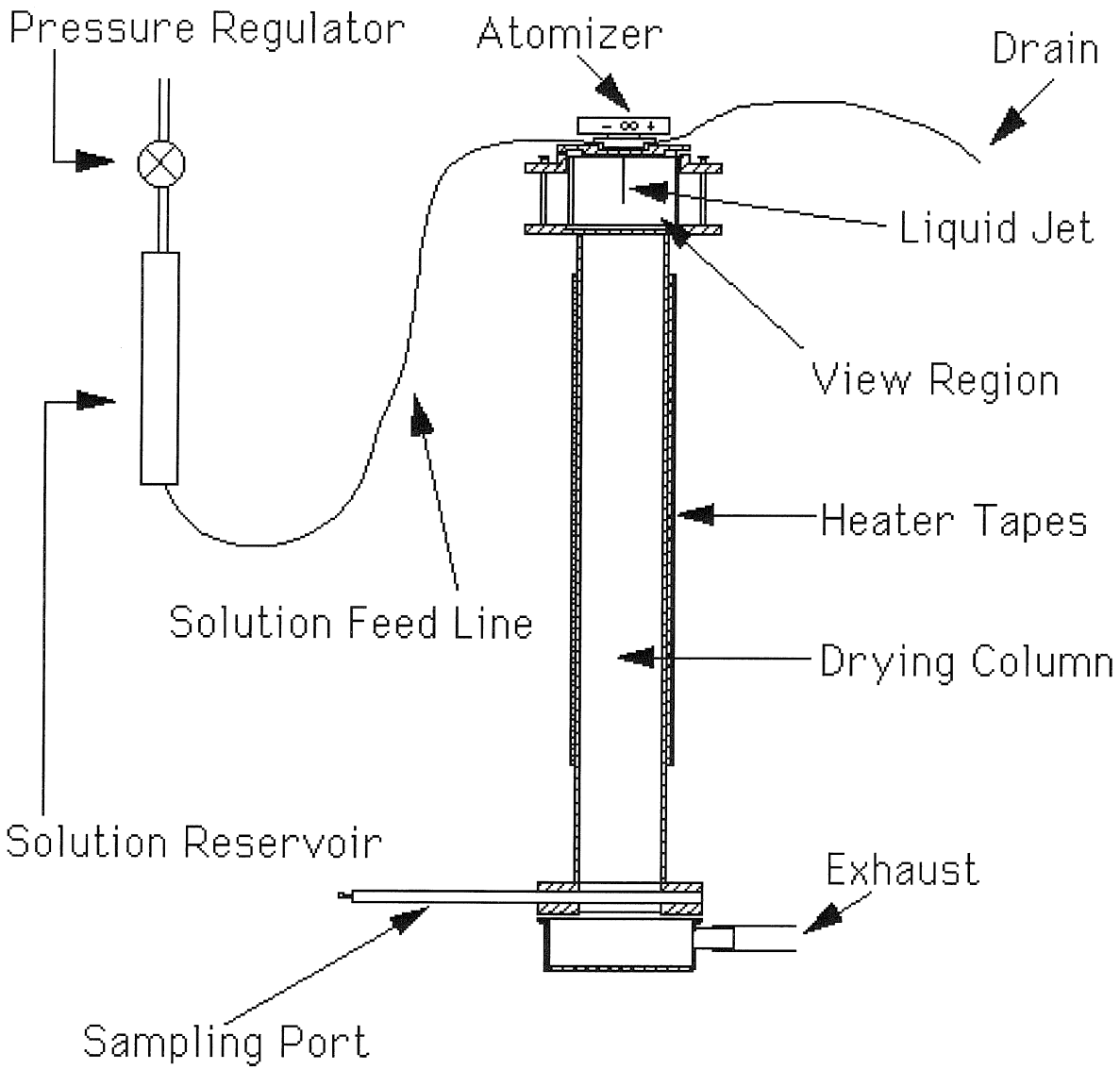

Figure 2.1: Schematic of monodisperse aerosol generator.

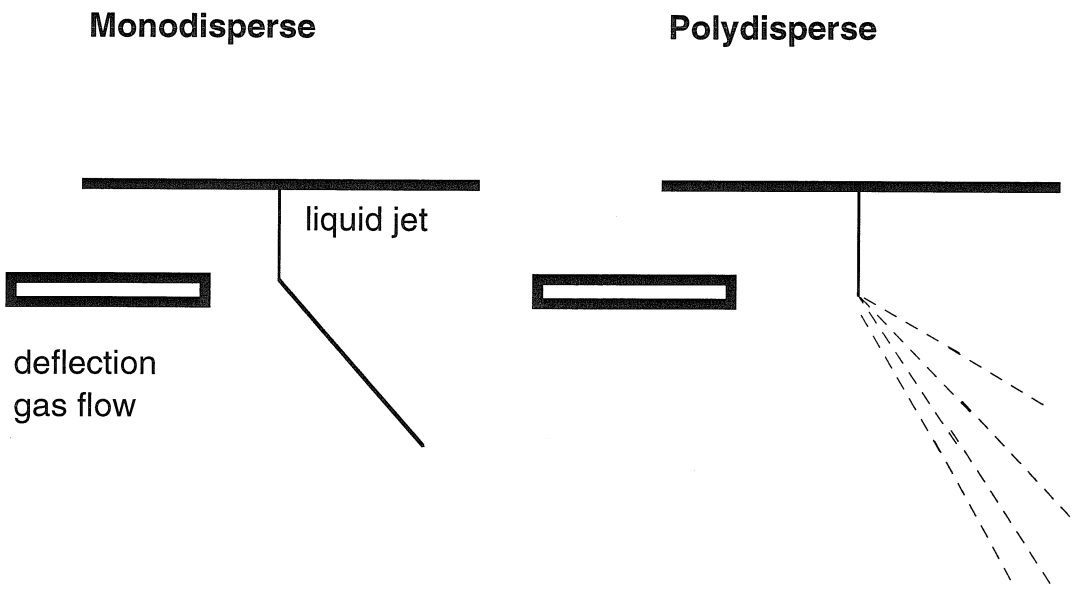

Figure 2.2: Visual check of monodispersivity.

2.2.2 View Region

The view region allows for a visual check of the monodispersivity of the droplets during generation. This is achieved by introducing a gas jet perpendicular to the liquid jet and observing the deflection, with the droplet dispersion gas flow turned off. Upon deflection, a monodisperse stream will remain a fine line, whereas a polydisperse stream will resemble a spray (see Fig. 2.2). Once the vibration frequency is adjusted so that monodispersivity is achieved, the deflection flow is turned off, and the dispersion flow is turned on allowing particle generation to resume.

2.2.3 Drying Column

The dispersed droplets are carried by a dry nitrogen sheath flow through the heated drying column. The sheath flow is introduced at the top of the column through an annular inlet. The sheath flow rate was monitored by measuring the pressure across 20 cm of straight 1/4 inch copper tubing before the entrance to the drying column. Since the final particle roughness is highly dependent on the drying time of the droplet [5], a reasonable temperature control in the drying column is essential. The required

temperature is dependent on the solvent used, the sheath flow rate, and the liquid flow rate through the orifice. Due to the many variables, some trial and error was involved in determining the adequate drying conditions for each solvent. The column was wrapped with three flexible fiberglass electrical heating tapes spanning 18 feet, and the temperature was controlled using an Omega 6100 temperature controller. Typical drying temperatures ranged from 50°C for alcohols, to 100°C for water or toluene.

2.2.4 Deposition

After drying, the particles are allowed to settle on an appropriate substrate - usually a glass slide or scanning electron microscope (SEM) stub. The substrates are placed in a sampling port that can slide in and out of the path of the particle laden sheath air exiting the drying column. The port is sealed on both sides with o-rings, and allowed to slide along the o-ring seals with the application of a generous amount of vacuum grease. A new sampling port was built and installed into the previous setup [4] in order to deposit particles directly onto SEM stubs, which require more clearance than glass slide substrates. The sampling region is located several inches below the heated drying region and is easily kept at room temperature to avoid any thermally induced alterations to the particles as they sit on the substrate during deposition. For a single set of substrates, sampling usually lasts 15 minutes, resulting in particle densities of a few hundred per square millimeter.

2.3 Procedure

The solution is forced from a solution reservoir through about 5 feet of 1/8 inch OD polyethylene tubing and into the atomizer using the pressure feed system. The disadvantage of using a pressure feed system instead of a conventionally used syringe pump is the uncertainty in the liquid flow rate into the atomizer and through the orifice. Consequently, in order to make particles of known size, there is some trial and error involved in determining the liquid feed rate. The advantage, however, is that

instead of a syringe, an arbitrarily large reservoir of solution may be used allowing particle generation to continue for long periods of time. The solution reservoir used throughout the study could contain close to 150 mL of solution. The pressure applied to the solution reservoir was provided by a dry nitrogen cylinder and adjusted using two pressure regulators. The first pressure regulator was set to 15 psi (the *high* setting), and the second was set to a lower pressure (the *low* setting) that was dependent on the desired solution feed rate through the orifice. A Swagelok T-fitting placed between the two pressure regulators and a three-way ball valve (see Fig. 2.3) were used to provide instantaneous high or low adjustment of the pressure applied to the solution reservoir.

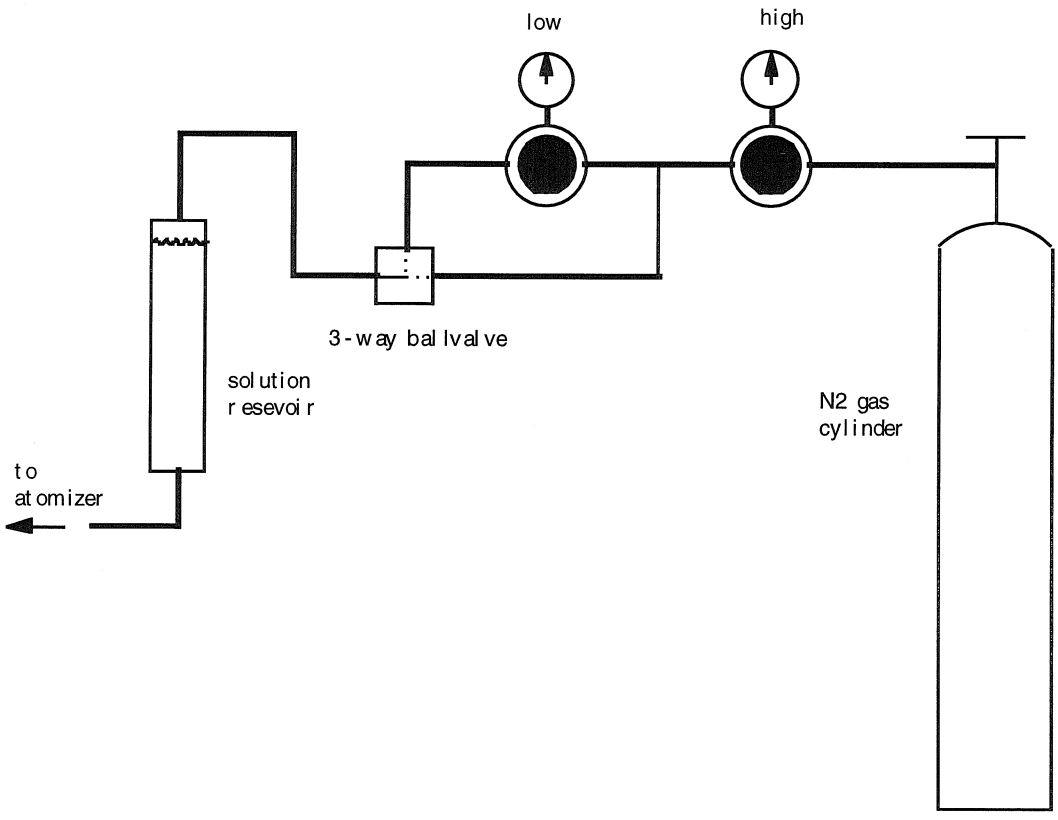

Figure 2.3: Solution pressure feed system.

The high pressure is initially applied to purge the system of air bubbles. Once the liquid feed system is free of air bubbles, the drain is plugged using a ball valve forcing the solution through the orifice. Once the jet is started, the applied reservoir pressure is immediately decreased to the low setting (typically 2 to 5 psi). Due to surface tension of the solvent, higher pressures are required to initiate flow through the orifice than to maintain a sufficiently strong jet. With the dispersion gas flow turned off, the deflection gas flow is turned on and the frequency of the mechanical disturbances applied to the jet is adjusted using the function generator, until the deflected jet appears monodisperse. Once monodisperse droplets are produced, the deflection gas flow is turned off, the dispersion gas flow is turned on, and sample generation is allowed to continue until the reservoir runs out of solution. One full reservoir can typically last for five 15 minute sampling periods.

2.4 Sample Quality

Figs. 2.4 and 2.5 exhibit sample size distributions of nominal 6.8 μm and 8.2 μm particles, respectively. These size distributions were obtained optically by a method described in Chapter 9. Note the presence of a smaller peak corresponding to doublets in both distributions. Although the number of doublets is minimized by the dispersion gas flow, it was observed that they could not be completely eliminated. Excessive increases in the dispersion gas flow rate resulted in droplet breakup and, thus, a polydisperse sample. Fortunately, the presence of doublets did not affect the results of the presented experiments, since the threshold conditions to resuspension of doublets and singlets are considerably different.

The model materials chosen for the resuspension experiments exhibited various mechanical and surface properties. In order to fabricate smooth spheres from these materials, the operating parameters of the particle generator needed to be adjusted based on these material properties as well as the solvent used for dissolution of the materials. Optimal parameters were not found for some of the materials, which then had to be eliminated from the experimental investigations.

2.4.1 Ammonium Fluorescein

The easiest spheres to produce were made from ammonium fluorescein dye, prepared by reacting fluorescein with ammonium hydroxide as described by Vanderpool and Rubow (1988) [5]. The reaction was allowed to occur in isopropanol, a much easier solvent to work with than water in these studies. It was found that smooth particles were achieved for a wide range column temperatures from solutions of ammonium fluorescein and isopropanol.

2.4.2 Sodium Fluorescein

The sodium salt of fluorescein is very soluble in water and solutions are quick and easy to make. Therefore, particle generation was attempted from solutions of water and sodium fluorescein. The resulting particles appeared smooth and spherical, but turned out to be so hygroscopic that they would soften in the laboratory air within seconds of exposure. A simple test was used to confirm that softening was occurring and, later, to check whether particles had dried completely after removal from the sampling port. Particles were pushed around the substrate under an optical microscope using the tip of a needle. It was observed that particles that had softened or had not yet dried completely would smear, whereas dry, solid particles would remain intact.

2.4.3 Polystyrene

Since the effect on the resuspension threshold of elastic modulus is of interest, molecular weight standards of polystyrene were used. Molecular weight has a much stronger effect on elastic properties of the glassy polymer than on surface energy allowing the effect of elastic modulus variation to be observed directly. Smooth, solid spheres were produced from solutions of toluene and molecular weight standards as low as 2,360 amu and as high as 216,00 amu. Higher molecular weights yielded particles that were very rough and not spherical. Optimal conditions could not be found for the higher molecular weight polymer. Polystyrene with molecular weight lower than 2,000 amu is no longer glassy at room temperature, and was therefore not used in

the presented model experiments. Nevertheless, molecular weights under 4,000 amu exhibited viscoelastic effects, as discussed in Chapter 9.

2.4.4 Other Materials

Other materials used for resuspension experiments included 2,4,6-trinitrotoluene (TNT) (see Chapter 10) and various densities of polyethylene and polyisobutylene. Toluene was used to dissolve all of these materials. TNT particles were found to maintain sphericity when placed in a polymer matrix (polystyrene was used for this purpose). Polyisobutylene and polyethylene yielded high quality particles, but only under 5 μm in size, due to solubility limits.

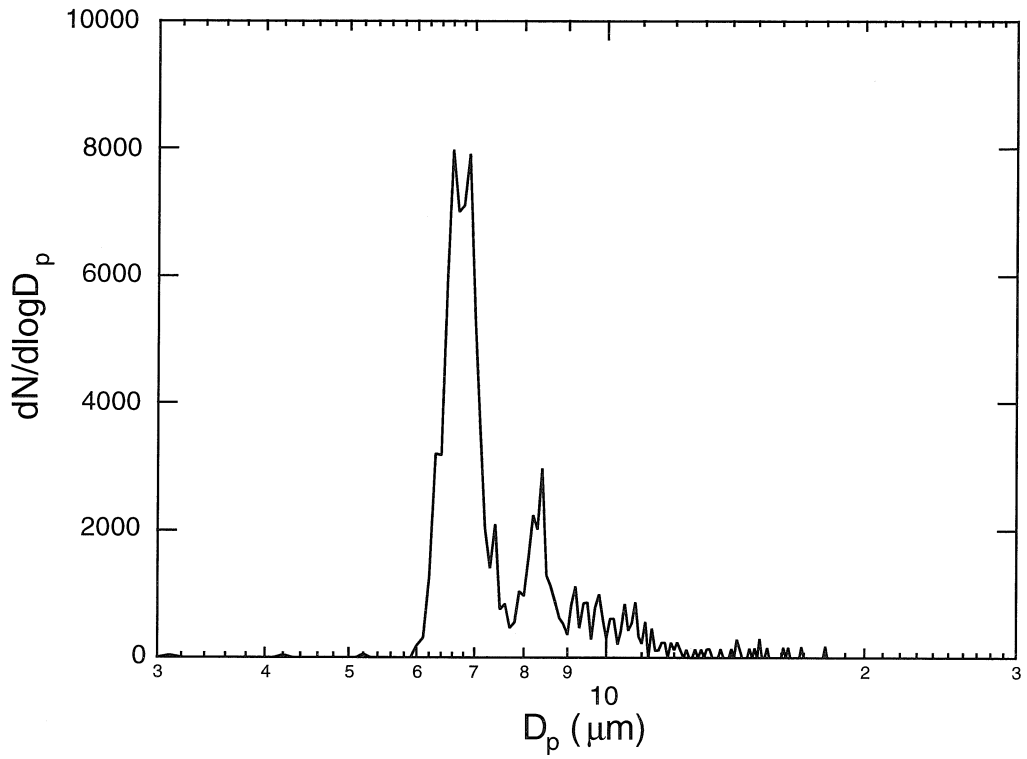

Figure 2.4: Size distribution of nominally 6.8 μm polystyrene particles produced with particle generator.

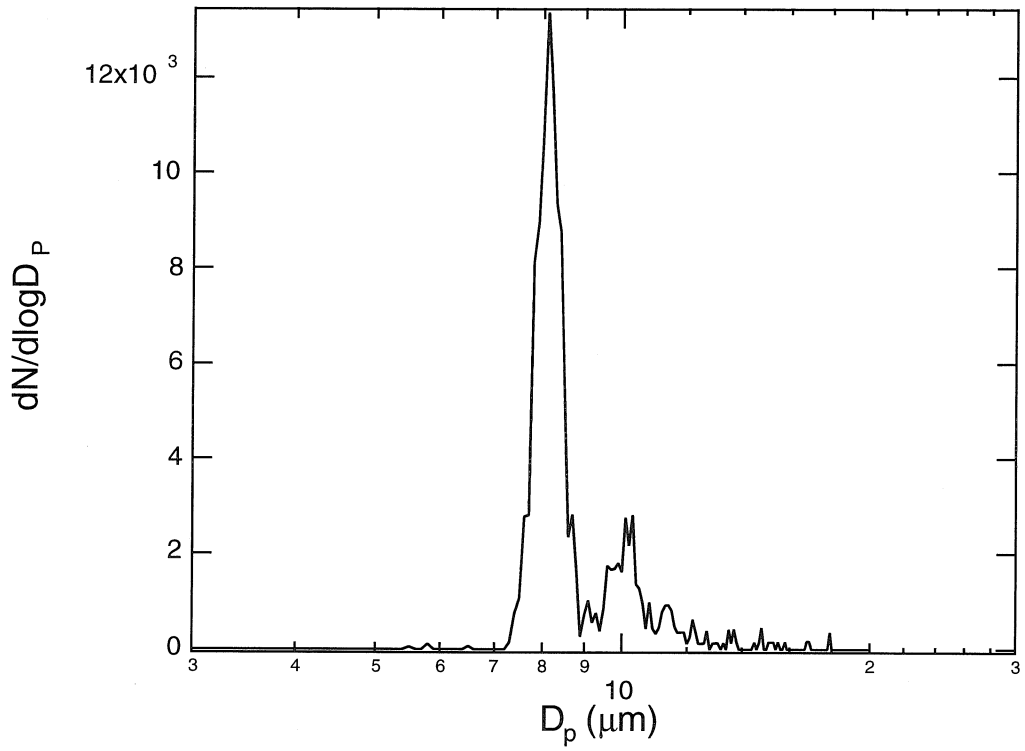

Figure 2.5: Size distribution of nominally 8.2 μm polystyrene particles produced with particle generator.

Chapter 3 Particle Resuspension by Particle Impaction

This chapter presents an experimental and theoretical study of the resuspension of a particle induced by the collision with an impacting particle. The motivation for this study stems from success reported in removing fine particles from silicon wafers using a cryogenic cleaning technique [6, 7]. Compressed carbon dioxide or argon gas is rapidly expanded through a nozzle so that solid particles form within the gas stream. The nozzle is directed at the contaminated surface and the cryogenic particles impact the fine contaminant particles such that enough energy is imparted to the adhered particles to knock them off of the surface.

An experiment, similar to that conducted by John and Vethi [8], has been designed to probe the threshold parameters in the impaction and subsequent resuspension of microspheres. These parameters include the speed and incident angle of the incoming particle, the size of the target particles, and the hardness of the target particle and surface. The results obtained here and in the previous work [8] will be used in the development of a model to describe particle resuspension caused by particle impaction.

3.1 Experimental Setup

The apparatus used in this study is displayed in Fig. 3.1.

The system consists of a TSI Berglund-Liu vibrating orifice aerosol generator, a KR-85 neutralizer, a plenum, and an impaction chamber specially designed to allow for particle laden jet impingement with variable angle of incidence (see Fig. 3.2). The particle laden flow is produced by the vibrating orifice aerosol generator, which ejects monosized solution droplets into a 40 L/min flow of clean, dry air. The droplets are dried and decharged in the neutralizer and held in the plenum before being carried

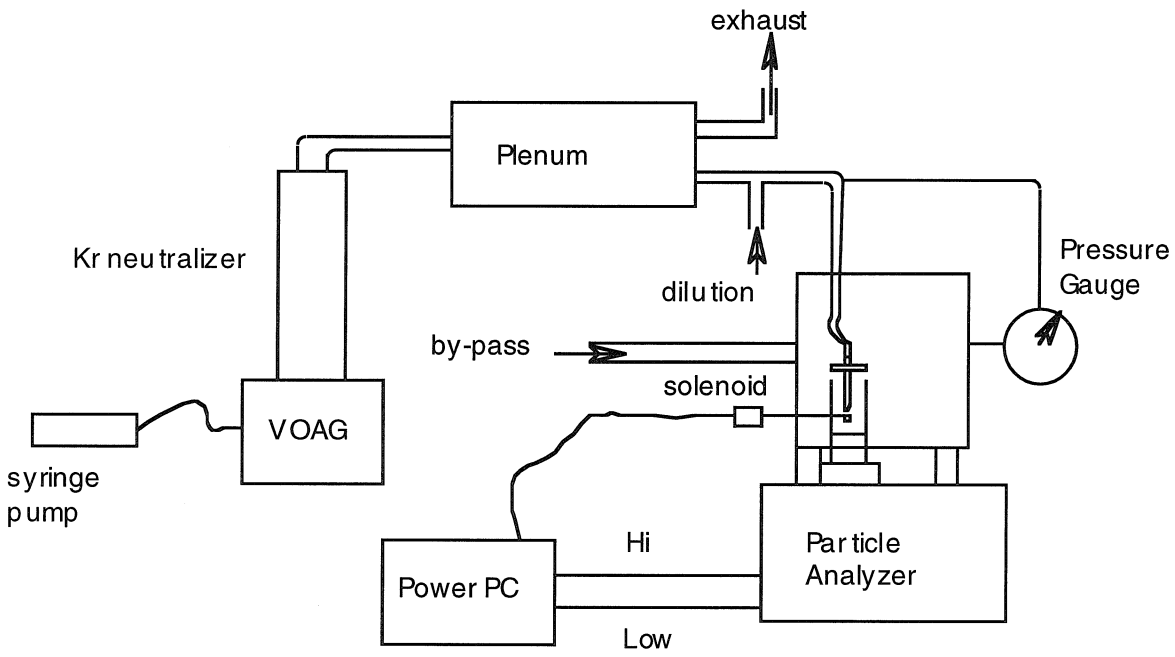

Figure 3.1: Experimental setup.

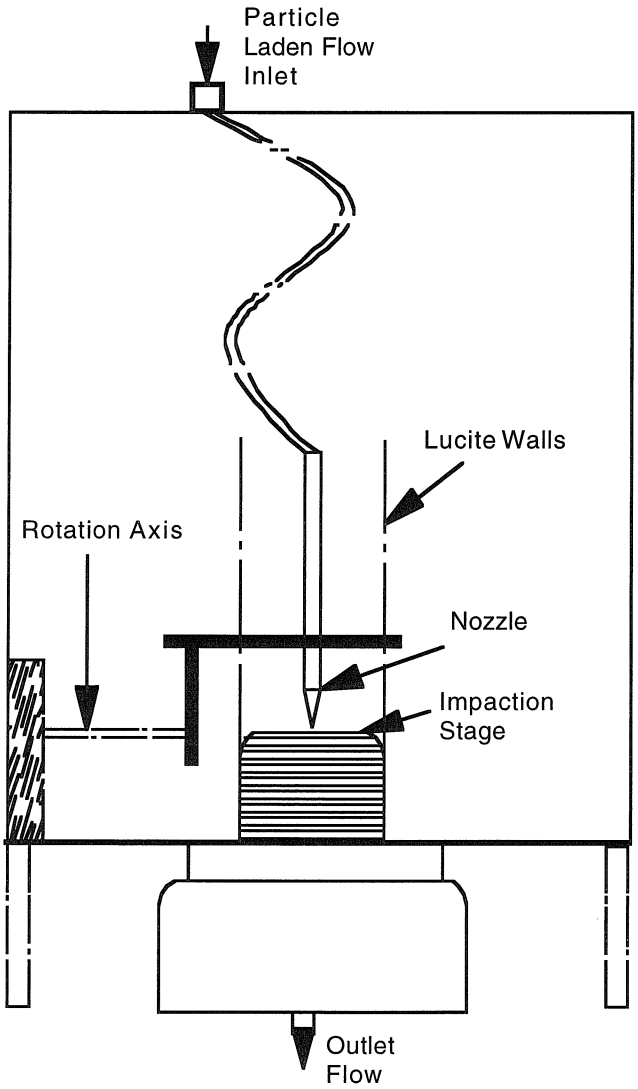

Figure 3.2: Impaction chamber.

into the impactor through a well defined glass nozzle. The impaction nozzle is a 5.5 cm long glass tube (1/4 in. OD) with an inside diameter tapered down to 1.5 mm at the nozzle exit. The nozzle exit was placed at one jet diameter above the impaction surface, and the incidence angle was held constant at 90 degrees throughout the experiments. The impaction surface is mounted on a solenoid-controlled retractable rod. The flow through the nozzle is monitored by measuring the pressure drop through the nozzle, and can be adjusted by varying a by-pass gas flow into the impaction box. The impaction chamber output flow is led directly into a Climet model 226 optical particle analyzer, which requires an influx flow rate of 7 L/min. Excess flow is vented through the plenum. Within the particle analyzer, the flow is illuminated by a white light source. The light scattered by a passing particle is detected within the analyzer by a photomultiplier tube, which creates a single voltage pulse whose amplitude is related to the particle's size and index of refraction. If two sizes of particles are monitored by the Climet, two pulse amplitudes can be detected, and will appear as two peaks in a pulse height analyzer. In this way, the impacting particles and adhered particles are distinguishable. The Climet 226 has a feature that allows the user to place two voltage windows - one high and one low - on the output. If a particle creates a pulse that falls into one of these windows, a single 5 volt pulse is emitted from the appropriate port (high or low). These pulses are counted by a simple data acquisition routine on a PC. By monitoring these pulses for various jet exit velocities, information can be obtained about the threshold parameters associated with particle resuspension.

3.2 Procedure

A uniform dusting of monodisperse particles, generated as described in Chapter 2, is allowed to settle on the appropriate substrate mounted on an SEM stub. The stub is then mounted onto the rod inside the impactor and secured with a set screw. Initially, the impaction surface is retracted and the vibrating orifice aerosol generator is disabled, while the flows are set to obtain the desired jet exit velocity. In order

to eliminate the effect of blow-off of loosely bound particles during the knock-off experiments, the surface is initially exposed to the clean air jet once the flows are set. Typically, a few particles were counted in the first few seconds of exposure to the clean jet, but none afterwards. The surface is once again retracted from the path of the jet, and the impacting particles are introduced into the flow. Once the particle stream is counted, the coated surface is rapidly moved under the particle laden jet, allowing impaction to occur. Impacting and resuspended particle count rates are measured for various nozzle velocities.

3.3 Results

3.3.1 Chamber Response

The response of the impaction chamber to instantaneous changes in the particle density of the flow was measured. A particle laden flow was introduced through the nozzle and allowed to impact on an SEM stub coated with vacuum grease. Since all of the particles stuck to the greased stub, almost no particles were counted by the analyzer. The stub was withdrawn from under the nozzle very quickly to create a near instantaneous increase in particle flow through the impactor box. Once the particle count rate stabilized, the greased stub was quickly moved under the jet again. Figure 3.3 shows the box response to two of these events occurring in succession. The response time is on the order of one second.

3.3.2 Resuspension Rate

Results were obtained for the case of 3.0 μm ammonium fluorescein spheres impacting a surface laden with a uniform distribution of 7.2 μm ammonium fluorescein spheres. Although experiments were run with polyvinyl chloride (PVC) and glass substrates, only those run with the PVC substrates gave meaningful results, since the particles on glass substrates were easily resuspended when exposed to a particle-free air jet. The substrates were epoxied to aluminum SEM stubs and wiped with acetone a few

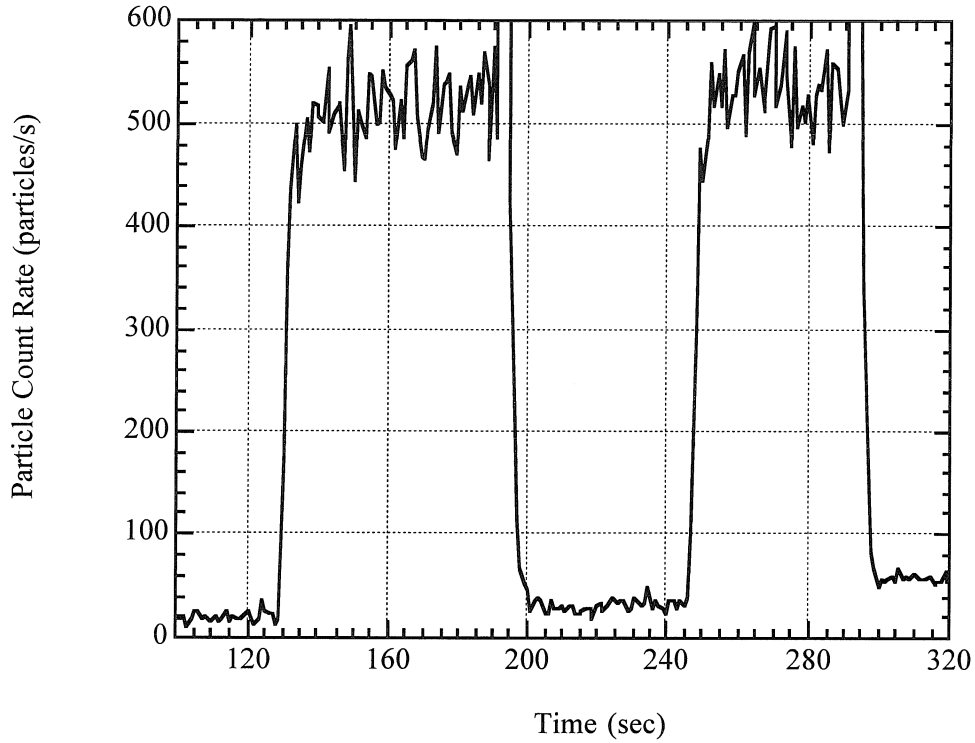

Figure 3.3: Impaction box response to instantaneous changes.

hours prior to being coated with particles. The coated substrates were subsequently allowed to sit in a dry box for one night after coating. Surface particle densities of 1000 particles per mm^2 were needed to achieve a good repeatable knock-off rate.

Figure 3.4 displays the count frequency of the larger 7.2 μm particles in the outflux flow versus time. This is equivalent to the knock-off rate from the substrate induced by collision the smaller impacting particles. This particular plot was obtained with a jet pressure of 4.2 inches of water, which corresponds to a Stokes number of $St = 1.17$, where

$$St = \frac{\rho_p C V_o D_p^2}{18 \mu R_j}, \tag{3.1}$$

and ρ_p is the particle density, C is the slip correction factor, V_o is the gas velocity at the nozzle exit, D_p is the impacting particle diameter, μ is the gas viscosity, and R_j is the nozzle radius. As expected, the knock-off rate falls off steadily as the target particles are being depleted.

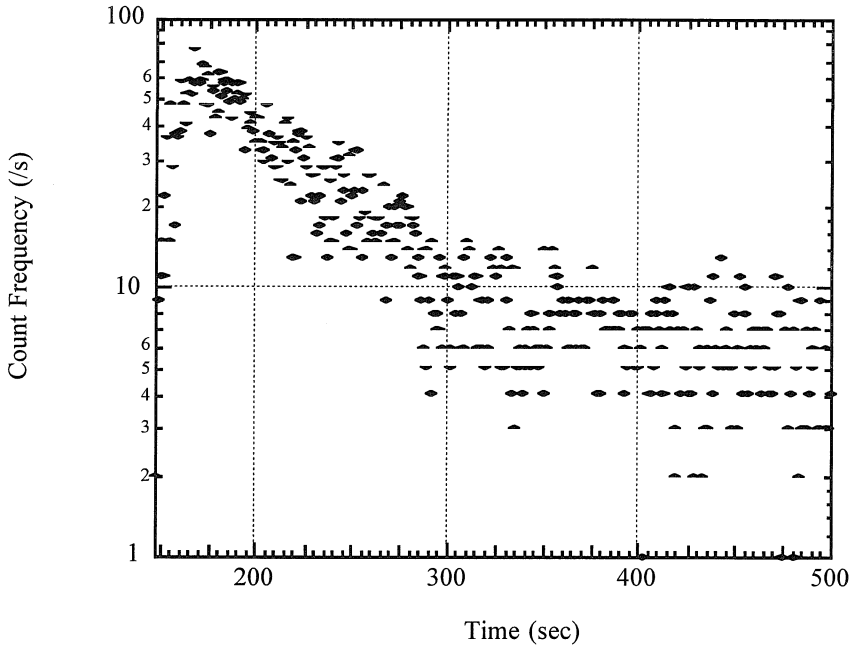

Figure 3.4: Particle knock-off rate at $St = 1.17$.

Fig. 3.5 exhibits a sample removal pattern on the PVC substrate after 5 minutes of exposure to the particle laden jet. A ring, approximately the same diameter as the jet exit, of remaining target particles is evident in the center of the removal region. Initial impaction of the 3.0 μm particles occurred within this ring. Removal of the target particles outside of the ring must have been caused by the collision with either 3.0 μm particles that bounced within the ring and then reimpacted outside of the ring, or 7.2 μm target particles that were knocked off the surface from within the ring and then impacted the surface outside of the ring. Both of these explanations suggest that resuspension caused by a collision can be induced by the transfer of momentum which is predominantly tangential to the surface, since particles reimpacting outside the ring must have a significant tangential velocity component. This point is important to understanding the mechanics of impaction-induced resuspension, as the mode of incipient motion is partially determined by the direction of the applied force.

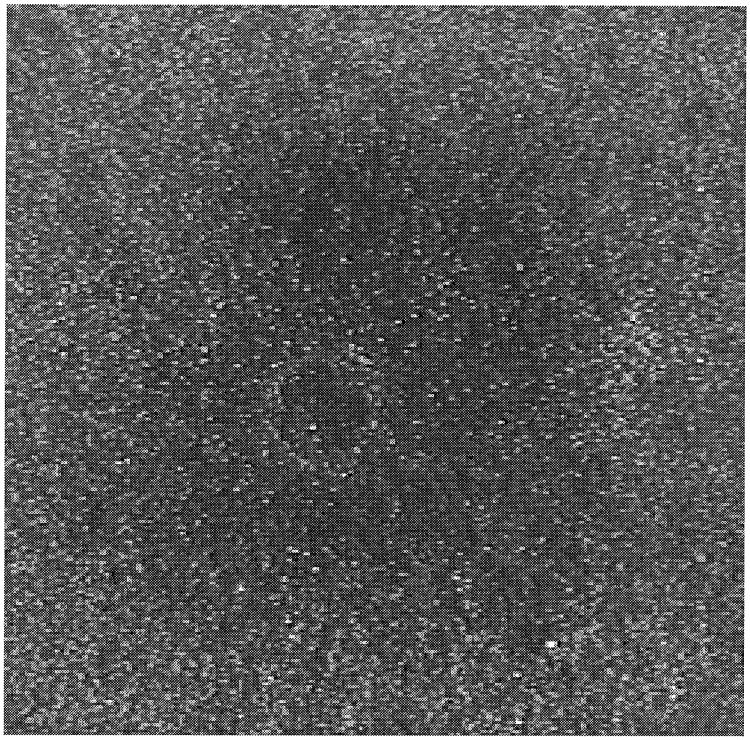

Figure 3.5: Observed particle removal pattern after 5 minutes of expsoure to particle laden jet ($St = 1.17$).

3.3.3 Resuspension Threshold

The knock-off rate during the first minute of jet exposure was measured for nine test samples, varying the jet exit velocity for each sample. The threshold Stokes number for particle resuspension was determined by extrapolating the value of $\sqrt{St}$ that would yield an initial knock-off rate of zero. Figure 3.6 displays the impaction data plotted as initial count rate versus $\sqrt{St}$. A critical Stokes number of $St = 0.54$ was extrapolated from the data. This value is in good agreement with the previous study [8], where a critical Stokes number of $St = 0.65$ was measured for the impaction of 3 micron ammonium fluorescein spheres on 8.6 micron ammonium fluorescein spheres adhered to a polyvinylfluoride substrate.

To enable comparison with model results, it is necessary to estimate the velocity and angle of incidence of the impacting particles at the instant of collision with the target particles for the extrapolated Stokes numbers. Both the impact velocity and the

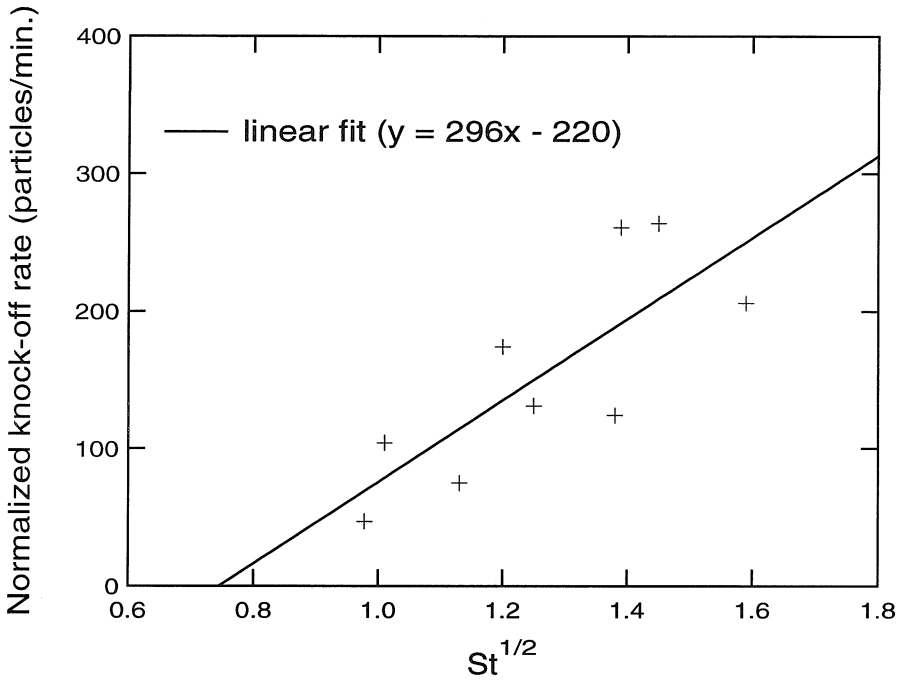

Figure 3.6: Initial knock-off rate, normalized to 1000 incident particles.

angle of incidence will depend on the initial location of the impacting particle within the jet nozzle. However, since threshold resuspension is being considered, it is only necessary to consider the trajectories of those impacting particles that will be the first to initiate resuspension. Based on the evidence in Section 3.3.2, these particles should have the greatest tangential momentum component, and must therefore include only the particles that pass close to the edge of the jet nozzle and impact the substrate at the shallowest angles of incidence.

Since the jet exit is located only 1 jet diameter above the surface in this study and less than 1 jet diameter in the previous study [8], then turbulent mixing can be neglected and the flow field can be approximated with the potential stagnation flow solution:

$$V_r = r \tag{3.2}$$

$$V_z = -2z. \tag{3.3}$$

Given this flow field, the governing equations for the motion of particles are [9]

$$St^* \frac{d^2r}{dt^2} + \frac{dr}{dt} = r \tag{3.4}$$

$$St^* \frac{d^2z}{dt^2} + \frac{dz}{dt} = -2z - \frac{\tau}{V_o} g, \tag{3.5}$$

where a coordinate system is chosen such that z is vertically upward, r is radially outward, and the origin is located at the stagnation point. In Eqs. (3.4) and (3.5), g is the gravitational acceleration, V_o is the jet exit velocity, V_r is the r component of the fluid velocity, V_z is the z component of the fluid velocity, and all lengths and velocities are nondimensionalized with R_j and V_o, respectively. Time is nondimensionalized with the characteristic time, τ, which is defined:

$$\tau = \frac{D_p^2 \rho_p C}{18\mu}. \tag{3.6}$$

Here, the Stokes number is defined in terms of the jet diameter, D_j:

$$St^* = \frac{\tau V_o}{D_j} \tag{3.7}$$

The solutions to Eqs. (3.4) and (3.5) for a particle initially located at the edge of the jet nozzle were given by Flagan and Seinfeld (1988) [9] to be

$$r(t) = e^{-p} \left[\cosh(pq) + \frac{1}{q} \sinh(pq) \right], \tag{3.8}$$

$$z(t) = \frac{1}{2}(1 - v_t) e^{-p} \cos(pq') + \frac{1}{2q'} \left(\frac{1 - q'^2}{2} - vt \right) e^{-p} \sin(pq') + \frac{v_t}{2}, \tag{3.9}$$

where $p = t/(4St^*)$, $q = \sqrt{1 + 8St^*}$, $q' = \sqrt{16St^* - 1}$, and $v_t = -\tau g / V_o$. Using these equations, the trajectories of the impacting particles that initiate resuspension can be easily calculated for the extrapolated threshold Stokes numbers. These are displayed in Fig. 3.7. The impaction velocity and angle of incidence are calculated to be 11.1m/s and 45 degrees for $St = 0.65$, and 10.0m/s and 38 degrees for $St = 0.54$. In the following section, a model is presented that allows for prediction of the threshold

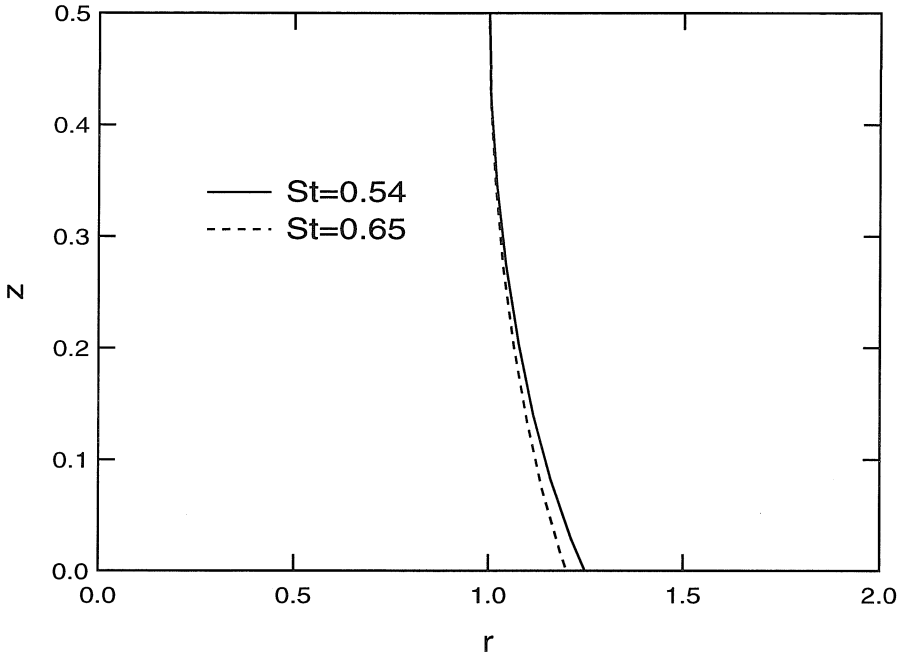

Figure 3.7: Calculated particle trajectories for $St = 0.54$, 0.65.

impact velocities given these incidence angles.

3.4 Knock-off Model

The first step to predicting the threshold impaction velocities that would cause particle resuspension is knowing how strongly the target particles are adhered to the substrate before impaction occurs. Several models have been developed to describe the adhesion between a sphere and surface at equilibrium (see Appendix A). It would be useful to determine which of these models of adhesion is applicable to the case of a 7.2 μm ammonium fluorescein sphere in contact with a PVC substrate. Following the method described in Appendix A.4, the calculation of a single adhesion parameter, Φ_{ad}, where

$$\Phi_{ad} = \frac{32}{3\pi}\left[\frac{\gamma^2 R(1-\sigma^2)^2}{2\pi E^2 \epsilon^3}\right]^{\frac{1}{3}}, \tag{3.10}$$

is sufficient for determination of the appropriate model. In Eq. (3.10), γ is the interfacial surface energy, σ is the Poisson ratio, E is the elastic modulus, and ϵ is the distance of closest approach, typically taken to be 4 Angstrom. The material properties of ammonium fluorescein are given in the previous study [8] to be $E = 1.17 \times 10^{10}$ Pa, $\gamma = 4.62 \times 10^{-2}\ \frac{J}{m^2}$, and $\sigma = 0.33$. Using these values, an adhesion parameter of $\Phi_{ad} = 1.7$ is calculated, indicating that the JKR model of adhesion (see Appendix A.3) is applicable, since $\Phi_{ad} > 1$.

The evidence presented in Section 3.3.2 indicates that, during impaction, a target particle experiences a force that is mainly tangential to the surface. The critical tangential removal force on an adhered particle obeying the JKR model of adhesion is given in Appendix B.2 to be

$$T_c = 4[(PP_c + P_c^2)\frac{K}{\lambda}]^{\frac{1}{2}} \tag{3.11}$$

where P is the applied normal force, $P_c = \frac{3}{2}\pi R\gamma$, and K and λ are elastic constants. Applying this expression to an impaction event requires breaking up the force applied to the target particle by the impacting particle into its normal and tangential components (see Fig. 3.8). The normal component, P in Eq. 3.11, causes the target particle to approach the surface, increasing the contact area; while the tangential component, T, simultaneously causes the particle to shift laterally along the surface, increasing the stress at the outer edge of the contact region. At the critical impaction velocity, the tensile stress at the back edge will surpass the maximum stress that can be maintained by the particle and surface, while still maintaining contact, and a crack will propagate along contact interface, releasing the particle from the surface. At this critical velocity, the tangential component of the applied force is T_c.

The average force applied on the target particle by the impacting particle can be calculated from Hertz theory, assuming that all deformations are purely elastic. According to Hertz [10], the duration, Δt of contact in the collision of an impacting sphere of mass, m, and radius, r, moving at a velocity, v, and a target sphere of

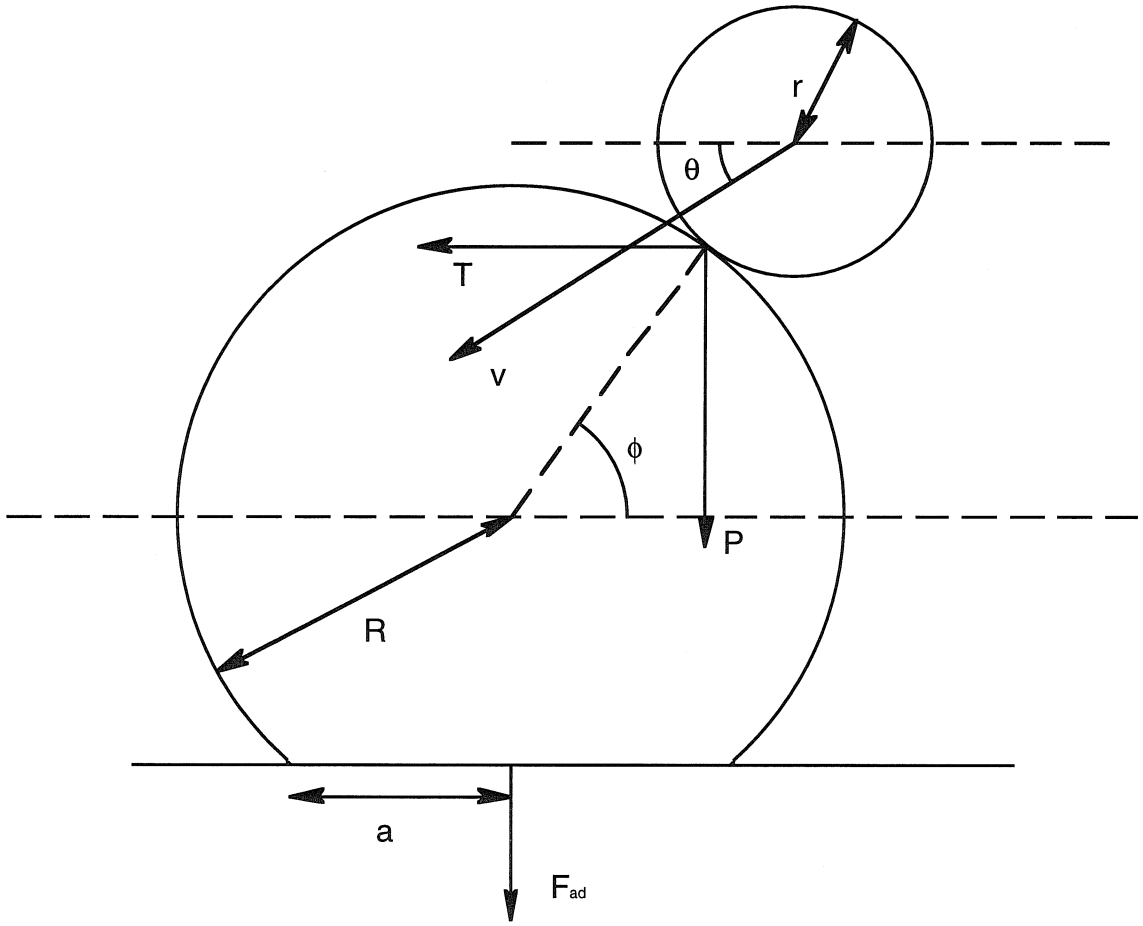

Figure 3.8: Schematic of impaction event.

radius, R, is given by

$$\Delta t = Cv^{-\frac{1}{5}},$$

$$C = 4.02\left(2\rho k_p\right)^{\frac{2}{5}}\left(\frac{rR}{r+R}\right), \tag{3.12}$$

where ρ is the particle density and k_p is a constant related to the elastic modulus and Poisson ratio of the particles:

$$k_p = \frac{3}{4\pi}\left(\frac{1-\sigma^2}{E}\right). \tag{3.13}$$

The average applied force, F, is thus given by

$$F = \frac{mv}{\Delta t}, \tag{3.14}$$

and the normal and tangential components are

$$T = \frac{mv}{\Delta t}\cos\theta \tag{3.15}$$

and

$$P = \frac{mv}{\Delta t}\sin\theta. \tag{3.16}$$

If the impacting particle is not aimed directly at the center of the target particle, then two extreme cases must be considered: (i) friction prevents any slip from occurring during impaction and the applied force is independent of the location angle, ϕ, of collision (see Fig. 3.8), and (ii) the particles slip perfectly off of each other and force is transmitted only along the line connecting the centers of the two particles. In the first case the velocity, v, used in the above calculations is equivalent to the velocity of the impacting particle regardless of where the collision occurs on the surface of the

target particle. Combining Eqs. (3.11), (3.12), (3.15), and (3.16) yields

$$v_{threshold} = \left[\frac{32CP_c \sin\theta}{3K\lambda m \cos^2\theta} + \left(\left(\frac{32CP_c \sin\theta}{3K\lambda m \cos^2\theta} \right)^2 + \frac{64C^2P_c^2}{3K\lambda \cos^2\theta} \right)^{\frac{1}{2}} \right]^{\frac{5}{6}}. \tag{3.17}$$

Eq. (3.17) predicts a threshold impact velocity of 6.4 m/s for a 3.0 μm ammonium fluorescein sphere impacting an 8.6 μm ammonium fluorescein sphere at an incident angle of $\theta = 45°$, and a threshold impact velocity of 4.2 m/s for a 3.0 μm ammonium fluorescein sphere impacting an 7.2 μm ammonium fluorescein sphere at an incident angle of $\theta = 38°$.

In the second case, only the component of the impacting velocity along the line of centers needs to be considered. Thus the velocity, v, used in the above development is replaced by $v\cos(\theta - \phi)$. Using this and combining Eqs. (3.11), (3.12), (3.15), and (3.16) yields

$$v_{threshold} = \left[\frac{32CP_c \sin\theta}{3K\lambda m \cos^2\theta} + \left(\left(\frac{32CP_c \sin\theta}{3K\lambda m \cos^2\theta} \right)^2 + \frac{64C^2P_c^2}{3K\lambda \cos^2\theta} \right)^{\frac{1}{2}} \right]^{\frac{5}{6}} \frac{1}{\cos(\theta - \phi)} \tag{3.18}$$

Fig. 3.9 depicts predicted threshold impact velocity as a function of impact location for various angles of incidence for the slip condition (Eq. 3.18). The impact velocity becomes very large as ϕ approaches 90°, as the model does not account for the effect of elastic rebound resulting from an applied normal force. However, since we are concerned with the threshold condition, the only meaningful quantity in the curve is the minimum velocity, which shifts in location depending on the angle of incidence, θ. Based on this approach the slip model predictions for threshold impact velocity are 3.2 m/s and 2.4 m/s for 8.6 μm and 7.2 μm target particles, respectively. It would appear from these calculations that the no-slip mechanism adequately describes the resuspension observed in the present experiment as well as the previous experiment [8].

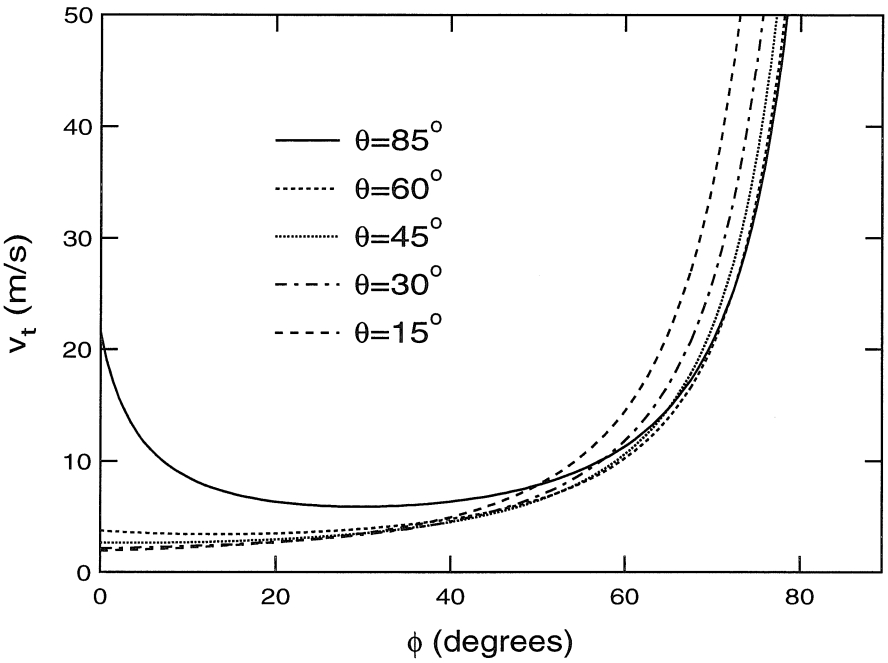

Figure 3.9: Slip model predictions for various angles of incidence.

3.5 Discussion

John and Sethi (1993) [8] suggested two mechanisms of removal. The first utilized only the normal component of the imparted momentum, as the particle was proposed to have been compressed downward onto the surface and rebound elastically upward with enough energy to break the adhesive bond. The second made use of Wang's rotation mechanism [11] (see Appendix B.1), and the resuspension threshold was taken as the point when the torque due to the impaction impulse matched the torque due to the adhesion force. It was found that the rotation model greatly underpredicted their measured threshold velocity of 9.3 m/s, whereas the elastic rebound model predictions were much more reasonable. The implication of these results is that the tangential component of the momentum imparted to the target particle has no effect; and consequently, glancing angle collisions would be less likely to cause resuspension than normal collisions. This is contrary to the evidence presented in Section 3.3.2 that resuspension occurs horizontally along the surface, and not vertically away from the

Table 3.1: Impaction-induced resuspension model results.

Experimental (m/s)	Model	Prediction (m/s)
11.1 (8.6 μm target particles)	Present model (no slip)	6.4
	Present model (slip)	3.2
	Elastic rebound	4.7
	Rotation	0.17
10.0 (7.2 μm target particles)	Present model (no slip)	4.2
	Present model (slip)	2.4
	Elasic rebound	2.3
	Rotation	0.12

surface. In Section 3.4, a model which explores the effect of the tangential momentum component is presented. The model results, which are summarized in Table 3.1, indicate that reasonable predictions can be made.

3.6 Conclusion

An experiment was conducted to investigate the resuspension of 7.2 μm ammonium fluorescein spheres from a PVC substrate when exposed to an air jet laden with 3.0 μm ammonium fluorescein spheres. A threshold Stokes number was estimated from observed knock-off rates for various jet flows, and was in good agreement with previous experimental results. A simple particle trajectory model was applied to calculate impaction velocities and incidence angles for the obtained Stokes numbers. The observed removal patterns suggest that particles are knocked off the surface in a direction nearly parallel to the surface rather than perpendicular to the surface, contrary to the predictions of previous impaction-induced resuspension models. A resuspension model, which incorporates this type of removal, was presented and shows good agreement with experiment.

Chapter 4 Particle Resuspension by Impinging Shock Waves

When a shock wave impinges on a surface, it reflects and propagates across the surface at supersonic velocity. The gas is impulsively accelerated by the passing shock wave. The resulting high-speed flow imparts sufficiently strong forces to particles on the surface to overcome strong adhesive forces and entrain the surface-bound particles into the gas. This chapter describes an experimental study of the removal of fine particles from a surface by impinging shock waves. The surfaces examined in this study were glass slides on which uniformly sized (8.3 μm diameter), spherical polystyrene particles had been deposited. Shock waves were generated in a small, open-ended shock tube at various heights above and impingement angles to the surface. Particle detachment from the carefully prepared substrates was determined from images of the surfaces recorded before and after shock impingement. A single shock wave effectively cleaned a large surface area. The centerline length of the cleared region was used to characterize the efficacy of shock cleaning. A model based upon the far field solution for a point source surface shock provides a good fit to the clearance length data and yields an estimate of the threshold shock strength for particle removal.

4.1 Introduction

Removal of fine particles from surfaces is important both for surface cleaning and for contaminant detection. In the semiconductor industry particulates lead to defects in etched features and ultimately reduce product yield. In forensic science, efforts to detect explosives, drugs, and other contaminants on surfaces are often limited by the low volatility of the particulate material. Aerodynamic entrainment of particles may provide a suitable non-contact means to clean surfaces and may improve transport to

analytical instruments thus enhancing the detectability of contaminants.

Many studies of particle entrainment by fluid flows have appeared in the literature. These can be classified as steady flow methods or unsteady flow methods. Steady methods include fully developed turbulent flow in a boundary layer [12, 13, 14], a pipe [15], or a jet [16, 17, 18, 19, 20, 21]. Unsteady methods include pulsed jets [22, 23, 24], vibrating jets [25], acoustic waves [26], and shock waves [27, 28, 29, 30, 31, 32]. Unsteady flow effects often play a vital role in particle removal even in the steady methods due to the start-up transient as the flow is initiated, although one recent study [21] has probed entrainment by a truly steady jet with no start-up transients. In most steady-flow experiments, a high entrainment rate is usually observed when the flow is first turned on and the entrainment rate decreases with time as the flow is established. The transients during flow start-up produce higher forces on the bound particles than the subsequent steady flows. In periodic unsteady flows, such as a pulsed jet, the transients are generated repeatedly. Otani *et al.* [22] studied particle removal by repeated jet pulses and observed that the entrainment rate was the same for each pulse and independent of the pulse duration. In contrast, other unsteady-flow experiments showed no enhancement of particle removal over that obtained in the steady flow case [23].

The most extreme unsteady flow is the shock wave. As a shock wave travels at supersonic speed across a surface, it impulsively accelerates the gas as it passes, creating a high speed flow behind the shock wave. When the shock wave is advancing into a quiescent gas, a boundary layer forms on the surface and grows with distance behind the shock. Thus, surface-bound particles are exposed to the highest shear forces immediately behind the shock where the boundary layer is thinnest. In this way, a shock wave of sufficient strength is able to remove even tightly bound particles from the surface.

Several investigators have examined the interaction between a dusty layer of particles and passing shock waves related to coal mine explosions [28, 29, 31]. These researchers have explored shock reflections within the dusty layer and the effect of layer depth. Others have investigated removal of thick deposits (scale) from boilers

and furnaces using detonation waves [33, 34]. A few investigators have examined shock wave interaction with sparse layers or single particles. Emmons and Pennebaker [27] measured vertical and downstream position of lycopodium particles (30 μm diameter) lifted from a monolayer (on the floor of the shock tube) by a Mach 1.27 planar shock. Studies of drag on a spherical particle subject to an impulsively started flow behind a shock wave [30], and detachment of a single 400 μm diameter particle from the wall of a shock tube [32] revealed that the drag coefficient was nearly twice that in an equivalent steady flow. This enhancement of the drag coefficient in an impulsive flow augments the high shear forces behind shock waves. Most of the previous studies employed large particles, for which the van der Waals adhesive forces are generally weak relative to aerodynamic forces. Moreover, only a limited range of shock strengths was employed in these studies [27, 30, 32]. The data from these studies, therefore, provides little insight into the relationship between shock strength and particle properties that will lead to particle entrainment, or the spatial distribution of particle removal.

The present work explores the potential use of impinging shock waves for extracting small particles from surfaces. A shock tube employing a fast-acting valve is used to generate the shock waves. The effect of shock strength, impingement angle, and shock tube exit height on the efficiency and spatial distribution of removal are examined using uniformly sized polymeric particles.

4.2 Experimental

4.2.1 Shock Wave Apparatus

The apparatus used for this investigation is illustrated in Fig. 4.1. A high speed rail table with a vacuum-chuck sample holder is used to position the sample alternately below a shock tube (OD = 6.35 mm; ID =4.24 mm; Length = 300 mm) mounted on a y-z-θ traverse or below a CCD camera. The shock waves are generated in the shock tube using a fast opening induced-eddy-current (IEC) valve (see Section 4.2.1). The

valve reservoir pressure is adjusted using a regulator and measured with a Lucas P4100 pressure transducer (2 kPa accuracy from 0 to 6.9 MPa gauge pressure). Helium, which has a sound speed (1007.4 m/s) greater than the sound speed in air (343.3 m/s), is used in the valve to increase the shock strength that can be achieved at a given pressure. The rail table motions are controlled via RS-232 communications from the computer to a Compumotor PDX-15 motor controller. The vertical (z) and horizontal (y) position of the shock tube are manually adjusted using linear micrometer stages. The impingement angle (θ) is set using a locking rotation stage.

The samples consisted of uniformly sized polymeric particles on microscope slides. A HeNe laser sheet provides glancing angle illumination of the particles on the glass substrate so that they appear bright against a dark background. Dark field images of the particle laden surfaces were recorded using a CCD camera equipped with a telephoto lens and connected to a Macintosh computer using a Scion LG3 frame grabber card.

IEC Valve

Conventional shock tubes employ a burst diaphragm that must be replaced after each firing and must be sized (thickness and material) to burst at the desired pressure. Other shock tubes, known as diaphragmless, substitute a fast-opening valve for the diaphragm; some representative examples are a ball valve [35], an induced-eddy-current (IEC) valve [36], and a pneumatic valve [37]. In the present study, replacing burst diaphragms for subsequent shocks would limit the pointing accuracy of the shock tube. Furthermore, diaphragm fragments may be generated when the diaphragm bursts and be carried downstream by the shock flow. Such foreign particles, which tend to be large, could impact on the surface and dramatically affect the observed removal. To avoid these problems, a shock-on-demand system was developed using a fast-opening IEC valve. The data reported here resulted from 126 shocks created by 14 different valve pressure ratios without changing the operational parameters of the valve.

The first reported use of an IEC valve was by Shpigel [38]. Since then, variations of

this valve have been used as a gas injection valve for plasma studies [39, 40, 41, 42], as a gas-gun valve for hydrogen pellet injection for fusion research [43], and as a diaphragm replacement for a shock tube [36]. The IEC valve used in the present experiments is a modification of a prototype valve that was used for plasma studies [44]. In the plasma application, the injected gas volume was minimized; a shock tube application requires that the injected gas volume be maximized. To this end, the internal volume of the valve was enlarged by decreasing the size of the internal components, and the impedance of the gas exit path was minimized by adding holes to the valve plate.

A schematic diagram of the valve is shown in Fig. 4.2. A light-weight aluminum valve plate is held by gas pressure and spring load against a small Teflon seal around the valve exit port. A coil is mounted in the front part of the valve opposite the valve plate. The valve is actuated by rapidly discharging a capacitor bank (500 μF at 500 volts) through the coil to produce a rapidly increasing magnetic field. The increasing magnetic field induces eddy currents in the valve plate. These eddy currents create a magnetic field opposite to that generated by the coil. The opposing magnetic fields repel the valve plate from the coil, thereby opening the valve, and allowing gas to flow downstream. The valve opens very quickly, generating a pressure pulse that produces a shock wave in the exit tube just downstream of the valve. As the current decays, the valve plate returns to its original position and closes the valve. The shock wave travels down the open-ended shock tube which is aimed at the sample surface to remove particles. The capacitor bank discharge is triggered using a TTL-level logic signal and it returns to full charge within four seconds, ready for the next firing.

4.2.2 Sample Preparation

Quantitative studies of particle entrainment require test samples that consist of well-characterized particles on well-characterized surfaces. The surfaces used in the present study were microscope slides that had been cleaned by scrubbing with phosphate-free detergent under a stream of distilled water, thoroughly rinsing with distilled water,

rinsing with 1:1 nitric acid, and then rinsing again with distilled water. The cleaned microscope slides were then baked at 300°C for one hour and cooled in a dry box for a minimum of 12 hours prior to the deposition of particles.

Uniformly-sized, spherical polystyrene particles (8.3 μm diameter, molecular weight = 114,200 amu) were produced from uniformly sized droplets of a toluene/polystyrene solution that were generated using a vibrating orifice aerosol generator (VOAG) that was specially designed to work with organic solvents [45]. The droplets were entrained in nitrogen carrier gas and transported through a heated drying column installed directly below the VOAG. The temperature in the upper part of the drying column was kept below the softening point of the polymer. The particles were gently deposited on the microscope slides by gravitational sedimentation. To avoid distortion of the particles after deposition, the lower part was maintained at room temperature to cool the particles prior to deposition on the cool slides. The particle generation and substrate cleaning procedures are described in more detail by Phares *et al.* [46].

4.2.3 Procedure

A microscope slide with particles deposited uniformly over the surface was mounted flush with the surface of the translation stage using the vacuum chuck. The stage was then moved in steps under the CCD camera to record images of the initial spatial distribution of deposited particles. A full set of three pictures, arranged to cover 58 mm of the slide surface with slight overlap (see Fig. 4.3), was taken both prior to firing any shocks at the sample and after each shock to record the spatial distribution of the particle removal. Time integrated images (12 frames) were acquired to provide a bright image with a high signal-to-noise ratio. The magnification (31 μm/pixel) in these images is insufficient to resolve individual particles, but the average pixel intensity of local regions is proportional to the local density of the particles. The first set of three pictures from each sample defined the initial state from which all subsequent changes were measured.

Once the initial images were recorded, the sample was moved to a known position

under the shock tube by using the edge of the frosted region of the slide as a fiducial mark. A shock wave was generated, with a valve pressure ratio of P_4/P_1, by opening the IEC valve and directed toward the surface by the shock tube. The slide was then returned to the camera location to record the changes in the surface density of the deposited particles. Figure 4.4 shows typical images obtained before and after the slide was exposed to a shock wave.

After the image set was recorded, the valve pressure ratio was increased, and the procedure was repeated. In a typical experiment, the sample was exposed to a series of 14 shocks at a fixed angle and exit height. The sequence of valve pressure ratios employed in these experiments was P_4/P_1: 1.39, 1.74, 2.09, 2.44, 2.79, 3.14, 3.50, 3.85, 4.55, 5.25, 5.96, 6.66, 7.36, and 8.07. For an ideal gas, the initial Mach numbers, M_0, of the shock waves can be calculated from the valve pressure ratios using Eqs. (4.1) and (4.2): 1.11, 1.19, 1.26, 1.32, 1.37, 1.43, 1.47, 1.52, 1.60, 1.67, 1.73, 1.79, 1.85, and 1.90. To examine the effect of multiple shocks, all 14 shocks fired at sample 3 (see Table 4.1) were generated with a fixed valve pressure ratio of 5.25 ($M_0 = 1.67$). Prior to the firing of each shock, the flush valve pictured in Fig. 4.1 was opened to blow out any helium that may have pooled in the upper portion of the shock tube.

To ensure that all experiments were performed using identical particles, a single production run of nine samples with the desired particle density ($\approx 300/\text{mm}^2$) was used in this study. Parametric investigations probed the influence of multiple shocks, the repeatability, and the effect of impingement angle ($\theta = 30°$, 45°, 60°, 75°, and 90°) and exit height ($H/D = 1.0$ and 2.0) on the removal, where H is the distance from the shock tube exit to the surface measured along the shock tube axis and D is the inside diameter of the shock tube. Table 4.1 summarizes the experimental conditions explored with each sample.

4.2.4 Data Analysis

As illustrated in Fig. 4.4, the samples initially exhibited a nearly uniform density of monodisperse particles. In the dark-field images, the particles appeared as a dense

distribution of bright spots on a dark background. A single shock wave generated with $P_4/P_1 = 5.25$ ($M_0 = 1.67$) and fired at the surface at $\theta = 30°$ and $H/D = 2.0$ created the cleaned region (dark area) shown in the right image. The length of the removal extends $\approx$ 40 mm beyond the right edge of the image. For reference, the shock tube was aimed to the right with the lower lip of the shock tube aligned with the frosted edge (indicated by a vertical white line) that is visible at the left of the two images. A rectangular strip through the center of each image set, shown schematically in Fig. 4.3, was analyzed to determine the density profile along the centerline of the removal region. An average pixel intensity was calculated for each vertical (in this figure) slice of the selected region and plotted as a point on the density profile for that 'x' location.

Unfortunately, neither the initial distribution of particles nor the intensity of the laser sheet used to illuminate them is perfectly uniform. To account for resulting intensity variations that were present even before the samples were exposed to the shock waves, the profiles for each image location of each sample were normalized by the profiles obtained from the images of the initial state. The density profiles of the adjacent images (numbered 1 through 3 in Fig. 4.3) were then concatenated, after removing the overlapping portions, to produce a density profile for the full length of the rectangular strip.

The background scattering noise in the cleaned region was estimated as the "cleaned" level from the highest removal region of the profile at the highest pressure ratio. This background signal was subtracted from each of the profiles before dividing by the initial profile. The resulting normalized profile has a value of "0" in the cleaned region and "1" in the uncleaned region. A multi-pass binomial filter was then used to smooth the profiles to reduce the noise. A full set of corrected and smoothed profiles, from Sample 1, is shown in Fig. 4.5. The horizontal line at a particle density of 1.0 represents the initial state prior to the firing of any shocks. The profiles located below the horizontal line have been offset horizontally and vertically (+1.0 mm, -0.1) from one another to show the progression of first deepening and then lengthening of the removal region as the shock strength is increased. The geometric intersection of the

shock tube axis with the surface occurs near $x = 12$ mm.

Several features of these profiles are noteworthy. The left (upstream) edge of the removal region is significantly steeper than the right (downstream) edge. The position of the left edge changes very little while the length of the cleaned region increases dramatically as the shock strength is increased. Moreover, the removal region is nonuniform at low shock strength. These observations are discussed further in Section 4.4 in the context of the fluid mechanics of the shock generation and impingement.

Once the corrected and smoothed profiles were obtained for each sample, hyperbolic tangent curve fits were applied to the upstream and downstream portions of the removal profiles to determine the location of the threshold removal points. Automation of the curve fitting is facilitated by the use of a hyperbolic tangent function, since two data ranges (one for the upstream edge and one for the downstream edge) are sufficient for the entire data set from a given sample. The determined threshold points represent the locations on the surface at which the shock strength decayed to a threshold value that is capable of removing 50% of the particles. The removal length, which we define as the horizontal distance from the center of the shock tube to the downstream 50% removal point, was determined from the known position and angle of the shock tube relative to the sample.

4.3 Results

The measured extent of removal is presented below in terms of the removal length in the direction aligned with the long axis of the sample, since the width of the removal region was generally greater than the field of view of the imaging system (see Fig. 4.4) and often greater than the width of the sample. As defined, the removal length is zero when the peak removal efficiency is less than 50%. Atmospheric conditions in the laboratory were $P_{atm} = 98.0$ kPa, T = 21°C, and relative humidity of 35%. The type of experiments performed with each of the 9 samples and the observed threshold shock strength are summarized in Table 4.1.

4.3.1 Multiple Shocks

Throughout the present investigation, a series of shocks of increasing strength was directed toward each sample in order to maximize the information obtained from a limited number of samples. This procedure is based on the assumption that all particles that can be removed by a particular shock strength are removed by the first shock of that strength. To test this assumption, Sample 3 was exposed to 14 equivalent shocks with a valve pressure ratio of 5.25 ($M_0 = 1.67$), at $\theta = 30°$ and $H/D = 2.0$. The removal lengths, determined for the successive shocks, are summarized in Fig. 4.6. The first shock cleared particles to $r/D \approx 12$; the removal length increased by only 6% during the next 4 shocks (see inset of Fig. 4.6), and was unchanged by the remaining 9 shocks. Thus, the removal obtained with one shock of a given strength is representative of the total removal that is possible for that strength.

4.3.2 Repeatability and Shock Strength

The repeatability of the experimental technique was evaluated at $\theta = 30°$ and $H/D = 2.2$ using samples 1 and 2. The measured removal lengths are shown in Fig. 4.7 as a function of the shock strength, which is defined as the ratio of the pressure immediately behind the shock, P_2, to that in the unperturbed gas ahead of the shock, P_1, at the exit of the shock tube. The shock strength is estimated from the valve pressure ratio, P_4/P_1, using the method described in Section 4.4.1. With increasing shock strength, r/D approached 13. The stronger the initial shock that exits the shock tube, the farther it travels across the sample before decaying below the threshold strength required to remove 50% of the particles. The two sets of data agree well. Curve fits to the data, determined using a model that is based on the decay of a hemispherical shock generated at a point source located on the surface (see Section 4.4.4), follow the data. The good repeatability reinforces confidence that the particle generation and substrate cleaning procedures employed to produce the samples yield nearly identical samples.

4.3.3 Impingement Angle

The impingement angle was varied from 30° to 90° in steps of 15° at $H/D = 2.0$. The measured removal lengths are shown in Fig. 4.8; the last three shocks at 30° impingement extended the cleaned region beyond the end of the sample, so no removal lengths were determined for those shock strengths. At a given shock strength, glancing angle shock wave impingement produced greater removal lengths than did shock wave impingement at larger angles. Furthermore, 30° shock impingement removed particles uniformly from the cleared region, while the normal incidence shock cleared particles from distinct bands. As discussed below, this more complex structure was attributed to the startup vortex and shock interaction with the surface.

4.3.4 Exit Height

The influence of shock-tube exit height was examined at $H/D = 1$ and 2 at $\theta = 90°$. The measured removal lengths are shown in Fig. 4.9. The particle removal length increases with decreasing height because of the corresponding increase in shock strength at the surface. Secondary reflections from the end of the shock tube may also play a role. With increasing height, the shock strength decays before reaching the surface, eventually dropping below the threshold value for particle removal.

4.4 Fluid Mechanics of Shock Waves

The fluid mechanical aspects of shock wave generation in shock tubes, shock wave exit from open-ended tubes, and shock wave interaction with surfaces have been studied extensively [47, 48, 49, 50, 51, 52, 53, 54]. Some of the findings from these references that are appropriate to the understanding of our results are summarized below.

4.4.1 Shock Wave Generation in Shock Tubes

Shock waves are generated in a shock tube by rapidly removing a barrier that separates a high pressure (P_4) driver section from a low pressure driven section (P_1). The ratio

P_4/P_1 is referred to as the diaphragm pressure ratio. The shock, produced in the driven gas, has a strength P_2/P_1 where P_2 and P_1 represent the absolute pressure behind and in front of the shock, respectively [47]. For an ideal gas, the diaphragm pressure ratio required to generate a particular shock strength is given by:

$$\frac{P_4}{P_1} = \frac{P_2}{P_1}\left[1 - \frac{(\gamma_4 - 1)(\frac{c_1}{c_4})(\frac{P_2}{P_1} - 1)}{(2\gamma_1)^{\frac{1}{2}}\left(2\gamma_1 + (\gamma_1 + 1)(\frac{P_2}{P_1} - 1)\right)^{\frac{1}{2}}}\right]^{\frac{-2\gamma_4}{(\gamma_4 - 1)}} \tag{4.1}$$

where c represents the sound speed, γ represents the ratio of specific heats, and the subscripts "4" and "1" refer to properties of the driver gas and the driven gas, respectively. In the present work, the barrier is established by the plate of the IEC valve, the driver section is filled with helium gas ($\gamma_4 = 1.667$) at elevated pressure, and the driven section downstream of the IEC valve contains ambient pressure air ($\gamma_1 = 1.402$). The shock strength calculated from Eq. (4.1) is used to determine the Mach number, M_1, of the shock (the shock speed u_s) and the gas velocity, u_2, behind the shock.

$$M_1 = \frac{u_s}{c_1} = \left(\frac{(\gamma_1 - 1) + (\gamma_1 + 1)\frac{P_2}{P_1}}{2\gamma_1}\right)^{\frac{1}{2}} \tag{4.2}$$

$$u_2 = c_1\left(\frac{P_2}{P_1} - 1\right)\left(\frac{\frac{2}{\gamma_1}}{(\gamma_1 - 1) + (\gamma_1 + 1)\frac{P_2}{P_1}}\right)^{\frac{1}{2}} \tag{4.3}$$

The calculated shock Mach numbers for the present experiments range from 1.11 to 1.90, with resulting gas velocities ranging from 57 m/s to 391 m/s behind the shock. These results for one-dimensional shock flow in a tube provide a useful estimate of the strength of the shock that leaves the end of the shock tube.

4.4.2 Shock Wave Exit from an Open Ended Tube

The exit of a shock wave from an open ended tube is generally important in missile launchers where the shock loading on personnel is of crucial concern [49]; it is also of interest to designers of tunnels for high speed trains [50]. As the shock wave exits a tube, it is diffracted in a manner similar to a sound wave as illustrated in Fig. 4.10.

A sound wave can be compared to an extremely weak shock ($M = 1.0$); in this limit, the shock strength $P_2/P_1 = 1$ and the gas velocity u_2 behind the shock is zero, i.e., no flow accompanies a sound wave as it exits from the tube. In contrast, a shock wave with $M > 1.0$ generates a gas flow that leads to the flow structure illustrated in Fig. 4.10. A vortex is generated, gains strength, and is shed downstream. Strong shocks also generate a normal shock downstream of the exit and other fine scale features [49]. Shortly after exiting the tube, the shock assumes a spherical shape with a shock strength that is stronger on-axis than toward the diffracted edges.

4.4.3 Shock Wave Interaction with a Surface

Figure 4.11 depicts a shock tube positioned at $\theta = 90°$ and $H/D = 2.0$. The flow features downstream of the exit have been omitted; the initial shock is depicted with a solid curve, and the reflected shock is depicted with a dashed curve. The initial shock is assumed to be spherical a short distance downstream of the exit [49]. Its radius grows with propagation time. The reflected shock is generally non-spherical because its strength depends on the local incidence angle of the initial shock. The shock first contacts the surface at normal incidence (angle measured between shock normal and the surface plane) and results in no net gas flow behind the reflected shock. As the initial shock continues to propagate away from the shock tube exit, a circular ring of reflection is formed at the intersection of the incident shock with the surface. The shock initially undergoes a regular reflection in which the incident and reflected shocks intersect at the surface. Later, after a critical radius is reached, a Mach reflection (irregular reflection) develops in which a third shock (Mach stem) extends to the surface from the two shock intersection.

One may develop a model of the shock interaction with the surface by assuming the shock source to be a unit-strength point source located a distance H above a plane surface. The reflected wave pattern is that which would be generated by a pair of unit-strength point sources (dipole) located a distance $2H$ apart [51, 52]. In the far field, the wave pattern from the dipole is equivalent to that generated by a single

point source of twice the unit-strength located midway between the two point sources. In a numerical study of the reflection of strong spherical shocks from a smooth plane, Galkowski [52] found that the transition from regular to irregular reflection occurred at the same radius as the convergence of the decay of the shock strength to the far-field (asymptotic) spherical wave solution. Thus the onset of the Mach reflection appears to be a manifestation of the asymptotic spherical wave behavior [51, 52, 53]. This far-field behavior provides a convenient model of the shock-strength decay with distance traveled across a sample.

4.4.4 Relationship between Shock Strength and Particle Removal

The force required to remove a spherical particle from a surface depends on the particle size and properties, and on the surface conditions. Assuming that the distribution of detachment forces is Gaussian, removal of 50% of the particles in a given region indicates that the shock induced flow produces a maximum force on the bound particles in that region that is equal to the mean force $\bar{f}$ required for particle removal. Higher removal efficiencies indicate that the force exerted by the flow exceeds $\bar{f}$, while lower removal efficiencies indicate that smaller forces are exerted. This simplified view excludes possible influences of particle relaxation response to imposed forces [21], but provides some insight into the range of effective removal of the shock induced flow.

Although the absolute force applied to the particles by the shock induced flow is difficult to determine, the measured removal length can be used to estimate the threshold shock strength for particle removal. In order to determine the threshold shock strength $(P_2/P_1)_{thresh}$, it is necessary to first find a relationship between the generated shock strength $(P_2/P_1)_o$ and the distance r that the shock wave travels along the sample before it decays to the threshold value. We assume that the experiments probe the far field region of the shock, so the shock propagation is the same as that from a source of strength $C_0(P_2/P_1)_o$ and initial radius r_o located

directly below the shock tube exit. The shock wave moves radially outward, decaying in strength as it travels.

We seek to model shock propagation from a source of finite size. Although the generated shock wave assumes a spherical shape shortly after exiting the tube, it differs from that generated by a point source since it has been diffracted. Furthermore, oblique impingement produces asymmetric removal, and the end of the shock tube interferes with the reflected shock, generating a complex wave field. A surface-bound particle located along the central-axis of the sample in the far-field region downstream of the shock tube exit experiences a local shock whose strength is related to the exit shock strength; although the energy released is the same for all shocks of a given strength, changes in the impingement angle or exit height will change the local shock strength. Since the surface bound particles provide a measure of the distance traveled by the shock before it decays to a threshold shock strength, the removal length data for a range of exit shock strengths provide insight into the decay of the shock strength along the central axis of the sample. The decay rate can be used to define the strength of a point source shock located at the surface that would be required to produce a threshold shock strength at the measured distances. Although the problem is complex, and the model simplistic, the derived function provides a satisfactory fit to the removal data, demonstrating that the downstream far-field behavior (along the central axis) can be modeled in this way.

To use a far-field model, the characteristics of the shock source must be known. It is reasonable to assume that the strength of the spherical shock at the surface, which is used to model the decay of the tube-generated shock, is less than that of the point source shock wave, i.e., less than twice the tube-generated shock strength. We therefore assume that the initial shock strength of the modeled point source at the surface to be $C_0(P_2/P_1)_o$ where C_0 is an empirical factor that is expected to be less than two. For the present purposes, the decay of the shock strength as the shock travels down the tube is assumed to be small.

A model of the propagation of a spherical shock wave from a source of strength $C_0(P_2/P_1)_o$ is derived in the Appendix. The model is singular at the origin ($r = 0$),

so we arbitrarily assume that the initial radius of the spherical shock, r_o, equals the radius of the shock tube exit. The observed removal length variation with exit shock strength can then be fitted to the form predicted by the model,

$$r = \left[\frac{\left[\left(\frac{P_2}{P_1} \right)_{thresh} - 1 \right]^{\frac{\gamma+1}{2\gamma}} - 1}{\left[C_0 \left(\frac{P_2}{P_1} \right)_o - 1 \right]^{\frac{\gamma+1}{2\gamma}} - 1} \right]^{-\frac{1}{3}} r_o, \tag{4.4}$$

to estimate C_0 and the threshold shock strength for particle removal, $(P_2/P_1)_{thresh}$. Although the choice of r_o for our data analysis is arbitrary, the long removal lengths observed in this study make the sensitivity to this choice very small. Doubling r_o has a negligible effect on the estimated values of C_0 and less than a 2% effect on the threshold shock strength estimate. The influence of this parameter is greatest for those cases that yield small removal lengths.

The curve fits to the shock removal data using Equation (4.4) compared favorably with the data for all of the experiments. The resulting fit parameters are given in Table 4.1. The threshold shock strength $(P_2/P_1)_{thresh}$ is the same for all the sets of data, as would be expected for a property determined by the surface and the particles rather than by the parameters investigated here. All curvefits have been extended to $r = r_o$, where the initial surface shock strength $C_0(P_2/P_1)_o$ is equal to the threshold shock strength $(P_2/P_1)_{thresh}$. It was not possible to collect data for such small values of r since the removal length is generally large by the time more than 50% of the particles have been removed (a requirement for the definition of a removal length). Furthermore, since Eq. (4.4) is a far-field solution, it is of limited validity for $r < H$ [52].

The strength of a shock that exits from an open-ended shock tube is a function of exit angle; stronger on axis ($\theta = 0°$) than at other angles [11, 49]. Therefore, the scaling factor, C_0, determined from curve fits to the data might also be expected to exhibit a similar trend. A cursory look at the scaling factors reported in Table 4.1 reveals that, although C_0 is largest at $\theta = 30°$, no clear trend with angle is evident. The absence of a clear trend is likely due to the interaction of the shock wave with the

surface and the end of the shock tube. A reviewer indicated that absence of a trend in the C_0 values may also be due to the use of single shocks at each strength, since multiple shocks at the same strength produce additional removal (see Section 4.3.1). Further investigation will be needed to determine whether single versus multiple shocks influences the value of C_0.

4.5 Removal Patterns

Figure 4.4 shows a deposit before and after 30° impingement of a shock generated with a valve pressure ratio of 5.25 ($M_0 = 1.67$) and Fig. 4.12 shows the more complicated removal pattern produced by 90° impingement of a shock generated with a valve pressure ratio of 2.79 ($M_0 = 1.37$). In both cases $H/D = 2.0$. The removal is more uniform for low impingement angles (Fig. 4.4) and strong shocks than for high impingement angles (Fig. 4.12) or weak shocks. When non-uniform removal was observed, the removal lengths reported in this chapter were to the most distant downstream position that exhibited 50% removal.

The structure of the particle removal pattern shown in Fig. 4.12 is produced as the various features of the flow exiting the shock tube illustrated in Fig. 4.10 interact with the surface. Since the normal shock reflection does not produce a radial flow near the axis, few particles are removed from the center of the interaction region. As the shock wave propagates along the surface, the reflection points move outward until the induced radial velocity exceeds the threshold velocity required to remove the particles. As the reflection points propagate radially and the angle between the shock normal and the surface decreases, the radial velocity increases and the incident shock strength decays. Eventually, the decrease in the shock strength overcomes the increases in post-shock velocity that accompany the decreasing incidence angle, causing the radial velocity to fall below that necessary to remove particles. The expected removal pattern, therefore, exhibits a single annulus of particle removal with inner and outer radii that demark the distances at which the radial velocity first exceeds and then falls below the threshold value.

In contrast to the removal pattern suggested by the shock evolution, the observed removal pattern shown in Fig. 4.12 clearly exhibits two annular removal regions. The expected annular region for particle removal by the shock wave lies between the marks labeled "B" and "C." The inner annulus has an average diameter, i.e., $0.5(\text{OD} + \text{ID}) = 5.4$ mm, the distance between the marks labeled "A," that is nearly equal to the average diameter of the shock tube exit (5.3 mm). This average diameter also corresponds to the approximate diameter of the startup vortex illustrated in Fig. 4.10. Therefore, the removal of particles from the inner annulus is likely due to the vortical flow, possibly in combination with the shock induced flow.

The double annulus removal pattern, depicted for 90° in Fig. 4.12, was observed at impingement angles as small as 45°. At oblique impingement angles, the removal annuli become increasingly more elliptic with their long axes aligned with the flow. Measurements of the major axes of the inner (α = distance A-A) and outer annuli (β = distance D-E), as well as the offset (δ = distance D-A) between their upstream (left) edges are presented in Fig. 4.13 for each impingement angle θ at fixed shock strength. The measured lengths have each been non-dimensionalized with respect to the shock tube exit diameter, D. The major axes of both the inner and outer annuli increased slightly and the offset between the annuli decreased dramatically with decreasing angle of impingement. At 45° the two annuli merged at the upstream edge, preventing accurate determination of β. At 30° the vortical removal region and the shock removal region were indistinguishable. The size of the error bars is determined from the standard deviation of annular dimensions measured for neighboring shock strengths at normal incidence. For practical applications, where particle removal is desired, glancing angles that produce less structure are preferable.

4.6 Summary

This chapter demonstrates that shock wave impingement can efficiently remove particles from surfaces. Limited gas is consumed in shock wave cleaning due to the short on-time of the IEC valve necessary to produce the shocks. In addition, since the shock

wave moves at supersonic speed, the particles are removed over a large area very quickly. Shallow impingement angles yielded uniform removal over larger areas. The observed removal patterns were consistent with the flow created as a shock wave exiting a tube interacts with a surface.

A model based on the far-field equivalence of an above surface shock source with a surface shock source was used to describe shock decay along the length of the surface. The curve fits of the observed removal length to this model yielded an estimate of the threshold shock strength required to remove the particles from the glass substrate.

Appendix

Galkowski [53] suggests that a unit-strength point shock source located a distance H above a plane surface produces a far-field wave pattern that is essentially equivalent to the wave pattern generated by a point source of double strength located on the surface directly below the elevated point source. A functional relationship between the initial shock strength generated at the surface and the distance that the spherical shock travels before decaying to a threshold value can be derived as follows.

The radius r of a strong shock that is produced at a point is dependent on the released energy E that generated the shock, the density ρ_1 of the undisturbed gas ahead of the shock, and the elapsed time t since the shock was produced. Dimensional analysis of these parameters yields only one nondimensional combination [48], η, that must, therefore, be constant. Rearrangement yields the following expression for the radius r:

$$r = \eta \left(\frac{E}{\rho_1} \right)^{\frac{1}{5}} t^{\frac{2}{5}} \tag{4.5}$$

Since the ambient density ρ_1 is constant in our experiments, the radial position r of the shock is dependent only on the released energy E and the elapsed time t.

Differentiation of Eq. (4.5) with respect to t and elimination of t using the original equation yields an expression for the variation of the shock speed u_s with radial

distance from the source.

$$u_s = \frac{2}{5}\left(\frac{\eta^5 E}{\rho_1 r^3}\right)^{\frac{1}{2}} \tag{4.6}$$

Note that, at $r = 0$, the shock speed is infinite. This derivation based on dimensional arguments does not account for the interactions that occur at the source and are, therefore, useful only for description of the far-field behavior.

Combining Eqs. (4.6) and (4.2) yields an expression for the dependence of the shock strength P_2/P_1 on the radius r, provided the released energy E is known:

$$\left(\frac{P_2}{P_1}\right) = 1 + \frac{2\gamma}{\gamma+1}\left[\frac{4\eta^5 E}{25\rho_1 c_1^2}\frac{1}{r^3} + 1\right] \tag{4.7}$$

In the present work, the released energy E is not known; however, a suitable choice of initial conditions for the shock strength at an initial radius can be used to determine the released energy. The initial shock strength is taken as $C_0(P_2/P_1)_o$ where $(P_2/P_1)_o$ is the generated shock strength at the tube exit and C_0 is a scaling factor for the proportional strength of the equivalent surface shock. The initial radius r_o is arbitrarily defined as the radius of the shock tube exit. Substitution of these initial conditions into Eq. (4.7) yields the following expression for the released energy:

$$E = \frac{25}{4}\frac{\rho_1 c_1^2}{\eta^5}\left\{\left[C_0\left(\frac{P_2}{P_1}\right)_o - 1\right]\frac{\gamma+1}{2\gamma} - 1\right\} r_o^3 \tag{4.8}$$

Finally, substitution of Eq. (4.8) into Eq. (4.7) yields Eq. (4.4) that was fitted to the threshold removal data to determine the shock-strength scaling factor, C_0, and the threshold shock strength, $(P_2/P_1)_{thresh}$.

Table 4.1: Parameters and fit results for each sample.

Sample	H/D	$\theta(deg)$	$\left(\frac{P_2}{P_1}\right)_{thresh}$	C_0
1	2.2	30	2.167	1.324
2	2.2	30	2.167	1.259
3	2.0	30	-	-
4	2.0	30	2.167	1.779
5	2.0	45	2.167	1.294
6	2.0	60	2.168	1.347
7	2.0	75	2.170	1.492
8	2.0	90	2.174	1.391
9	1.0	90	2.167	1.346

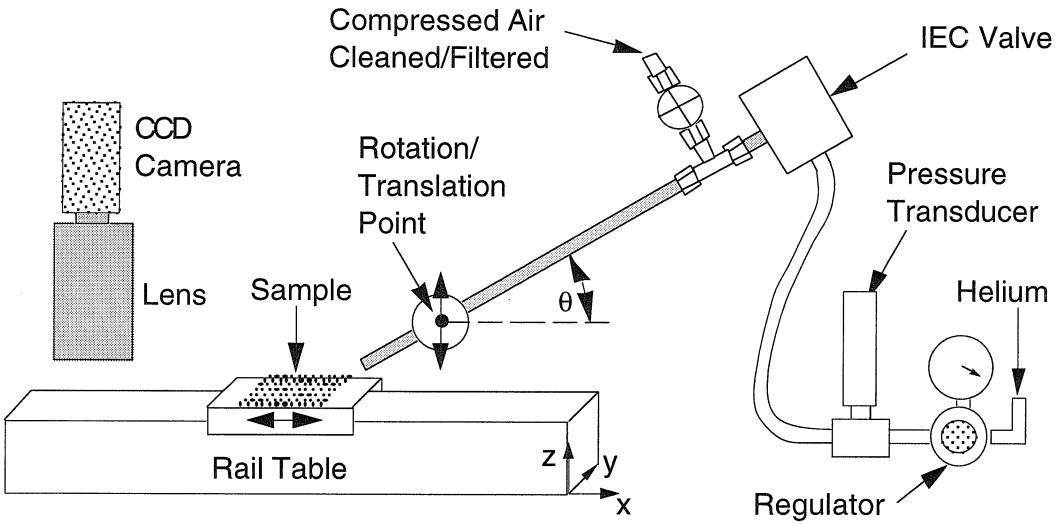

Figure 4.1: Shock wave apparatus.

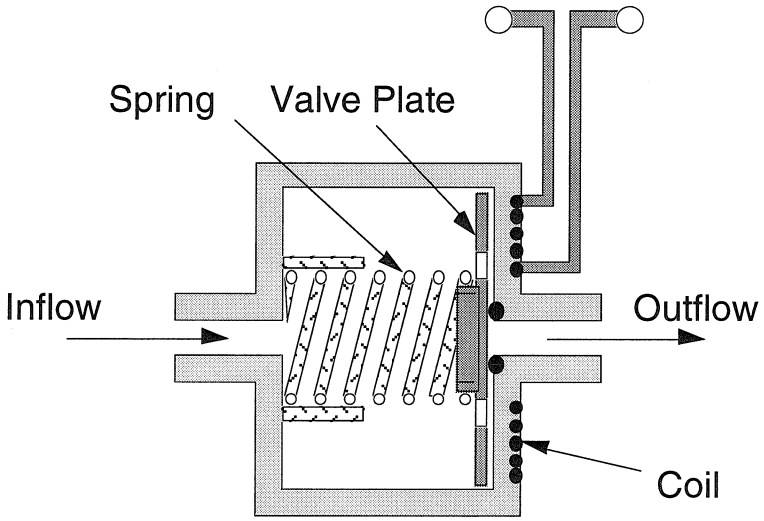

Figure 4.2: Detail of induced eddy current (IEC) valve.

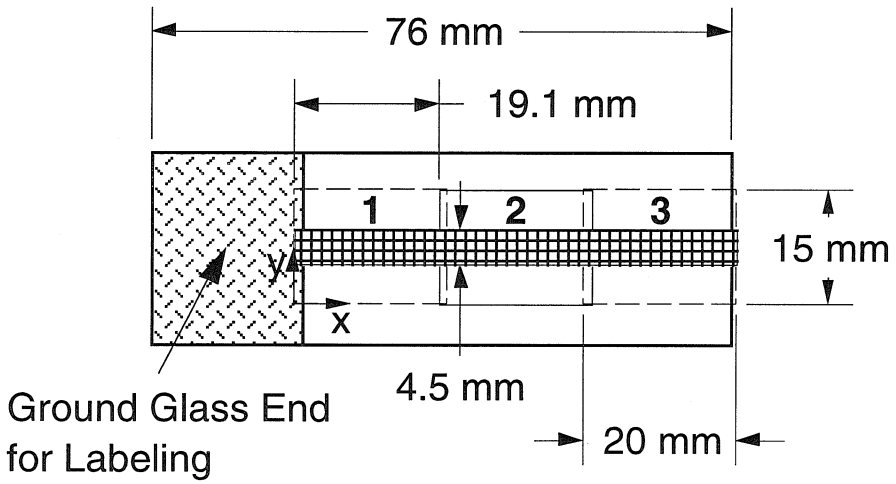

Figure 4.3: Microscope slide showing three image locations.

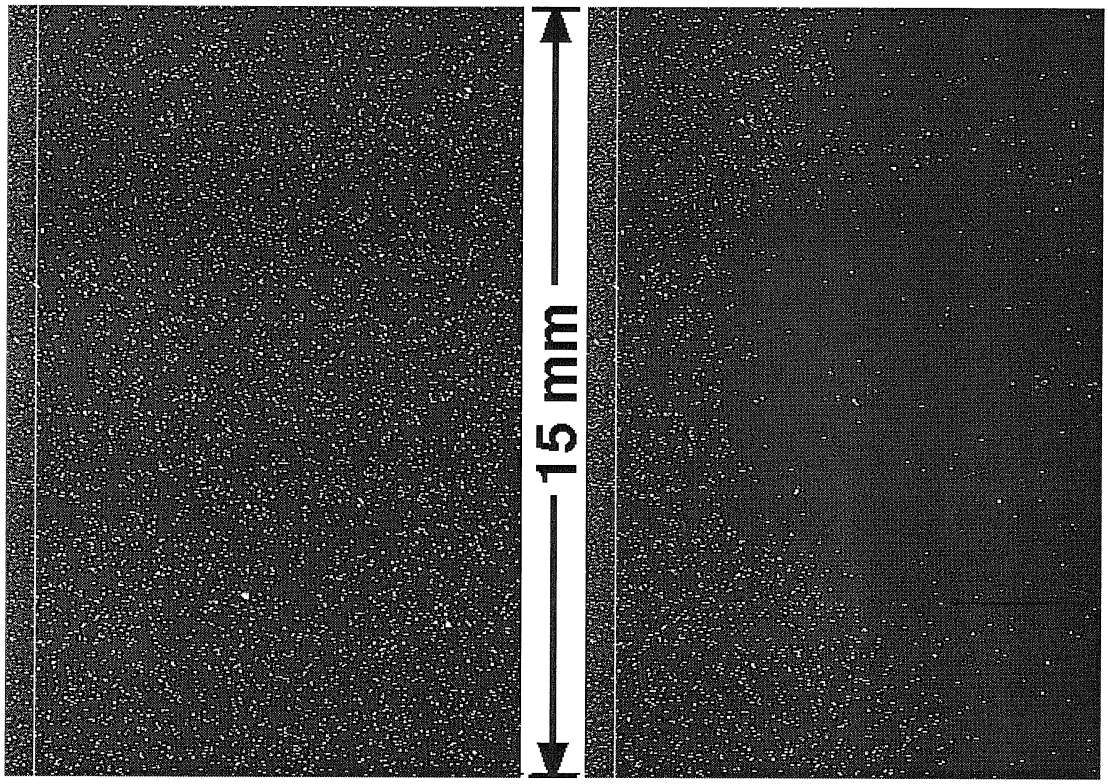

Figure 4.4: Raw images from Sample 3 recorded before (left) and after (right) firing the first shock wave.

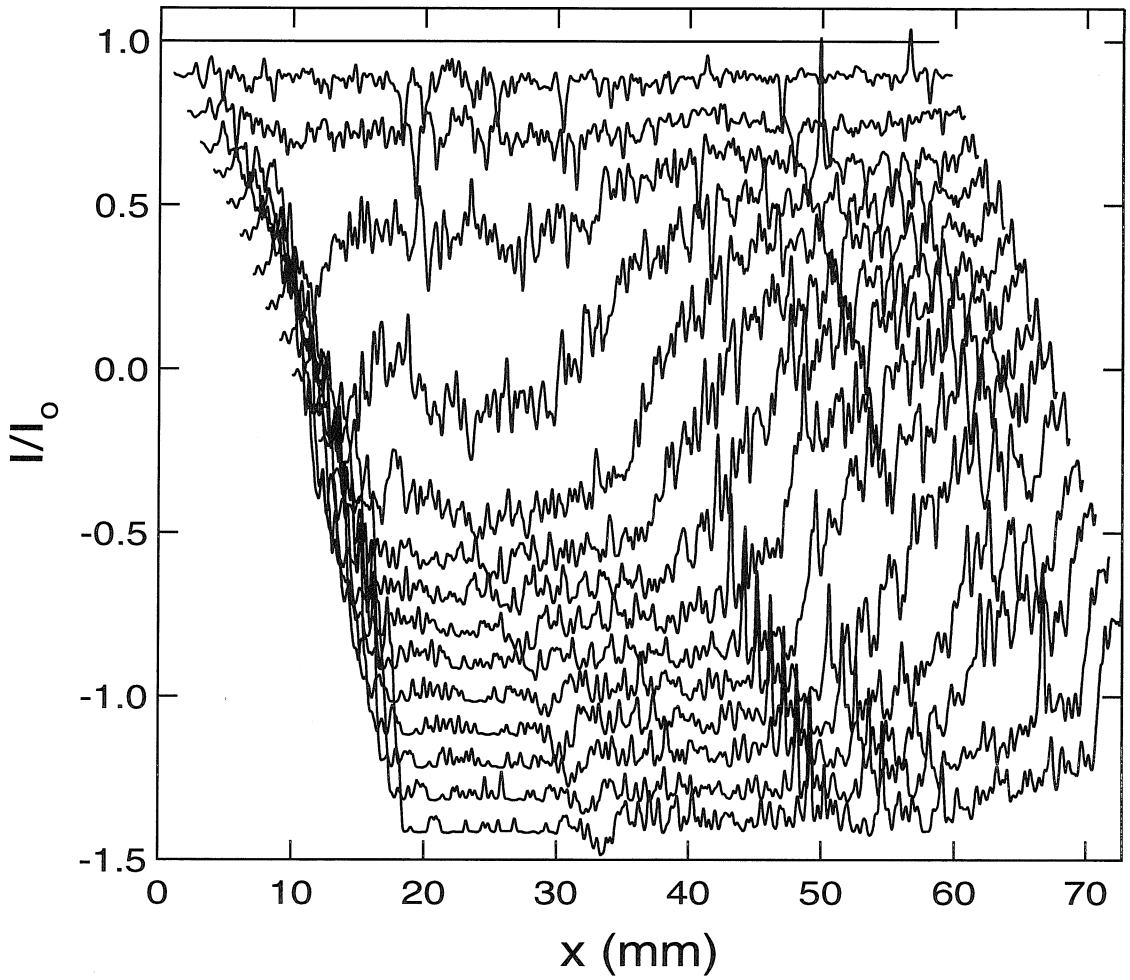

Figure 4.5: Set of corrected and smoothed profiles from Sample 1. Successive profiles are offset.

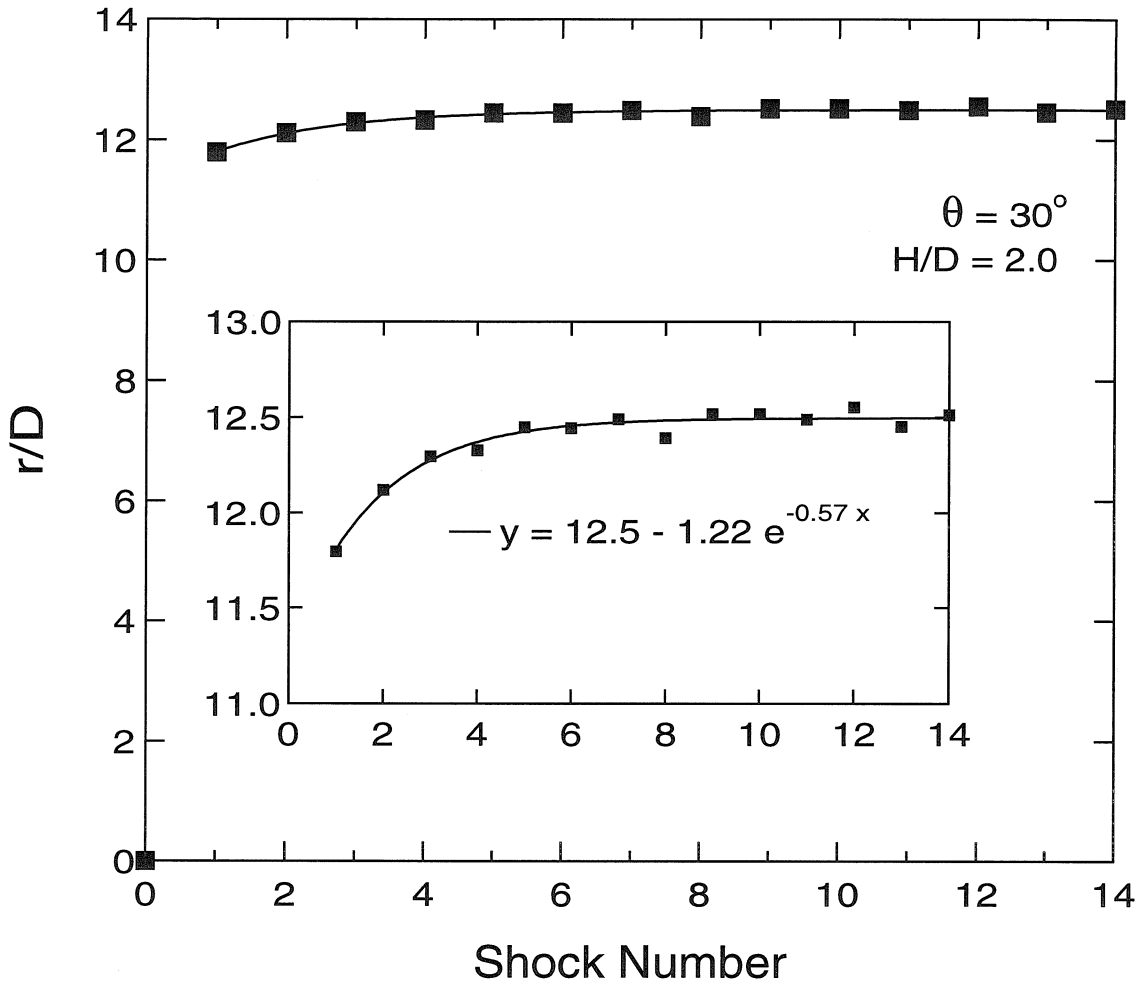

Figure 4.6: Effect of multiple shocks on removal length.

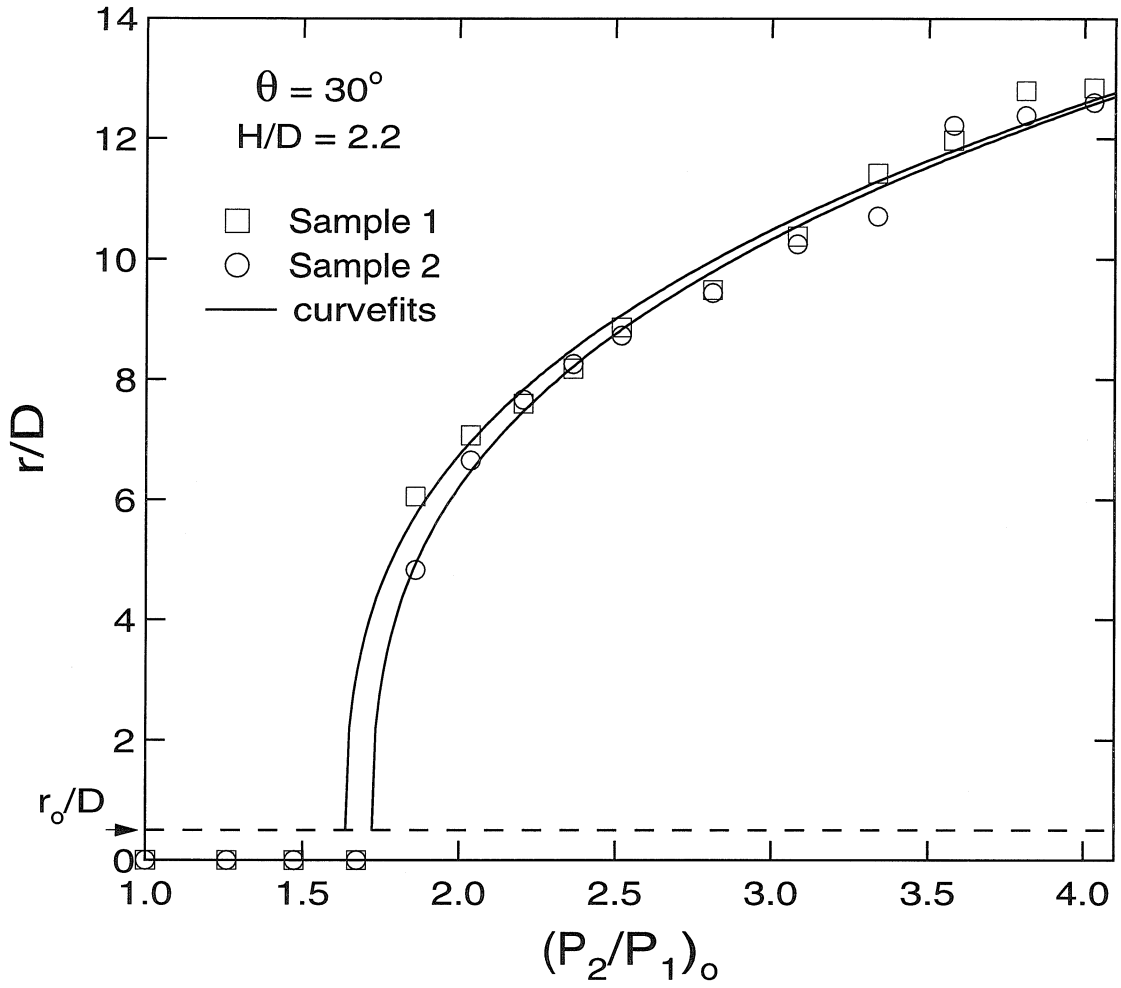

Figure 4.7: Repeatability of removal.

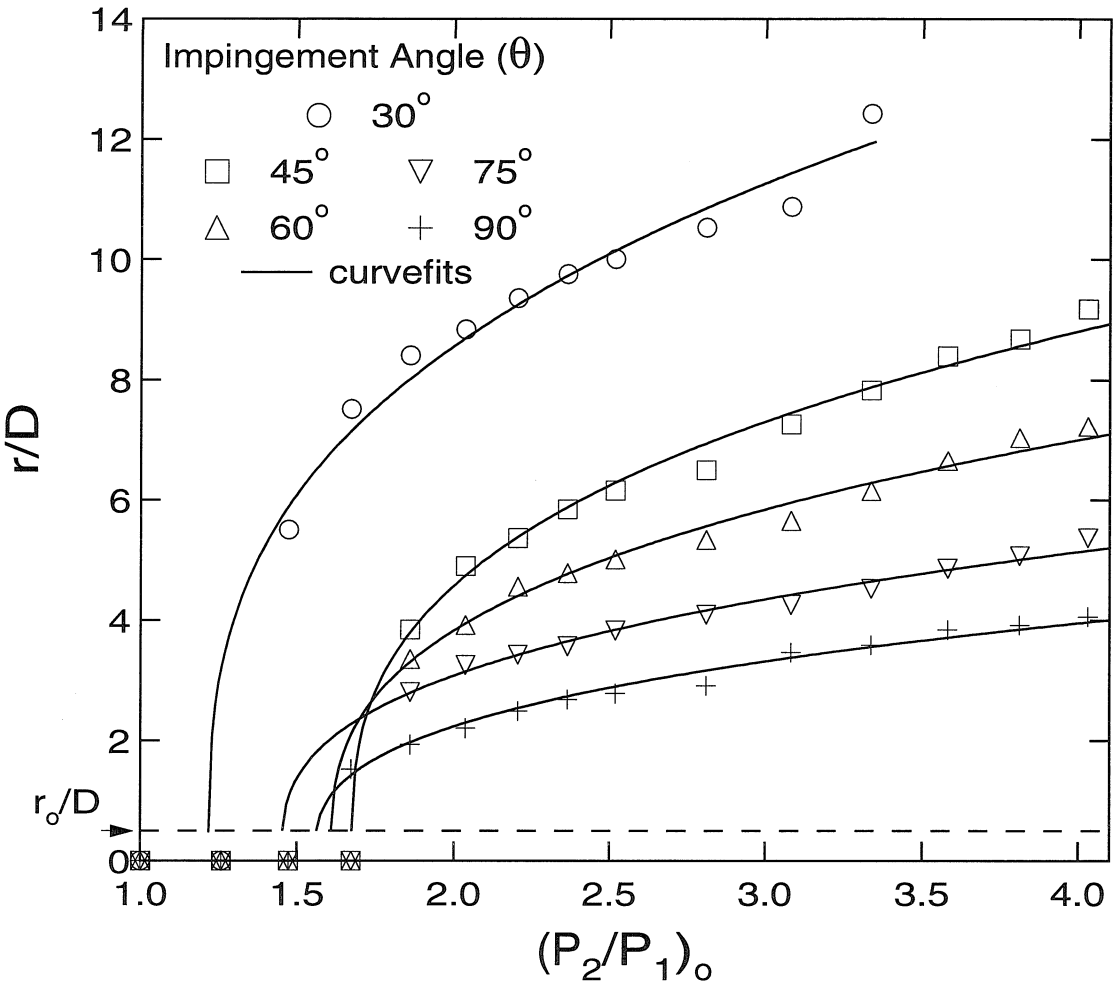

Figure 4.8: Effect of impingement angle on removal length.

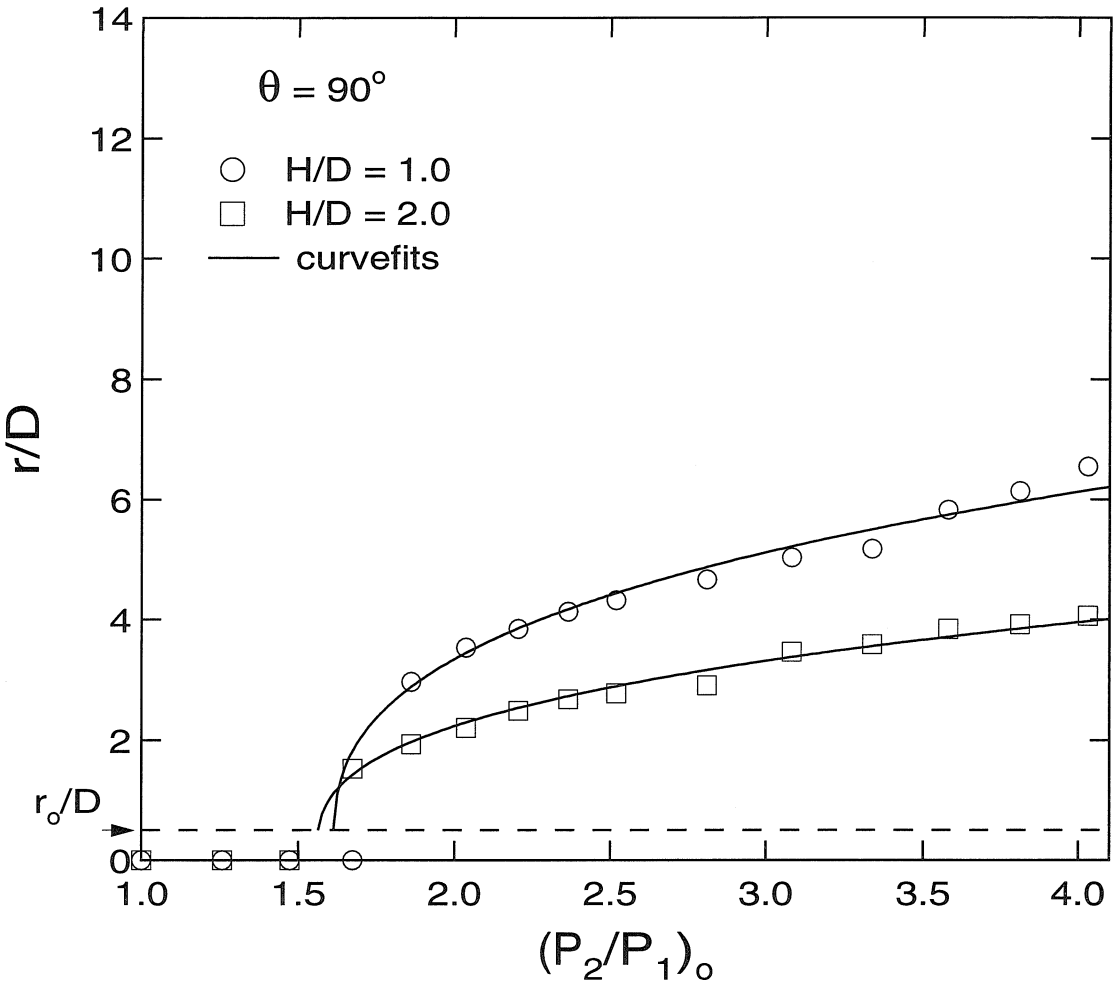

Figure 4.9: Effect of shock-tube exit height on removal length.

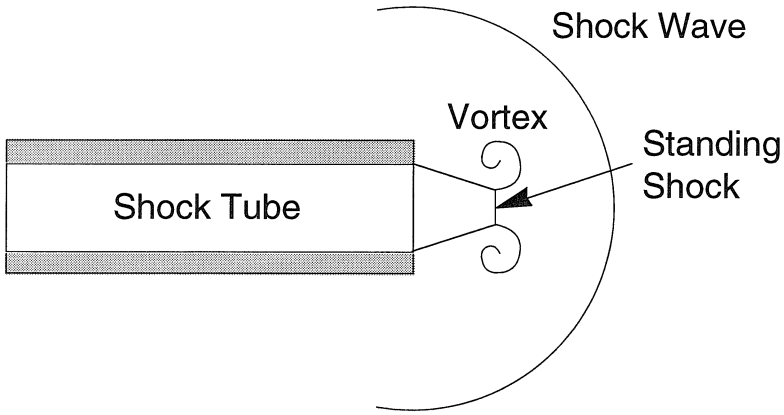

Figure 4.10: Flow features of shock exit from an open tube.

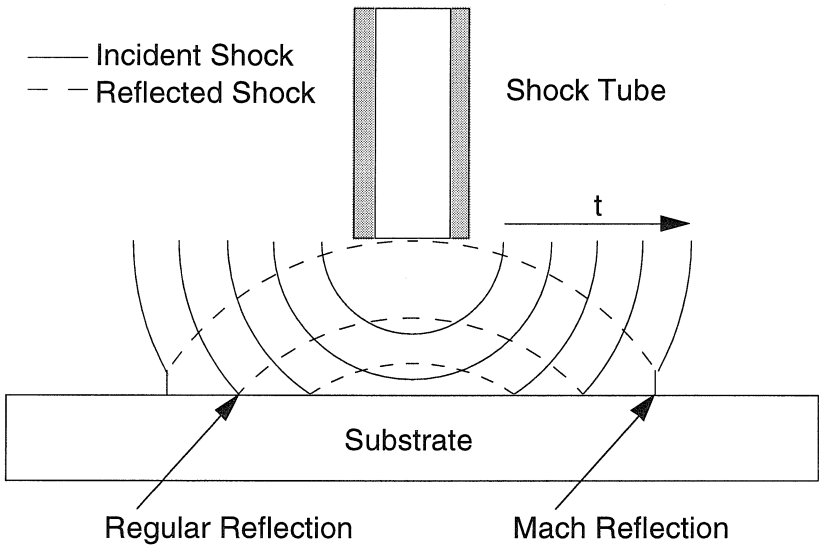

Figure 4.11: Shock reflection from a surface: normal impingement.

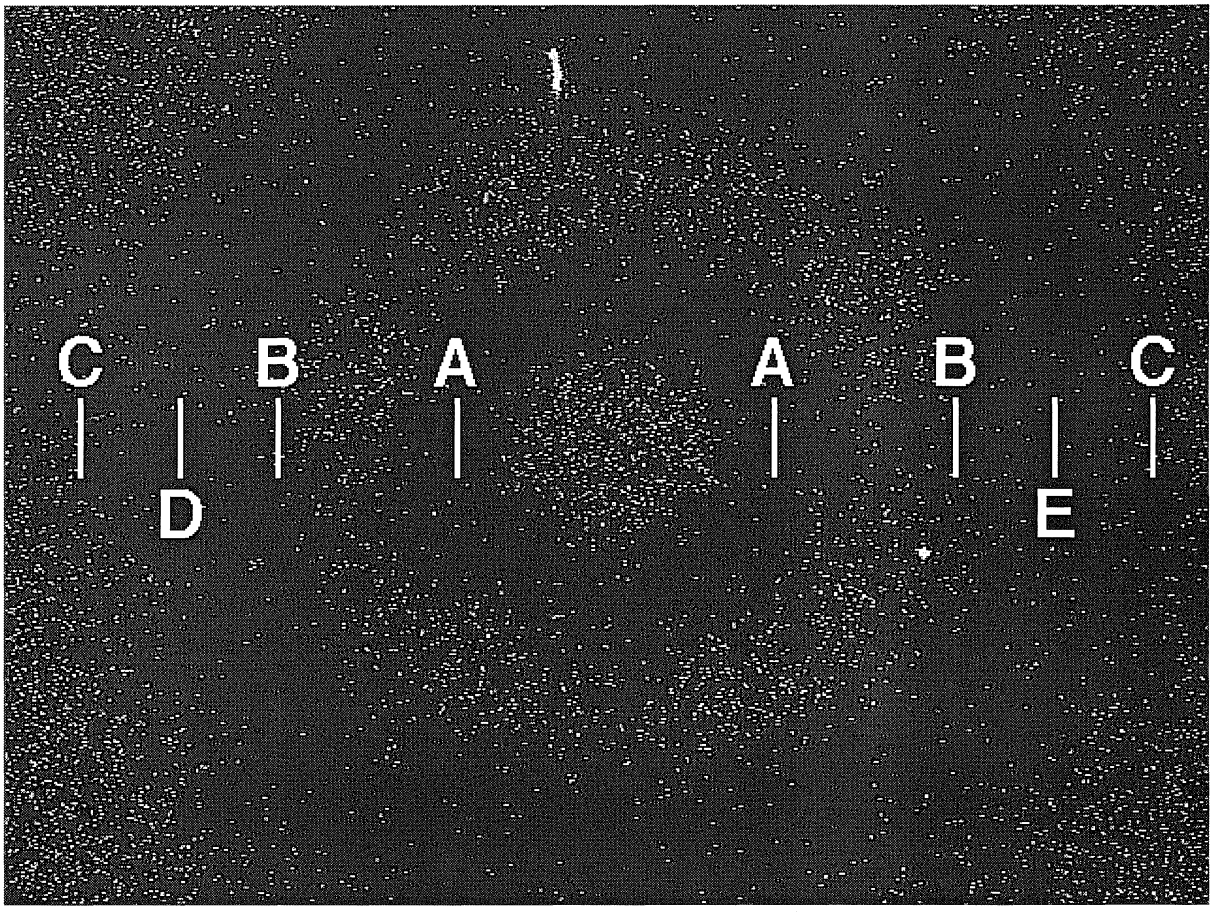

Figure 4.12: Particle removal pattern created by normal impingement.

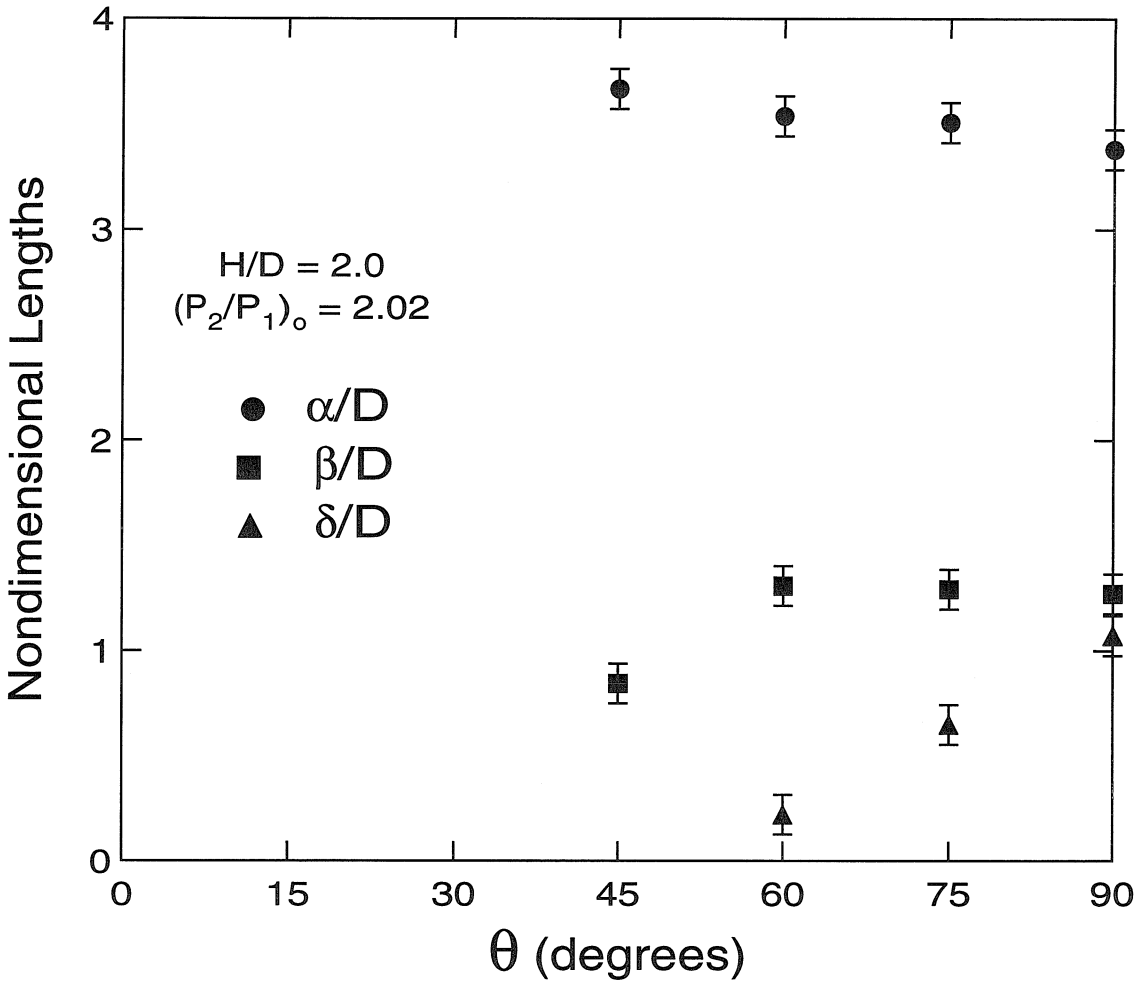

Figure 4.13: Dependence of annular removal dimensions on impingement angle.

Chapter 5 Entrainment of Fine Particles from Surfaces by Gas Jets Impinging at Normal Incidence

5.1 Abstract

This chapter describes an experimental study of the removal of fine (8.3 μm) polystyrene particles from a glass substrate using a gas jet at normal impingement. In order to avoid transient effects associated with jet startup, the sample was slowly translated under a steady jet. The translating gas jet produces a long clean path that provides very good statistics for exploring the effect of jet parameters. The dependence of the spatial distribution of removal efficiency on the jet pressure ratio, the jet height, and the translation speed is examined. Clean paths greater than 16 jet diameters wide are produced with a jet pressure ratio of 7 translating at 9.0 mm/s at a dimensionless height of 10. The path width is independent of the jet height at high pressure ratios and inversely dependent on the jet translation speed. A harmonic oscillator model for particle detachment accounts for the effect of translation speed. Results suggest that the particles act as nearly-quantized shear stress sensors that provide a direct, though as yet uncalibrated, measure of the surface shear stress. Further, knowledge of the pressure required to remove 50% of the particles from the central region of the path is sufficient to predict the extent of particle removal at higher pressures.

5.2 Introduction

Small particles adhere tenaciously to surfaces through a combination of physical attractions, chemical bonds, and mechanical stresses. Extraction of these particles is important both for cleaning surfaces and for detection of surface contaminants. In the semiconductor industry removal of foreign particles is a critical technology since particulate contaminants lead to defects in the micron-sized structures being fabricated and, ultimately, reduce product yield. Although prevention is the most effective way to control contamination [55], surface cleaning is still necessary to deal with those contaminant particles that manage to find their way to the clean surfaces. Detection of traces of explosives, drugs, and other contaminants is often limited by the low volatility of the particulate contaminants. Aerodynamic extraction of these tightly bound particles may greatly enhance transport to analytical instruments and dramatically enhance the ability to detect these substances.

Many fundamental studies of particle entrainment from surfaces have appeared in the literature [12, 15, 13, 14, 56]. The prior work has largely focused on particle entrainment by fully developed turbulent flows, either boundary layer or pipe flows where turbulent bursts are thought to account for most of the entrainment. In most experiments, the entrainment rate is initially high due to the start-up of the flow and then gradually decreases with time as the easily dislodged particles are removed and only more tightly bound particles remain [14, 57, 58, 59].

Aerodynamic extraction of particles from surfaces for either cleaning or chemical analysis is typically accomplished by impinging a gas jet on the surface to impart sufficient aerodynamic forces to the target area of the substrate to dislodge the particles. A number of investigators have probed particle removal by stationary jets by counting particles in a small region centered at the geometric intersection of the jet axis and the particle laden surface [22, 23, 16, 17, 18, 19, 20]. The removal efficiency has generally been found to increase with increasing jet pressure and decreasing jet height, both of which tend to increase the impinging gas velocity, and with increasing particle diameter which leads to an increase in the relative importance of aerodynamic

forces over adhesion forces.

A number of experiments have been designed to probe the efficacy of transient jets for particle extraction, including studies of pulsed gas jets [22, 23, 24], and so-called vibrating gas jets [25]. Using repeated jet pulses, Otani *et al.* [22] observed that the removal efficiency was better correlated with the number of times that the jet was started than with the time the surface was exposed to the jet. Otani *et al.* [24] later used repeating jet pulses of 1 s duration to enhance surface cleaning. In contrast, Masuda *et al.* [23] found that pulsing an impinging jet did not significantly enhance particle removal. Gotoh *et al.* [25] compared the removal efficiency obtained with a plane jet and a plane jet with a vibrating plate at the exit. He reported that the vibratory flow improved the removal, although variation in the ratio of the jet height above the surface to the width of the jet nozzle from 40 for the plane jet to 10 for the vibratory plane jet likely accounts for much of the difference. These contradictory conclusions may result from subtle differences in the experiments. The position of the jet nozzle and its flow characteristics couple with the jet-surface interaction and the dynamics of the valve opening process. Both effects are important, but they cannot be resolved with the presently available data.

The forces imparted to a surface-bound particle by an impinging jet have not been quantified in the previous studies. Typically, the jet was started while the sample was positioned under the nozzle [22, 23, 18, 19, 20], with the jet flow and duration being controlled by a solenoid valve. This procedure exposes the sample to the start-up transient with a strength that depends on the opening speed of the valve and on the length and impedance of the tubing and other components in the flow system. The transient weakens after exiting the jet nozzle, so the effect on particle removal decreases with increasing jet height. Liu *et al.* [16] also positioned the sample under the jet prior to starting the jet flow; however, the jet flow was controlled using a manually operated needle valve that probably produced a more gradual start-up of the jet than did the systems with solenoid valves.

In the present work, we seek to understand particle entrainment by a steady impinging jet. To avoid the start-up transients, well characterized samples are slowly

translated under a fully developed jet that impinges normal to the surface. Translation of the jet relative to the surface cleans a stripe on the surface, from which some of the forces involved in particle removal can be probed. Because the start-up transients are eliminated from this study, results from prior studies of fully developed impinging jet flow provide a basis for assessing the forces that contribute to particle detachment from the surface.

5.3 Experimental

5.3.1 Translating Jet Apparatus

The apparatus used for this investigation is illustrated in Fig. 5.1. The system consists of a high speed rail table with a vacuum-chuck sample holder, and a circular jet nozzle mounted to a y-z traverse at the translation point. The rail table motions were controlled via RS-232 communications from the computer to a Compumotor PDX-15 motor controller. The jet pressure is adjusted using the regulator and measured with a Lucas P4100 pressure transducer reported to have an accuracy to 0.03% of full scale with a range 0 to 6.9 MPa sealed gauge relative to standard atmospheric pressure. The height (z) and horizontal position (y) of the jet are adjusted using linear micrometer stages. A HeNe laser sheet provides glancing angle illumination of the particles on the glass substrate so that they appear bright against a dark background. Dark-field images of the particle laden surfaces were recorded using a CCD camera equipped with a telephoto lens and connected to a Macintosh computer using a Scion LG3 frame grabber card.

5.3.2 Sample Preparation

Quantitative studies of particle entrainment by impinging gas jets require test samples that consist of well characterized particles on well characterized surfaces. The surfaces were prepared by scrubbing with phosphate-free detergent under a stream of distilled water, rinsing thoroughly with distilled water, rinsing with 1:1 nitric acid, and then

rinsing again with distilled water. Finally, the microscope slides were baked at 400°C for one hour and cooled in a dry box for a minimum of 12 hours prior to the deposition of particles.

Well characterized particles of polystyrene (8.3 μm diameter, Mw = 114,200 amu) were produced in a particle synthesis apparatus. A vibrating orifice aerosol generator (VOAG), specially designed to work with organic solvents [45], generated uniformly sized droplets of toluene/polystyrene solutions. Although the standard deviation for the particles used in this study was not measured, the standard deviation was approximately 0.2 μm for similarly sized particles produced with the same apparatus. The droplets were entrained in nitrogen carrier gas and transported through a heated drying column installed directly below the VOAG. Inside the drying column, the temperature of the upper part was maintained below the softening point of the polymer while the temperature of the lower part was maintained near ambient to minimize necking of the particles after they were deposited on the cool slides by gravitational sedimentation. The particle generation procedure was described in more detail in Chapter 2. The prepared samples were then stored in a dry box for a minimum of 24 hours prior to use in the experiments.

5.3.3 Procedure

A microscope slide with particles deposited uniformly over the surface was mounted flush with the surface of the translation stage using the vacuum chuck. The stage was then moved in steps under the CCD camera to record images of the initial spatial distribution of deposited particles. A full set of three images, arranged to cover 58 mm of the slide surface with slight overlap (see Fig. 5.2), was obtained both prior to passing the jet over the surface, and after each subsequent jet pass to record the spatial distribution of particle removal. Each recorded image contained 640 x 480 pixels with 256 levels of grey and was integrated on the CCD chip for a total of 12 frames (0.4 s) to enhance the signal-to-noise ratio. The level of magnification (32 μm/pixel) in these images is not sufficient to resolve individual particles; however,

pixel intensity is proportional to the density of the particles within that imaged region of the sample. Particle loadings were small enough that few pixels see multiple particles. The first set of three images from each sample served as the definition of the initial state from which all variations were measured.

Once the initial images were recorded, the air jet with a pressure ratio P_{jet}/P_{atm} was started on the opposite side of a barrier that was positioned to isolate the slide from the start up transient. The slide was then translated at a constant velocity under the barrier and then under the air jet. The slide was then returned to the camera location to record the changes in the surface density of deposited particles. Fig. 5.3 shows typical images obtained before and after the slide was exposed to the jet.

In a typical experiment, the sample was passed under the jet 12 times at a fixed translation speed and jet height but with successively increasing jet pressure. This was done to maximize the information obtained from a small number of samples based on the assumption that all particles that can be removed by the jet at a particular pressure are removed in the first pass. This assumption was tested prior to conducting the reported set of experiments. The sequence of jet pressure ratios (P_{jet}/P_{atm}) employed in these experiments was: 1.11, 1.25, 1.39, 1.53, 1.67, 1.88, 2.10, 2.45, 3.16, 4.57, 5.98, and 6.97. Pressure ratios less than 1.89 produce a subsonic jet flow while those greater than 1.89 produce sonic flow at the jet outlet. For pressure ratios greater than 1.89, further expansion of the jet gas downstream of the exit leads to supersonic flows, so the jets in this regime are termed underexpanded supersonic jets.

Constraints of the particle synthesis apparatus limited single-run production to nine samples with the desired particle density ($300/mm^2$). Due to slight run-to-run variations in the polymer particles, the parametric variations reported here are based upon nine samples produced in a single synthesis run. Parametric investigations explored the effect of translation speed (1.8, 9.0, 45, and 270 mm/s) and jet height (2.5, 5, 7.5, and 10 mm) on particle removal. Table 5.1 summarizes the experimental conditions explored with each sample. The translation speed was fixed at 9.0 mm/s and the jet height was fixed at 5 mm when they were not the object of parametric

variation.

5.3.4 Data Analysis

The samples initially contained a nearly uniform density of monodisperse particles. In the dark-field images, the particles appeared as bright spots on a dark background (see Fig. 5.3). After passing the sample under the jet, a path (stripe) appeared in the image as a cleaned (dark) area. This path widened as the jet pressure was increased. A rectangular region of the images that included the entire "y" extent of the image and extended from x=2.2 to x=16.0 mm was selected for determining the density profile of the removal path. The origin and axes of the image coordinate system (x,y) are shown in Fig. 5.2. The selected "x" extent was limited to avoid inclusion of the frosted region of the slide on the left of frame 1 and to avoid edge effects at the right edge of frame 3 (see Fig. 5.2). An average pixel intensity was calculated for each row of pixels in the selected region and plotted as a point on the density profile of that region. Neither the initial distribution of particles nor the intensity of the laser sheet used to illuminate them is perfectly uniform. To account for the variations in intensity that were present even before particles were removed by the jet, the pixel intensity profiles for each frame of each sample were corrected by dividing by the corresponding intensities obtained from the images of the initial state.

The effect of background scattering noise in the cleaned region was reduced by first determining the "cleaned" level from the center of the path at the highest pressure and subtracting it from all the profiles before dividing by the initial profile. The final division process produces a normalized average row intensity (I/I_0) profile with a value "0" in the cleaned region and a value "1" in the uncleaned region. To further reduce the noise on the density profiles, the profiles from each acceptable image location were averaged. A full set of these corrected and averaged profiles is shown in Fig. 5.4 that was taken from Sample 1. As the pressure is increased, the profiles first deepen and then widen.

Several features of these profiles are noteworthy: (1) In some profiles, particularly

at the lower pressures where particles are just beginning to be removed from the path, particles are redeposited on the sample beyond the edge of the path to produce a higher than initial intensity. (2) As the particles start to be removed and form a dip near the center of the profile, a ridge is visible at the center of the dip. This ridge represents a region at the center of the path, directly beneath the jet, where the particles are not being removed as effectively as they are toward the edge of the path. (3) The slopes of the profiles in the transition from the cleaned path to the uncleaned edges are similar for all of the profiles except at the highest pressures.

Once the profiles were corrected and averaged for each sample, the path width w, the removal efficiency ϵ at the center of the path, and the threshold pressure ratio $(P_{jet}/P_{atm})_{50\%}$ were determined. The path width was simply defined as the distance between the 50% particle density points on the two sides of the removal path. The removal efficiency was determined by averaging 25 profile values (0.8 mm) centered within the removal path. The resulting removal efficiency data were plotted versus the jet pressure ratio and fitted with a hyperbolic tangent of the form

$$y = 50 + 50 \tanh(C_0(x - C_1)) \tag{5.1}$$

where C_0 is representative of the slope of the transition region and C_1 is the value of the pressure ratio at which 50% of the particles are removed, the threshold pressure ratio.

5.4 Results

The influence of jet height and translation speed on the removal efficiency and path width, and the repeatability of these measures, were examined using the data from nine samples. In some cases, the data revealed an anomalous narrowing of the removal path toward the edge of the glass slide (image location 3). Therefore, the density profiles from the third image location were eliminated from the profile averages calculated for samples 1, 3, 4, 6, and 7. In addition, the density profiles from the

second image location of sample 9 were also eliminated due to significantly reduced removal compared with the first and third image locations from the same sample. A total of 6 sets of density profiles were eliminated from the 27 sets obtained from the nine samples; the remaining sets were used to obtain the results reported here. Examination of the cleaning and deposition process revealed that the edge effect might be the result of vapor deposition from the metal holder used to support the samples during the baking process. In the presentation of these results, the removal efficiency and the path width have been set to zero at a pressure ratio of one, since this represents the case of no flow. Typical atmospheric conditions in the laboratory were P_{atm} = 97.7 kPa, T = 22°C, and relative humidity of 58%.

The viability of the assumption that all particles that can be removed by the jet at a particular pressure are removed in the first pass was tested by passing a jet of a fixed pressure ratio (2.45) over a sample several times at 9.0 mm/s. The resulting intensity profiles are shown in Fig. 5.5. Note, that there is little change in the removal profile during the three passes. In fact, the path width only increased by 3% on the second pass and did not increase further on the third pass. Therefore, the removal obtained with one pass of the jet is considered representative of the total removal that is possible for the given conditions.

5.4.1 Repeatability

The experimental repeatability was evaluated using samples 1, 2, and 4 listed in Table 5.1. The removal efficiency curves and the path widths are shown in Figs. 5.6 and 5.7 respectively. As the jet pressure ratio is increased, both the removal efficiency and the path width increase. There is some variability in the removal efficiencies achieved at particular values of the pressure ratio, particularly in the region of rapid variation. However, the variability of the threshold pressure ratio, $(P_{jet}/P_{atm})_{50\%}$ = 1.41, determined from the standard deviation of the C_1 parameter of the hyperbolic tangent fits to these repeatability data, is small, ±0.07. Errors in the pressure ratio measurement, based on the instrumentation used, account for less than half of the

measured standard deviation. The path width data reveal a fixed offset that persists to the highest pressures. The path width uncertainty (± 0.4 mm) can, therefore, be estimated in terms of the standard deviation of the path width at the five highest pressures in the repeatability data set. The average removal efficiency and path width curves that are shown are used as the baselines for comparison in the parametric studies of jet height and translation speed. The uncertainties in these parameters are used to estimate error bars for other data sets.

5.4.2 Jet Height

The jet height was varied from $H/D = 5$ to 20 at a fixed translation speed of 9.0 mm/s. The resulting path widths are shown in Fig. 5.8. The threshold pressure ratios are reported in Table 5.1. Particle removal begins at a low pressure ratio when the jet is close to the surface. The path widths appear to converge to within experimental uncertainty after an initial startup. Thus, the overall path width is either independent of or weakly dependent on the jet height at high pressure ratios. This jet-height independence suggests that the removal threshold has moved from the impingement region (Section 5.5.2) to the wall-jet region of the impinging jet flow. In this region, the jet momentum dictates the extent of the removal rather than the proximity of the jet to the surface.

5.4.3 Translation Speed

The effect of translation speed on particulate removal was examined over the range from 1.8 to 270 mm/s at a fixed $H/D = 10$. The measured path widths are shown in Fig. 5.9. Both the threshold pressure ratios and the path widths are independent of speed at 1.8 and 9.0 mm/s. At speeds of 45 and 270 mm/s, the threshold pressure ratios increase significantly, and the path width is dramatically reduced. The other parametric studies discussed in this chapter were conducted at a speed of 9.0 mm/s (see Table 5.1), i.e., at the asymptotic limit of slow translation speed where all the particles that can be removed by the jet are removed in the first pass.

Initially, these results were somewhat surprising, since the translation speed is much smaller than the jet exit velocity. However, consideration of the resuspension process indicates that translation speed should influence entrainment. Essentially, a force must be applied to the particles long enough for them to be removed from the surface; the higher the force, the shorter the required time. Of course, if the force is too small, then the particles will never detach.

5.5 Particles as Shear Stress Sensors

The results described in Section 5.4 indicate that the particle laden surfaces provide a sensitive means for probing the effect of jet parameters on the spatial distribution and the effectiveness of particle removal by impinging gas jets. These variations were determined from the depth and width of the removal paths. Other features of the removal profiles (See Fig. 5.4), such as the presence of minima in paths with incomplete removal and the shape of the path edges, provide additional insight into aspects of the shear stress imposed by the jet and the distribution of particle removal forces.

5.5.1 Relationship between Shear Stress and Particle Removal

The force required to remove a particle from a surface will be affected by variations in the particle size and variations in the surface conditions. We assume that the distribution of required forces is Gaussian. Removal of 50% of the particles in a given region then indicates that the jet produces a maximum force on the bound particles in that region that is equal to the mean force $\bar{f}$ required for particle removal. Higher removal efficiencies indicate that the force exerted by the jet is greater than $\bar{f}$, and lower removal efficiencies indicate that smaller forces are exerted.

The removal efficiency data were used to determine the threshold pressure ratio $(P_{jet}/P_{atm})_{50\%}$ that is required to remove 50% of the particles from the central region of the removal path. At higher jet pressures, where a clear path was created, the path width was defined as the distance between the 50% removal points in the particle

density profile. These points indicate locations where the force exerted by the jet is also equal to $\bar{f}$. The sharp transitions in deposit density, seen in Figs. 5.4 and 5.6, suggest that the particles yield a nearly quantized force measurement at the surface. Thus, the removal force distribution function must be quite narrow. It is reasonable to assume that the imposed force $\bar{f}$ is a tangential force that is proportional to a threshold surface shear stress, $\tau_{50\%}$.

5.5.2 Shear Stress of Impinging Jets

The impinging jet flow consists of three regions: (1) the free jet region, upstream of any interaction with the surface, (2) the impingement region, where the jet is deflected to flow along the surface, and (3) the wall jet region, downstream of the impingement region, where the flow is aligned with the surface.

Beltaos and Rajaratnam [60, 61] made extensive measurements on both plane (two dimensional) and circular (axisymmetric) impinging incompressible jets ($(P_{jet}/P_{atm}) < 1.05$). They measured both static pressure and wall shear stress within the impingement region and emphasized that this region of the flow produces the most severe hydrodynamic action on the boundary. High values of wall shear stress in the impingement region indicate that strong tangential forces are being imposed on the surface and any particles that are bound to it. Both the shear stress, τ_o, data of Beltaos and Rajaratnam and those of Bradshaw and Love [62], for $\lambda = r/H \leq 0.22$, are well described by a single non-dimensional curve:

$$\frac{\tau_o}{\tau_{om}} = 0.18\left(\frac{1-e^{-114\lambda^2}}{\lambda}\right) - 9.43\lambda e^{-114\lambda^2} \tag{5.2}$$

The maximum shear stress τ_{om} is given by

$$\tau_{om} = 0.16\,\frac{\rho U^2}{\left(\frac{H}{D}\right)^2} \tag{5.3}$$

and occurs at $\lambda \approx 0.14$. In Eq. (5.3) ρU^2 represents the dynamic pressure (See Appendix) at the jet exit, and H and D represent the height of the jet exit above the

surface and the jet exit diameter. These equations and constants were determined from an approximation to the equations of motion in the impingement region using the functional form of the pressure and the shear stress determined from measurements [61]. It is also noteworthy that these measurements were conducted at values of $H/D > 15$ and the velocity profile of the jet was fully developed prior to reaching the surface.

The expressions for the shear stress given in Eqs. (5.2) and (5.3) were derived for incompressible ($P_{jet}/P_{atm} < 1.05$) impinging circular jets at normal incidence. The authors are unaware of any shear stress measurements that have been performed in the impingement region of compressible impinging jets. Since the present work employs jets with pressure ratios up to 6.97 for which the flow is compressible but for which no shear stress data are available, we shall use relative shear stress estimates based upon particle detachment data to examine and extend the applicability of Eqs. (5.2) and (5.3) to the compressible jets used here.

The removal profiles shown in Fig. 5.4 for those cases with incomplete removal over the entire path reveal a central ridge flanked by two valleys where the removal is more effective. These valleys indicate the location of the maximum shear stress. Measurements of the distance, d, between these minima are plotted as a function of jet height in Fig. 5.10. The error bars represent the standard deviation of this measured distance, determined from the repeatability data sets, divided by $2H$. The horizontal lines represent the location of the maximum shear stress for incompressible flow ($\lambda = 0.14$) and the average location of the maximum shear stress ($\lambda = 0.09$) data at $H/D \geq 10$ where the value appears to be constant. The threshold pressure ratio for $H/D = 5$ (see Table 5.1) is 1.23, which is not much larger than the maximum of 1.05 studied by Beltaos and Rajaratnam [61]. Although a ratio of 1.23 produces compressible flow, the density at the jet exit is only 15% greater than the ambient density. The threshold pressure ratios for the larger heights extend from 1.41 to 2.06, well beyond the incompressible flow limit. Thus, a shift in the location of the maximum shear stress is not unexpected and may be the result of an increase in the length of the potential core for these compressible jets [63].

Dimensional analysis indicates that $(\tau_{om}/\rho U^2)$ should scale with (H/D). Eq. 5.3 indicates that, for incompressible fully-developed impinging jets at $H/D > 15$, $(\tau_{om}/\rho U^2)$ scales like $(H/D)^{-2}$. Clearly, as (H/D) decreases, the maximum shear stress diverges. Also, it is not clear what effect compressibility has on the functional relationship. The present data enable a limited test of this relationship.

In the present work, the threshold pressure ratio $(P_{jet}/P_{atm})_{50\%}$ and thus the threshold dynamic pressure $(\rho U^2)_{50\%}$ is determined at a range of jet heights (see Section 5.4.2). In each case, the imposed shear stress within the removal region is $\tau_{50\%}$. Therefore, it is reasonable to assume that the maximum shear stress, τ_{om}, imposed by each of the threshold jets is equal. Plotting the threshold dynamic pressure versus $(H/D)^2$ (see Fig. 5.11), therefore, yields the relationship between these quantities independent of variations in τ_{om}. The error bars used in the plot were determined from the repeatability data. A linear relationship exists among the first three points, but the point at $H/D = 20$ does not lie on the line. The high threshold pressure ratio (2.06) for that point indicates that the jet was supersonic, while all of the others were subsonic. Additional data will be necessary to understand the change in the relationship. Note that the threshold pressure ratio at each value of H/D is determined using a fixed central width (25 pixels or 0.8 mm) that corresponds to $\lambda \leq 0.08$ for $H = 5.0$ mm; adjustment of the central width to maintain a fixed value of λ for each H/D yielded no significant change in the results. The linear relationship that exists among the first three points suggests the following expression for the maximum shear stress imposed by compressible subsonic jets at modest to low values of H/D.

$$\tau_{om} = B_0 \frac{\rho U^2}{30.77 + 0.48\left(\frac{H}{D}\right)^2} \tag{5.4}$$

where the constant of proportionality B_0, originally 0.16 in Eq. (5.3), is left undefined since it is not clear what effect compressibility has on its value. This expression is used to compute relative threshold shear stresses, $\tau_{50\%}$, for each of the nine samples (see Table 5.2). The value is nearly B_0 for all but the two highest translation speeds and the largest jet height. The threshold shear stress increases with the translation

speed, since larger forces are required to remove the particles when the duration of the applied force is decreased (see Sections 5.4.3 and 5.5.4). The anomalously low value of $\tau_{50\%}$ for sample 9 simply reflects the lack of applicability of Eq. (5.4) to this case.

Since the particles provide a measure of the applied shear stress, the path width data can be used to probe the radial profile of shear stress and to test the validity of Eq. (5.2) and its extendability to the description of compressible jets. The threshold pressure ratio provides a common reference point for jets that are operated at different conditions. From the threshold pressure ratio, a threshold dynamic pressure $(\rho U^2)_{50\%}$ (See Appendix) and a threshold shear stress $\tau_{50\%}$ (Eq. (5.4)) can be estimated. This threshold shear stress is the same at each location where 50% of the particles are removed for jet pressure ratios exceeding the threshold value. In this way, the location of the threshold shear stress is determined with each jet pass beyond the threshold pressure ratio. Non-dimensionalizing the threshold shear stress by the maximum shear stress of the jet operating at a pressure greater than the threshold yields:

$$\frac{\tau_{50\%}}{\tau_{jet}} = \frac{(\rho U^2)_{50\%}}{(\rho U^2)_{jet}} \tag{5.5}$$

where (ρU^2) is determined at the jet exit, i.e., the shear-stress ratio is the same as the dynamic-pressure ratio. Using this ratio alleviates concern regarding the magnitude of B_0 and the functional dependence of the maximum shear stress on the jet height. The λ from Eq. (5.2) is simply the dimensionless halfwidth $w/2H$ determined in this study.

A plot of the dependence of the dynamic pressure ratio on radius, λ, is shown in Fig. 5.12 for all of the observations for which it was possible to define a path width. Eq. (5.2) is also shown on the plot as a solid curve. The data follow the general trend of Eq. (5.2), although most of the data lie to the left of the curve. Careful examination reveals that measurements obtained from sample 7 ($\triangle$) lie almost directly on the curve; these observations were made at $H/D = 5$ for which the location of the shear stress maximum coincided with that of the incompressible jet (see Fig. 5.10). The

observed shift to smaller radii for the other jet heights is consistent with the maximum shear stress occurring at $\lambda = 0.09$. The coefficients in Eq. (5.2) were determined from a curve fit to incompressible jet data. By fitting the functional form of Eq. (5.2) to the present data for $H/D \geq 10$, the dashed curve was obtained.

5.5.3 Distribution of Particle Removal Forces

We assumed in Section 5.5.1 that the distribution of forces necessary to remove particles from a surface is Gaussian. The standard deviation of this Gaussian would provide an indication of the uniformity of particle size and surface condition within the generated samples. The shape of the removal profiles in the region of transition from complete removal to non-removal provides insight into the removal force distribution provided the spatial variation of the applied forces is also known.

The dependence of dynamic pressure ratio on measured path width and the dependence of maximum shear stress on exit height are well described by Eq. (5.2) (or modified form for $H/D \geq 10$) and Eq. (5.4), respectively. These equations are used to convert the spatial coordinate of Fig. 5.4 to a shear stress coordinate, expressed in terms of the unknown constant B_0. The normalized intensity values, I/I_0, of Fig. 5.4 are converted to removal probability values by subtracting them from one. The result, shown in Fig. 5.13 for a single density profile, is the dependence of removal probability on the applied shear stress. It is reasonable to assume that the applied shear stress is proportional to the applied force.

The assumed Gaussian distribution [64] for the shear stress (force),

$$P_G = \frac{1}{\sigma\sqrt{2\pi}} \exp\left[-\frac{1}{2}\left(\frac{\tau - \tau_{50\%}}{\sigma}\right)^2\right], \tag{5.6}$$

is integrated up to a particular shear stress value, τ, to determine a removal probability, P_{rem}, for that applied shear stress. The integration is repeated for the full range of applied shear stresses until a complete removal probability vs. shear stress curve is generated for the selected mean $\tau_{50\%}$ and standard deviation σ. The calculated probability curve is compared to the data and the mean and standard deviation are

adjusted until a suitable fit is found. The integration process necessary to determine P_{rem} is conveniently eliminated by using tabulated values of the error function:

$$\mathrm{erf}(w) = \frac{1}{\sqrt{\pi}} \int_{-w}^{w} e^{-q^2} dq \tag{5.7}$$

so that

$$P_{rem} = \begin{cases} 0.5(1 - \mathrm{erf}(w/\sqrt{2})) & w \leq 0 \\ \\ 0.5(1 + \mathrm{erf}(w/\sqrt{2})) & w > 0 \end{cases} \tag{5.8}$$

where the factors of $\sqrt{2}$ provide consistency with the definition of the Gaussian probability, P_G, given in Eq. (5.6), $w = (\tau - \tau_{50\%})/\sigma$, and q is the integration parameter.

Removal probability curve fits were determined for all density profiles with definable path widths and the averaged parameters for each sample are listed in Table 5.2. The threshold shear stresses are close to those obtained with Eq. (5.4), demonstrating reasonable closure. This closure is expected, since Eq. (5.4) is used to convert the spatial scale to a shear-stress scale; discrepancies between the threshold shear stresses are due to the differences between the data and Eq. (5.2) (or its modified version) shown in Fig. 5.12. The standard deviation of the removal force distribution is near 0.26 B_0 for all but two cases, $H/D = 20$ and $V_{rem} = 270$ mm/s (see Table 5.2).

5.5.4 Influence of Translation Speed

It was noted in Section 5.4.3 that the path width decreased as the translation speed was increased. Fig. 5.14 depicts an alternative view of the same data. The solid curves, calculated with Eq. (5.2) using the appropriate coefficients, represent the relative magnitude of the wall shear stress distributions for each of the twelve pressure ratios. The shear stress curve for the maximum jet pressure ratio has been normalized to a maximum value of one and the curves for lower jet pressure ratios were divided by the same factor. The vertical extent of the plot has been limited to 0.5 to provide a clearer view of the data. The purpose here is to show the relative magnitudes

of the wall shear stress for the various pressure ratios without making any claims regarding the absolute magnitudes. The dashed curves are the calculated shear stress distributions for the threshold pressure ratio jets at each of the four speeds (also divided by the same factor used for the maximum pressure ratio). The two lowest dashed curves in the plot that lie nearly on top of one another are for 9.0 and 1.8 mm/s and, as noted above, represent the asymptotic translation speed limit. The threshold curves for 45.0 mm/s and 270.0 mm/s lie near the fourth and sixth solid curves. The measured path widths have been plotted on the appropriate solid curves for the jet pressure ratios that generated the cleaned paths. Each of these data sets begins at the peak of the applicable threshold shear stress curves. The shear stress is nearly independent of the path width for each of the translation speeds.

Fig. 5.15 shows the influence of translation speed on the threshold dynamic pressure. The shear stress required to remove 50% of the particles increases with translation speed. A line fit to the data indicates that the threshold dynamic pressure for a stationary sample is 78.8 kPa. For applied shear stresses below this threshold value, removal efficiencies will not reach 50% no mater how long the exposure time. The range of validity of this linear relationship cannot be determined with the present data.

The influence of translation speed on particle removal can be captured with a model following the approach of Reeks and Hall [65] who used an oscillator model to explain removal of particles in turbulent flows in cases where the average hydrodynamic forces did not exceed the surface forces. They assumed that the particle motion was that of a very stiff lightly damped oscillator that accumulated energy from the turbulent flow until it had sufficient energy to escape the surface forces.

For the present study, the surface-bound particle is modeled as a simple damped harmonic oscillator that is subjected to a time varying forcing as the jet passes. As a first order approximation, a fixed force F is assumed to be exerted on the particles for a short duration of time Δt. This time is proportional to the translation speed.

The particle equation of motion is written as:

$$m\ddot{z} + \beta\dot{z} + kz = F[H(t) - H(t - \Delta t)] \tag{5.9}$$

where m represents the particle mass, β and k represent the damping coefficient and the spring constant, respectively, and $H(t)$ represents the Heaviside step function. If the particle's vertical displacement z exceeds a threshold value z_o, the particle is assumed to detach from the surface. The response of the particle to the applied force is damped by the energy lost in the detachment of the particle. In the limit of infinite exposure time, the particle will only be removed if the magnitude of the applied force exceeds the threshold force $F_o = kz_o$. If the time duration of the applied force is too short, the threshold displacement will not be reached and the particle will not be removed. Thus the applied force must be increased in order to achieve the threshold displacement within the available exposure time. In this way, the model qualitatively captures the inverse dependence of the applied threshold force on the exposure time. Quantitative application of the model will require knowledge of the particle's adhesive forces and internal damping.

5.6 Summary

The translating jet is a useful tool for probing particle removal by impinging jets. The variation of particle removal with location in the cleaned stripe can be related to the local shear stress of the steady impinging jet since start-up transients are avoided.

The threshold pressure ratio for particle removal increases with jet height and with translation speed. At high pressure ratios the path width is independent of jet height. By relating the threshold dynamic pressure to the wall shear stress profiles, an observed reduction in path width with increasing translation speed is explained. A harmonic oscillator model for particle detachment accounts for the influence of translation speed on the threshold dynamic pressure.

The relationship between the dynamic-pressure ratio of the jet and the width

of the cleaned path is similar to that between the surface shear-stress ratio and radial distance for an incompressible circular jet at normal impingement [61]. For jet pressure ratios beyond the incompressible flow limit, similar trends are observed although the maximum shear stress shifts to smaller radii. The close agreement between the shear stress distribution inferred from particle removal profiles and published measurements of the surface shear stress suggests that the monodisperse polymer particles developed for this study provide a direct, though as yet uncalibrated, measure of the surface shear stress. Further, the assumption of a Gaussian distribution of the removal forces yields an estimate for their standard deviation. From these results, it appears that knowledge of the pressure ratio that is required to remove 50% of the particles from the central region of the removal path provides sufficient input to predict particle removal at higher pressure ratios.

Appendix

The dynamic pressure at the jet exit $(\rho U^2)_{exit}$ is determined from the jet pressure ratio P_{jet}/P_{atm} and the reservoir conditions using the compressible flow equations. P_{jet} represents the absolute pressure just upstream of the jet nozzle (reservoir pressure) and P_{atm} represents the absolute pressure in the laboratory. In the following discussion, the flow is assumed to be isentropic and the gas is assumed to be ideal [47]. The subscript *exit* refers to conditions at the nozzle exit (the minimum opening or throat). For an ideal gas, the sound speed a is:

$$a^2 = \gamma RT \tag{5.10}$$

where $\gamma = C_p/C_v$ is the ratio of specific heats, R is the gas constant and T is the absolute temperature. Assuming isentropic flow, Eq. (5.10) yields:

$$a_{exit}^2 = a_{jet}^2 \left(\frac{P_{jet}}{P_{exit}}\right)^{-\left(\frac{\gamma-1}{\gamma}\right)} \tag{5.11}$$

Applying conservation of energy to the isentropic flow, the jet velocity is found to be:

$$U_{exit}^2 = a_{jet}^2 \left[1 - \left(\frac{P_{jet}}{P_{exit}}\right)^{-\left(\frac{\gamma-1}{\gamma}\right)}\right] \left(\frac{2}{\gamma-1}\right) \tag{5.12}$$

Further using the isentropic flow relations to determine the gas density at the jet exit and the ideal gas law to relate the reservoir density to the ambient density, the dynamic pressure for subsonic flow conditions becomes:

$$(\rho U^2)_{exit} = \rho_{atm} a_{jet}^2 \left[\left(\frac{P_{jet}}{P_{atm}}\right)^{\frac{\gamma-1}{\gamma}} - 1\right] \left(\frac{2}{\gamma-1}\right) \tag{5.13}$$

For choked flow, $P_{exit} > P_{atm}$ and the velocity at the exit U_{exit} is equal to the sound speed at the exit a_{exit}. In this limit, the pressure ratio becomes:

$$\frac{P_{jet}}{P_{exit}} = \left(\frac{\gamma+1}{2}\right)^{\frac{\gamma}{\gamma-1}} \tag{5.14}$$

and the sound speed and the density become:

$$a_{exit}^2 = a_{jet}^2 \left(\frac{2}{\gamma+1}\right) \tag{5.15}$$

$$\rho_{exit} = \rho_{jet} \left(\frac{2}{\gamma+1}\right)^{\frac{1}{\gamma-1}} \tag{5.16}$$

Since $U_{exit} = a_{exit}$ the dynamic pressure at the nozzle exit is:

$$(\rho U^2)_{exit} = \rho_{atm} a_{jet}^2 \left(\frac{2}{\gamma+1}\right)^{\frac{\gamma}{\gamma-1}} \left(\frac{P_{jet}}{P_{atm}}\right) \tag{5.17}$$

When the flow at the nozzle exit is choked, the dynamic pressure is linearly proportional to the jet pressure ratio. When the pressure ratio exceeds the choked flow limit, the flow will continue to accelerate in the free jet region leading to supersonic flows.

Table 5.1: Parameters and threshold results for each sample.

Sample	H (mm)	H/D	V_{trans} (mm/s)	$(P_{jet}/P_{atm})_{50\%}$ (C_1)	$(\rho U^2)_{50\%}$ (kPa)
1	5.0	10	9.0	1.45	78.8
2	5.0	10	9.0	1.37	67.2
3	5.0	10	1.8	1.46	80.2
4	5.0	10	9.0	1.51	88.8
5	5.0	10	45.0	1.53	91.1
6	5.0	10	270.0	1.90	142.4
7	2.5	5	9.0	1.23	42.7
8	7.5	15	9.0	1.86	138.0
9	10.0	20	9.0	2.06	154.2

Table 5.2: Threshold shear stress and its standard deviation (Values expressed in terms of unknown constant B_0).

Sample	$\tau_{50\%}(kPa)$ Eq. (5.3)	$\tau_{50\%}(kPa)$ (Gaussian Fit)	σ (Gaussian Fit)
1	1.00	1.05	0.25
2	0.85	0.95	0.26
3	1.02	1.03	0.29
4	1.13	1.14	0.26
5	1.16	1.16	0.28
6	1.81	1.67	0.46
7	1.00	1.07	0.26
8	0.99	1.00	0.24
9	0.69	0.76	0.15

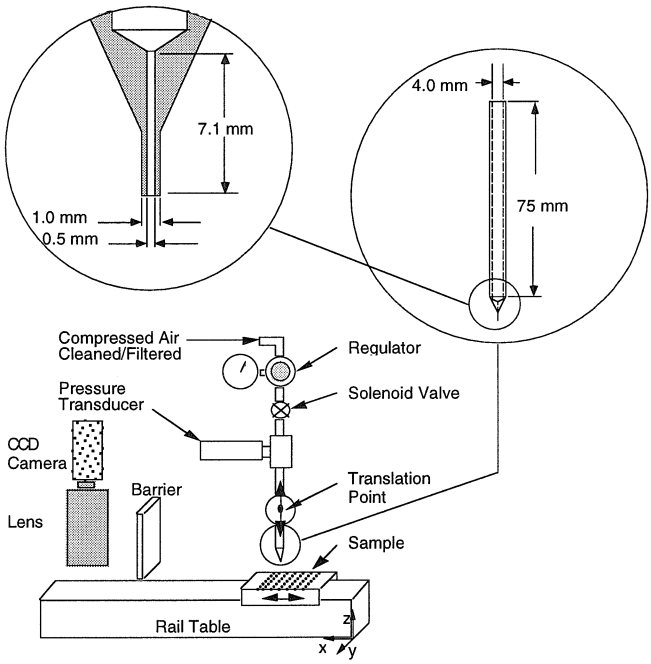

Figure 5.1: Translating jet apparatus.

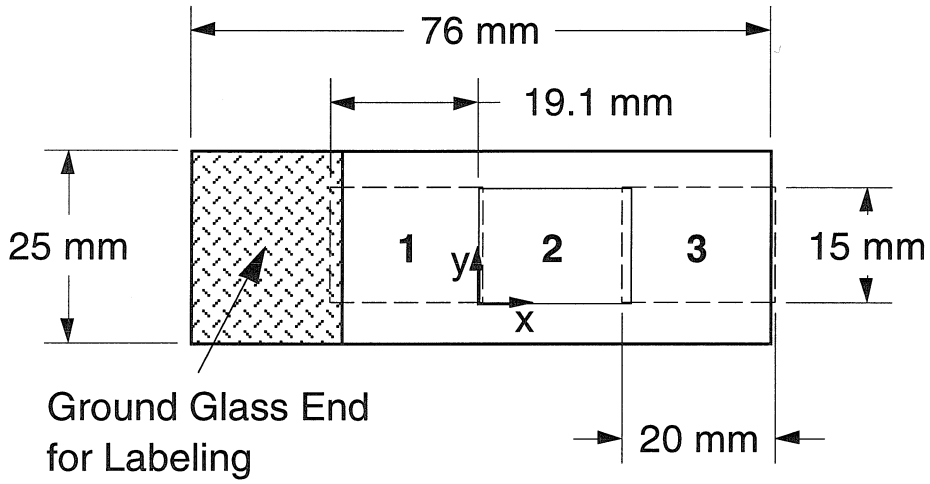

Figure 5.2: Microscope slide showing the three image locations.

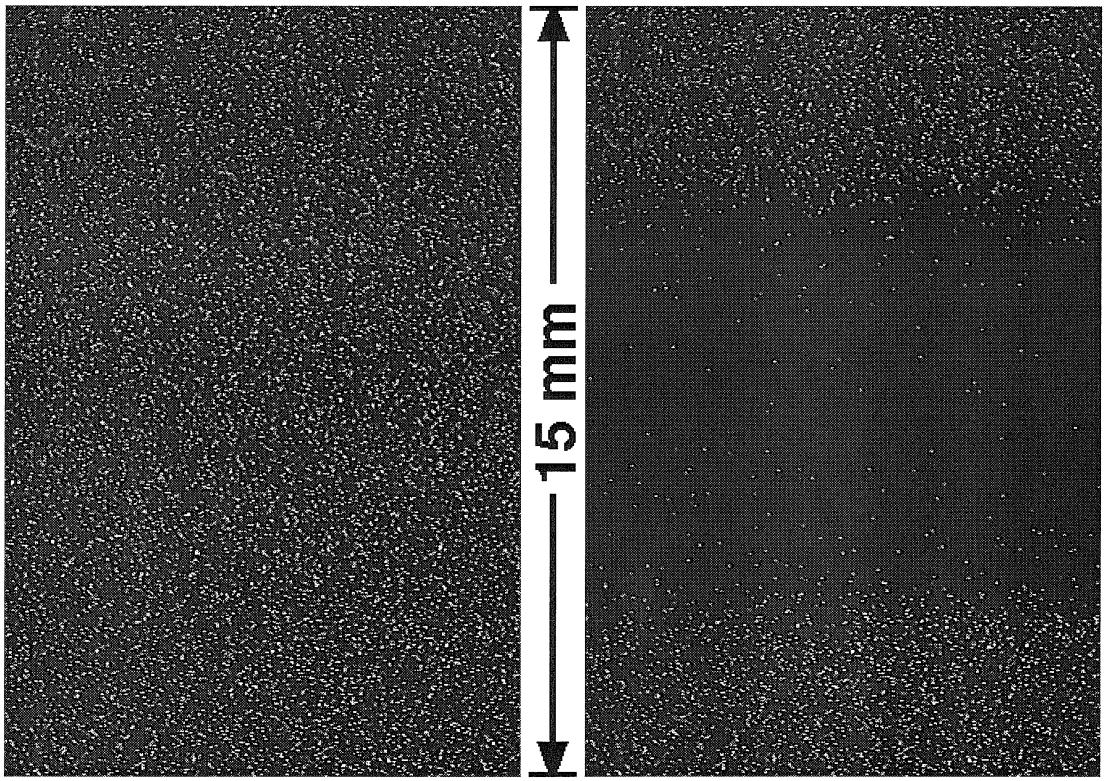

Figure 5.3: Raw images before and after exposure to translating jet.

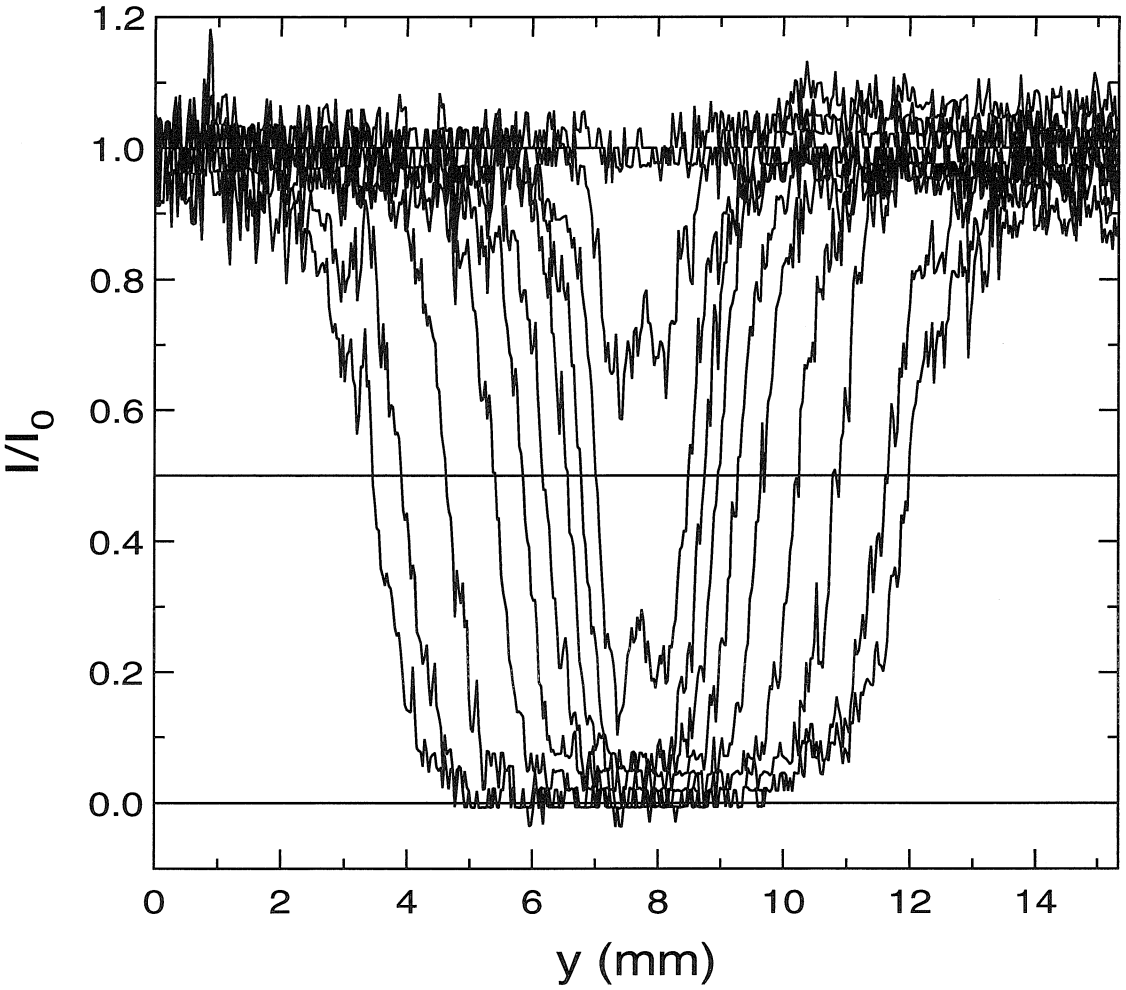

Figure 5.4: Set of corrected profiles from Sample 1.

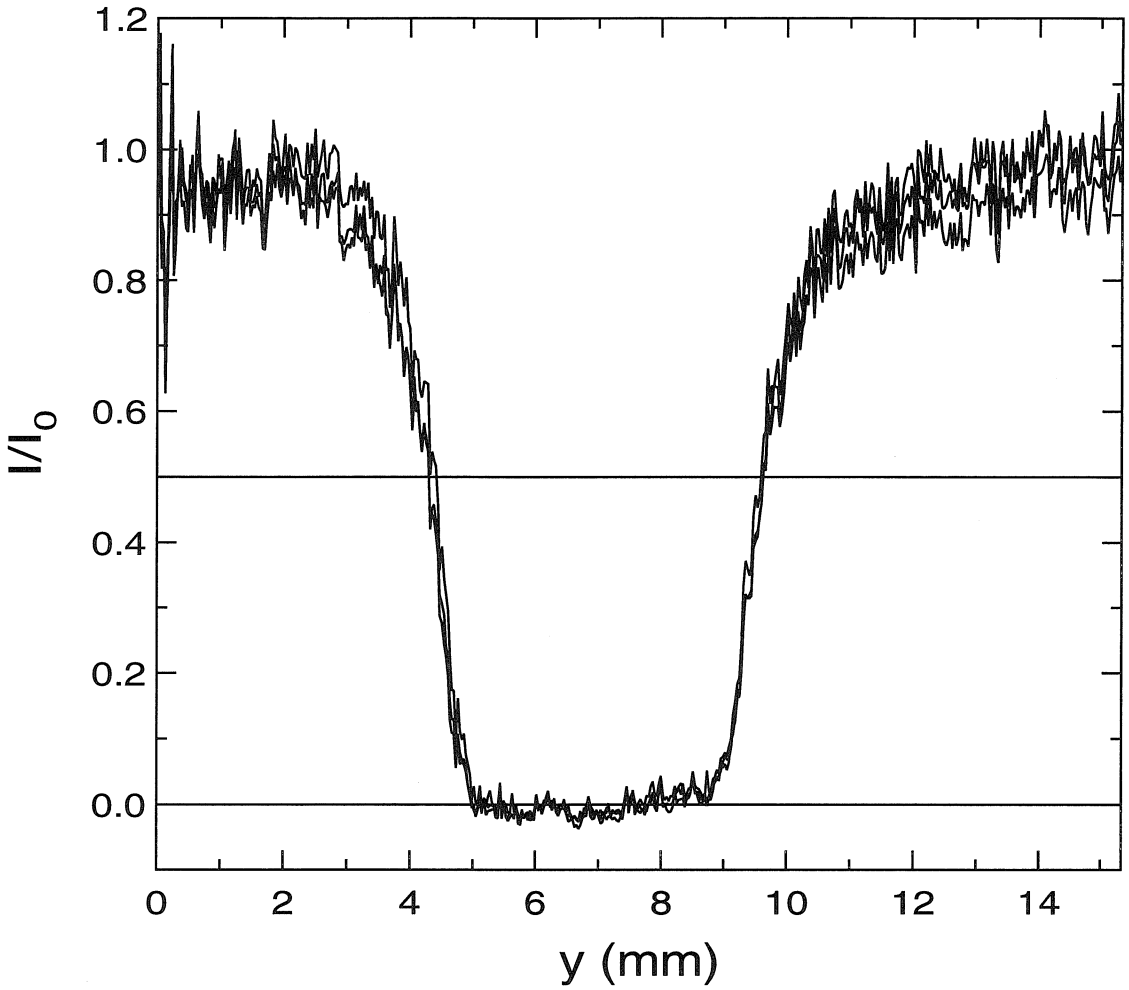

Figure 5.5: Corrected profiles from three jet passes at $H/D = 10$ and $V_{trans} = 9.0$ mm/s and a fixed pressure ratio of 2.45.

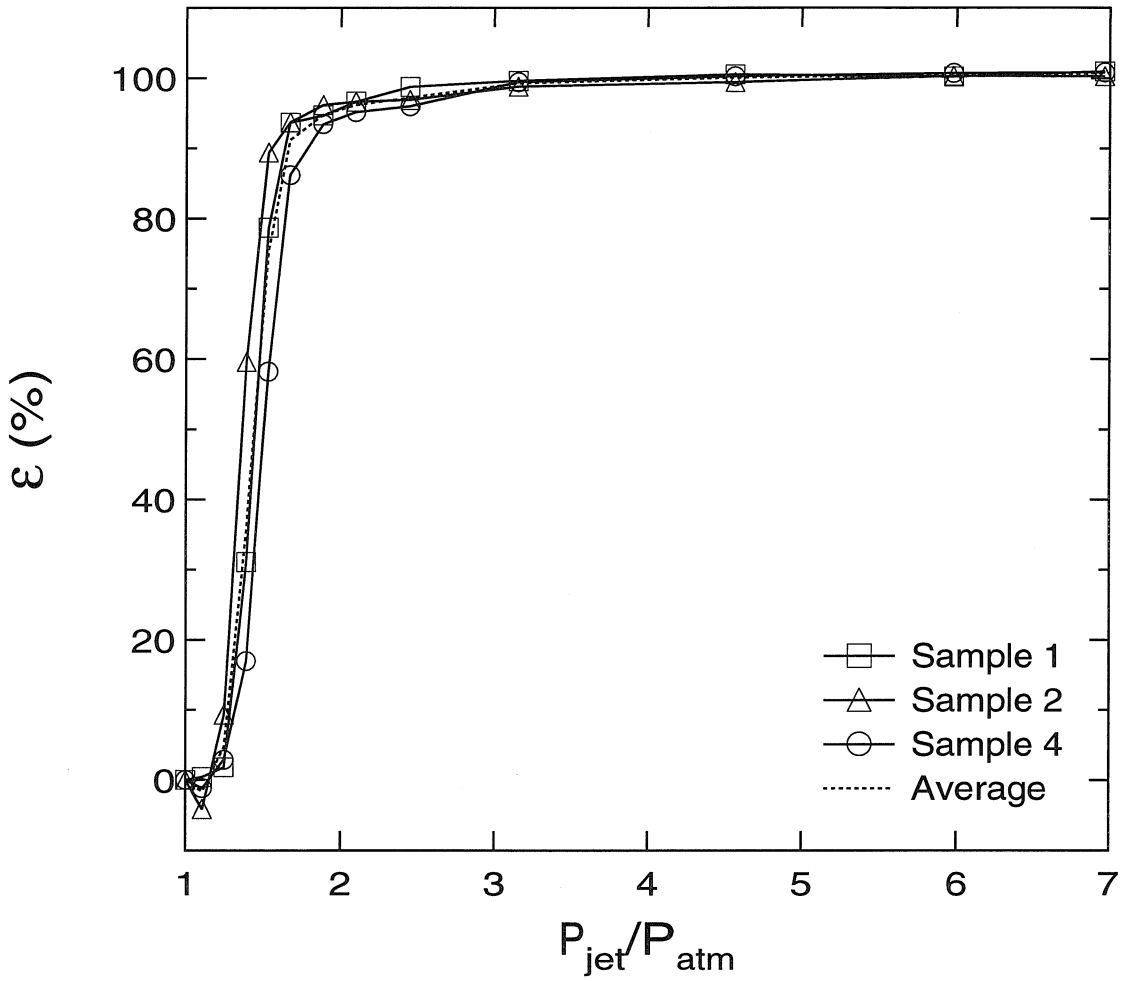

Figure 5.6: Repeatability of removal efficiency.

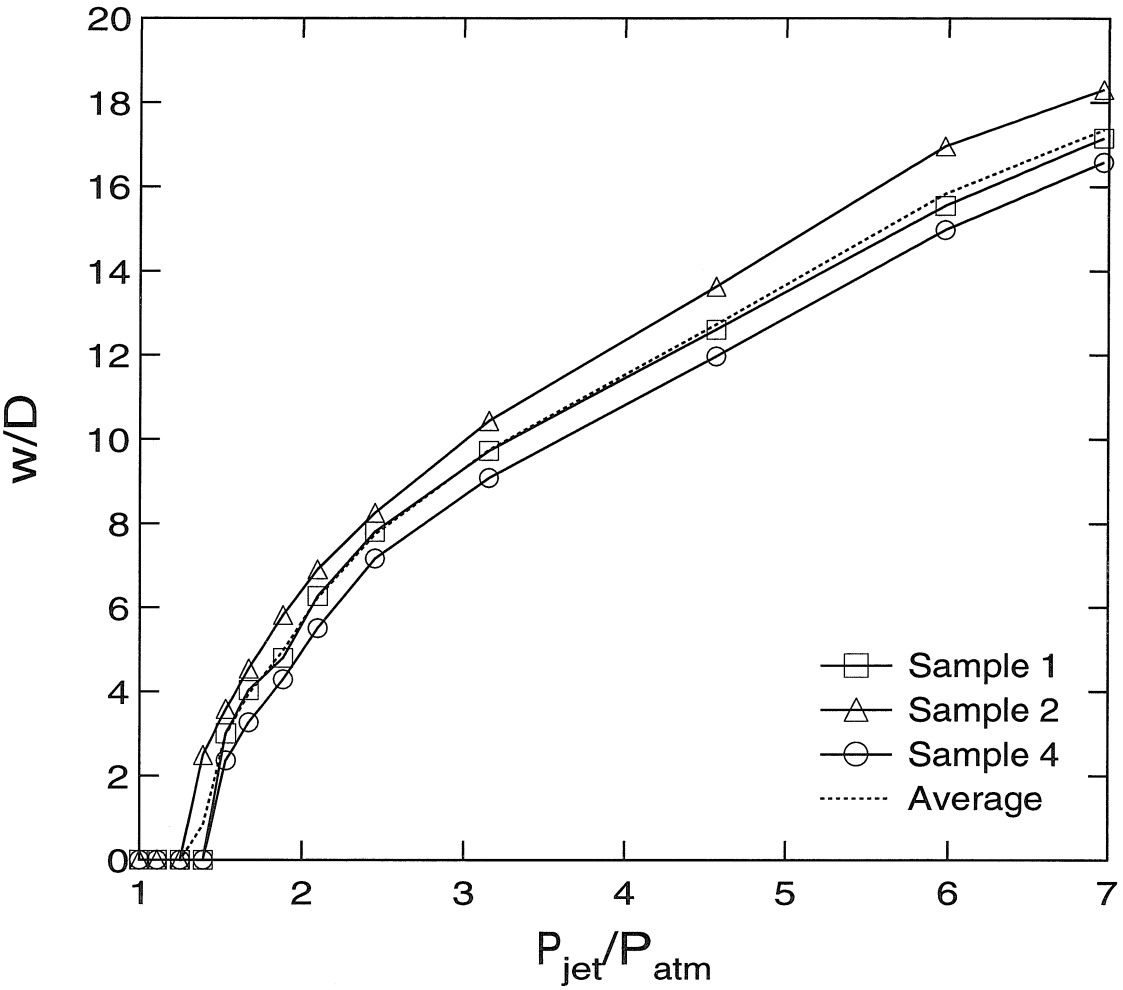

Figure 5.7: Repeatability of path width.

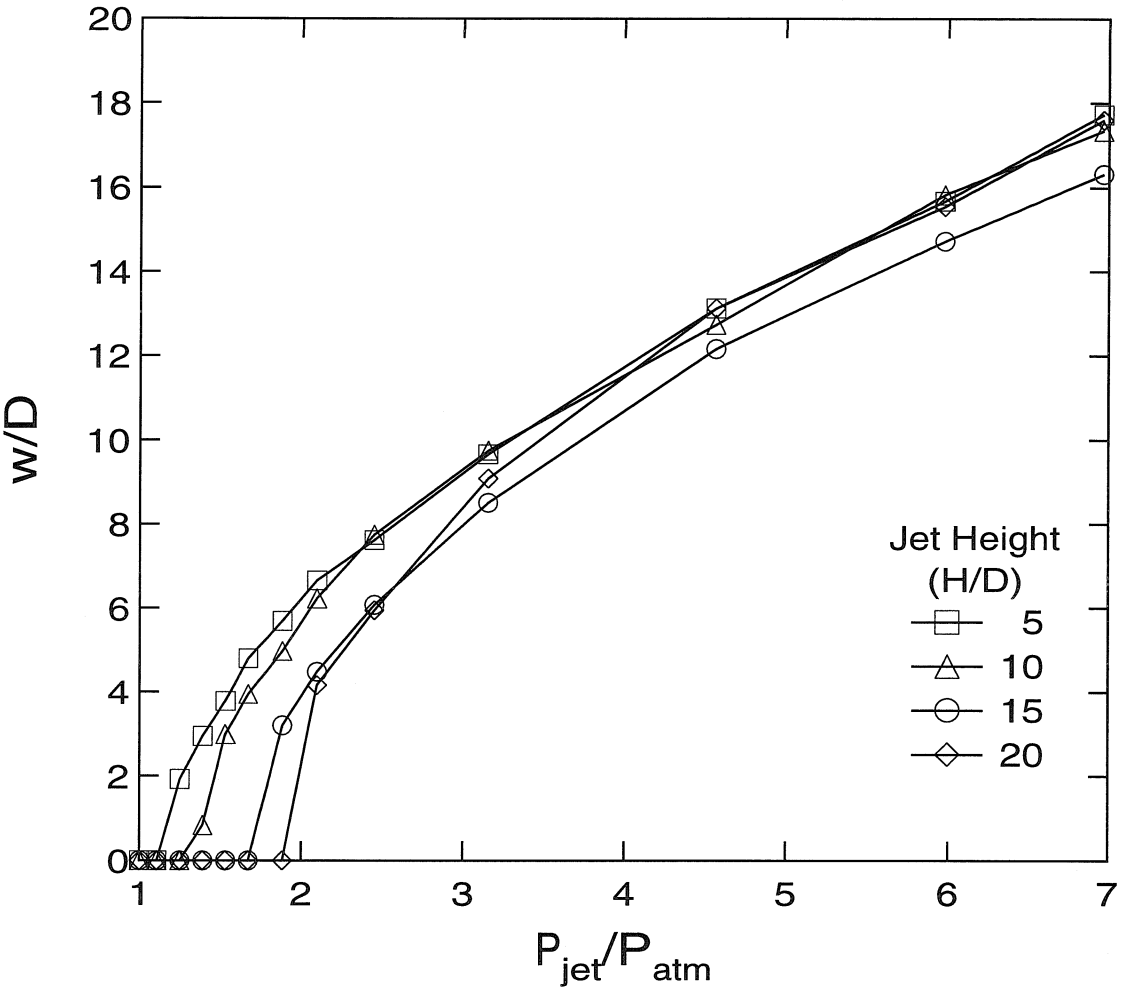

Figure 5.8: Effect of jet height on path width.

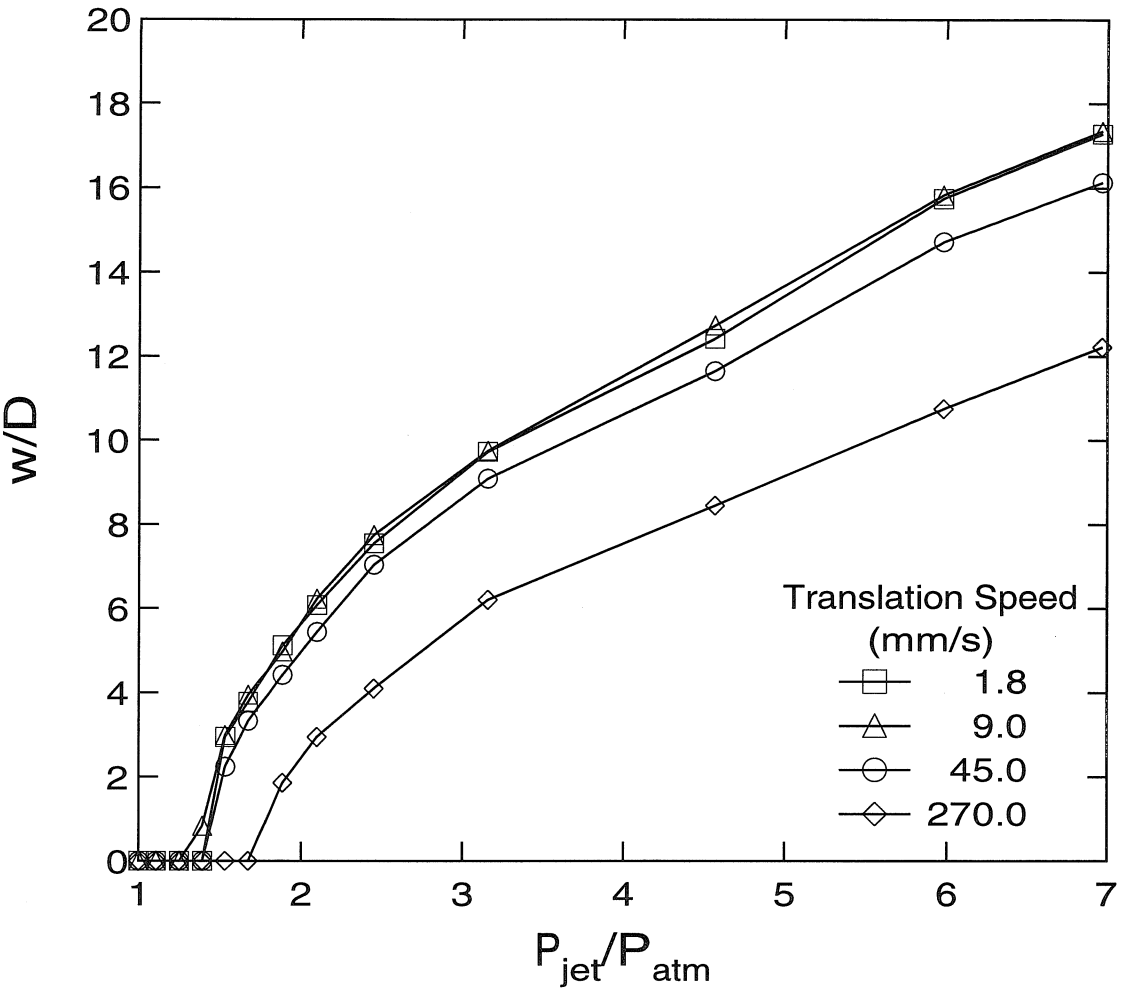

Figure 5.9: Effect of translation speed on path width.

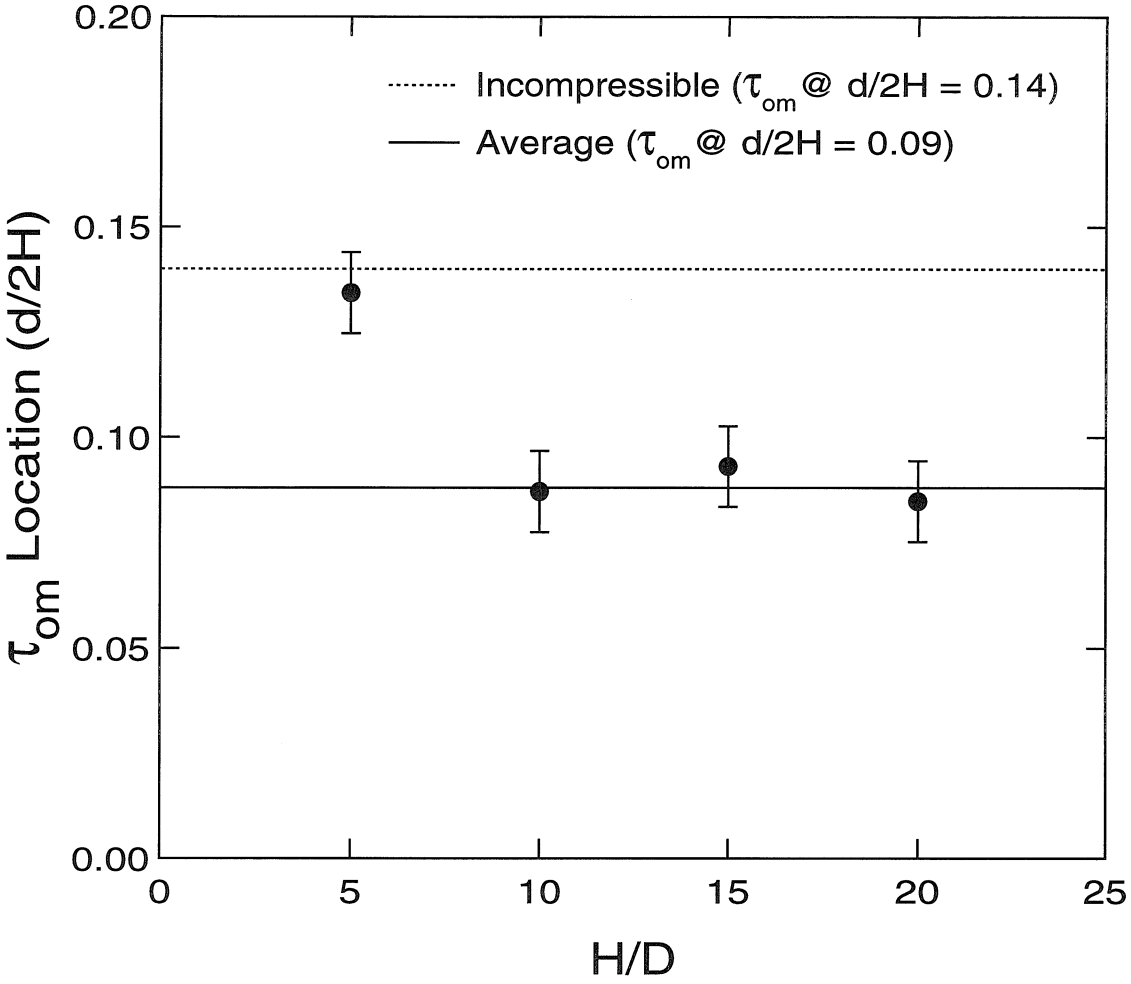

Figure 5.10: Dependence of the τ_{om} location on the jet height.

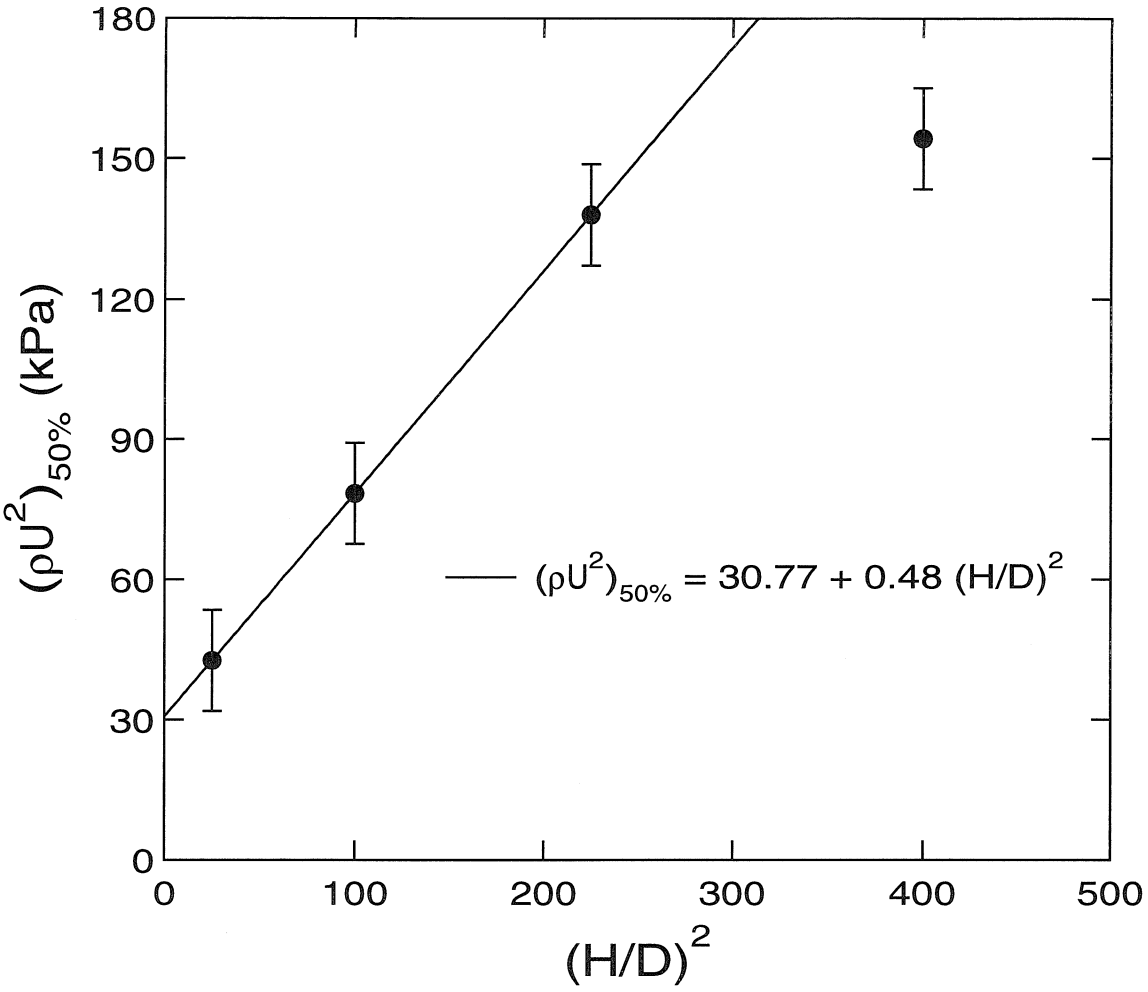

Figure 5.11: Dependence of threshold dynamic pressure on the jet height.

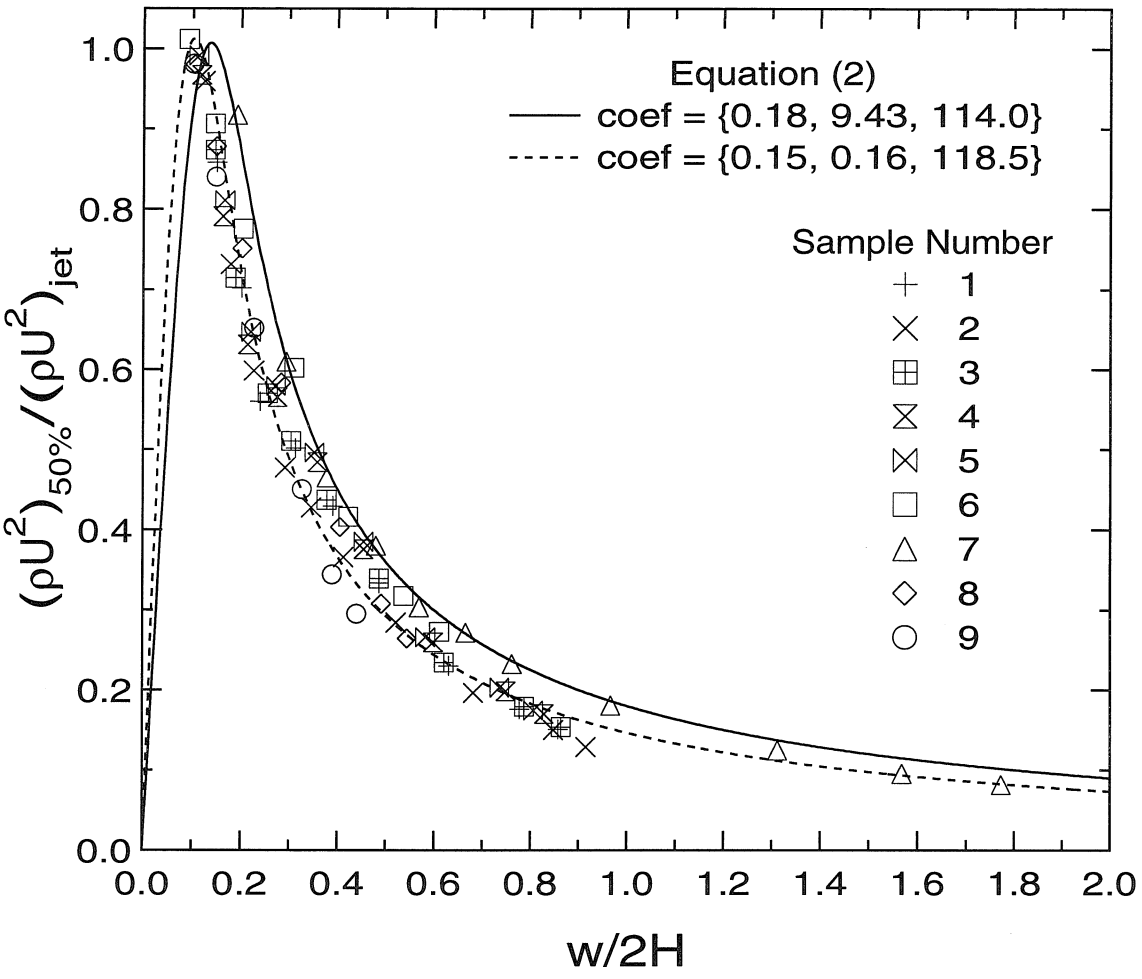

Figure 5.12: Measured dynamic-pressure ratio at various radial distances.

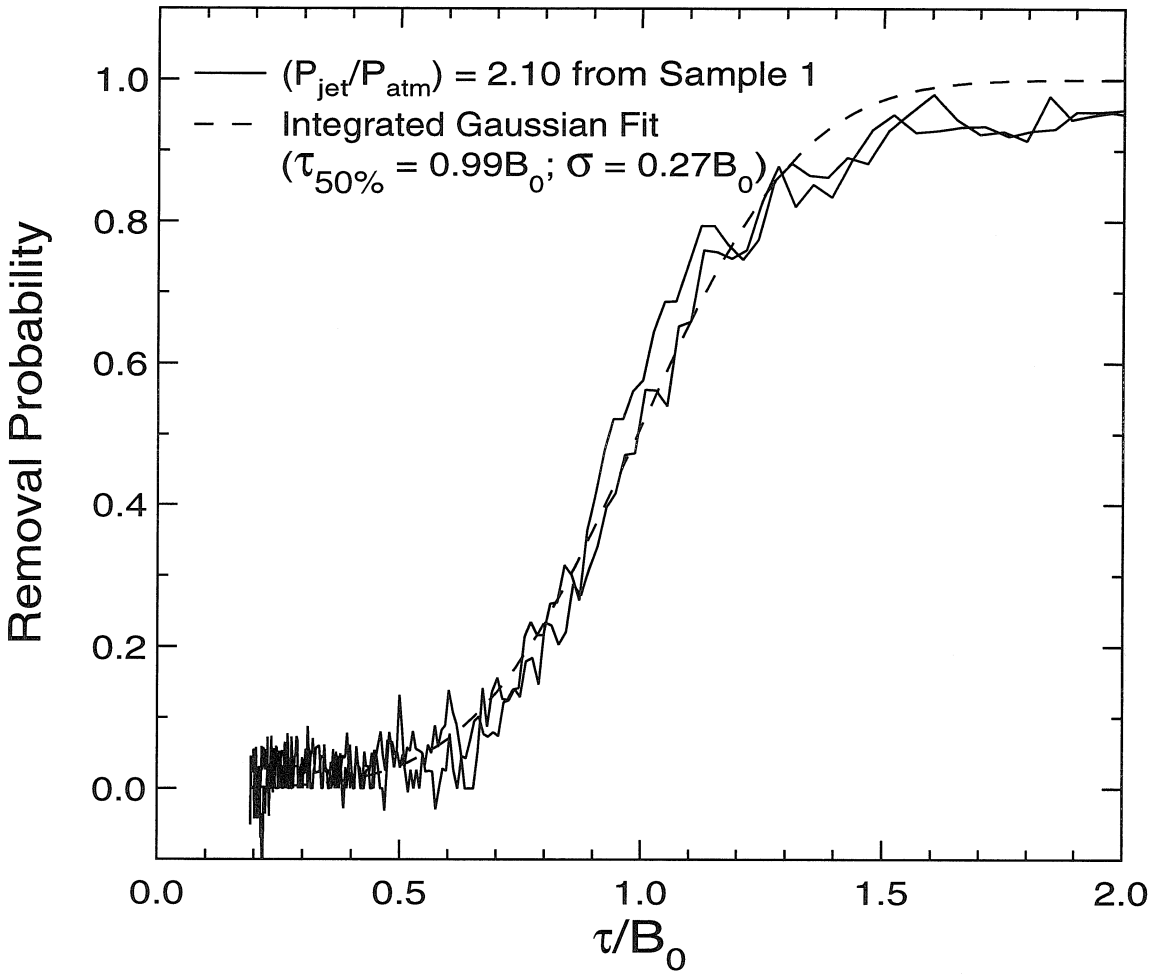

Figure 5.13: Dependence of the probability of removal on the applied shear stress.

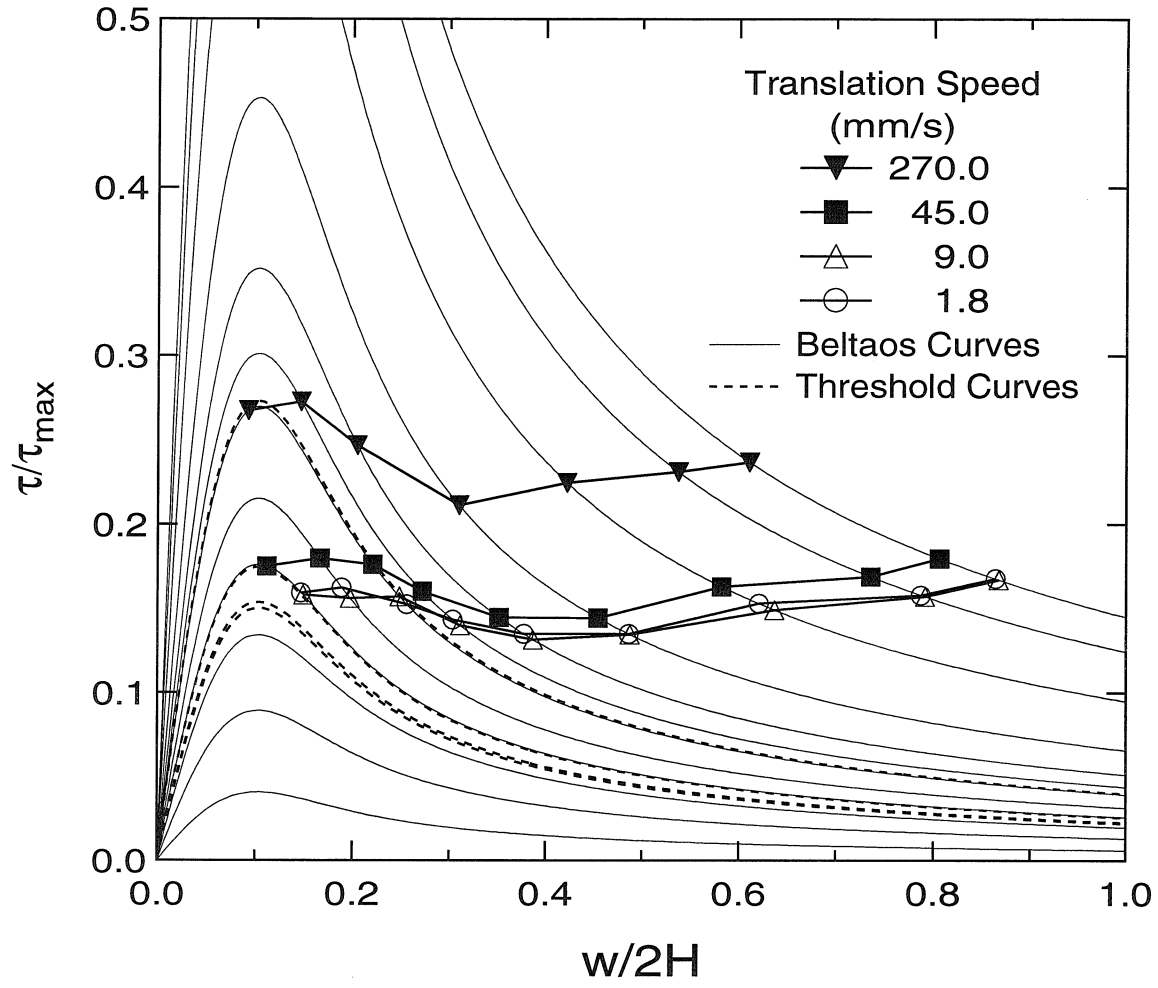

Figure 5.14: Path width data from a relative shear stress perspective for various translation speeds.

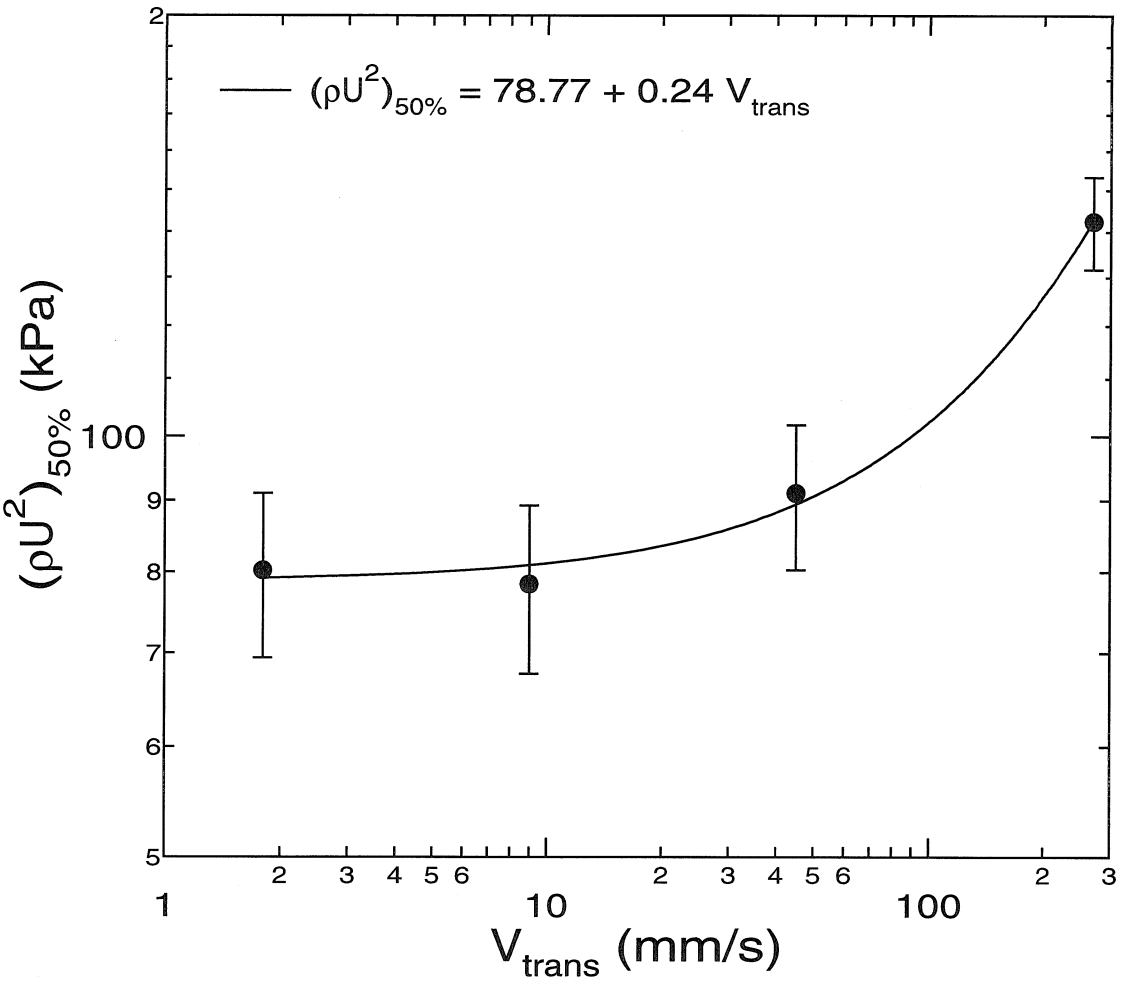

Figure 5.15: Effect of translation speed on threshold dynamic pressure.

Chapter 6 Entrainment of Fine Particles from Surfaces by Gas Jets Impinging at Oblique Incidence

6.1 Abstract

This chapter describes an experimental study of the removal of fine (12 μm) polystyrene particles from a glass substrate using a gas jet that impinges obliquely onto a particle laden surface. In order to avoid transient affects associated with jet startup, the sample was slowly translated under a steady jet. The translating gas jet produces a long clean path that provides very good statistics for exploring the effect of jet parameters. This study focuses on the dependence of the spatial distribution of removal on the jet pressure ratio and impingement angle. The jet is translated over the sample both longitudinally and transversely to determine both the width and the length of the particle removal footprint. The width of the removal footprint increases and the length decreases as the impingement angle is increased. Previous researchers have reported contradictory results regarding the dependence of removal efficiency on impingement angle; this chapter seeks to resolve these differences. For the steady jet, the threshold pressure ratio required for 50% particle removal increases with decreasing impingement angle. In addition, the well characterized particles on well characterized substrates provide insight into the surface shear stress imposed by the oblique jet.

6.2 Introduction

Removal of fine particles from surfaces is vital to surface cleaning and contaminant detection. In the semiconductor industry, particles cause defects that reduce product yield. In forensic science, detection of explosives, drugs, and other contaminants on surfaces is often limited by the low volatility of the particulate material. Aerodynamic entrainment of particles may provide a suitable non-contact means to clean surfaces and may improve transport to analytical instruments, thus enhancing the detectability of contaminants.

Impinging gas jets are commonly used for aerodynamic extraction of fine particles from surfaces, and several investigators have studied them. Methods examined include particle removal using steady gas jets [22, 23, 16, 17, 18, 19, 20, 21], pulsed gas jets [22, 23, 24], and oscillating gas jets [25]. The term "steady" is applied to studies in which no intentional effort was made to enhance removal with dynamic variation of the jet flow. Most of the "steady"-jet studies employed solenoid valves to turn the jet flow on and off while the sample was positioned below the jet so the particle laden samples were exposed to a jet start-up transient [22, 23, 17, 18, 19, 20]. Liu *et al.* [16] may have had smaller start-up transients, since they used a manual needle valve to control the jet flow. In our previous work, a sample was passed under a steady jet at normal impingement after the startup transient had subsided [21].

Previous studies of the effect of impingement angle on particle removal have yielded conflicting results [22, 20]. To facilitate comparison of these studies, a dimensionless jet height H/D is introduced. The jet height, H, is measured along the jet axis from the center of the nozzle exit to the surface and D is the nozzle exit height or diameter. Otani *et al.* [22] found that the removal efficiency during 60 second exposure to the jet improved with decreasing angle of impingement from 90° to 30°, while Gotoh *et al.* [20] found that an impingement angle of 30° was least effective and 45° was most effective when they exposed samples to a jet for 10 seconds. Three notable aspects of the two studies may account for the resulting contradiction: (1) both studies exposed the samples to startup transients, (2) Otani

et al. [22] operated their jet at $H/D = 12$, while Gotoh *et al.* [20] operated their jet at $H/D = 40$, and (3) both studies employed small measurement areas located at the geometric intersection of the jet axis and the surface, *i.e.*, Gotoh *et al.* [20] measured removal within an area 1 x 1 mm^2 while Otani *et al.* [22] measured removal within an area 1 x 4 mm^2. The strength of the startup transient of the jet flow will depend on the opening time of the solenoid valve and the length and impedance of tubing and other flow components upstream of the nozzle. Moreover, the resulting transient will decay with downstream distance after exiting the jet nozzle. At normal incidence, the stagnation point, which produces no particle removal, is located at the geometric intersection of the jet axis with the surface; as the incident angle is decreased, the stagnation point moves upstream along the surface. Therefore, the use of a small measurement area at the geometric impingement point may yield misleading results as the impingement angle is decreased, if the stagnation point moves a significant fraction of the length of the measurement area. Further discussion of these contradictory results is provided in Section 6.5.

The present study is aimed at understanding the affect of impingement angle on particle removal by steady gas jets. Previous work on particle removal using an impinging jet at normal incidence [21] has demonstrated that translating the sample under a steady jet provides a sensitive means to evaluate the effect of jet parameters on particle removal by impinging steady gas jets. Here, we apply the same technique to the study of impingement angle effects. Translation of the jet relative to the surface cleans a stripe on the surface. Some of the forces imposed by the jet can be deduced from the spatial distribution of removal efficiency.

6.3 Experimental

6.3.1 Translating Jet Apparatus

The apparatus used for this investigation, which is illustrated in Fig. 6.1, is the one used in the previous study of normal impingement [21]. A rotation stage has been

added to manually set the impingement angle. The camera mount has also been modified to allow alignment of the long axis of the image with the short axis of the sample (see Fig. 6.2).

6.3.2 Sample Preparation

Quantitative studies of particle entrainment by impinging gas jets require test samples that consist of well characterized particles on well characterized surfaces. The surfaces were prepared using the same procedure described in Smedley *et al.* [21]. Uniformly-sized, spherical polystyrene particles (12 μm diameter, Mw = 18,700 amu) were produced in a particle synthesis apparatus [21]. The prepared samples were then stored in a dry box for a minimum of 24 hours prior to use in the experiments.

6.3.3 Procedure

The procedure followed for these experiments is nearly identical to that used in the normal jet study [21] with a few notable changes. The position and orientation of the three images were changed to provide a wider view of the sample (see Fig. 6.2). The impingement angle was the central focus of this study, so the jet height ($H/D = 10$) and the translation speed (1.8 mm/s) were held fixed. The jet exit diameter remains 0.5 mm. The jet pressure was stepped through the following sequence of pressure ratios (P_{jet}/P_{atm}): 1.11, 1.18, 1.25, 1.39, 1.53, 1.67, 2.09, 2.45, 3.16, 4.57, 5.98, and 6.97.

Previous constraints on the particle synthesis apparatus that limited single-run production to nine samples with the desired particle density (300/mm^2) [21] have been overcome so that 12 or 15 samples could be produced in a single run. The experiments reported here were conducted using samples from three synthesis runs: (A) 12 samples for the oblique jet experiments, (B) 3 samples for the multipass experiments, and (C) 15 samples for the transverse-oblique jet experiments. Due to slight run-to-run variations in the polymer particles, comparisons between synthesis runs must be done cautiously. Parametric investigations explored the influence of impingement

angle, measured with respect to the sample surface, (30°, 45°, 60°, 75°, and 90°) on particle removal. The jet was translated over the sample both longitudinally and transversely to determine both the width and the length of the particle removal footprint. Figure 6.3 depicts a conceptual view of the 50% removal contour (removal footprint), based on shear stress measurements of previous investigators [66], produced by an oblique impinging jet. The velocity vectors, labeled V_L and V_T, indicate the longitudinal and transverse directions of motion for this footprint. The dimensions (u, d, w, L) included on the figure are used in subsequent plots of the results.

To study the removal produced by the transverse motion of the jet, the jet supporting and adjustment hardware was repositioned. A scribed line was used as a fiducial mark to facilitate alignment of the geometric impingement point of the jet with the central long axis of the sample. It was necessary to first manually align the geometric impingement point with the fiducial mark and then offset the jet location a known amount to ensure that both path edges would be visible in the imaged region of the sample. Table 6.1 summarizes the experimental conditions explored with each sample.

6.3.4 Data Analysis

The dark-field images were processed to determine the pressure ratio required to remove 50% of the particles (threshold pressure ratio) and the path width [21]. As before, the threshold dynamic pressure is calculated from the threshold pressure ratio. Since the orientation of the present images is different from the previous study, the selected rectangular region of the images included the entire "x" extent of the image and extended from y=0 to y=14.6 mm. The origin and axes of the image coordinate system (x,y) are shown in Fig. 6.2. The selected "y" extent was limited to avoid inclusion of the frosted edge of the slide at the top of frame 1 and the overlapping regions between the frames. An average pixel intensity was calculated for each column (x = constant) of the selected region and plotted as a point on the density profile of that region.

6.4 Results

The influence of multiple passes and impingement angle (longitudinal and transverse translation) on the removal threshold and path width, and the repeatability of these measures, were examined using data from 24 samples (see Table 6.1). All 24 samples yielded well defined uniform path-widths in at least two of the three recorded frames from each pass. Of the six samples excluded from the final data, two were not subjected to the jet flow and four exhibited non-uniform removal. In the presentation of these results, the path width is set to zero at a pressure ratio of one (no flow) and the path width is non-dimensionalized with respect to the jet exit diameter, D. Atmospheric conditions in the laboratory were P_{atm} = 97.4 kPa, T = 22°C, and relative humidity of 54%.

6.4.1 Multiple Passes

The assumption that the path width produced by the first pass of the jet is representative of its particle removal capability was tested by passing a fixed pressure ratio (4.57) jet over a sample 12 times at 1.8 mm/s and $H/D = 10$. The resulting path widths are shown in Fig. 6.4. There is little change in the removal profile during the 12 passes. In fact, the path width increased by only 11% by the third pass and did not increase further on the subsequent passes. The removal obtained with one jet pass therefore represents the total removal that is possible for the given conditions. The square point on the plot, with error bars, indicates the mean ($\pm\sigma$), from seven samples (see Table 6.1), of the path widths produced by a normal jet at a pressure ratio of 4.57 using the standard incremented pressure method. The measured agreement between the path widths produced by the multipass method and the incremented pressure method further reinforces the use of a single pass to characterize the jet removal potential. Exposure of particles to subthreshold forces does not significantly influence their subsequent removal.

6.4.2 Repeatability

The experimental repeatability is similar to that reported in Smedley *et al.* [21]. In the present experiments, at least two samples were used for each impingement angle. The measured threshold pressure ratios for each angular case are within 2.5% of each other, with the majority within 1.0%. These variations are within the measurement error of the jet pressure.

The repeatability of the path width at 90° impingement is shown in Fig. 6.5 for each of the three synthesis runs. The path width uncertainty is determined by averaging the standard deviations of the measured path widths at the five highest pressure ratios for each synthesis run. The uncertainties are ±0.35 mm (Run A), ±0.69 mm (Run B), and ±0.10 mm (Run C). Inclusion of all seven of these cases yields an overall uncertainty of ±0.45 mm, less than one exit diameter. In subsequent plots, average path widths (see Fig. 6.5) from relevant synthesis runs are used for comparisons among the various impingement angles. The uncertainties in the threshold pressure ratios and path widths are used to estimate error bars for the data sets.

6.4.3 Impingement Angle

The effect of impingement angle on path width and removal threshold was examined over the range from 30° to 90° for both longitudinal and transverse translation. Samples from synthesis run A and C were used for the longitudinal and transverse studies, respectively. The path widths determined from longitudinal and transverse translation, shown in Fig. 6.6, are measures of the width, w, and length, L, of the removal footprint produced by the jet (see Fig. 6.3). The width increases and the length decreases with increasing impingement angle. As expected, the removal footprint becomes more oblong as the impingement angle is decreased from 90°.

Since the long axis of the removal footprint is asymmetric relative to the geometric impingement point, the path width is not expected to increase symmetrically at each edge. Figure 6.7 depicts the growth of each edge of the path, for transverse translation, as the jet pressure ratio is increased. At 90° impingement both u and d

increase symmetrically, while at smaller angles d increases more rapidly than u. In all cases, the stagnation point was assumed to be at the center of the first visible partial removal path. Disagreement between this estimate of the stagnation point location and the location of the geometric impingement point based on alignment with the fiducial mark (see Section 6.3.3) was found to be less than $D/2$. Since no consistent trend was found, the deviation is likely dominated by error in the manual alignment of the geometric impingement point with the fiducial mark.

The dependence of the threshold dynamic pressure on the impingement angle is shown in Fig. 6.8 for both the longitudinal and transverse cases. The threshold dynamic pressures increase with decreasing impingement angle and are independent of the translation direction. A higher pressure ratio is required to remove 50% of the particles at 30° than at larger angles.

6.5 Discussion of Results

6.5.1 Comparison to Previous Research

Previous researchers have reported diametrically opposed trends in the dependence of the threshold pressure on the angle of impingement [22, 20]. The present study demonstrates that the threshold pressure ratio decreases as the impingement angle is increased from 30° to 90°. Our measured trend agrees with that found by Gotoh *et al.* [20]; however, this agreement does not imply that the results of Otani *et al.* [22] are invalid.

The present measurements suggest that the results of Gotoh *et al.* [20] and Otani *et al.* [22] disagree because they were studying different systems. Both of the previous studies used a solenoid valve to turn the jet flow on and off while the sample was located below the jet exit; thus exposing the sample to the jet start-up transient. The jet of Gotoh *et al.* [20] was positioned at $H/D = 40$, while the jet of Otani *et al.* [22] was positioned at $H/D = 12$. Since the start-up transient decays with distance downstream of the jet exit, the jet would be expected to appear more "steady" at

$H/D = 40$ than at $H/D = 12$. The present study prevents exposure of the sample to the jet start-up transient; therefore, agreement with the trend observed by Gotoh *et al.* [20] indicates that their jet, despite being turned on and off above the sample, produced removal trends that are characteristic of a "steady" jet.

The above explanation also aids in clarifying another set of contradictory results. Masuda *et al.* [23] concluded that pulsing a jet on and off yielded removal equal to a steady jet left on for the same total on-time of the pulsed jet. In contrast, Otani *et al.* [22] found that 10 to 20, 1 second pulses produced greatly enhanced removal compared to 120 seconds of exposure to a steady jet. The jet of Otani *et al.* [22] was closer ($H/D = 12$) to the sample surface than the jet of Masuda *et al.* [23] ($H/D = 40$), so the start-up transient produced a measurable advantage. Later, Gotoh *et al.* [25] compared removal produced by an oscillating jet with their original jet and found a factor of 42 (76.3% versus 1.8%) improvement in the removal efficiency. However, the oscillating-jet nozzle had an exit height of 1.0 mm while the original-jet nozzle had an exit height of 0.25 mm. In the reported experiments, both jets were directed at the sample surface with an impingement angle of 45° at a distance of 10 mm; therefore, $H/D = 10$ for the oscillating jet and $H/D = 40$ for the original jet. Since the maximum surface shear stress produced by the jet is inversely proportional to $(H/D)^2$ [61] and the jet transients are stronger at smaller H/D, it is not surprising that the removal was greatly enhanced. However, to determine the true benefit derived from the oscillating jet relative to their original one, the experiments would have to be repeated at the same H/D values.

A curious result was found by Gotoh *et al.* [20] that is perhaps worthy of mention since it may in fact be an artifact of their measurement technique. At several jet pressure ratios they found that the fraction of removed particles, measured in a 1x1 mm^2 area centered on the geometric impingement point, reached a maximum near 45°. The result may in fact be due to the movement of the jet stagnation point as the angle is changed [63]. Measurements by Donaldson and Snedeker [63] for a round jet at $H/D = 39.1$ indicate that the stagnation point shift ranges from 1.8D to 2.2D for jet pressure ratios ranging from 1.25 to 6.75 as the impingement angle

is decreased from 90° to 45°. Assuming the shift is similar for the planar jet used by Gotoh *et al.* [20], a shift of 2D (0.5 mm) is half the length of their measurement area. Since the stagnation-point shift is a significant fraction of their measurement area, it may have a significant affect on their measured removal; therefore, it is likely that the measured maximum is anomalous. For the present study, the expected shift based on the results of Donaldson and Snedeker [63] is 1D (0.5mm). However, since the removal efficiency is determined by averaging the central region of the density profile of the removal path [21] and the position of the removal path is not assumed in advance, the computed removal efficiency is not sensitive to the stagnation-point shift.

6.5.2 Shear Stress of Oblique Jets

The relationship between shear stress and particle removal was discussed in Smedley *et al.* [21] along with a suitable non-dimensionalization for the shear stress that was taken from Beltaos and Rajaratnam [61]. It is sufficient for the present discussion to state that the dynamic pressure ratio is effectively identical to the shear stress ratio. The same non-dimensionalization is applied to the measured footprint widths, w, and presented in Fig. 6.9 to collapse them to a single curve. The excellent collapse of the data indicate that the impingement angle has no significant affect on the shear stress distribution across the width, w, of the impingement footprint (see Fig. 6.3). Once again, provided the threshold dynamic pressure is known, the width of the removal path can be determined from the dynamic pressure of the impinging jet.

The results for the measured footprint lengths, L, do not collapse when non-dimensionalized in the same way as the width results; therefore, the shear stress distribution along the length of the removal footprint changes significantly with impingement angle. However, the dependence of this shear stress distribution can be revealed by the particles since they provide a measure of the shear stress. The data are shown in Fig. 6.10 with the upstream u and downstream d edges of the path plotted separately. The separation of the upstream and downstream measurements clearly

shows that the shear stress gradient increases on the upstream side and decreases on the downstream side as the impingement angle is decreased. This is consistent with previous researchers [66] and with the observation that the edges of the removal path were more abrupt on the upstream side than the downstream side.

6.6 Summary

The translating jet is a useful tool for probing particle removal by oblique impinging jets. The width of the removal footprint increased and the length decreased as the impingement angle was increased from 30° to 90°. The threshold dynamic pressure monotonically increased with decreasing impingement angle, demonstrating that a steady impinging jet can more easily remove particles at 90° incidence than at smaller angles.

The spatial variation of particle removal in the cleaned path can be compared to the local shear stress of the steady impinging jet since start-up transients are avoided. The dynamic-pressure ratios of the jet and the widths of the removal footprint collapse to a single curve for the range of impingement angles studied here. Therefore, the impingement angle has no significant affect on the shear stress distribution across the width of the removal footprint (see Fig. 6.3). The measured lengths of the removal footprint do not collapse to a single curve when the same non-dimensionalization is used. However, since the particles provide a direct, though uncalibrated, measure of the surface shear stress, their removal reveals the relative shear stress distribution along the length of the removal footprint.

The results presented here for the oblique impinging jet provide a plausible explanation of the diametrically opposed trends reported by previous researchers [22, 20]. The evidence suggests that the large H/D used by Gotoh *et al.* [20] weakened the transient flow effects at the sample surface such that the reported trend in removal threshold with impingement angle is consistent with those for the steady jet explored here. Otani *et al.* [22] employed a jet at a smaller H/D; therefore, transient flow effects at the sample surface were non-negligible and yielded an opposite trend in the

removal threshold with impingement angle when compared to the steady jet.

In practical applications of particle removal and collection, the critical issue to address is the best angle to use. The present results indicate that although normal impingement yields the lowest threshold pressure ratio, transverse translation of the jet at 30° impingement yields the widest removal path at a given pressure ratio. The collection efficiency must also be maximized if particle collection is the goal. Small angle impingement combined with collection downstream of the impingement point should minimize directional changes of particle trajectories and yield higher collection efficiency. Whether the jet should be translated in the transverse or longitudinal direction (or some angular orientation in between) may be dependent on the particles being removed and collected, since the time history of the magnitude and direction of the applied shear stress is dependent on the orientation and translation speed of the jet.

Table 6.1: Parameters and threshold results for each sample.

Synthesis Run	θ (degrees)	$(P_{jet}/P_{atm})_{50\%}$	$(\rho U^2)_{50\%}$ (kPa)
A	90	1.18	34.3
	90	1.18	34.3
	90	1.19	36.1
	75	1.20	37.9
	75	1.19	36.1
	60	1.19	36.1
	60	1.19	36.1
	45	1.21	39.7
	45	1.20	37.9
	30	1.24	45.0
	30	1.24	45.0
B	90	1.17	32.5
	90	1.18	34.3
	90	multipass	multipass
C	90	1.19	36.1
	90	1.16	30.7
	75	1.18	34.3
	75	1.18	34.3
	60	1.23	43.2
	60	1.18	34.3
	45	1.21	39.7
	45	1.20	37.9
	30	1.23	43.2
	30	1.22	41.5

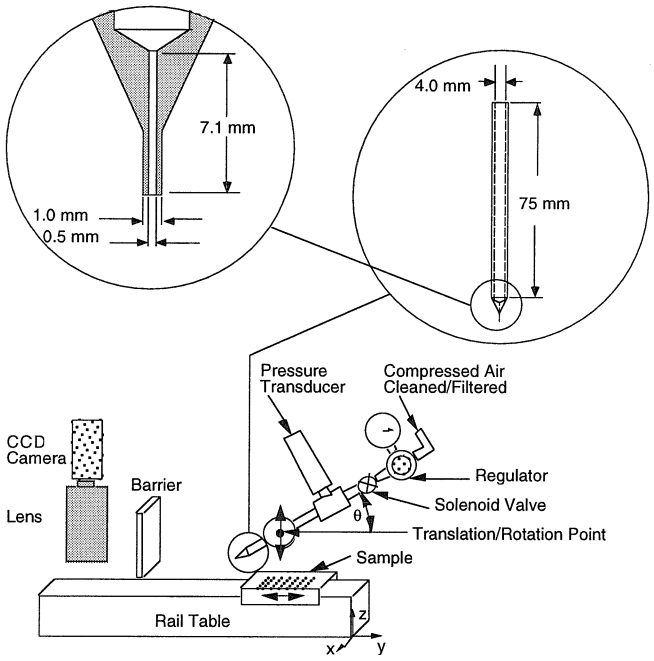

Figure 6.1: Translating jet apparatus.

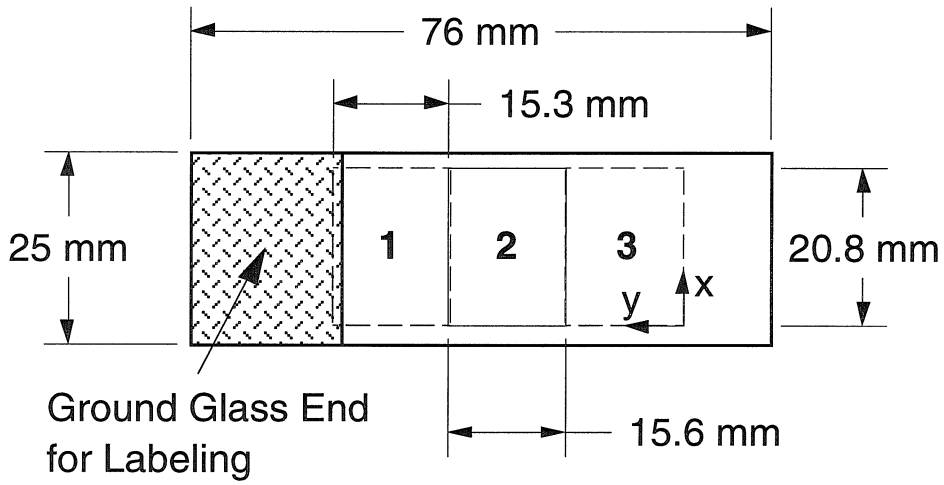

Figure 6.2: Microscope slide showing the three image locations.

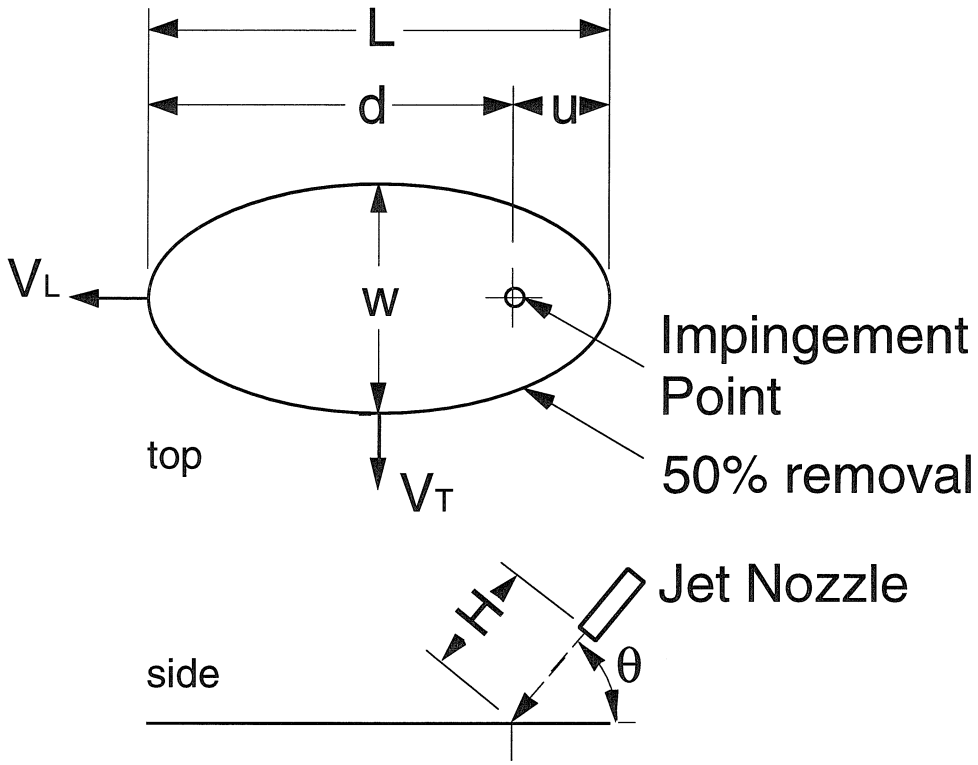

Figure 6.3: Conceptual shape of 50% removal footprint produced on the sample by the oblique impinging jet. The jet was translated over the sample in both the longitudinal, V_L, and transverse, V_T, directions.

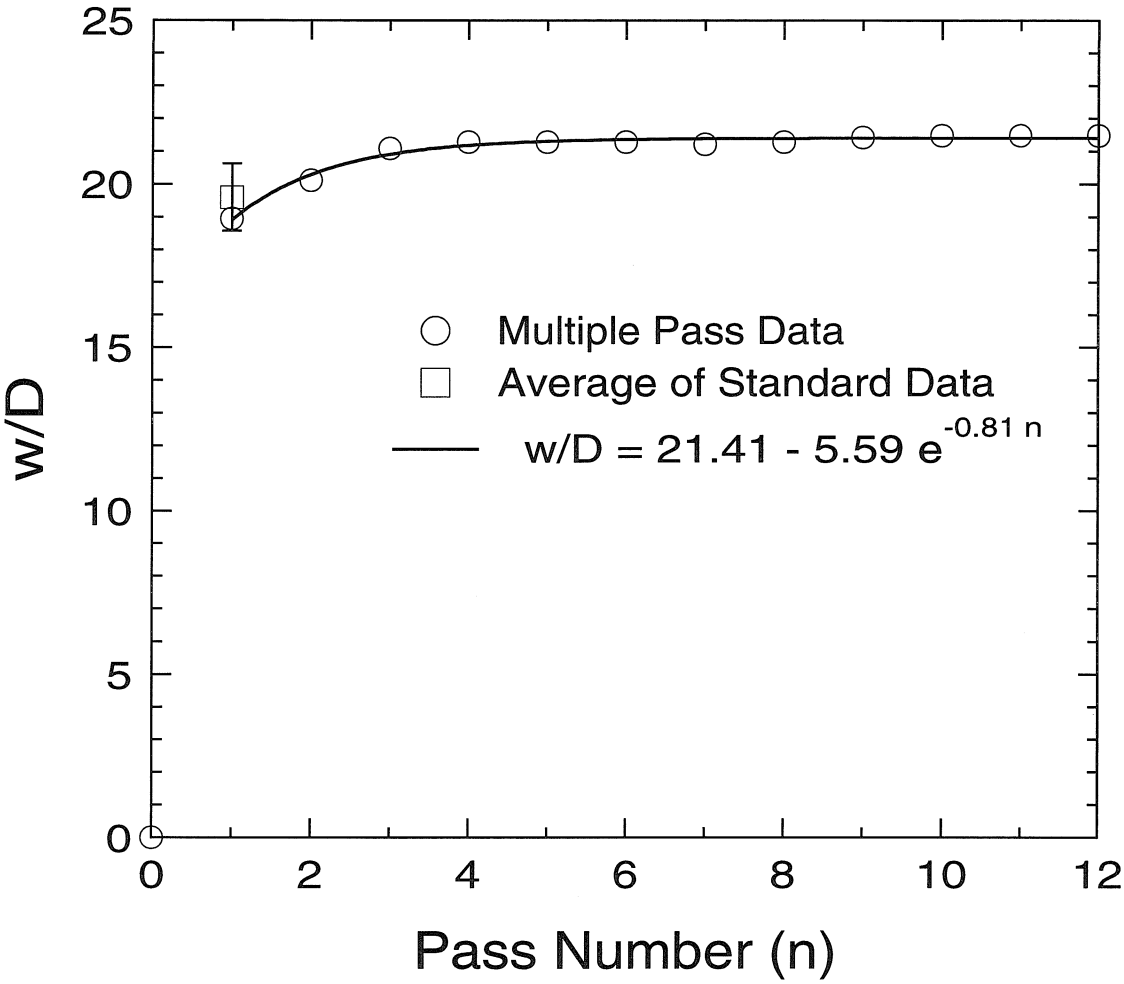

Figure 6.4: The effect of multiple passes at $P_{jet}/P_{atm} = 4.57$ and $\theta = 90°$ on the path width.

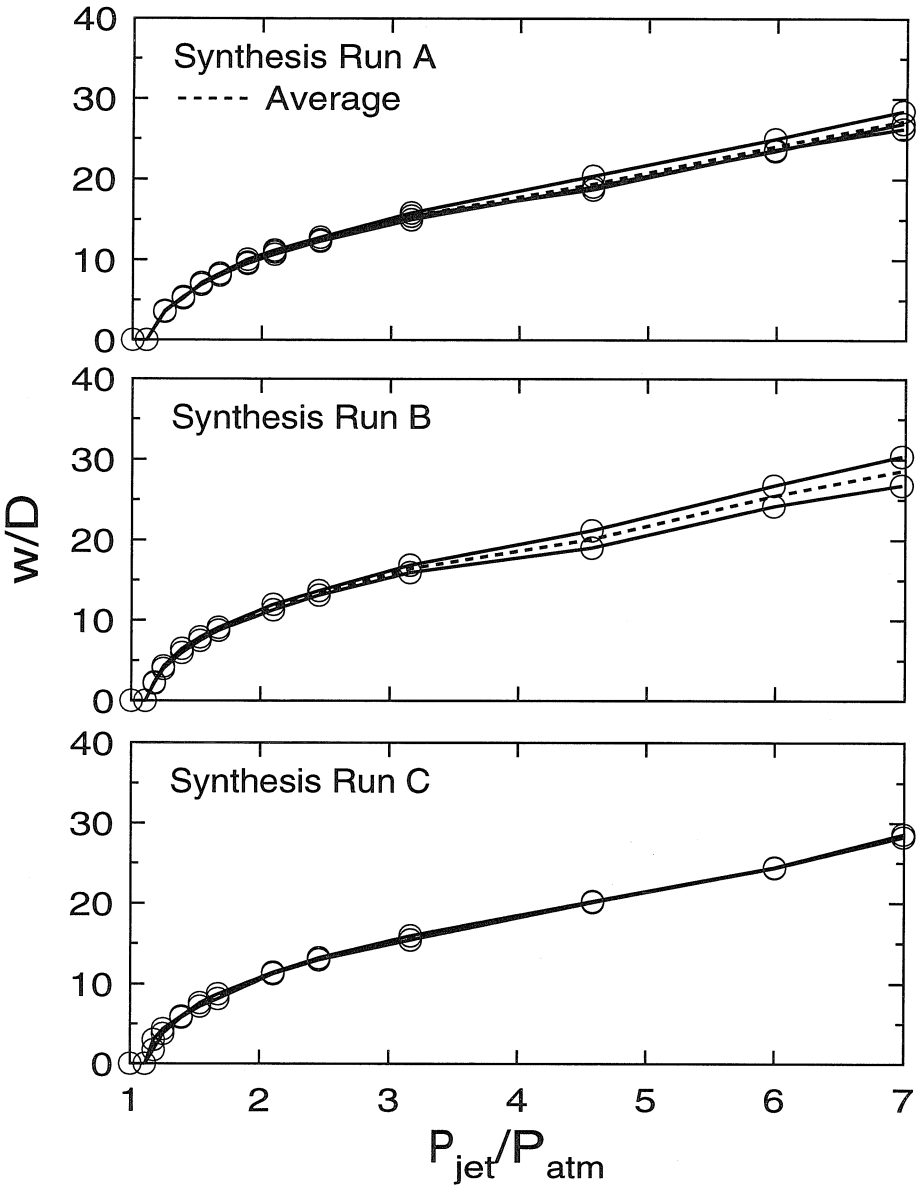

Figure 6.5: Repeatability of the path width for each synthesis run.

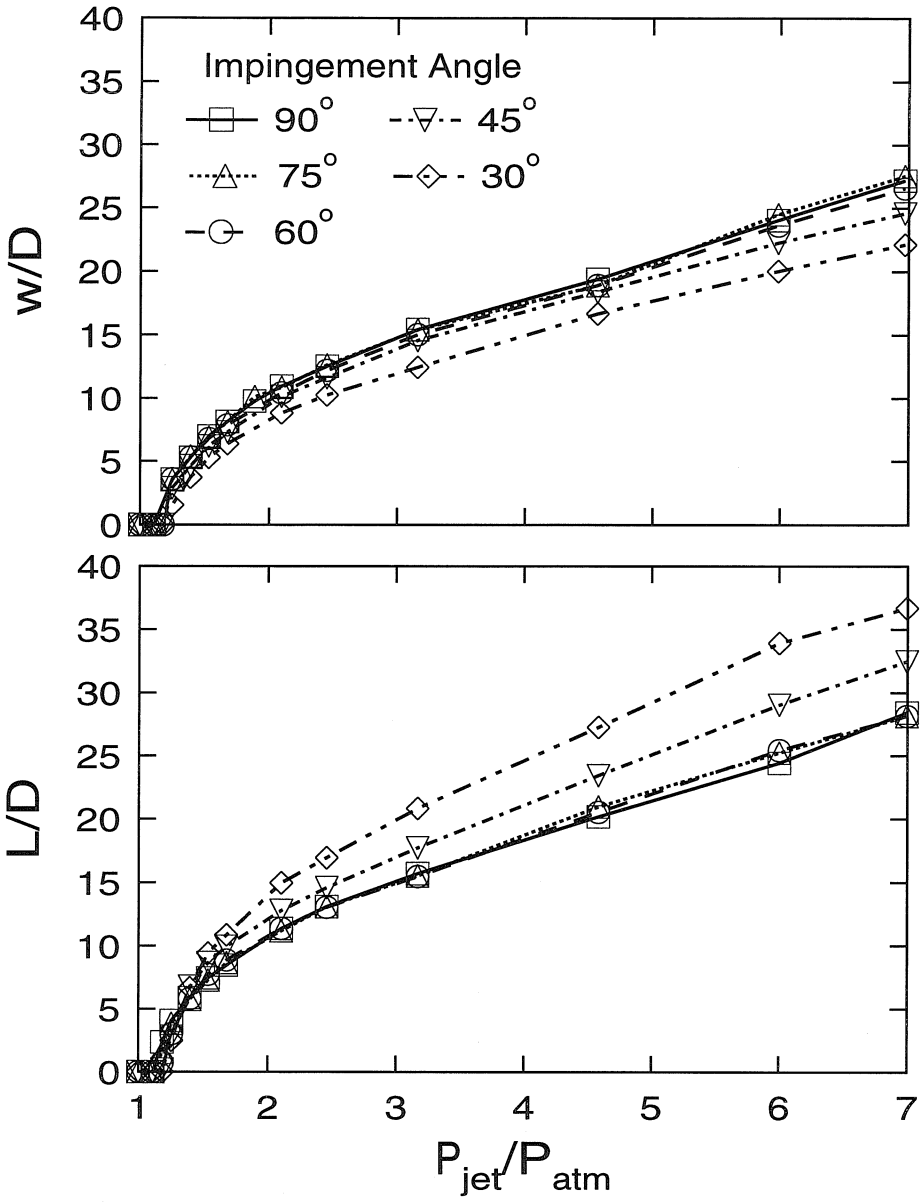

Figure 6.6: The measured width and length of the removal footprint.

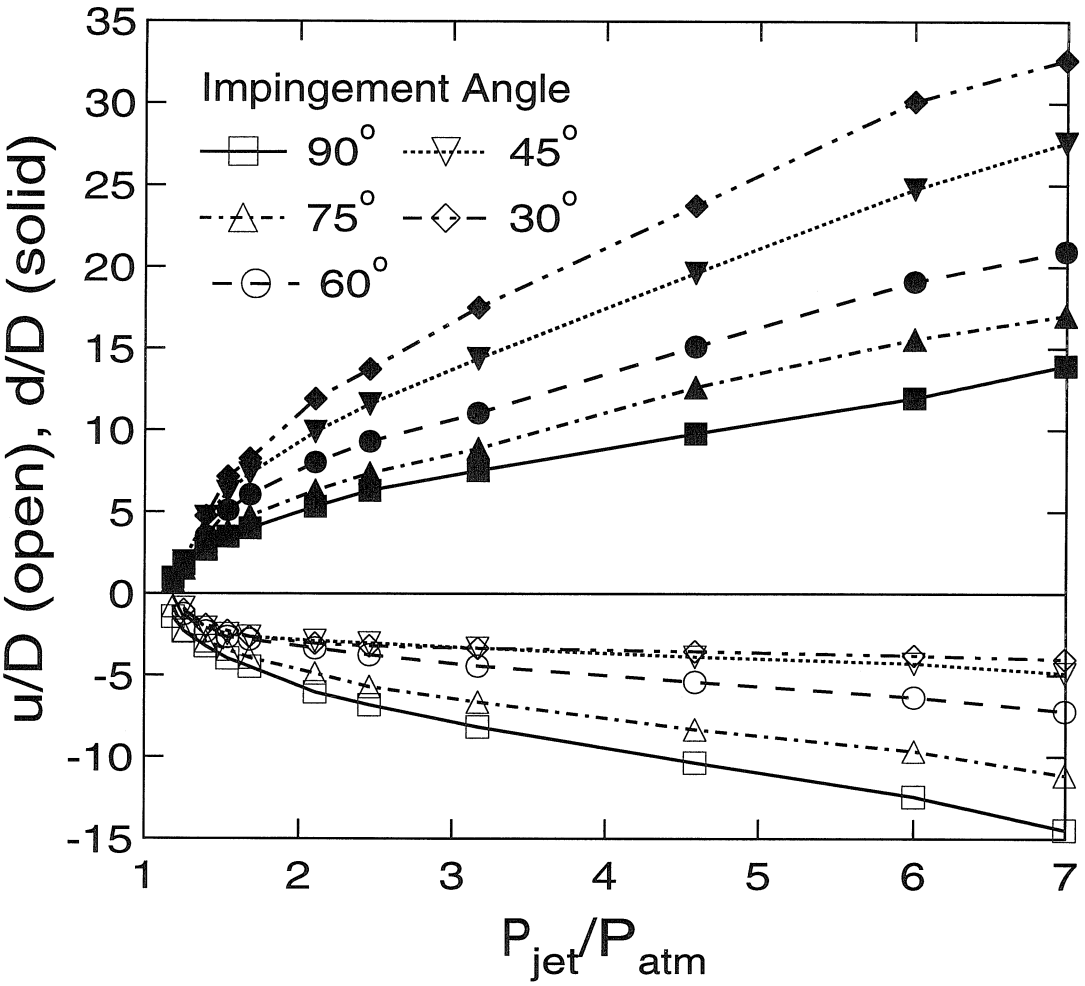

Figure 6.7: Asymmetric growth of removal path at downstream (positive, solid points) and upstream (negative, open points) edges.

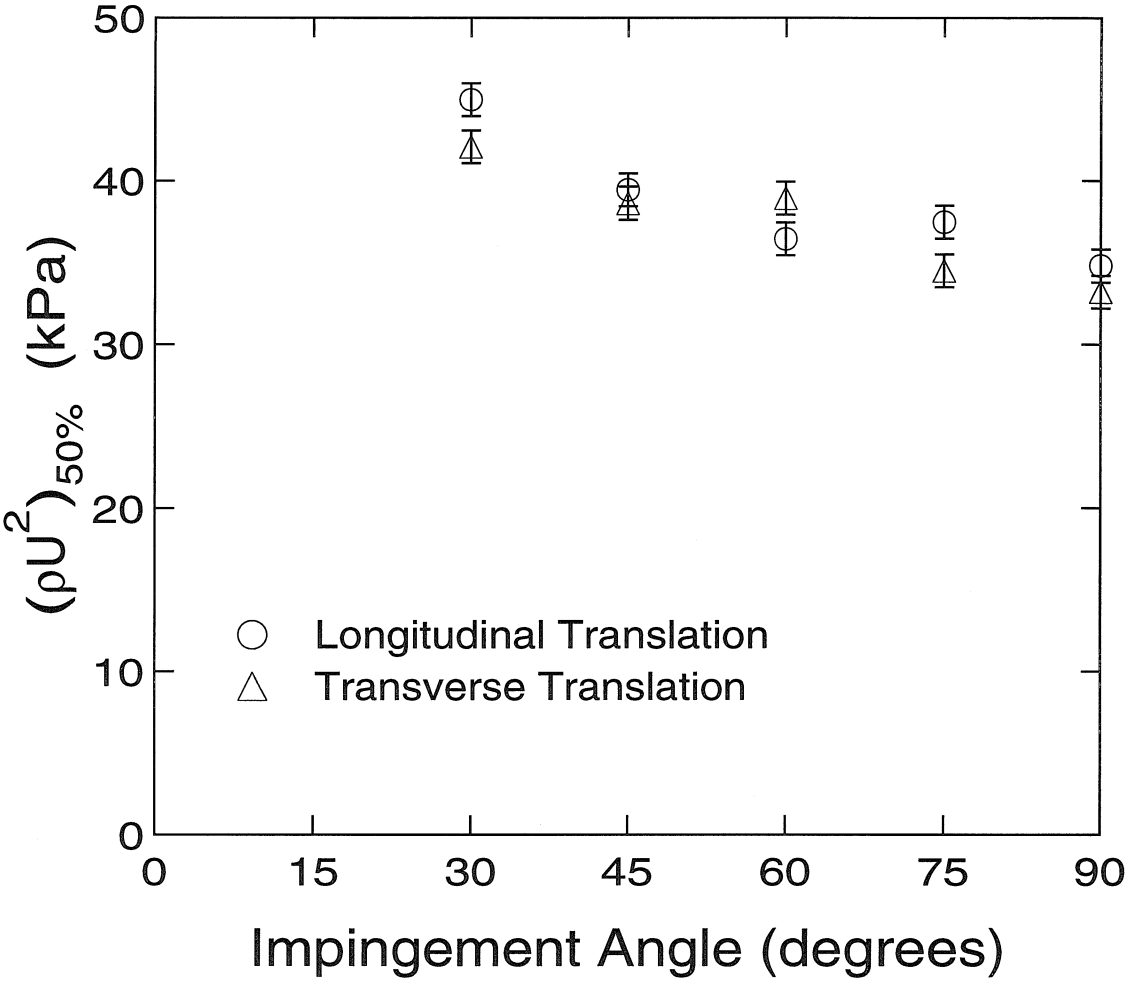

Figure 6.8: The effect of impingement angle on threshold dynamic pressure for both longitudinal and transverse translation.

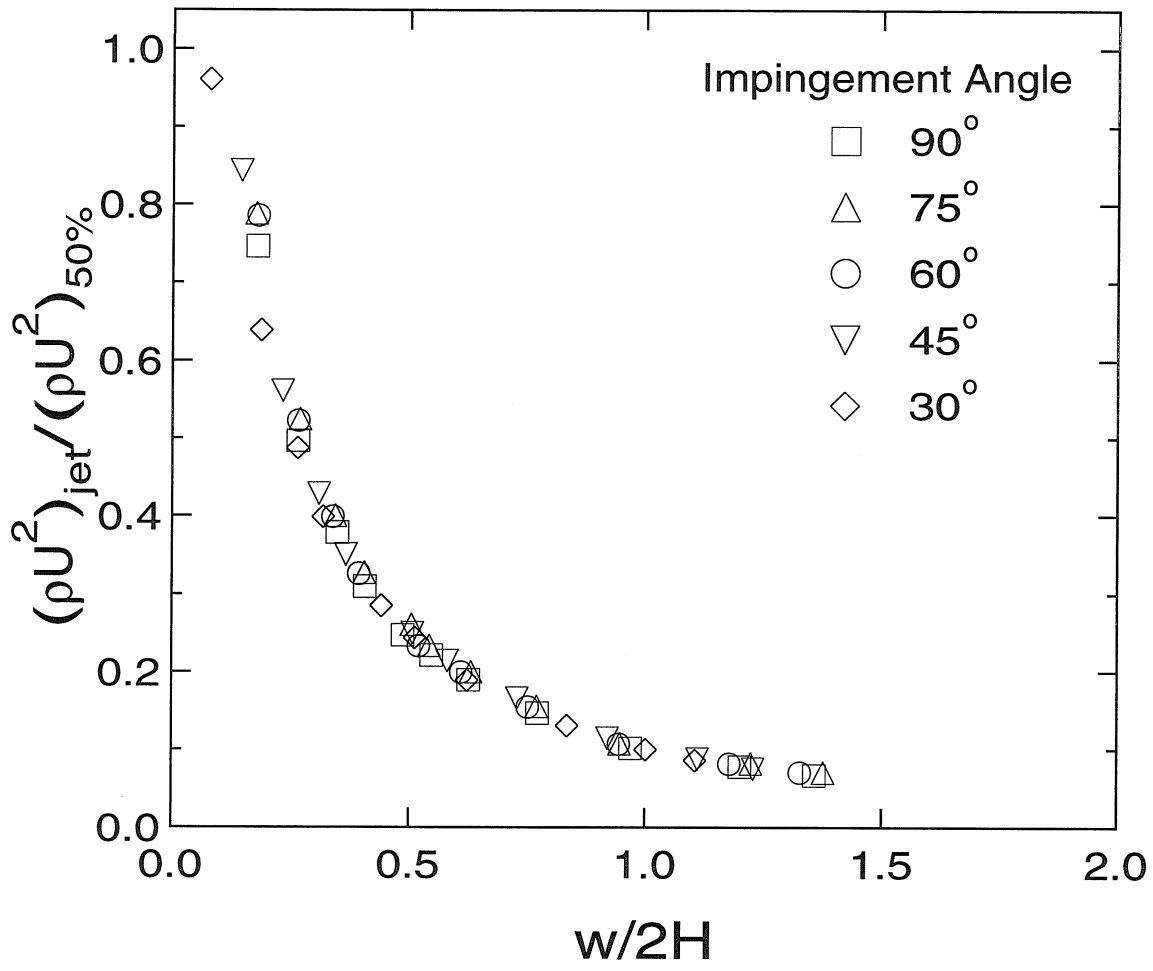

Figure 6.9: Relative shear stress distributions across the width of the removal footprint.

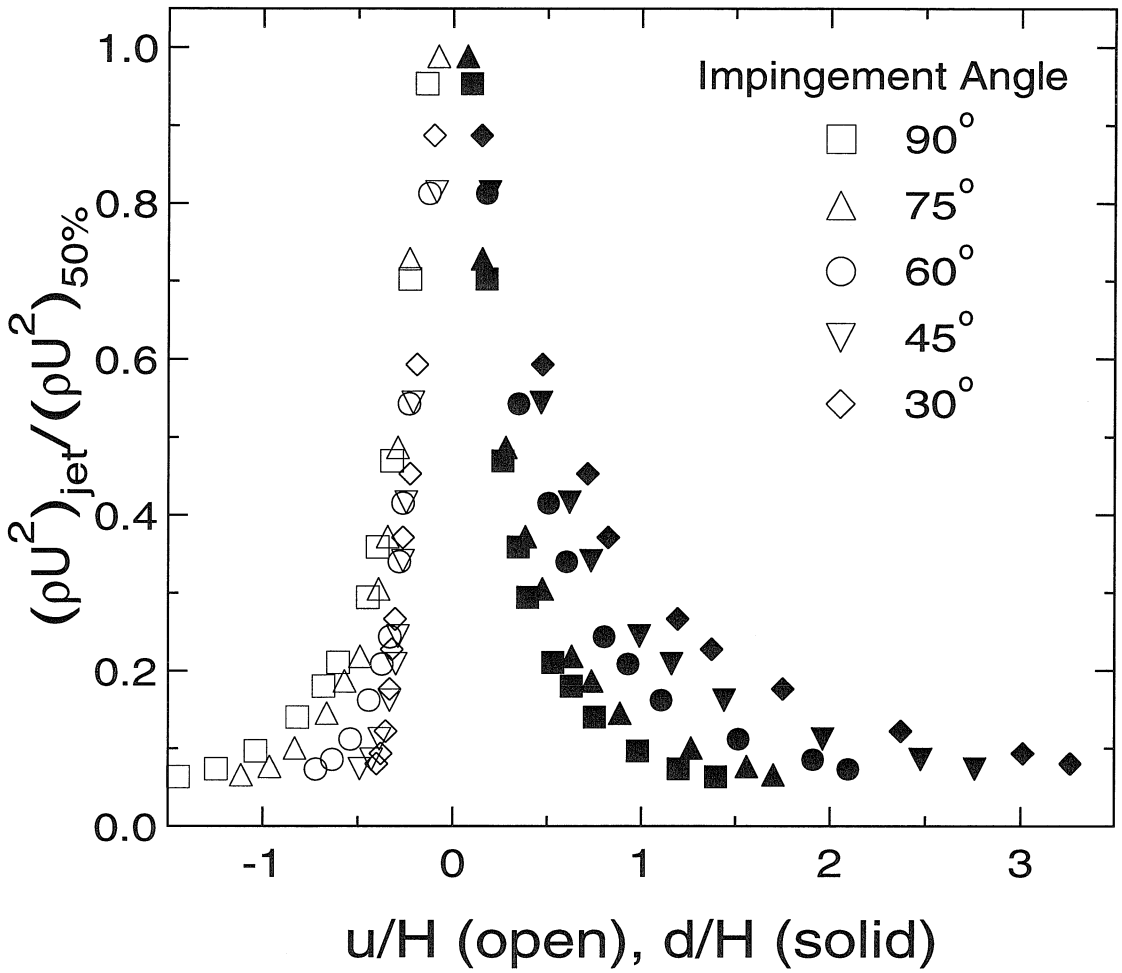

Figure 6.10: Relative shear stress distributions along the length of the removal footprint.

Chapter 7 Inviscid Jet Impingement

7.1 Abstract

Exact solutions to the stream-vorticity equation for two-dimensional and axisymmetric impingement flow with arbitrary velocity profile are found in terms of a surface integral involving the vorticity function. These solutions are applied to the normal impingement of a jet onto a flat surface by approximating the vorticity integral within the impingement region. Surface pressure distributions and streamline plots are calculated for various impinging jet configurations, including plane, round, and annular jet nozzles. The calculations show excellent agreement with previous experimental and numerical results.

7.2 Introduction

Gas jet impingement on surfaces is used in technologies including jet stripping [67], impingement drying, and surface cleaning. The shear induced along the surface provides the impetus for these technologies. The inviscid flow just outside the boundary layer provides the boundary conditions for solution of the boundary layer equations that are needed to determine the heat and mass transfer to the surface.

A number of investigators have developed inviscid flow models for this region [68, 69, 70, 71, 72]. Strand [68] analytically obtained the flow field for potential jet impingement. This solution is relevant to the impingement of a jet very close to the surface, so that impingement occurs before the emanating fluid has mixed with the quiescent fluid. The inviscid impingement of fully developed laminar pipe flow was considered by Scholtz and Trass [69], who determined an analytical solution assuming a parabolic influx velocity profile. Again, this solution is valid only for small pipe to plate spacings. Parameswaran [70] used a Green's function method to solve

the two-dimensional stream-vorticity equation for impingement of a fully developed turbulent plane jet. Rubel [71, 72] considered jet impingement that included the turbulent mixing that occurs with the quiescent fluid, by using the fully developed and developing free jet velocity profile as the influx flow to the impingement region. Rubel cast the two-dimensional and axisymmetric stream-vorticity equations into finite-difference form and solved using relaxation techniques. Although Rubel considered a wider variety of influx velocity profiles than the previous inviscid models, divergence of the iterative procedure limited the profiles to ones that included small velocity defects.

In the present work, Rubel's formulation of the problem for two-dimensional and axisymmetric inviscid jet impingement is used as a starting point. A converging infinite series solution to the governing equations is derived for an arbitrary influx streamfunction in terms of a surface integral of the vorticity function over the whole region of interest. Assumptions concerning the vorticity throughout the flow allow an approximate determination of this integral, and thus a semi-analytical solution of the full flowfield. The final solutions are compared with Rubel's numerical solutions and experimental measurements of the surface pressure distributions created by fully developed and developing jet impingement. The present method of calculation requires significantly less computation time than Rubel's iterative method, since only series coefficients need to be computed. Furthermore, the present method can handle influx velocity profiles with arbitrarily large velocity defects. To illustrate this point, the impingement of an annular jet profile, which resembles a fully developed round jet profile with a severe core velocity deficiency, is considered in Section 7.6.2. The flow field created by the impingement of an annular jet is relevant to the interaction of V/STOL aircraft exhaust with the ground [73].

7.3 Formulation

In accordance with Rubel's formulation, all lengths and velocities are nondimensionalized with the influx velocity halfwidth and the maximum influx velocity,

respectively. The coordinate system is shown in Fig. 7.1 with y upward and perpendicular to the surface, x horizontally outward for the two-dimensional case, and r radially outward for the axisymmetric case. The velocity components are u, parallel to the surface, and v, perpendicular to the surface. The governing equations are:

$$\frac{\partial^2\psi}{\partial y^2} + \frac{\partial^2\psi}{\partial x^2} = \Omega(x,y) \tag{7.1}$$

and

$$\frac{\partial^2\psi}{\partial y^2} + \frac{\partial^2\psi}{\partial r^2} - \frac{1}{r}\frac{\partial\psi}{\partial r} = r^2\Omega(r,y) \tag{7.2}$$

for two-dimensional and axisymmetric impingement, respectively. In Eq. (7.1), the stream and vorticity functions are defined:

$$\frac{\partial\psi}{\partial x} = -v, \quad \frac{\partial\psi}{\partial y} = u \tag{7.3}$$

$$\Omega = \frac{\partial u}{\partial y} - \frac{\partial v}{\partial x} \tag{7.4}$$

and in Eq. (7.2):

$$\frac{\partial\psi}{\partial r} = -rv, \quad \frac{\partial\psi}{\partial y} = ru \tag{7.5}$$

$$\Omega = \frac{1}{r}\left(\frac{\partial u}{\partial y} - \frac{\partial v}{\partial r}\right) \tag{7.6}$$

The stream function is defined to be zero along the jet centerline and the surface. The influx stream function, $F(x)$, can be determined from the given influx velocity profile at some distance, b, above the surface. The outflux streamlines are assumed to become parallel at some sufficiently large distance, a, from the jet centerline. These boundary conditions are written:

$$\psi(x,0) = 0 \tag{7.7}$$

$$\psi(0,y) = 0 \tag{7.8}$$

$$\frac{\partial\psi}{\partial x}(a,y) = 0 \tag{7.9}$$

$$\psi(x, b) = F(x) \tag{7.10}$$

where x is simply replaced by the radial coordinate, r, for the axisymmetric case.

7.4 Analytical Solutions

7.4.1 Two-dimensional Solution

To solve Eq. (7.1) analytically, given the inhomogeneous mixed boundary conditions, Eqs. (7.7)-(7.10), the general solution was assumed to be the sum of the solution, ψ_H, to the Laplace equation subject to the given boundary conditions and the solution, ψ_I, to the given Poisson equation subject to homogeneous boundary conditions. The most general solution to the former is found by separating the variables:

$$\psi_H(x, y) = [A\sin(kx) + B\cos(kx)][C\sinh(ky) + D\cosh(ky)] \tag{7.11}$$

Applying the first three boundary conditions, Eqs. (7.7)-(7.9), the solution becomes:

$$\psi_H(x, y) = \sum_{n=1}^{\infty} A_n \sin(\gamma_n x)\sinh(\gamma_n y) \tag{7.12}$$

where $\gamma_n = \frac{2n-1}{2a}\pi$. The constants A_n are determined by applying the last boundary condition, Eq. (7.10):

$$\sum_{n=1}^{\infty} A_n \sin(\gamma_n x)\sinh(\gamma_n b) = F(x) \tag{7.13}$$

Multiplying both sides of Eq. (7.13) by $\sin(\gamma_m x)dx$ and integrating from 0 to a yields:

$$A_n = \frac{2}{a\sinh(\gamma_n b)} \int_0^a F(x')\sin(\gamma_n x')dx' \tag{7.14}$$

The solution to the Poisson equation subject to homogeneous mixed boundary conditions is found by expanding both the stream and vorticity functions in the

following Fourier series:

$$\psi_I(x,y) = \sum_{m=1}^{\infty}\sum_{n=1}^{\infty} C_{mn}\sin(\alpha_m y)\sin(\gamma_n x) \tag{7.15}$$

$$\Omega(x,y) = \sum_{m=1}^{\infty}\sum_{n=1}^{\infty} B_{mn}\sin(\alpha_m y)\sin(\gamma_n x) \tag{7.16}$$

where $\alpha_m = \frac{m\pi}{b}$. The Fourier coefficients, B_{mn}, in Eq. (7.16) are written as a surface integral involving the vorticity function:

$$B_{mn} = \frac{4}{ab}\int_0^a \int_0^b \Omega(x',y')\sin(\alpha_m y')\sin(\gamma_n x')dy'dx' \tag{7.17}$$

Using Eqs. (7.1), (7.15), and (7.16), we can solve for C_{mn}:

$$C_{mn} = \frac{-B_{mn}}{\gamma_n^2 + \alpha_m^2} \tag{7.18}$$

The general solution to Eq. (7.1) is the sum of ψ_H and ψ_I:

$$\psi(x,y) = \sum_{n=1}^{\infty}\left[A_n\sinh(\gamma_n y) - \sum_{m=1}^{\infty}\frac{B_{mn}}{\gamma_n^2+\alpha_m^2}\sin(\alpha_m y)\right]\sin(\gamma_n x) \tag{7.19}$$

This result is the stream function distribution assuming parallel influx and outflux flow far from the origin. Note that the simple inviscid corner flow solution, $\psi \sim xy$, is recovered as x and y become very small.

Applying Eq. (7.19) to impinging jets requires knowledge of the vorticity function throughout the whole region so that the coefficients, B_{mn}, can be determined from Eq. (7.17). Although we don't have the information necessary to compute B_{mn} exactly, an approximation of the surface integral is provided in Section 7.5.

7.4.2 Axisymmetric Solution

The procedure to calculate the general solution of the axisymmetric case is identical to that presented in Section 7.4.1 for the two-dimensional case. The resulting homogeneous

stream function is:

$$\psi_H(r,y) = \sum_{n=0}^{\infty} D_n r J_1(\lambda_n r)\sinh(\lambda_n y) \tag{7.20}$$

where λ_n are defined such that $J_0(\lambda_n a) = 0$. Again, the coefficients, D_n, are determined from the fourth boundary condition, Eq. (7.10):

$$D_n = \frac{2}{a^2 J_1^2(\lambda_n a)\sinh(\lambda_n b)} \int_0^a F(r') J_1(\lambda_n r') dr' \tag{7.21}$$

The inhomogeneous solution, ψ_I, is determined by expanding the stream function and the right-hand side of Eq. (7.2) into the following series:

$$\psi_I(r,y) = \sum_{m=1}^{\infty}\sum_{n=1}^{\infty} F_{mn} r J_1(\lambda_n x)\sin(\alpha_m y) \tag{7.22}$$

$$r^2\Omega(r,y) = \sum_{m=1}^{\infty}\sum_{n=1}^{\infty} E_{mn} r J_1(\lambda_n x)\sin(\alpha_m y) \tag{7.23}$$

where, once again, a surface integral involving the vorticity function is embedded in the series coefficients, E_{mn}:

$$E_{mn} = \frac{4}{ba^2 J_1^2(\lambda_n a)} \int_0^a \int_0^b r'^2 \Omega(r',y') J_1(\lambda_n r')\sin(\alpha_m y') dy' dr' \tag{7.24}$$

Using Eqs. (7.2), (7.22), and (7.23);

$$F_{mn} = \frac{-E_{mn}}{\alpha_m^2 + \lambda_n^2} \tag{7.25}$$

The general solution to Eq. (7.2) subject to the boundary conditions, Eqs. (7.7)-(7.10), is:

$$\psi(r,y) = \sum_{n=0}^{\infty}\left[D_n\sin(\lambda_n y) - \sum_{m=0}^{\infty}\frac{E_{mn}}{\alpha_m^2+\lambda_n^2}\sin(\alpha_m y)\right] r J_1(\lambda_n r) \tag{7.26}$$

7.5 Evaluating the Vorticity Function Integral

To apply Eqs. (7.19) and (7.26) to the physical problem of impingement flow, the surface integrals in Eqs. (7.17) and (7.24) must be evaluated. Therefore, some information about how the vorticity function behaves within the region of interest is required. Due to the inviscid approximation, the vorticity is constant along streamlines; so $\Omega = \Omega(\psi)$. This alone is not sufficient to solve the surface integral; however, if we also assume that the influx velocity halfwidth is small compared to the integration limits, a and b, then we can approximate the stream function (and thus the vorticity function) over most of the region with a far-field expression. This implies that redirection of flow possessing non-negligible vorticity is confined to a very small area compared to the whole domain. However, because of thus, vorticity introduced into the flow far from the jet centerline cannot be accurately accounted for using this approach. Fortunately, for the case of simple jet impingement, this constraint doesn't pose a problem.

The small near-field region close to the intersection of the jet centerline and the surface must be treated separately. Hence the surface integrals are split into the three regions portrayed in Fig. 7.1: the inflow region, **I**, and the outflow region, **III**, which require far-field solutions, and the impingement region, **II**, which requires a near-field solution.

7.5.1 Far-field Solutions

The approximation for region **I** stems from the assumption that the influx near the centerline does not sense the presence of the surface until it is very close to the surface. The vorticity function is, therefore, determined by the influx condition and can be expressed in terms of the influx stream function, $F(x)$, as

$$\Omega_{\mathbf{I}}(x) = F''(x), \tag{7.27}$$

$$\Omega_{\mathbf{I}}(r) = \frac{F''(r)}{r^2} - \frac{F'(r)}{r^3}, \tag{7.28}$$

for two-dimensional and axisymmetric cases, respectively.

Similar to the reasoning for region **I**, we assume that the vorticity close to the surface in region **III** approaches the outflux condition very soon after redirection. This condition is a little harder to implement directly since the outflux boundary condition only assumes parallel streamlines. Therefore, we refer to Rubel's method [71] for converting the mixed boundary conditions to Dirichlet boundary conditions. For the two-dimensional case, Rubel showed that Eqs. (7.1) and (7.9) imply the outflux condition, $\psi(a, y) = F(y)$. Hence, the vorticity function in region **III** is taken to be:

$$\Omega_{\mathbf{III}}(y) = F''(y) \tag{7.29}$$

for the two-dimensional case.

Similarly, Rubel showed that Eqs. (7.2) and (7.9) imply the axisymmetric outflux condition, $\psi(a, y) = F(\sqrt{2ay})$. Since the outflux stream function profile depends on the radial location of the boundary, a, it seems reasonable that, as the outflux condition is approached for large radial distances, the far-field stream function could be written as $\psi(r, y) = F(\sqrt{2ry})$, which approaches the parallel outflux condition far from the origin. Therefore, we have for the axisymmetric case:

$$\Omega_{\mathbf{III}}(r, y) = \frac{F''(\xi)}{\xi^2} - \frac{F'(\xi)}{\xi^3} \tag{7.30}$$

where $\xi = \sqrt{2ry}$.

7.5.2 Near-field Solutions

The vorticity function in region **II** is determined from the streamfunction behavior close to the origin. As mentioned earlier, $\psi \sim xy$ for small x and y in the two-dimensional case. Since vorticity is constant along streamlines, then Ω is a function of xy:

$$\Omega(x, y) = G(xy) \tag{7.31}$$

where the function G is determined by matching the vorticity function at $x = \delta$ and $y = \epsilon$ with the far-field solutions (see Fig. 7.1). Since $\psi(x, \delta) = F''(x)$ and $\psi(\epsilon, y) = F''(y)$, then:

$$G(xy) = \Omega_{\mathbf{II}}(x, y) = F''(\frac{xy}{\epsilon}) \tag{7.32}$$

and $\delta = \epsilon$.

For the axisymmetric case, $\psi \sim r^2 y$ for small r and y; and matching the vorticity function at δ and ϵ yields:

$$\Omega_{\mathbf{II}}(r, y) = \frac{F''(\zeta)}{\zeta^2} - \frac{F'(\zeta)}{\zeta^3} \tag{7.33}$$

where $\zeta = r\sqrt{\frac{y}{\epsilon}}$ and $\delta = 2\epsilon$.

7.5.3 The Total Integral

Since we have estimated the value of the vorticity function in the three regions, the surface integral in Eqs. (7.17) and (7.24) can be split into three integrals of known functions. For the two-dimensional case, we have:

$$\int_0^a \int_0^b \Omega(x', y') \sin(\alpha_m y') \sin(\gamma_n x') dy' dx' = I_1 + I_2 + I_3 \tag{7.34}$$

where

$$I_1 = \int_0^a \int_\epsilon^b F''(x') \sin(\alpha_m y') \sin(\gamma_n x') dy' dx' \tag{7.35}$$

$$I_2 = \int_0^\epsilon \int_0^\epsilon F''(\frac{x'y'}{\epsilon}) \sin(\alpha_m y') \sin(\gamma_n x') dy' dx' \tag{7.36}$$

$$I_3 = \int_\epsilon^a \int_0^b F''(y') \sin(\alpha_m y') \sin(\gamma_n x') dy' dx' \tag{7.37}$$

These integrals can be computed numerically for an arbitrary influx stream function, $F(x)$. Fortunately, only I_2 requires a two-dimensional integration, since I_1 can be integrated directly with respect to y; and I_3, with respect to x. Note that the I_1 and I_3 integrals overlap where $x, y > \epsilon$, but at least one of the vorticity functions is essentially zero in this region.

The computation of the surface integral in the axisymmetric case is more time consuming than the two-dimensional case, since the corresponding I_3 integral requires integration over both r and y:

$$\int_0^a \int_0^b \Omega(r', y') r'^2 J_1(\delta_n r') \sin(\alpha_m y') dy' dr' = I_1 + I_2 + I_3 \tag{7.38}$$

$$I_1 = \int_0^a \int_\epsilon^b \left(F''(r') - \frac{F'(r')}{r'} \right) J_1(\lambda_n r') \sin(\alpha_m y') dy' dr' \tag{7.39}$$

$$I_2 = \int_0^\delta \int_0^\epsilon \left(F''(r'\sqrt{\frac{y'}{\epsilon}}) - \frac{F'(r'\sqrt{\frac{y'}{\epsilon}})}{r'\sqrt{\frac{y'}{\epsilon}}} \right) J_1(\lambda_n r') \sin(\alpha_m y') dy' dr' \tag{7.40}$$

$$I_3 = \int_\delta^a \int_0^b \left(F''(\sqrt{2r'y'}) - \frac{F'(\sqrt{2r'y'})}{\sqrt{2r'y'}} \right) J_1(\lambda_n r') \sin(\alpha_m y') dy' dr' \tag{7.41}$$

7.6 Results and Discussion

Section 7.4 presents an analytical solution for a jet impinging on a flat surface assuming complete knowledge of the vorticity distribution within the entire impingement region. Although vorticity is constant along streamlines, the final stream function distribution is not determined by approximating the vorticity. The far-field/near-field stream function approximations used in the vorticity integrals in Section 7.5 provide an initial estimate of the flow solution, that is corrected through the solving process. To maximize the accuracy of the final solution, it is essential that the initial guess be as close to the final solution as possible. The structure of the initial guess was justified in Section 7.5, and the matching location, ϵ, is chosen such that the outflux surface velocity approaches the influx centerline velocity. The discussion that follows compares published surface pressure data with the present calculations. The surface pressure is determined from Bernoulli's equation, i.e.,

$$P(x) = 1 - \left(\left. \frac{\partial \psi}{\partial y} \right|_{y=0} \right)^2 \tag{7.42}$$

and

$$P(r) = 1 - \left(\frac{1}{r} \frac{\partial \psi}{\partial y} \bigg|_{y=0} \right)^2 \tag{7.43}$$

for the two-dimensional and axisymmetric cases, respectively.

7.6.1 Two-dimensional Jet

Fully developed jet impingement

Surface pressure measurements for the impingement of fully developed two-dimensional jets were made by Schauer and Eusits [74], Kumada and Mabuchi [75], and Beltaos and Rajaratnam [60] for a variety of jet heights, H, and jet Reynolds numbers. A comparison between their experimental data and the calculated surface pressure distribution, normalized with the maximum stagnation pressure, P_m, is shown in Figure 7.2. All of the experimental data exhibit collapse when distances are scaled with H. In order to convert to the present convention, it was necessary to determine the velocity halfwidth, b_u, at the prescribed influx location. For a free jet, Beltaos and Rajaratnam [60] found

$$\frac{b_u}{H} = 0.10(\frac{y^\star}{H} + 0.15) \tag{7.44}$$

where $y^\star$ is the dimensional distance from the jet nozzle. Furthermore, it was found that the influx location - taken to be the surface of departure of the jet from free jet behavior - is consistently located at $0.7H$ from the nozzle. Therefore, conversion simply involved dividing distances by the factor $\frac{b_u}{H} = 0.085$, and the collapse remains.

The solid line in Figure 7.2 represents the predicted pressure distribution for a matching location of $\epsilon = 1.1$. The values of the integration limits, a and b, were chosen such that any increase in these values had no effect on the solution. Similar to Rubel's observations, the values $a = 5$ and $b = 5$ placed the boundaries sufficiently far from the origin. The fully developed two-dimensional free jet velocity profile as

derived by Gortler [76] was used for the influx profile, i.e.,

$$-v(x) = (1 - \tanh^2(cx)) \tag{7.45}$$

where $c = \tanh^{-1}(\frac{1}{\sqrt{2}})$.

The pressure distribution represented by the dashed line in Figure 7.2 was obtained using the numerical method of Rubel [71]. In accordance with his suggestions, a 41x41 grid spanning a 5x5 square was utilized for the finite difference calculations. The maximum deviation between the two methods of calculation was 8% and occurs at a location of 0.9.

Figure 7.3 exhibits a comparison of the predicted streamlines for an impinging fully developed two dimensional jet using both methods of calculation. The parallel outflux boundary condition, which could only be approximated by an outflux stream function distribution in Rubel's calculations, is met exactly in the present calculations. This is evident in Fig. 7.3, especially for the higher valued streamlines.

Developing jet impingement

When a turbulent jet nozzle is located less than about 6 jet widths above the surface ($\frac{H}{D} < 6$), then the jet potential core will impinge upon the surface [77]. Since the jet velocity profile is no longer self-similar due to the uniform velocity of the potential core, it would not be surprising if the form of the surface pressure profile deviated from similarity. Indeed, as will be shown in Section 7.6.2, similarity does break down for unconfined axisymmetric jet impingement. In contrast, Tu and Wood [67] observed pressure profile similarity for jet heights as low as $\frac{H}{D} = 1$. The strong interaction of the potential core with the surface was evidenced by peak stagnation pressures equal to the dynamic pressure at the jet outlet.

The experiments of Tu and Wood [67] include conditions that allow direct comparison with Rubel's [71] numerical results. To facilitate comparison of the present model with that of Rubel, we employ the developing jet velocity profile used

in the previous calculations,

$$-v(x) = \frac{1}{2}\left[1 + \mathrm{erf}\left(\frac{1-x}{\sigma}\right)\right] \tag{7.46}$$

where σ is a spreading parameter. The difference between this velocity profile and that for the fully developed jet is shown in Fig. 7.4. Figure 7.5 compares the surface pressure distributions predicted with the two models with the experimental data of Tu and Wood [67]. Rubel's calculations show a greater sensitivity to σ than does the present model. This may result from the relatively coarse grid used in the former calculations, leading to inaccuracies in the description of sharp gradients encountered in the developing jet.

7.6.2 Axisymmetric Jet

A major difference between treatment of the two-dimensional jet and the axisymmetric jet is the handling of the parallel outflux boundary condition. It was shown in Section 7.5.1 that parallel outflux implies an essentially parallel far-field flow for the two-dimensional case, whereas the far-field streamlines resemble hyperbolas for the axisymmetric case. The hyperbolic streamlines approach the parallel outflux condition infinitely far from the origin; therefore, placement of the outflux boundary at a finite radial location results in a premature parallelization of the outflux streamlines. This in turn creates a decrease in velocity approaching the boundary. To ensure that this effect does not infringe upon the region of strong pressure gradient, the outflux boundary must be farther from the origin than in the two-dimensional case. A radial location of $a = 10$ was sufficient for the present calculations.

Fully developed jet impingement

The Schlichting similarity solution [76] for a fully developed axisymmetric free jet is used to define the influx velocity profile:

$$-v(r) = \frac{1}{(1 + (\sqrt{2}-1)r^2)^2} \tag{7.47}$$

This similarity solution is applicable to jet impingement for $\frac{H}{D} > 8$ [78]. Surface pressure measurements for normally impinging axisymmetric jets at these heights were made by Bradbury [79] ($12 < \frac{H}{D} < 20$), Beltaos and Rajaratnam [61] ($20 < \frac{H}{D} < 66$), and Giralt, Chia, and Trass [78] ($8 < \frac{H}{D} < 20$). These data are presented in Fig. 7.6 along with the calculated surface pressures using the present method and Rubel's numerical method. A matching location of $\epsilon = 0.5$ produces excellent agreement with the pressure data throughout the entire impingement region. It is encouraging that the scatter in the axisymmetric pressure data is significantly less than in the two-dimensional data (Fig. 7.2), since agreement between theory and experiment is better for the axisymmetric case.

Developing jet impingement

Unlike for the two-dimensional case, similarity of the surface pressure profiles breaks down when the axisymmetric jet potential core impinges onto the surface ($\frac{H}{D} < 8$) [78]. Furthermore, we expect that the pressure profile should approach that predicted by the inviscid impinging potential jet model of Strand [68] as the jet height is decreased. Surface pressure data for impinging developing jets are provided by Giralt, Chia, and Trass [78], who measured the surface pressures for several jet heights in the range $1.2 < \frac{H}{D} < 6.0$. These data are presented in Fig. 7.7 along with Strand's solution and calculations for various potential core radii, r_{core}. Note the good agreement between the lowest jet height data, Strand's potential solution, and the calculations for the widest core radius. The developing jet velocity profiles used for the calculations were defined such that $u = 1$ for $r \leq r_{core}$ and Eq. (7.47) applied for $r > r_{core}$. They are presented in Fig. 7.8.

Stagnation bubbles and annular jet impingement

The shock waves produced within the potential core of an underexpanded free jet cause a decrease in the centerline jet velocity [63]. The velocity profile downstream will resemble the fully developed profile described in Eq. (7.47) with a velocity deficient core. The impingement of this type of profile was also investigated numerically by

Rubel [72], who predicted the conditions at which areas of recirculation would develop near the stagnation point. Rubel used a family of velocity profiles described by the location of the maximum velocity, r_m, and the core velocity deficiency, d_w - the difference between the maximum and centerline velocities. These profiles were defined such that Eq. (7.47) applied for $r > r_m$ and the centerline vorticity was non-zero for $d_w > 0$:

$$\begin{aligned} -v(r) &= 1 - d_w + 2d_w \frac{r^2}{r_m^2}\left(1 - \frac{1}{2}\frac{r^2}{r_m^2}\right) \quad ; \qquad 0 \le r \le r_m \\ -v(r) &= (1 + c_m(r - r_m)^2)^{-2} \quad ; \qquad r \ge r_m, \end{aligned} \tag{7.48}$$

where $c_m = \frac{\sqrt{2}-1}{(1-x_m)^2}$. Using these profiles, Rubel found recirculation regions for $\frac{d_w}{r_m} > 0.22$; but was unable to find solutions for $\frac{d_w}{r_m} > 0.47$. The present method yields results similar to Rubel for $\frac{d_w}{r_m} < 0.47$ and solutions are also possible for $\frac{d_w}{r_m} > 0.47$. Fig. 7.9 displays a sample comparison of streamlines calculated with the present method and with Rubel's method [72] for the case $x_m = 0.35$ and $d_w = 0.16$. The stagnation bubble appears as the area within the dividing streamline corresponding to $\psi = 0$.

Further increase in the core deficiency produces a velocity profile that resembles the near-nozzle profile of a free annular jet. Fig. 7.10 compares the profile calculated using Eq. (7.48) ($x_m = 0.65$,$d_w = 0.80$) with the free annular jet velocity data of Sheen, Chen, and Jeng [80] at a downstream distance of about one outer diameter. In this case, the inner diameter was close to one-half of the outer diameter. Because of the severe core velocity deficiency ($\frac{d_w}{r_m} = 1.23$), the impingement of such a flow could not be treated with Rubel's method. Fig. 7.11 depicts streamlines calculated with the present method for this case. Since no experimental data was found in the literature on the size of the recirculating region under an impinging annular jet, comparison with measurements is not possible. However, some predictions of the shape of the recirculation region are presented in Fig. 7.12, which depicts the streamlines corresponding to $\psi = 0$ for several core velocity deficiencies. A plot of the locations of the dividing streamline along the jet centerline and the surface (z_d

and r_d, respectively) against the relative core velocity deficiency, $\frac{d_w}{r_m}$, for $r_m = 0.3$ and $r_m = 0.6$ is presented in Fig. 7.13. The critical value of the relative core velocity deficiency leading to formation of a recirculation region is close to Rubel's predicted value of $\frac{d_w}{r_m} = 0.22$. The value of r_d could easily be determined experimentally, as it would be accompanied by a maximum in the surface pressure profile. Experimental verification of these predictions would require knowledge of the velocity profile at the top of the impingement region. Reasonable agreement with experiment would confirm the validity of inviscid models for the impingement region of annular and underexpanded jet impingement on a flat surface, and would support Rubel's [72] suggestion that the inviscid total pressure defect mechanism is responsible for the observed stagnation bubbles under impinging underexpanded jets.

7.7 Conclusion

A method for calculating the flow field for axisymmetric and two-dimensional inviscid impingement flow is presented. Exact solutions were derived in terms of the vorticity function distribution which was approximated by matching far-field and near-field expressions at prescribed locations, thus yielding a corrected solution. The method was applied to flow calculations for various two-dimensional and axisymmetric impinging jet configurations, including annular jet impingement, which has not been considered in previous inviscid calculations. The accuracy of the present calculations is sufficient to demonstrate agreement with previous numerical results and, within the relatively large scatter, with the available data. The accuracy of the present calculations might be improved by using the final stream function distribution to interpolate vorticity function values throughout the impingement region and subsequently recalculating the vorticity integral to obtain a corrected solution. This increases the computation time, however, and is unnecessary for the present comparisons.

Acknowledgments

This work was supported by the Federal Aviation Administration under grant number FAA-93-G-060.

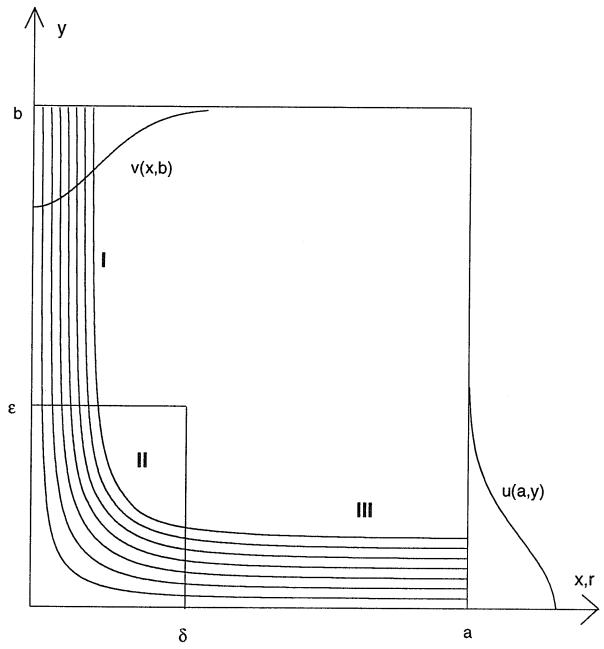

Figure 7.1: Approximate view of the flow region for determining vorticity surface integral.

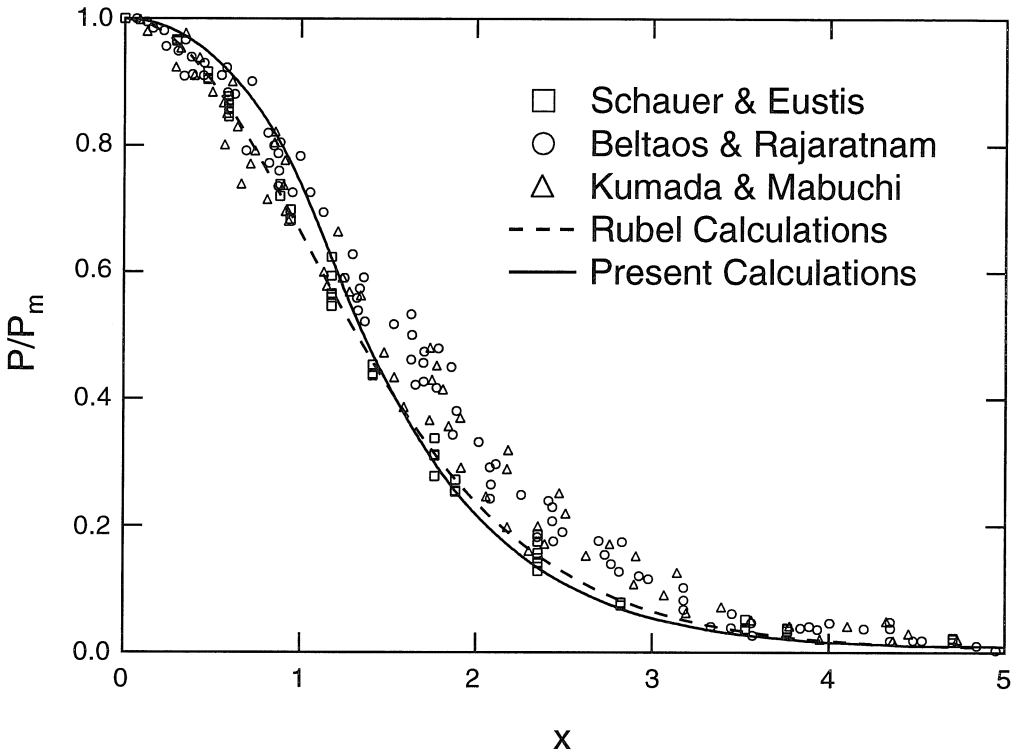

Figure 7.2: Comparison of predicted surface pressure distribution with experimental and numerical results for an impinging two-dimensional jet.

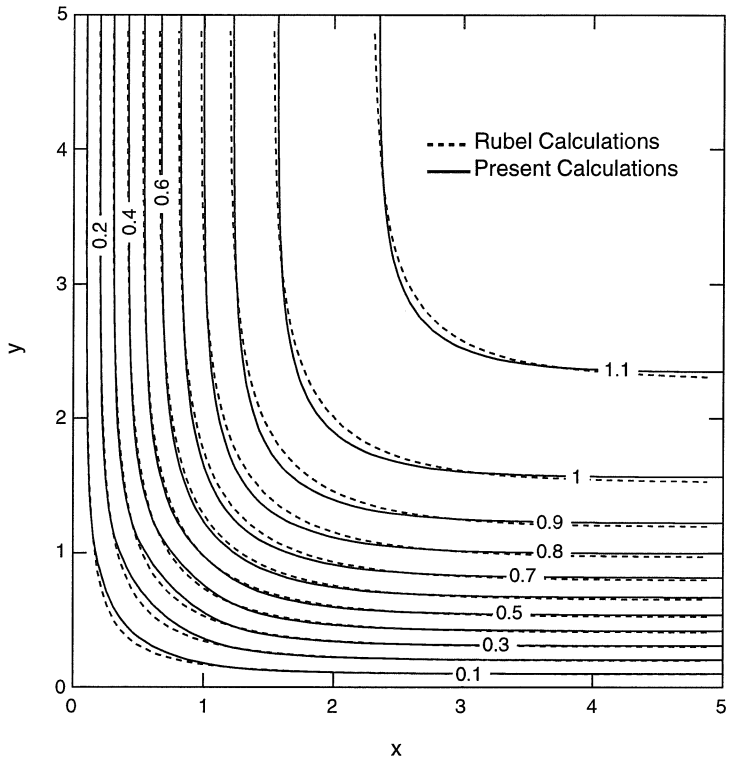

Figure 7.3: Two-dimensional impinging jet streamlines as calculated using Rubel method and the present method.

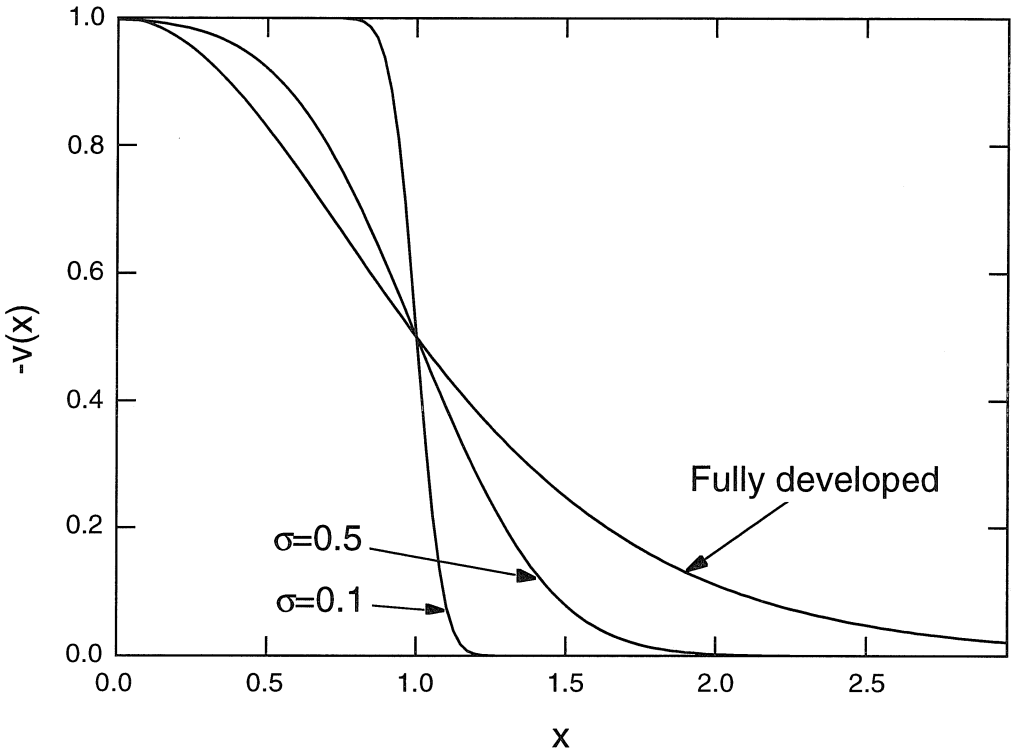

Figure 7.4: Influx velocity profiles used for calculations.

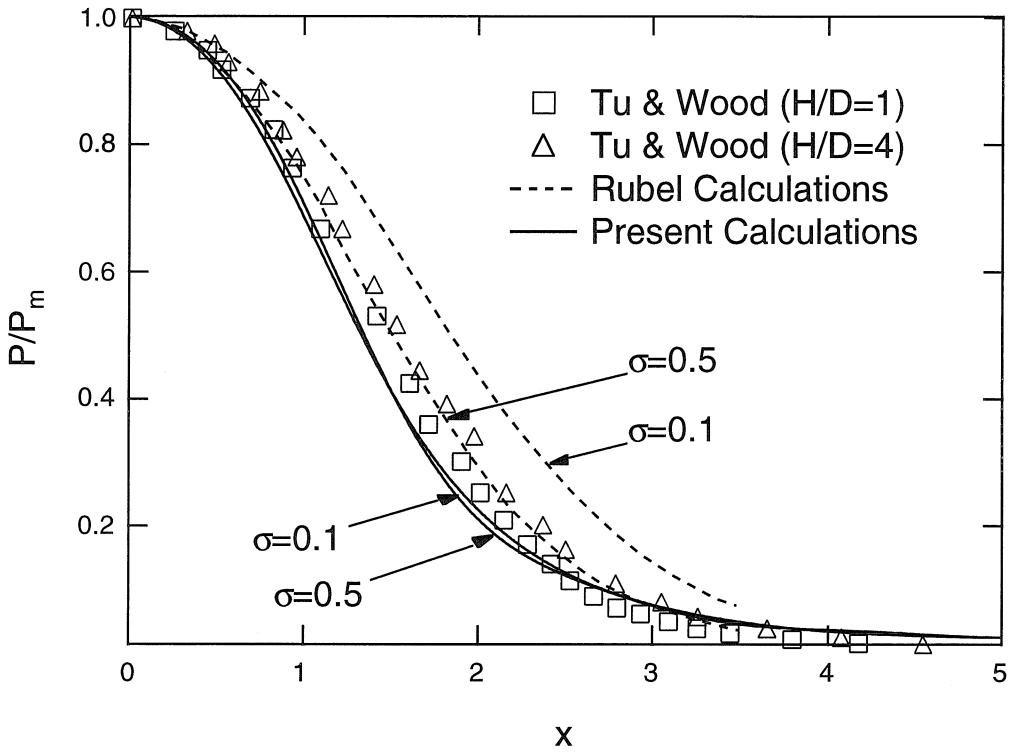

Figure 7.5: Observed and predicted surface pressure distributions for two-dimensional developing jet impingement for $\sigma = 0.1$ and $\sigma = 0.5$.

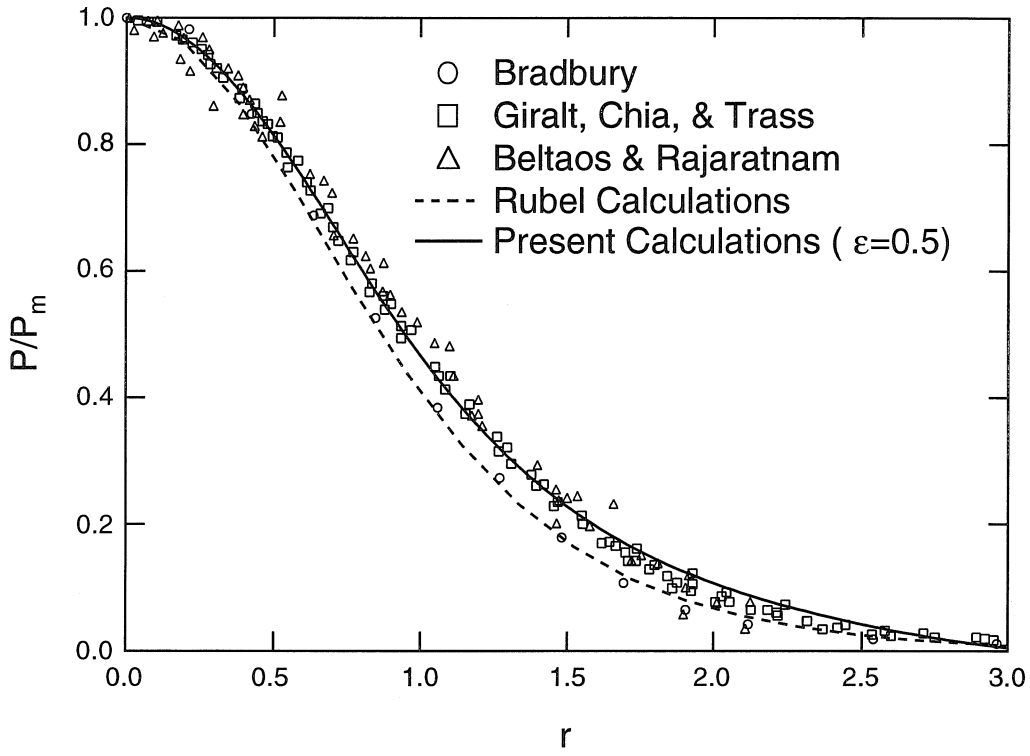

Figure 7.6: Comparison of predicted surface pressure distribution with experimental and numerical results for a fully developed impinging axisymmetric jet.

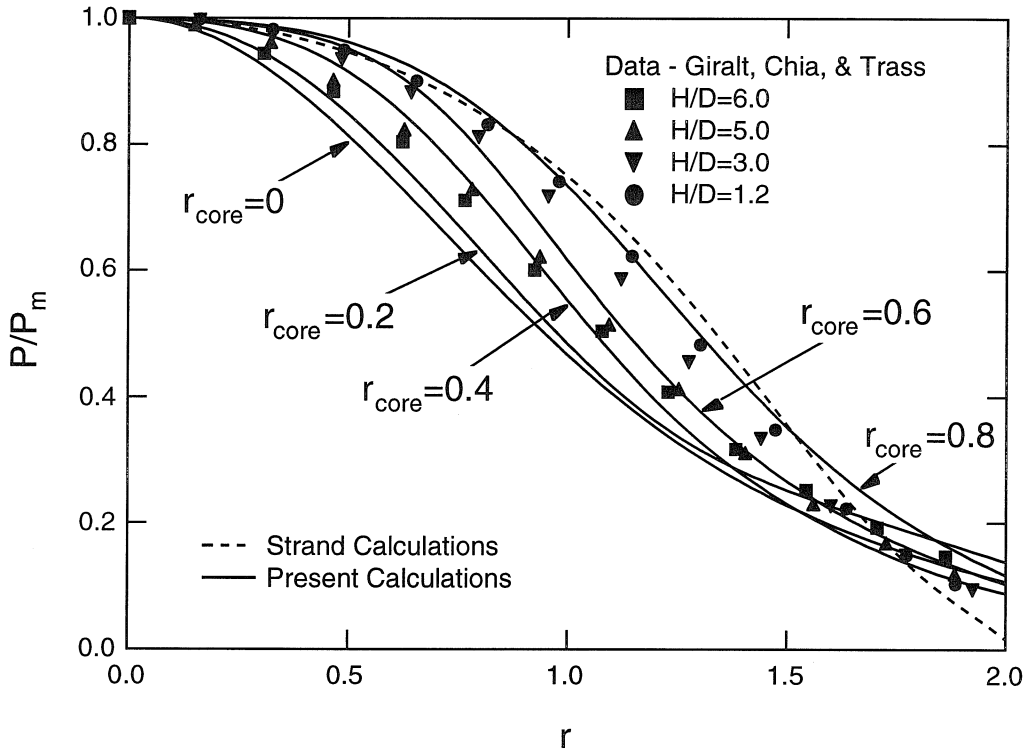

Figure 7.7: Measurements of Giralt, Chia, and Trass for various jet heights compared with present calculations for developing jet impingement and Strand's potential jet solution.

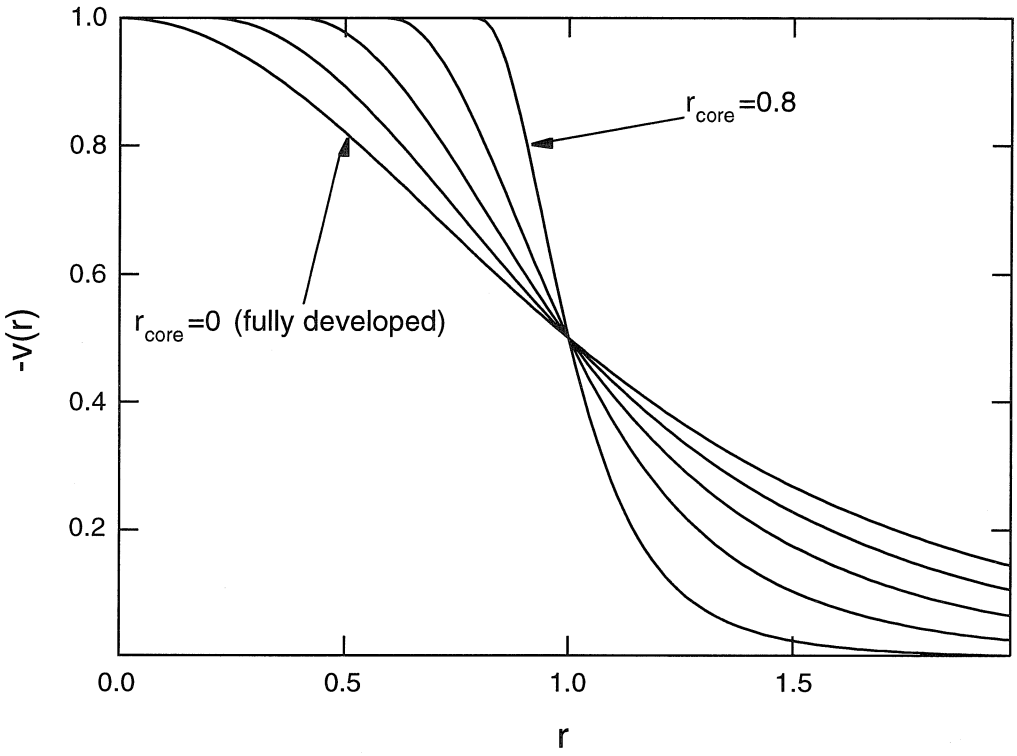

Figure 7.8: Developing jet velocity profiles.

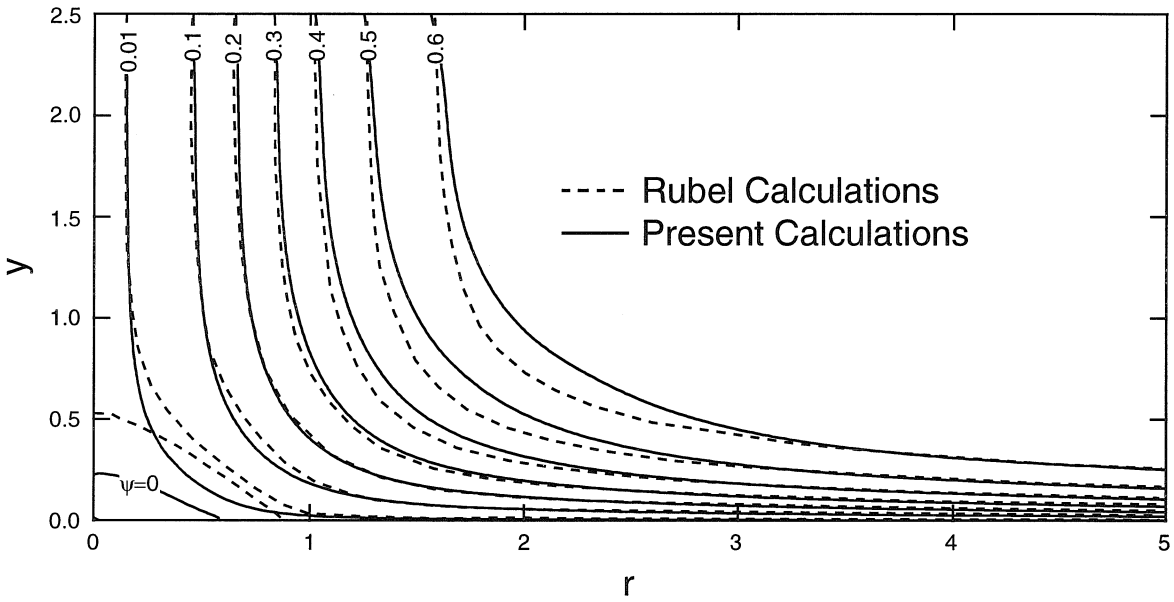

Figure 7.9: Streamline plot with stagnation bubble for $x_m = 0.35$ and $d_w = 0.16$.

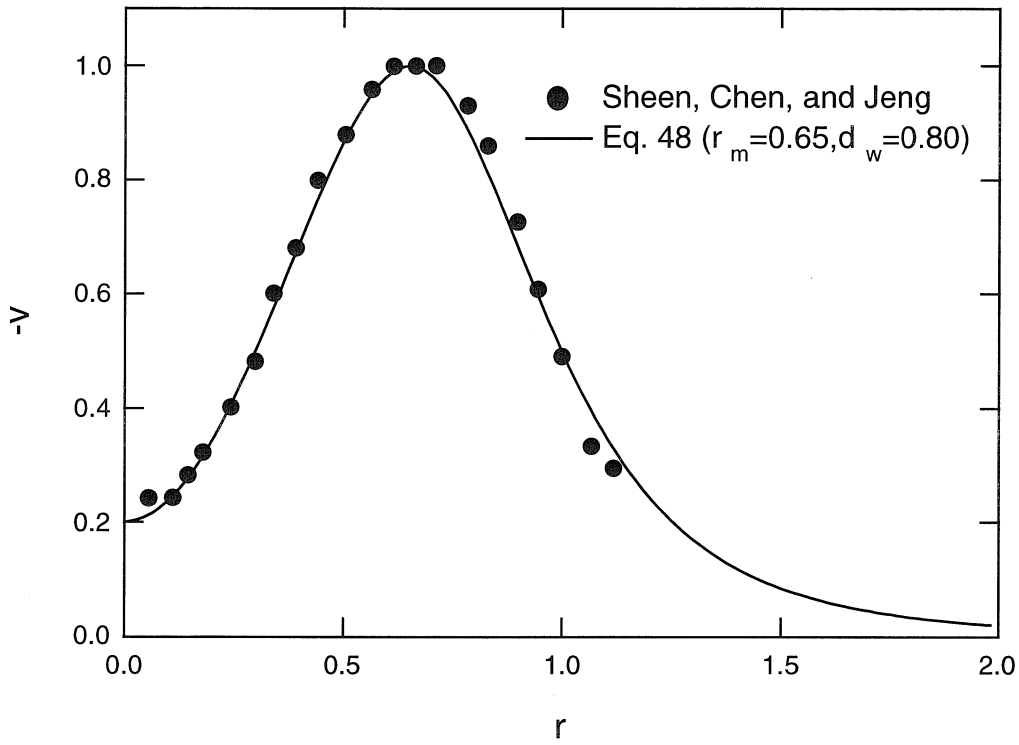

Figure 7.10: Comparison of free annular jet velocity data with Equation (refdef).

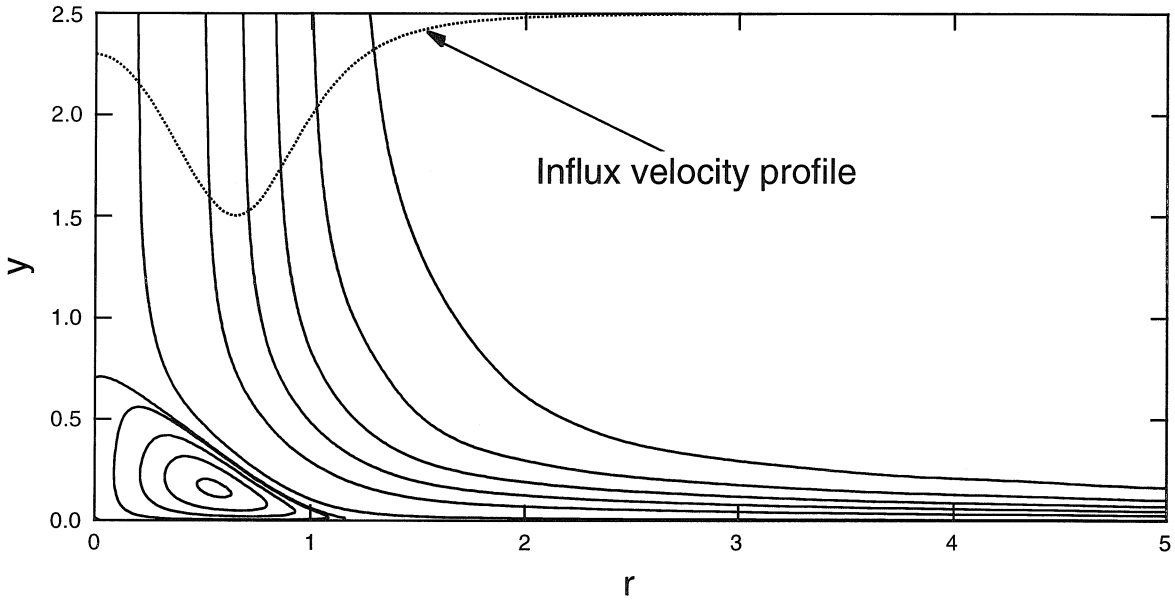

Figure 7.11: Streamline plot with overlaid influx velocity profile for annular jet impingement.

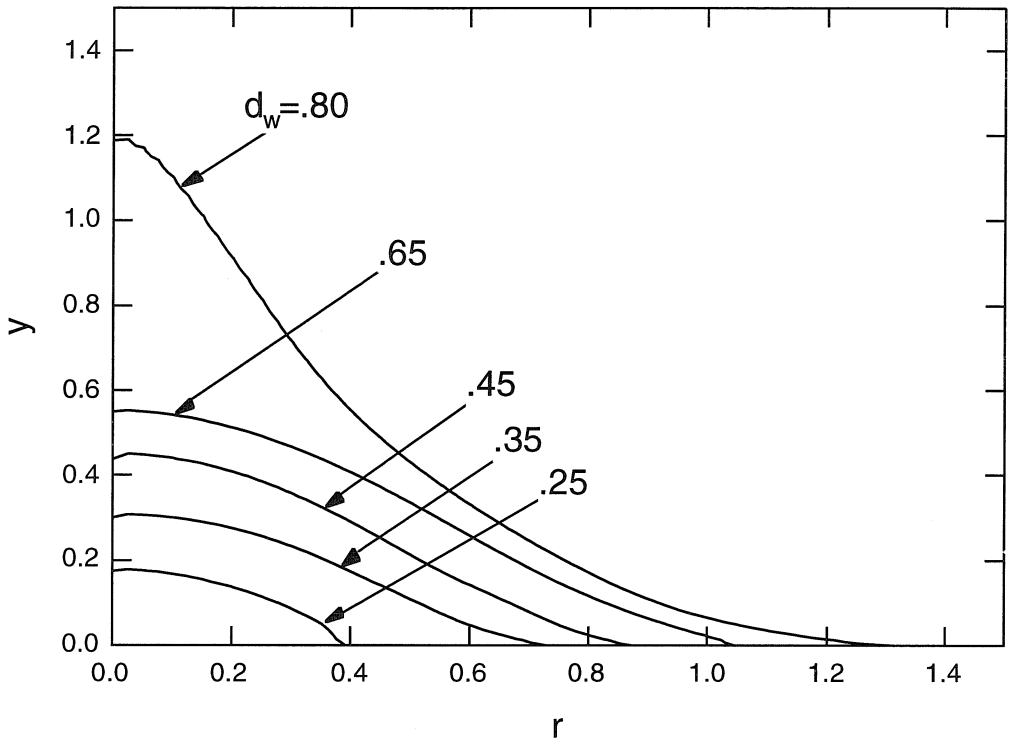

Figure 7.12: Shape of recirculation zone for various core velocity deficiencies ($r_{core} = 0.60, d_w = 0.25, 0.35, 0.45, 0.65, 0.80$).

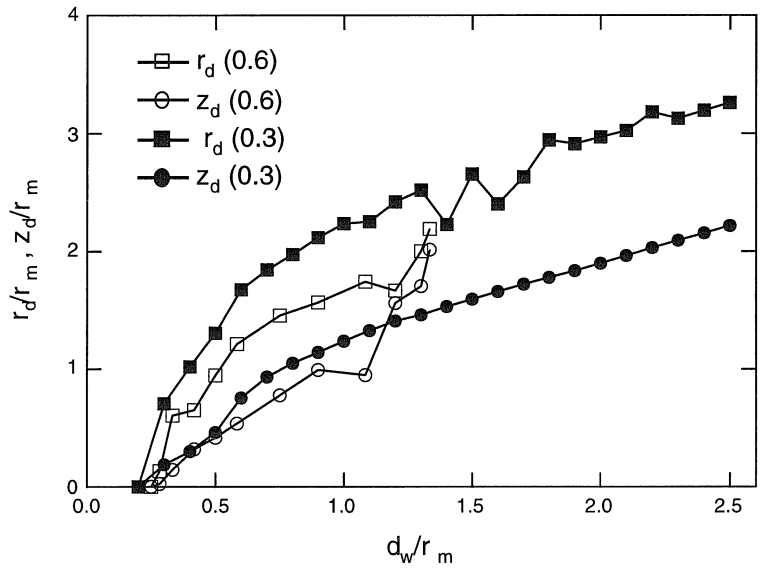

Figure 7.13: Predicted dependence of dividing streamline location on core deficiency for $r_m = 0.3, 0.6$.

Chapter 8 The Wall Shear Stress Produced by the Normal Impingement of a Jet on a Flat Surface

8.1 Abstract

A method for the theoretical determination of the wall shear stress under impinging jets of various configurations is presented. Axisymmetric and two-dimensional incompressible jets of all Reynolds numbers and jet heights are considered. Theoretical predictions from this approach are compared with available wall shear stress measurements. These data are critically evaluated based on the method of measurement and its applicability to the shape of the boundary layer under consideration. It was found that impingement region wall shear stress measurements using the electrochemical method in submerged impinging liquid jets provide the greatest accuracy of any indirect method. A unique wall shear stress measurement technique, based on observing the removal monosized spheres from well-characterized surfaces, was used to confirm the presented impinging jet analysis for gas jets. The technique was also used to determine an empirical relation describing the rise in wall shear stress due to compressibility effects in impinging high velocity jets.

8.2 Introduction

Impinging gas jets have most commonly been exploited for their enhanced heat and mass transfer characteristics when applied to industrial processes. Consequently, impinging jet research has generally focused on understanding and quantifying heat and mass transfer to a surface for a wide variety of impinging jet configurations.

The present work is concerned with an often overlooked aspect of the flow - the wall shear stress produced on the surface. Recently, a few applications that utilize the shear imposed at the surface by impinging jets have been discussed in the literature. Deshpande & Vaishnav (1982) [81] used submerged impinging saline jets to probe the shear strength of the endothelial surface of a vascular tissue. The structure of this delicate layer of cells can be visibly altered by excessive applied shear. Tu & Wood (1996) [67] and Bouainouche, Bourabaa & Desmet (1997) [82] described a process known as *jet stripping* in which impinging plane jets are used to control liquid coating thickness on continuous metal strips. Impinging jets can also be used to extract particles from surfaces either as a cleaning method or to collect samples for chemical analysis, e.g., for detection of explosives or other contraband. Smedley, Phares & Flagan (1999) [21] explored the entrainment of uniformly sized spherical particles by a normally impinging gas jet. The transition from complete adhesion to complete entrainment was abrupt, indicating that the micron-sized particles ($D_p = 8.3$ μm) could be used effectively as quantized shear stress sensors once calibrated with an appropriate experiment. This chapter presents a theoretical and experimental study aimed at obtaining a reliable wall shear stress map for a wide range of jet Reynolds numbers and jet-to-plate spacings. In light of the aforementioned applications, both two-dimensional and axisymmetric jets will be considered, and we will restrict ourselves to the normal impingement of unconfined jets onto a flat surface.

Previous theoretical descriptions of the impinging jet flow field have involved two main schemes. The first entails numerically solving the full Navier-Stokes equations for the entire flow region. Several such studies have included calculations for the wall shear stress distribution. Deshpande & Vaishnav (1982) [81] considered the impinging laminar axisymmetric jet. Looney & Walsh (1984) [83] and Bouainouche *et al.* (1997) [82] considered the impinging turbulent plane jet. The second approach to describing impinging jet flow fields involves separating the flow into regions where distinct approximations of the Navier-Stokes equations are valid. The latter approach is more desirable for our purposes, since we are mainly concerned with the small region of flow located just above the impingement plane, where boundary layer

approximations can be made. An analysis is presented in Section 8.3 which divides the flow into four regions: the free jet region, the inviscid impingement region, the impingement boundary layer, and the wall jet region. Flow solutions in the free jet and inviscid impingement regions provide the free stream conditions for solution of the boundary layer equations needed to determine the wall shear stress in the impingement region. Farther from the stagnation point, as strong pressure gradients vanish, wall shear stress trends should approach those predicted by previous wall jet analyses [84, 85, 86].

Only a few of the many experimental investigations of impinging jets have included measurements of the wall shear stress, but the scatter in the data is higher than the reported uncertainties. In Section 8.4, we use the model developed in Section 8.3 to explore the cause of this scatter and examine the influence of measurement method. In Section 8.5, we present wall shear stress measurements under an impinging circular jet using the measurement technique described by Smedley *et al.* (1999) [21],which involves monitoring the removal of monodisperse microspheres from the impingement surface. Results from this experiment confirm the incompressible model from Section 8.3, and allow the development of an empirical correction factor based on the jet Mach number, M, for impinging compressible jets.

8.3 Theoretical Analysis

Dividing impinging jet flow into separate flow regions was suggested by Bradshaw & Love (1961) [62], who stated that, since flow redirection occurred in such a small region, an inviscid impingement solution coupled with a boundary layer solution might accurately describe the flow. Scholtz & Trass (1970) [69] applied this method to the short range impingement of a laminar axisymmetric jet and made accurate predictions for mass transfer in the impingement region. Kataoka & Mizushina [87] used empirical free stream conditions and a laminar boundary layer analysis at the surface to accurately predict wall shear stress in the impingement region of an axisymmetric impinging turbulent jet. The objective in this section is to generalize

these approaches to include the effect of free jet velocity profile on the inviscid solution and the transition to turbulence in the boundary layer.

8.3.1 The Free Jet Region

A free jet consists of a near-field region, where a potential core has not yet experienced turbulent mixing with the quiescent fluid, and a far-field region, where the jet may be treated as a point source (or line source in the case of the plane jet) and the mean velocity profiles become similar (see Fig. 8.1). Mean velocity similarity generally occurs at a downstream distance of about 8 jet diameters. The wall pressure distribution produced by an impinging jet depends on the mean velocity profile of the fluid at the top of the inviscid impingement region - taken to be the surface of departure from the free jet profile due to the effect of the wall. To maximize the range of applicability of the present work, both near-field and far-field mean velocity profiles for two-dimensional and axisymmetric free jets must be considered for the ensuing inviscid analysis.

The far-field free jet region

The far-field axial velocity profiles for the laminar free jet are shown by Schlichting (1960) [76] to be

$$u(x,y) = 0.4543 \left(\frac{K^2}{\nu x}\right)^{\frac{1}{3}} (1 - \tanh^2 \xi),$$

$$\xi = 0.2752 \left(\frac{K^{\frac{1}{3}}}{\nu^{\frac{2}{3}}}\right) \frac{y}{x^{\frac{2}{3}}} \tag{8.1}$$

for the two-dimensional jet, and

$$u(x,r) = \frac{3}{8\pi} \frac{K}{\nu x} (1 + \frac{1}{4}\eta^2)^{-2},$$

$$\eta = \frac{1}{4} \left(\frac{3}{\pi}\right)^{\frac{1}{2}} \frac{K^{\frac{1}{2}}}{\nu} \frac{r}{x} \tag{8.2}$$

for the axisymmetric case, where ν and K are the kinematic viscosity and jet momentum, respectively. As shown in Fig. 8.1, the coordinate system is chosen such that x is oriented downstream along the jet axis, and y and r are oriented perpendicularly outward from the jet centerline for the two-dimensional and axisymmetric jet, respectively. The laminar solution is accurate only for jet Reynolds numbers under 30 [83]. Extending the axisymmetric development to the turbulent jet simply involves replacing the kinematic viscosity, ν, with the virtual kinematic viscosity, ϵ_o [76]. The far-field mean axial velocity profile for the two-dimensional turbulent jet is

$$u(x,y) = \frac{3^{\frac{1}{2}}}{2}\left(\frac{K\sigma}{x}\right)^{\frac{1}{2}}(1-\tanh^2\zeta),$$

$$\zeta = \frac{\sigma y}{x} \tag{8.3}$$

where σ is an empirical constant.

In addition to providing the influx conditions to the inviscid impingement region for larger jet to surface separations, these similar velocity profiles also possess convenient length and velocity scaling factors in the velocity halfwidth, b_u, and the centerline velocity, u_m. Table 8.1 lists these quantities in terms of the jet exit conditions, where D is the nozzle size (diameter, for a circular jet, and slit width, for a plane jet), u_o is the jet exit velocity, and $\mathrm{Re}_o = u_o D/\nu$ is the jet Reynolds number. Accepted values for the empirical constants, σ and $\epsilon_0/K^{\frac{1}{2}}$, are $7.5 - 7.7$ [76, 83] and $0.016 - 0.018$ [76, 79, 61], respectively.

The near-field free jet region

Close to the jet nozzle, the development of the turbulent mixing zone between the potential core and the quiescent fluid must be considered. For a uniform velocity at the jet exit, the mixing zone mean velocity profile in a two-dimensional jet is well

	Velocity Halfwidth	Centerline Velocity
Two-Dimensional Laminar	$\frac{b_u}{x} = 3.20\mathrm{Re}_o^{-\frac{2}{3}} \left(\frac{x}{D}\right)^{-\frac{1}{3}}$	$\frac{u_m}{u_o} = 0.454\mathrm{Re}_o^{\frac{1}{3}} \left(\frac{x}{D}\right)^{-\frac{1}{3}}$
Axisymmetric Laminar	$\frac{b_u}{x} = 4.67\mathrm{Re}_0^{-1}$	$\frac{u_m}{u_o} = 0.0938\mathrm{Re}_o \left(\frac{x}{D}\right)^{-1}$
Two-Dimensional Turbulent	$\frac{b_u}{x} = \frac{0.881}{\sigma}$	$\frac{u_m}{u_o} = 0.866\sigma^{\frac{1}{2}} \left(\frac{x}{D}\right)^{-\frac{1}{2}}$
Axisymmetric Turbulent	$\frac{b_u}{x} = 5.27\frac{\epsilon_o}{K^{\frac{1}{2}}}$	$\frac{u_m}{u_o} = 0.106\frac{K^{\frac{1}{2}}}{\epsilon_0} \left(\frac{x}{D}\right)^{-1}$

Table 8.1: Velocity halfwidth and centerline velocity in far-field region in terms of jet exit parameters.

described by Tollmein's solution [88]:

$$\frac{u}{u_o} = 0.0176\exp(-\phi_1) + 0.1337\exp\left(\frac{\phi_1}{2}\right)\cos\left(\frac{3^{\frac{1}{2}}}{2}\phi_1\right) + 0.6876\exp\left(\frac{\phi_1}{2}\right)\sin\left(\frac{3^{\frac{1}{2}}}{2}\phi_1\right),$$

$$\phi_1 = \frac{1}{\sigma'}\left(\frac{0.5D - y}{x}\right), \tag{8.4}$$

where the empirical constant is given by $\sigma' = 0.09$. In this case, the jet halfwidth, b_u, grows very slightly with down stream distance:

$$\frac{b_u}{D} = 0.5 + 0.03\frac{x}{D} \tag{8.5}$$

For the near-field axisymmetric jet, the mixing zone mean velocity profile is well described by the empirical expression of Wall, Subramanian & Howley (1982) [89]:

$$\frac{u}{u_o} = 0.5(1 + \cos(\pi\phi_2)),$$

$$\phi_2 = \frac{r + 0.12x - 0.5D}{0.28x}, \qquad 0 \leq \phi_2 < \frac{1}{2} \tag{8.6}$$

and

$$\frac{b_u}{D} = 0.5 + 0.02\frac{x}{D} \tag{8.7}$$

8.3.2 The Inviscid Impingement Region

The velocity profile of the oncoming fluid deviates from the free jet result as the fluid begins to sense the presence of the surface. Within the small region bounded by this location and the top of the boundary layer on the surface, the streamlines are redirected from roughly perpendicular to parallel to the surface (see Fig. 8.2). Using the coordinate system shown in Fig. 8.2, the inviscid flow is described by the stream-vorticity equation:

$$\frac{\partial^2\psi}{\partial y^2} + \frac{\partial^2\psi}{\partial x^2} = \Omega(x,y) \tag{8.8}$$

and

$$\frac{\partial^2\psi}{\partial y^2} + \frac{\partial^2\psi}{\partial r^2} - \frac{1}{r}\frac{\partial\psi}{\partial r} = r^2\Omega(r,y) \tag{8.9}$$

for two-dimensional and axisymmetric impingement, respectively. In Eq. (8.8), the stream and vorticity functions are defined:

$$\frac{\partial\psi}{\partial x} = -v, \quad \frac{\partial\psi}{\partial y} = u,$$

$$\Omega = \frac{\partial u}{\partial y} - \frac{\partial v}{\partial x}$$

and in Eq. (8.9):

$$\frac{\partial\psi}{\partial r} = -rv, \quad \frac{\partial\psi}{\partial y} = ru,$$

$$\Omega = \frac{1}{r}\left(\frac{\partial u}{\partial y} - \frac{\partial v}{\partial r}\right)$$

Defining the stream function such that $\psi = 0$ along the surface and centerline and assuming parallel outflow far from the stagnation point provide three boundary conditions. The fourth is determined by the influx velocity profile. It is apparent from Section 8.3.1 that a variety of impinging fluid velocity profiles are possible depending

on the jet Reynolds number, Re_o, and the jet height, H, from the surface. Therefore, treatment of the inviscid impingement region must not be confined to a single velocity profile.

Phares, Smedley & Flagan (1999) [90] solved Eqs. (8.8) and (8.9) for an arbitrary influx stream function profile, Ψ, in terms of a surface integral involving the vorticity function, Ω. By assuming an appropriate stream function distribution, the vorticity function and, thus, the surface integral could be calculated, yielding a corrected stream function distribution. For the purpose of calculating wall shear stress, the significant quantity needed from the inviscid analysis is the velocity, U, at the surface $y = 0$, which is assumed to be the velocity at the top of the boundary layer. It follows from the development of Phares *et al.* [90] that this velocity distribution is the converging infinite series:

$$\frac{U(x)}{u_s} = \sum_{n=1}^{\infty} \left[A_n \gamma_n - \sum_{m=1}^{\infty} \frac{B_{mn}\alpha_m}{\gamma_n^2 + \alpha_m^2} \right] \sin(\gamma_n x),$$

$$A_n = \frac{2}{a \sinh(\gamma_n b)} \int_0^a \Psi(x') \sin(\gamma_n x') dx',$$

$$B_{mn} = \frac{4}{ab} \int_0^a \int_0^b \Omega(x', y') \sin(\alpha_m y') \sin(\gamma_n x') dy' dx',$$

$$\gamma_n = \frac{2n-1}{2a}\pi \qquad \alpha_m = \frac{m\pi}{b} \tag{8.10}$$

for the two-dimensional case, and

$$\frac{U(r)}{u_s} = \sum_{n=0}^{\infty} \left[D_n \lambda_n - \sum_{m=0}^{\infty} \frac{E_{mn}\alpha_m}{\lambda_n^2 + \alpha_m^2} \right] r J_1(\lambda_n r),$$

$$D_n = \frac{2}{a^2 J_1^2(\lambda_n a) \sinh(\lambda_n b)} \int_0^a \Psi(r') J_1(\lambda_n r') dr',$$

$$E_{mn} = \frac{4}{ba^2 J_1^2(\lambda_n a)} \int_0^a \int_0^b r'^2 \Omega(r', y') J_1(\lambda_n r') \sin(\alpha_m y') dy' dr',$$

$$J_0(\lambda_n a) = 0 \tag{8.11}$$

for the axisymmetric case. In Eqs. (8.10) and (8.11), u_s is the centerline velocity of the influx flow and a and b are the boundary locations chosen far enough away from the stagnation point so as to not affect the solution. Equations (8.10) and (8.11) are compared with available measurements for near-field and far-field jet impingement in Figs. 8.3 and 8.4, respectively. The presented experimental data were all calculated from Bernoulli's equation using surface pressure measurements. For fully developed jet impingement (Figs. 8.3a and 8.4a) the data collapse to the inviscid solution when scaled with b_u. For developing jet impingement, the inviscid theory predicts no effect of jet height on the surface velocity for the two-dimensional case (Fig. 8.3b), and only a slight effect for the axisymmetric case (Fig. 8.4b). The experimental data support these predictions.

8.3.3 The Impingement Boundary Layer

Having obtained the free stream conditions for a wide range of impinging jet configurations, we can now proceed with the boundary layer analysis that will enable the determination of the wall shear stress distribution on the surface. Theoretical treatment of the boundary layer requires some initial intuition about the flow. It could be inferred that the strong favorable pressure gradients close to the stagnation point not only suppress turbulence close to the surface, but also cause the boundary layer to at least behave in a laminar fashion. This inference is strongly supported by the work of Kataoka & Mizushina (1974) [87] and Kataoka *et al.* (1982) [91], who observed that, in contrast to heat and mass transfer, the wall shear stress close to the stagnation point is insensitive to the level of turbulence in the free stream. As the pressure gradients subside, we expect the boundary layer to become turbulent. The location of this transition will be explored from the available data later.

Laminar boundary layer

Following Polhausen [76], the wall shear stress, τ_o in a laminar boundary layer subject to a pressure gradient is given by

$$\frac{\tau_o \delta}{\mu U} = 2 + \frac{\Lambda}{6} \tag{8.12}$$

where δ is the boundary layer thickness, and Λ is a boundary layer velocity profile shape factor defined as

$$\Lambda = \frac{\delta^2}{\nu}\frac{dU}{dx} \tag{8.13}$$

Calculation of δ and Λ by the method of Holstein and Bohlen is detailed by Schlichting (1960) [76] for the two-dimensional case and by Kataoka & Mizushina (1974) [87] for the axisymmetric case and is thus not presented here.

It follows from Eqs. (8.12) and (8.13) that the wall shear stress distribution can be written in the universal form

$$\frac{\tau}{\rho u_s^2}\left(\frac{u_s b_u}{\nu}\right)^{\frac{1}{2}} = f\left(\frac{x}{b_u}\right),$$

for fully developed turbulent jet impingement, where x is replaced by r for the axisymmetric case. Using this scaling and Table 8.1, the wall shear stress can be scaled in terms of the jet nozzle parameters yielding the universal functions f_1 and f_2:

$$\frac{\tau}{\rho u_o^2}\mathrm{Re}_o^{\frac{1}{2}}\left(\frac{H}{D}\right)^{\frac{5}{4}} = f_1\left(\frac{x}{H}\right) \tag{8.14}$$

for the two-dimensional case, and

$$\frac{\tau}{\rho u_o^2}\mathrm{Re}_o^{\frac{1}{2}}\left(\frac{H}{D}\right)^{2} = f_2\left(\frac{r}{H}\right) \tag{8.15}$$

for the axisymmetric case. These functions are plotted in Fig. 8.5 for two-dimensional and axisymmetric fully developed jet impingement along with the non-similar wall shear stress distributions resulting from developing jet impingement ($H/D < 8$). The

magnitude, τ_m, and location, x_m (r_m), of the shear stress maximum for fully developed jet impingement are

$$\tau_m = 7.30\rho u_o^2 \mathrm{Re}_o^{-\frac{1}{2}} \left(\frac{H}{D}\right)^{-\frac{5}{4}}, \qquad \frac{x_m}{H} = 0.12 \tag{8.16}$$

and

$$\tau_m = 44.6\rho u_o^2 \mathrm{Re}_o^{-\frac{1}{2}} \left(\frac{H}{D}\right)^{-2}, \qquad \frac{r_m}{H} = 0.09 \tag{8.17}$$

for two-dimensional and axisymmetric impingement, respectively.

Turbulent boundary layer

The transition from laminar to turbulent boundary layer within the impingement region can be accompanied by a sharp increase in the wall shear stress as observed by Kataoka & Mizushina (1974) [87] and Alekseenko & Markovich (1994) [92] (see Section 8.4). The location and magnitude of this increase is variable within these experiments. In the following boundary layer analysis, the magnitude of the increase will be calculated in terms of the transition location, r_t. Since the available measurements involve circular jets, only axisymmetric case will be considered here.

Schlichting (1960) [76] showed that the axisymmetric momentum equation could be written:

$$U^2 \frac{d\theta}{dx} + (H+2)\frac{\theta}{U}\frac{dU}{dx} + \frac{\theta}{x} = \frac{\tau}{\rho U^2}, \tag{8.18}$$

where θ is the momentum thickness and the ratio, H, of the displacement and momentum thicknesses is generally taken to be equal to 1.4. The shear stress, τ, can be related to θ for turbulent boundary layers:

$$\frac{\tau}{\rho U^2} = \alpha \left(\frac{U\theta}{\nu}\right)^{\frac{1}{n}}, \tag{8.19}$$

where the constants were given by V.M. Falkner to be $\alpha = 0.0065$ and $n = 6$ [76].

Combining Eqs. (8.18) and (8.19) and integrating directly yields

$$\theta = \left[0.0076\nu^{\frac{1}{6}}U^{-3.97}r^{-\frac{7}{6}}\left(C + \int_{r_t} r^{\frac{7}{6}}U^{3.80}dr\right)\right]^{\frac{6}{7}}. \tag{8.20}$$

The constant of integration, C, is determined from the laminar result at r_t.

Figure 8.6 depicts the wall shear stress distribution for fully developed jet impingement assuming three different turbulence transition locations, $r_m/H = 0.2$, 0.3, and 0.4. Based on this analysis, it appears that the magnitude of the shear stress jump will increase as the distance of the transition location from the stagnation point increases. This is consistent with the observation of Alekseenko & Markovich [92] that the turbulence transition is more pronounced for lower jet heights, which exhibit lower free stream turbulence levels, and thus longer laminar boundary layer lengths from the stagnation point.

Soon after the transition to turbulent boundary layer occurs, viscous dissipation results in a wall jet and the free stream conditions obtained from inviscid theory are no longer accurate. Wall jets have been studied thoroughly both experimentally and theoretically (see Launder & Rodi (1983) [86]) and are, therefore, beyond the scope of the present work. However, we will make use of the empirical expression of Poreh, Tsuei & Cermak (1967) [85] for the mean shear stress in a radial wall jet,

$$\frac{\tau}{\rho u_o^2}\mathrm{Re}_o^{\frac{1}{2}}\left(\frac{H}{D}\right)^2 = 0.34\mathrm{Re}_o^{\frac{1}{5}}\left(\frac{r}{H}\right)^{-2.3}, \tag{8.21}$$

in order to describe the presented circular jet data beyond the turbulence transition location.

8.4 Wall Shear Stress Measurements

8.4.1 Axisymmetric Jets

Table 8.2 lists available wall shear stress measurements under impinging axisymmetric jets. The most notable feature of these measurements is the agreement with laminar

Study	H/D	Re_o	Measurement technique
Bradshaw & Love (1959)	18	1.50×10^5	flat Preston tube
Beltaos (1974) "Run 4"	21.1	8.04×10^4	standard Preston tube
& Rajaratnam "Run 5"	65.7	3.00×10^4	
Kataoka & Mizushina (1974)	3.86 & 8.24	$9.60 \times 10^3 - 3.62 \times 10^4$	electrochemical method
Kataoka *et al.* (1982)	6	$4.00 \times 10^3 - 1.50 \times 10^4$	electrochemical method
Alekseenko & Markovich (1994)	$2 - 8$	4.16×10^4	electrochemical method

Table 8.2: Impingement region wall shear stress data for axisymmetric impinging jets.

boundary layer theory of the wall shear stress distribution under the submerged impinging liquid jets (see Fig. 8.7), and the lack of agreement for the impinging gas jets (see Fig. 8.8). Figure 8.7 displays the wall shear stress measurements of Kataoka & Mizushina [87], Kataoka *et al.* [91], and Alekseenko & Markovich [92] for various jet heights and jet Reynolds Numbers obtained using mass transfer techniques. Not only is the collapse to the predicted scaling for laminar flow clear, but the transition from laminar to turbulent boundary layer is evidenced by a sharp increases in shear stress in some of the distributions.

In the case of the normally impinging axisymmetric gas jet, the only impingement region wall shear stress data found in the literature were provided by Bradshaw & Love (1961) [62] for one jet configuration and Beltaos & Rajaratnam (1974) [61] for two jet configurations (labeled "Run 4" and "Run 5," by the authors of that study). The latter compiled all three data sets, and nondimensionalized the wall shear stress distributions with the maximum shear stress. The resulting curves appeared to collapse to a general curve derived from the axial boundary layer equation, and given by:

$$\frac{\tau}{\tau_m} = 0.18 \left(\frac{1 - e^{-114\lambda^2}}{\lambda} \right) - 0.9.43\lambda e^{-114\lambda^2}, \tag{8.22}$$

where $\lambda = r/H$ and the maximum shear stress, τ_m, is given by

$$\tau_m = 0.16 \frac{\rho u_o^2}{\left(\frac{H}{D}\right)^2} \tag{8.23}$$

The agreement between the data and this theoretical approach is misleading. Since the equation of motion was solved in the axial direction, the wall shear stress was erroneously defined as proportional to the radial variation in the radial velocity. Thus, the subsequent theoretical development and Eq. (8.22) are not valid. The correct approach would have been to solve the boundary layer equation in the radial direction along the surface, as in Section 8.3.3. Equation (8.23) is an empirical relation deduced from the three distributions, and appears to hold only to within 15% for these cases.

Figure 8.8 displays the three measured wall shear stress distributions along with the predictions from laminar boundary layer theory for the same jet parameters. It is curious that the measured shear stresses are not consistently higher or lower than the corresponding laminar predictions. In Run 4 from the experiments of Beltaos and Rajaratnam, laminar theory seems to overpredict the measured shear stress closer to the stagnation point and then switches to underpredicting at a nondimensional radius of about 0.12. Laminar theory underpredicts the shear stresses from Run 5 and overpredicts the Bradshaw and Love shear stresses throughout the impingement region.

An explanation of the differences observed between gas jet data and submerged liquid jet data may be derived from the manner in which the wall shear stress was measured. Kataoka & Mizushina [87], Kataoka *et al.* [91], and Alekseenko & Markovich [92] used electrochemical probes and shear stress was calculated from the diffusion current. Bradshaw and Love used a flat Preston tube of height 0.38 mm, and Beltaos and Rajaratnam used a standard Preston tube with an outside diameter of 1.2 mm. In both cases, the probes were calibrated in fully developed turbulent flows. The use of Preston tubes to measure wall shear stress in pressure gradients was examined by Patel (1965) [93], who found that laminarization of a turbulent boundary layer severely affects Preston tube accuracy in favorable pressure gradients. Since there is strong evidence from the submerged liquid jet experiments that the boundary layer in the impingement region is laminar, we would expect that the Preston tube cannot be used to measure shear stress within the impingement region of an impinging gas jet. Whether this holds for jets of larger Reynolds numbers or large jet heights -

Study	H/D	Re_o	Measurement technique
Schauer & Eustis (1963)	40	4.3×10^4	flat Preston tube
Beltaos & Rajaratnam (1973)	43.6 & 66.1	$5.3 \times 10^3 - 7.1 \times 10^3$	flattened Preston tube
Baines & Keffer (1980)	3.86 & 8.24	7.0×10^3	hot film, hot wire
Tu & Wood (1996)	$1 - 21$	$3.04 \times 10^3 - 1.10 \times 10^4$	Preston and Stanton tubes

Table 8.3: Impingement region wall shear stress data for two-dimensional impinging jets.

such as the three analyzed here - requires additional analysis of the boundary layer in conjunction with the available Preston tube data.

Patel found that reducing the diameter of the Preston tube counterintuitively increases the overestimate of the actual wall shear stress in a strong favorable pressure gradient. This can be attributed to the departure of the boundary layer profile from the logarithmic law for fully turbulent flows to a laminar profile. Figures 8.9(a-c) depict the laminar velocity profiles, as calculated from the method of Holstein and Bohlen, for all three impinging jets at three nondimensional radii. The markers represent the location of the Preston tube within the boundary layer. Similar to the observations of Patel, it appears that the data of Beltaos and Rajaratnam are more accurate because the deviations from the logarithmic law are not as great at the location prescribed by the size of the Preston tube, despite the fact that their tube is three times the size of the tube used by Bradshaw and Love. Furthermore, there is correlation between the deviation of the measured shear stress from the laminar prediction and the difference between the laminar velocity profile and the logarithmic law at the Preston tube location. Figure 8.9(d) displays this loose correlation for Run 4. A better correlation could be achieved by considering the integral of the velocity over the entrance surface of the Preston tube rather than the velocity at the top of the tube; but the presented correlation is sufficient to demonstrate the high error that could result from using Preston tubes close to the stagnation point of an impinging jet.

The prominent shear stress rise indicative of the transition to a turbulent boundary

layer appears under impinging jets with lower jet heights and jet Reynolds Numbers. A few of these examples are displayed in Fig. 8.10 along with the predictions from Section 8.3.3. The wall shear stress immediately after transition is well described by turbulent boundary layer theory, and quickly conforms to the wall jet expression (Eq. 8.21).

8.4.2 Plane jets

Indirect measurements of wall shear stress under impinging plane jets (including the measurements of Schauer & Eustis (1963) [74], Beltaos & Rajaratnam (1973) [60], and Tu & Wood (1996) [67]) provide similar results as those presented for impinging circular jets and are not analyzed here. However, one experiment run by Tu & Wood [67] may provide some additional insight into the form of the boundary layer close to the stagnation point. Various sized Stanton and Preston probes were used to map the wall shear stress distribution under a single impinging jet configuration (H/D = 20.6, Re_o = 6300). The smaller probes yielded consistently higher wall shear stresses along the surface. Figure 8.11(a) exhibits the measured wall shear stress at the location of maximum shear stress as function of probe height. The dashed line represents the maximum shear stress value as calculated from Eq. 8.16. Figure 8.11(b) displays the laminar velocity profile at the location of maximum shear stress for the given jet with the markers representing the location of the probe within the boundary layer. Again, the correlation between the measurement error and the difference between the laminar and turbulent boundary layer profiles at the probe location is clear. It can be concluded from these analyses that shear stress probes calibrated in turbulent boundary layers yield misleading results close to the stagnation point in an impingement flow. This is significant because the maximum shear stress, a quantity important to the processes of surface cleaning and coating thickness control, is located within this region. The electrochemical method seems to provide the most accurate data close to the stagnation point, but there is no such available data for impinging gas jets. The hot film and hot wire measurements of Baines & Keffer

(1976) [94] exhibit large discrepancies close to the stagnation point and are unlikely to be accurate for circular jet impingement due to the three dimensionality of the flow. The next section presents a unique method to probe wall shear stress under impinging circular gas jets in order to support the theoretical development in Section 8.3 and the previous analyses.

8.5 Particle Resuspension Experiments

A main motivation of the present work is to predict the conditions under which impinging gas jets produce efficient resuspension of fine particles from surfaces. Usually, the surface needing to be cleaned contains a polydisperse distribution of uncharacterized particles possessing a wide distribution of particle-surface adhesion forces. In this case, knowledge of the wall shear stress distribution under an impinging jet is necessary to predict removal efficiencies. However, if the surface is laden with a uniform distribution of identical spherical particles, then all removal occurs within a very narrow wall shear stress range and the particles behave as quantized shear stress sensors. The removal patterns beneath the jet serve as contours of constant shear stress and can aid in determining the complete shear stress distribution. In these experiments, a particle laden surface was translated underneath an impinging air jet so that a larger number of particles could be examined in a single experiment, and no particles were exposed to jet startup transients that might affect resuspension.

8.5.1 Apparatus and Sample Preparation

The translating jet apparatus, illustrated in Fig. 8.12, used in this study is identical to that used in the particle entrainment experiments of Smedley *et al.* (1999) [21]. The system consists of a high speed rail table with a vacuum-chuck sample holder, and a circular jet nozzle mounted to a y-z traverse at the translation point. The rail table motions were controlled via RS-232 communications from the computer to a Compumotor PDX-15 motor controller. The jet pressure is adjusted using the regulator and measured with a Lucas P4100 pressure transducer reported to have

an accuracy to 0.03% of full scale with a range 0 to 6.9 MPa sealed gauge relative to standard atmospheric pressure. The height and horizontal position of the jet are adjusted using linear micrometer stages. A HeNe laser sheet provides glancing angle illumination of the particles on the glass substrate so that they appear bright against a dark background. Dark-field images of the particle laden surfaces were recorded using a CCD camera equipped with a telephoto lens and connected to a Macintosh computer using a Scion LG3 frame grabber card.

Well characterized monodisperse particles of polystyrene and ammonium fluorescein were produced with a vibrating orifice aerosol generator (VOAG), specially designed to work with organic solvents [45]. The particles were deposited on clean microscope slides by gravitational sedimentation and then stored in a dry box for a minimum of 24 hours prior to use in the experiments. The standard deviation for the particles used in this study was less than 0.5 μm.

8.5.2 Procedure

The procedure and data analysis was described in detail by Smedley *et al.* [21], so only the main points will be summarized here. A glass slide with a uniform deposit of monodisperse microspheres ($\sim$ 300 particles/mm^2) was mounted flush on the translation stage and secured with the vacuum chuck. Three dark-field images spanning 58 mm of the length of the slide were recorded. The gas jet was started and the slide translated at a constant velocity, V_{trans}, under the jet. The slide was then returned to the camera location and three more images were taken to record changes in the average pixel intensity profile across the width of the slide. Particle uniformity ensured that equal light intensity was scattered by each particle and, thus, the average pixel intensity in the images was directly related to the surface density of the deposited particles.

A typical experiment involved passing the slide under the jet 12 times with successively increasing jet pressure ratios, P_{jet}/P_{atm}. As the jet pressure ratio was increased, an increasing number particles was entrained from a path directly beneath

the jet until 100% removal was achieved in the path, now resembling a dark stripe. Further increase in the jet pressure ratio resulted in a widening of the path (see Fig. 8.13). The two quantities measured from the recorded images were: 1) the removal efficiency in the removal path passing directly beneath the jet, and 2) the width, w, of the removal path, which was measured from the location of 50% removal efficiency.

Since a narrow distribution of particle-surface adhesion forces exists for a given sample, due to slight variation in particle size and nonuniformities in the glass surface, the threshold shear stress for particle resuspension is defined as the shear stress needed to entrain 50% of the particles exposed to the shear. Thus the threshold shear stress, $\tau_{50\%}$, is the maximum shear stress under a jet with pressure ratio, $(P_{jet}/P_{atm})_{50\%}$, which causes 50% removal efficiency in the removal path. As the path widens, the removal path halfwidth, $w/2$, represents the radial location of the shear stress contour corresponding to $\tau_{50\%}$ for the subsequent increasing jet pressures. This technique can be used to map the $\tau_{50\%}$ contour only outside of the maximum shear stress location, since all particles within the initial removal path are exposed to the maximum shear stress during translation.

A total of 16 samples were analyzed: six 15.7 μm ammonium fluorescein particle samples and ten 10.0 μm polystyrene particle samples. For the ammonium fluorescein samples, the jet height was held constant ($H/D = 10$) and the translation speed was varied. For the polystyrene samples, the translation speed was held constant ($V_{trans} = 1.8$ mm/s) and the jet height was varied. Tables 8.4 and 8.5 summarize the experimental parameters imposed on the ammonium fluorescein and polystyrene samples, respectively.

8.5.3 Results

Ammonium fluorescein particles

Table 8.4 lists the threshold results for the ammonium fluorescein particle samples. The threshold shear stresses, $\tau_{50\%}$, were calculated from the threshold jet pressure

Sample	V_{trans} (mm/s)	$(P_{jet}/P_{atm})_{50\%}$	$(\rho u_o^2)_{50\%}$ (kPa)	$\mathrm{Re}_{50\%}$	$\tau_{50\%}$ (Pa)
1	1.8	1.15	2.85	5031	179
2	1.8	1.16	3.05	5211	189
3	9.0	1.21	3.99	5959	231
4	9.0	1.19	3.69	5728	217
5	270.0	1.24	4.46	6300	251
6	270.0	1.25	4.66	6440	259

Table 8.4: Experimental parameters and threshold results for 15.7 μm ammonium fluorescein particle samples.

ratio, $(P_{jet}/P_{atm})_{50\%}$, and jet dynamic pressure, $(\rho u_o^2)_{50\%}$, using Eq. 8.17. The threshold shear stress increase with translation speed suggests an effect of force duration on the threshold particle resuspension force. This dynamic property of particle resuspension allowed different shear stress contours to be examined with identical test samples by varying the translation speed.

Figure 8.14 presents the shear stress distribution, scaled with the appropriate jet exit conditions, for all of the ammonium fluorescein test samples. The predicted impingement region shear stress distribution is represented by a solid line; and the wall jet region distribution, by a dashed line. Despite the variation in threshold shear stress for the various translation speeds used, all of the data collapse to the curve predicted by the impingement region model close to the maximum shear stress location. Farther from the stagnation point, the data lie above the wall jet region shear stress curve. This suggests that particle resuspension scales with some percentage of the amplitude of the wall shear stress fluctuations, which increases significantly at the transition location.

Polystyrene particles

The smaller polystyrene particles required significantly higher jet pressure ratios to achieve removal efficiencies comparable to those observed for the ammonium fluorescein particles. For the higher jet heights, the threshold jet pressure ratios produced compressible jets, which were not considered theoretically in Section 8.3. Although

Sample	H/D	$(P_{jet}/P_{atm})_{50\%}$	$(\rho u_o^2)_{50\%}$ (kPa)	$\mathrm{Re}_{50\%}$	$M_{50\%}$
7	3	1.17	1.84	4182	0.36
8	4	1.08	1.46	3708	0.32
9	6	1.09	1.48	3726	0.32
10	10	1.20	3.67	6103	0.52
11	10	1.24	4.39	6764	0.56
12	10	1.21	3.97	6389	0.53
13	12	1.36	6.46	8482	0.68
14	15	1.45	7.96	9640	0.75
15	17	1.54	9.28	10623	0.81
16	20	1.62	10.49	11496	0.86

Table 8.5: Experimental parameters and threshold results for 10.0 μm polystyrene particle samples.

large jet pressure ratios were used in the ammonium fluorescein experiments, particle removal had already extended far into the wall jet region of the flow and, thus, the effect of compressibilty could not be studied. In the polystyrene experiments, threshold jet pressure ratios, $(P_{jet}/P_{atm})_{50\%}$, produced compressible jets facilitating investigation of the effect of compressibility on impingement region wall shear stress. Table 8.5 lists the threshold results measured for each case, including the threshold Mach number at the jet exit, $M_{50\%}$.

Since translation velocity was held constant, the threshold shear stress, $\tau_{50\%}$, was assumed to be the same for all of the polystyrene samples. This notion was tested with three repeatability experiments run at the same jet height (H/D=10) on Samples 10, 11, and 12. Only a 3% variability in $(P_{jet}/P_{atm})_{50\%}$ was measured, supporting the assumption of threshold shear stress uniformity among all samples.

The variation in measured threshold jet conditions with jet height is presented in Fig. 8.15 along with the predictions from incompressible theory. The data show a definite trend away from the incompressible model for increasing jet heights. The measured threshold jet conditions of Smedley *et al.* [21] for 8.3 μm polystyrene particles, also plotted in Fig. 8.15, exhibit a similar deviation from the incompressible model, but for even lower jet heights. This suggests that the deviation is indeed due

to jet compressibility.

To account for the deviation, we introduce a compressibility correction factor to Eq. 8.17:

$$\tau_m = 44.6\rho u_o^2 \mathrm{Re}_0^{-0.5} \left(\frac{H}{D}\right)^{-2} [1 + f(\mathrm{M})], \tag{8.24}$$

where $f(M)$ is some function of the Mach number. Figure 8.16 displays the values of $f(M)$ calculated from the present data set and from the measurements of Smedley *et al.* [21]. The data were fit to a fourth order polynomial to obtain an empirical expression for the compressibility correction factor in an impinging air jet given by

$$f(\mathrm{M}) = 0.66\mathrm{M} - 3.2\mathrm{M}^2 + 3.9\mathrm{M}^3. \tag{8.25}$$

8.6 Concluding Remarks

The assumption of a fully developed turbulent boundary layer close to the stagnation point of an impinging jet has led to inaccuracies in the description of the wall shear stress distribution. Reported measurements using pressure probes calibrated in fully developed turbulent boundary layers have included errors in the magnitude and location of the maximum wall shear stress, two quantities which are of great importance to predicting shear induced resuspension for surface cleaning or particulate sampling applications. Similarly, numerical solutions [83, 82] of the impinging jet flow field have also assumed a fully developed turbulent boundary layer throughout the impingement region by employing turbulent wall functions as the surface boundary condition, resulting in underpredictions of the mean shear stress in the impingement region. Observing the removal of monosized spheres to map out wall shear stress contours yielded results which corroborated with the predictions of laminar boundary layer theory. This technique was also applied to impinging compressible jets, and the wall shear stress rise due to compressibilty effects was measured for various Mach numbers. An empirical expression relating the wall shear stress maximum and the jet Mach number was obtained for impinging air jets.

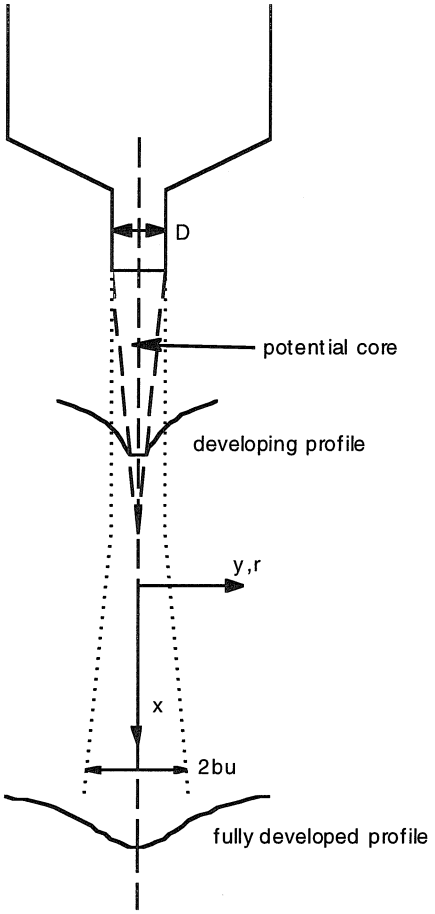

Figure 8.1: Schematic of free jet region.

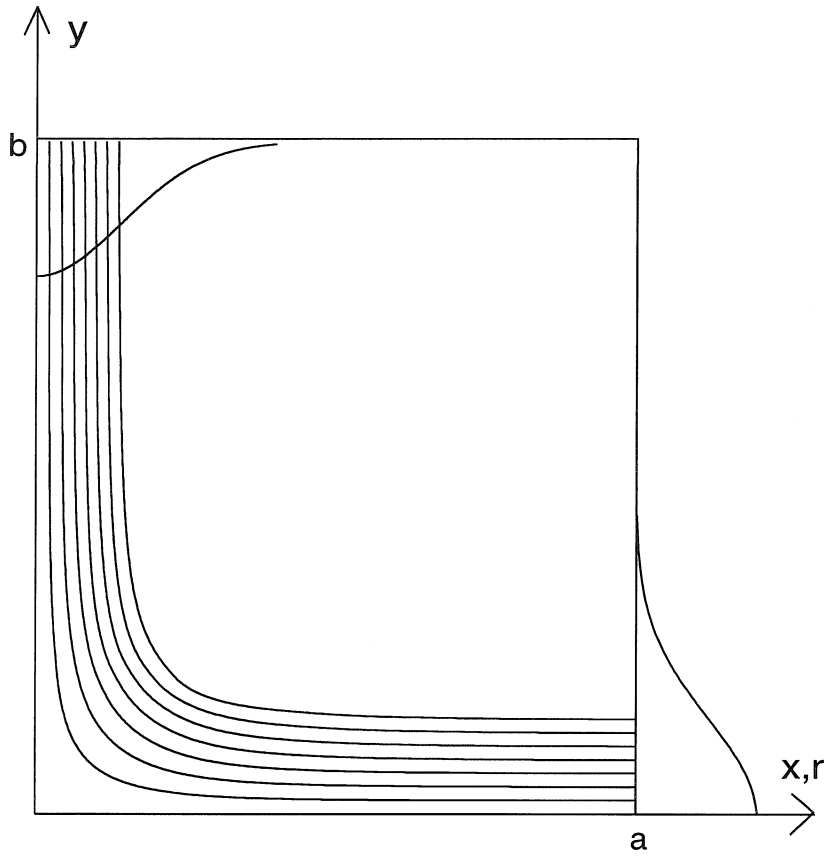

Figure 8.2: Schematic of inviscid impingement region.

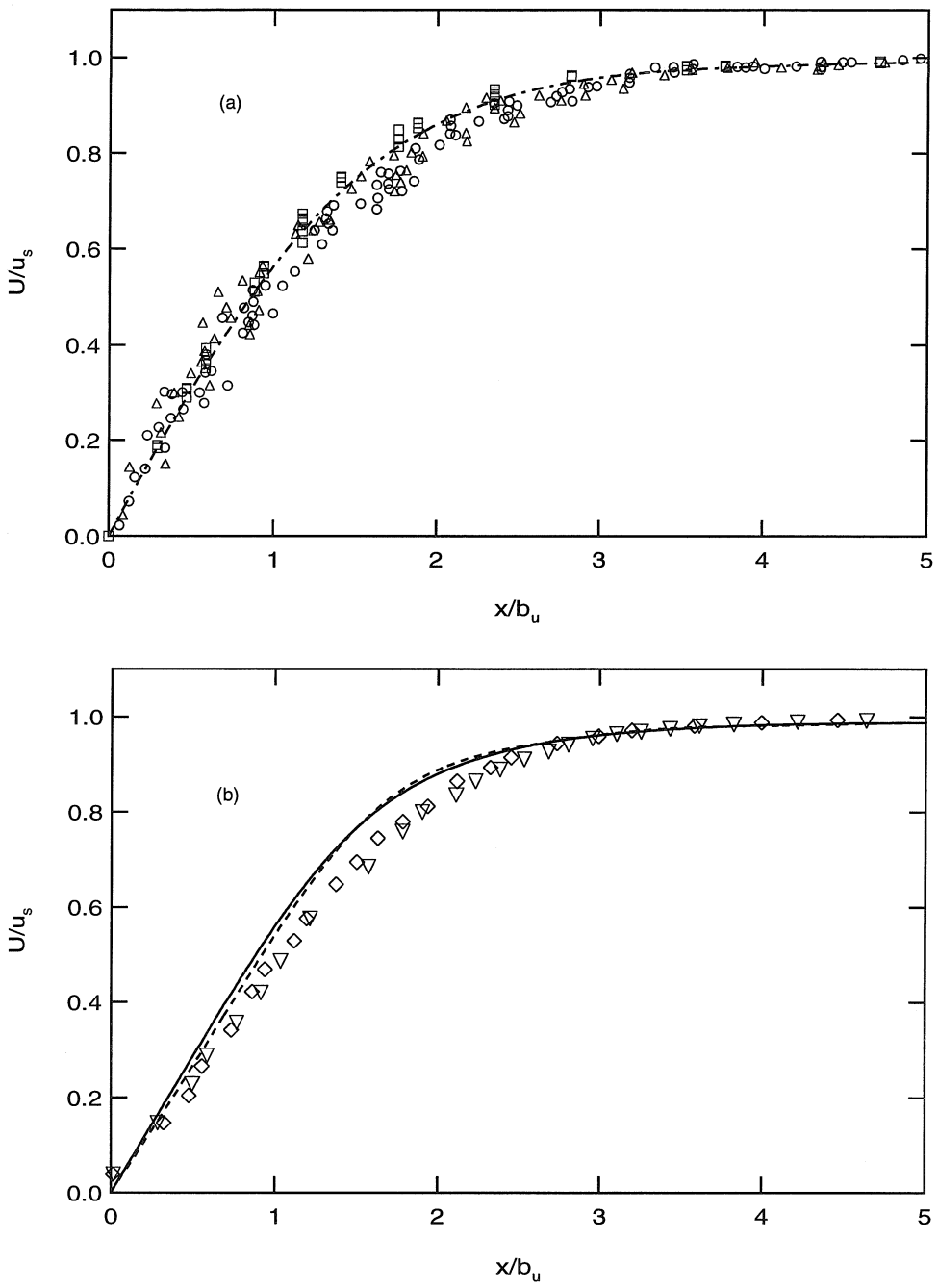

Figure 8.3: Comparison between Eqs. (8.10) with influx boundary condition given by Eqs. (8.3)(--) and (8.4), $H/D = 1$ (_), $H/D = 5$ (....), and impinging plane jet measurements for: (a) fully developed turbulent jet impingement ($H/D > 6$), Schauer & Eustis ($\Box$); Kumada & Mabuchi ($\triangle$); Beltaos & Rajaratnam ($\circ$); (b) developing jet impingement ($H/D < 6$), Tu & Wood, $H/D = 1$ (∇) and $H/D = 4$ ($\diamond$).

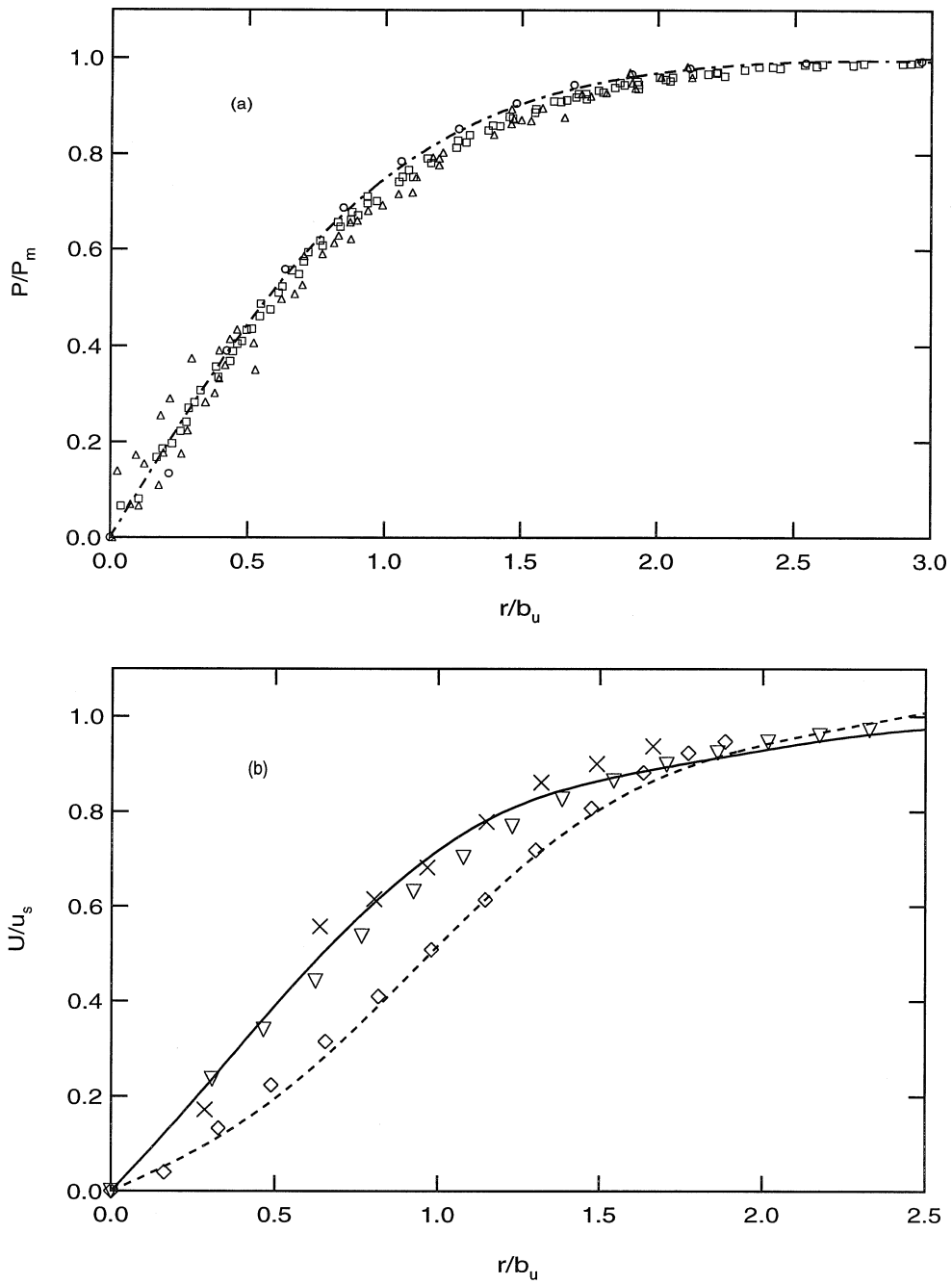

Figure 8.4: Comparison between Eq. (8.11) with influx boundary condition given by Eqs. (8.2)(--) and (8.4), $r_c = 0.2D$ (_), $r_c = 0.8D$ (....), and impinging circular jet measurements for: (a) fully developed turbulent jet impingement ($H/D \geq 8$), Bradbury ($\circ$); Beltaos & Rajaratnam ($\triangle$); Giralt *et al.* ($\square$); (b) developing jet impingement ($H/D < 8$), Giralt *et al.*, $H/D = 6$ (∇) and $H/D = 1.2$ ($\diamond$); Kataoka *et al.*, $H/D = 6$ ($\times$).

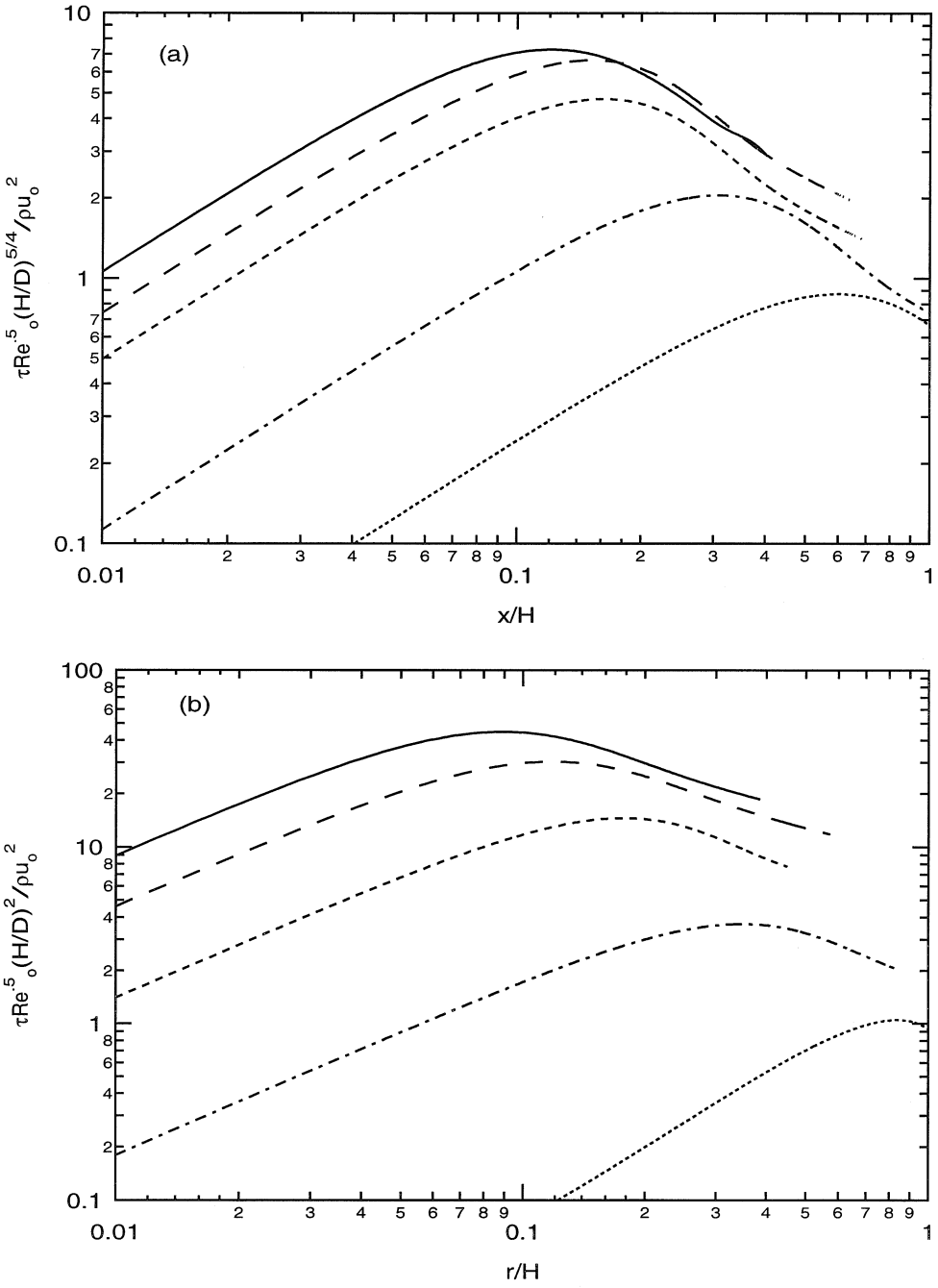

Figure 8.5: Predicted wall shear stress distributions based on laminar boundary theory for $H/D \geq 8$ (_), $H/D = 6$ (--), $H/D = 4$ (...), $H/D = 2$ (- -), and $H/D = 1$ (.....) for: (a) plane jet impingement; (b) circular jet impingement.

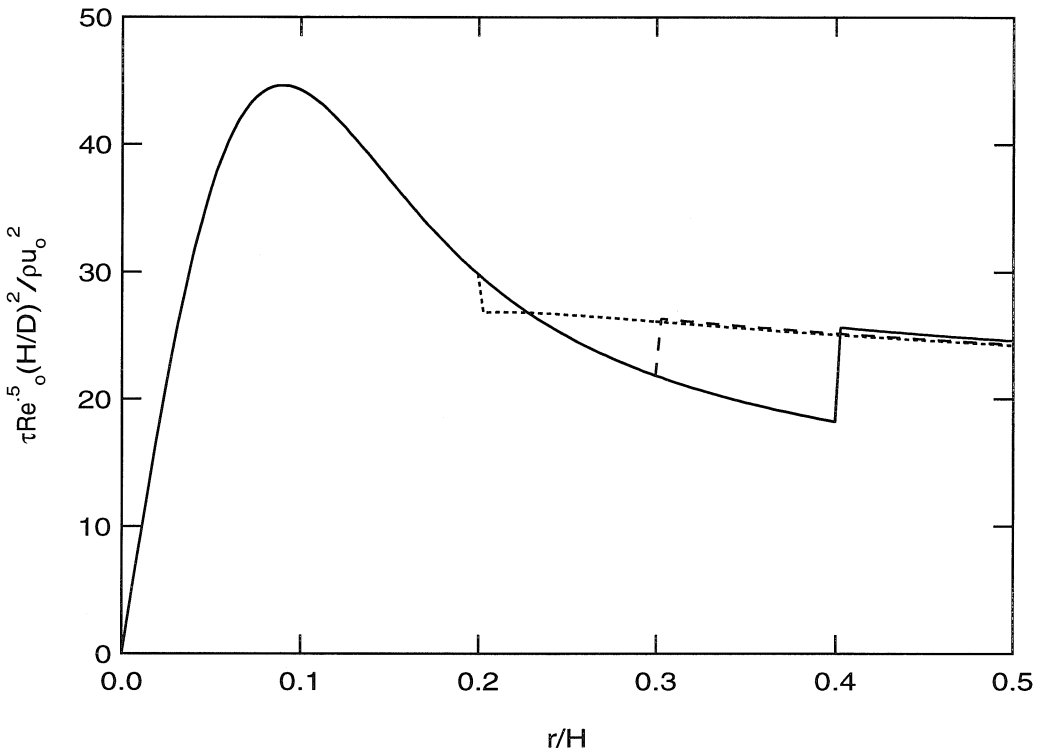

Figure 8.6: Wall shear stress distribution for three turbulence transition locations: $r_m/H = 0.2$(.....), $r_m/H = 0.3$ (---), and $r_m/H = 0.4$ (_).

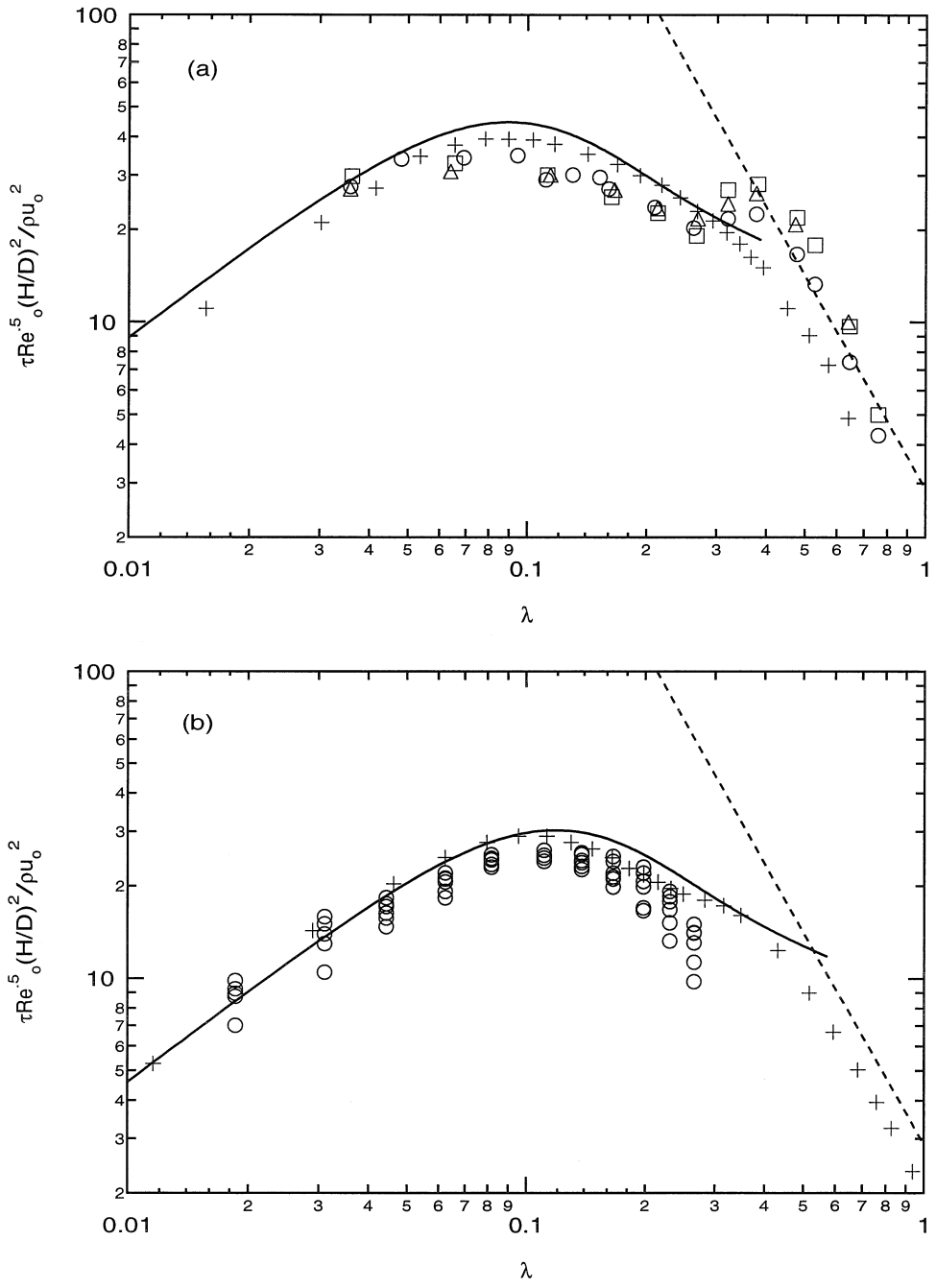

Figure 8.7: Wall shear stress measurements of Kataoka & Mizushina (1974) ($\mathrm{Re}_o = 10600 - 36200$) ($\triangle$); Kataoka *et al.* (1982) ($\mathrm{Re}_o = 4000 - 15000$) ($\circ$); and Alekseenko & Markovich (1994) ($\mathrm{Re}_o = 41600$) (+); compared with impingement region model (_) and wall jet region expression (Eq. 8.21) (....) for (a) $H/D \geq 8$; (b) $H/D = 6$.

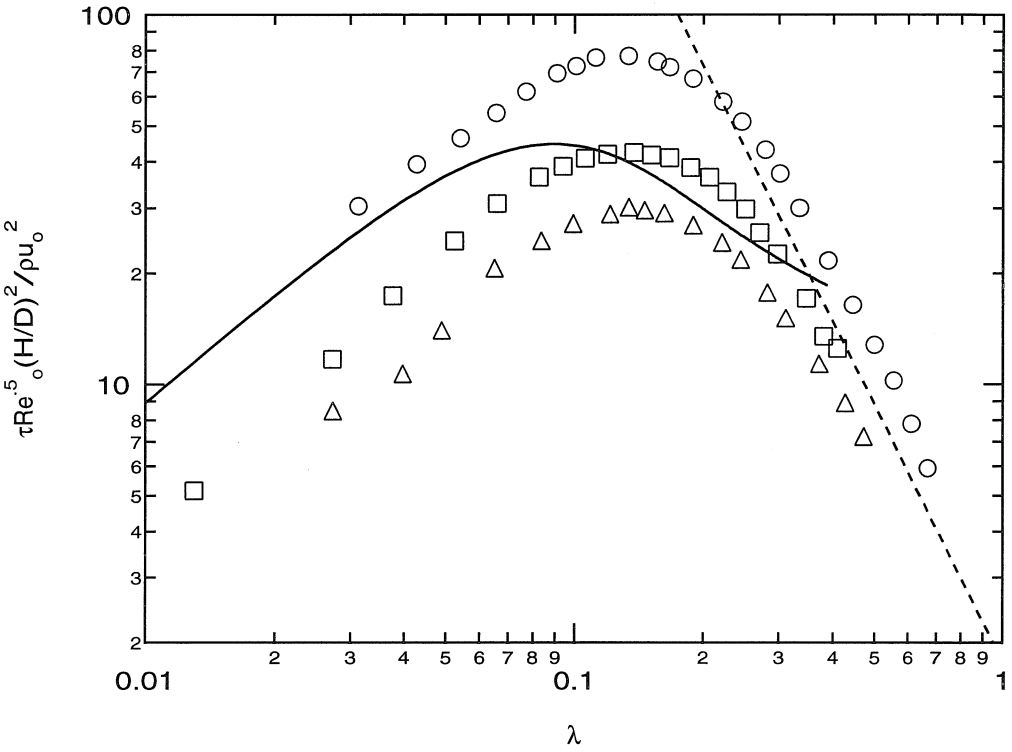

Figure 8.8: Wall shear stress measurements of Bradshaw & Love (1961) (Re_o = 150000, H/D = 18) (○); and Beltaos & Rajaratnam (1974), Run 4 (Re_o = 80400, H/D = 21.1) (□); and Run 5 (Re_o = 30000, H/D = 65.7) (△); compared with impingement region model (_) and wall jet region expression (Eq. 8.21) (....).

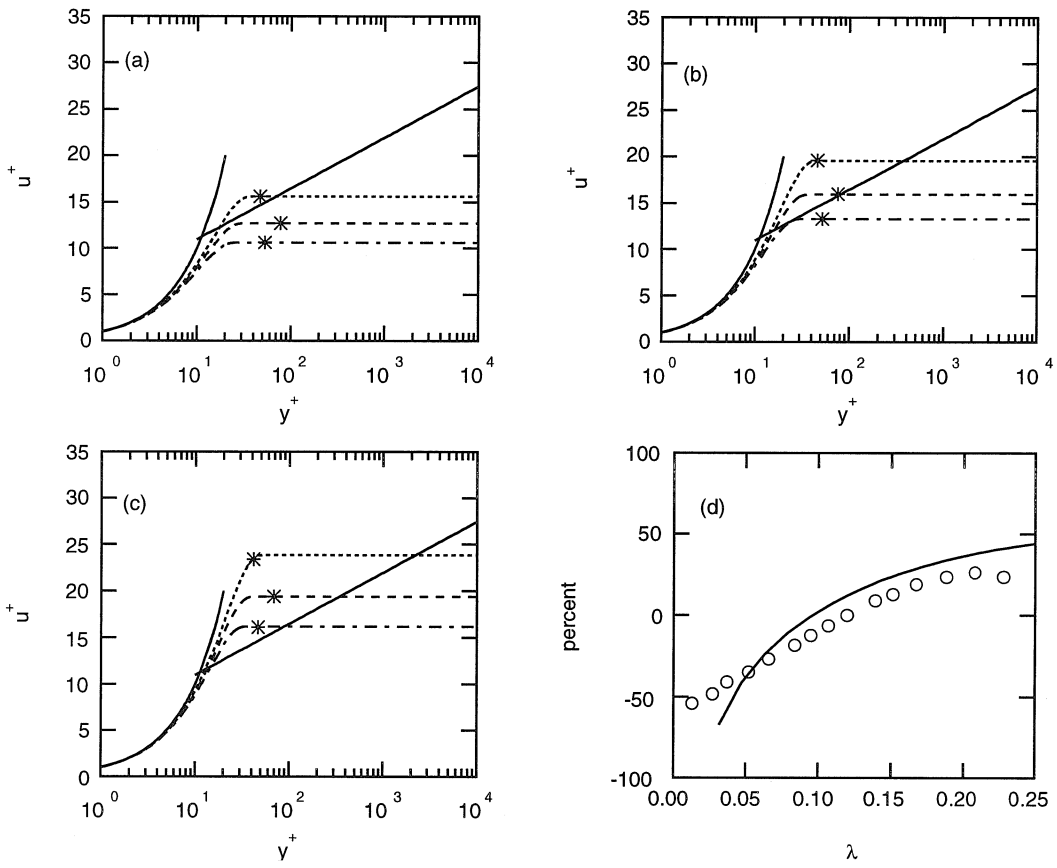

Figure 8.9: Turbulent boundary layer (_) compared to location of top of Preston Tube (∗) in laminar boundary layer under impinging jet studied by Bradshaw & Love (1961) (.....) and Beltaos & Rajaratnam (1974), Run 4 (....) and Run 5 (__) at radial locations of (a) $\lambda = 0.08$, (b) $\lambda = 0.12$, and (c) $\lambda = 0.17$; and (d) correlation of relative shear stress measurement error for Run 4 (○) and relative difference between assumed boundary layer profiles.

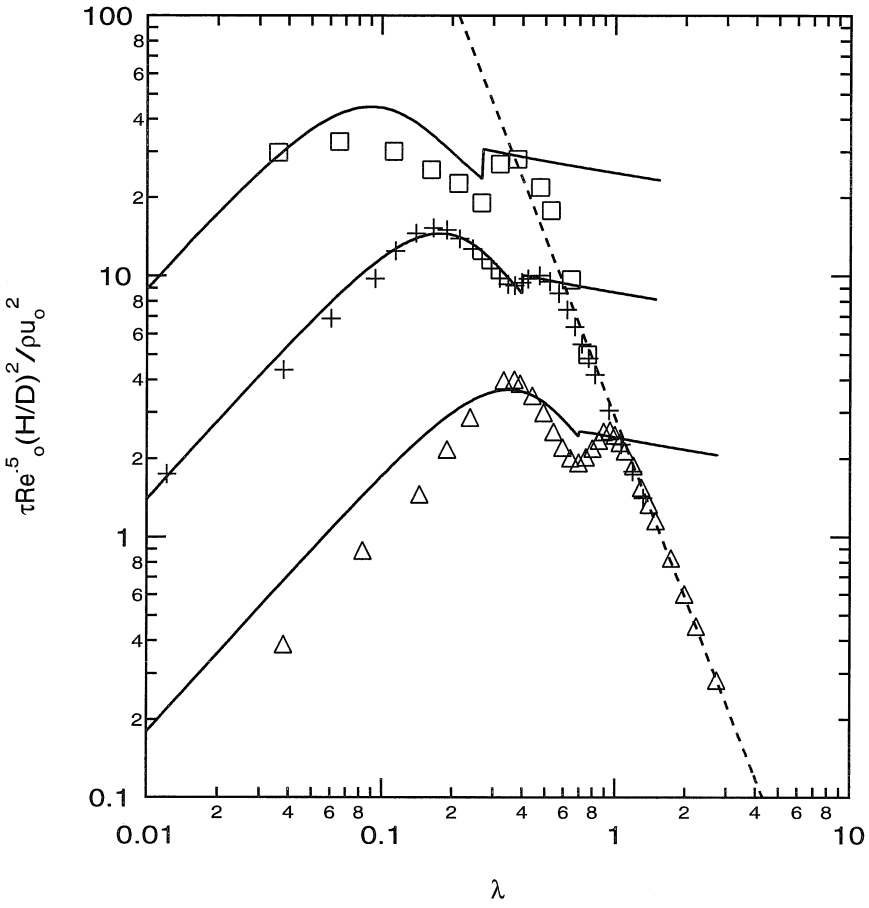

Figure 8.10: Transition to turbulence exhibited in three impinging jets: $\mathrm{Re}_o = 21500$, $H/D = 8$ (□) (Kataoka & Mizushina, 1974 [87]), $\mathrm{Re}_o = 42600$, $H/D = 4$ (+) and $H/D = 2$ (△) (Alekseenko & Markovich, 1994 [92]); compared with transition theory (Eq. 8.19) (_) and wall jet theory (Eq. 8.21) (....).

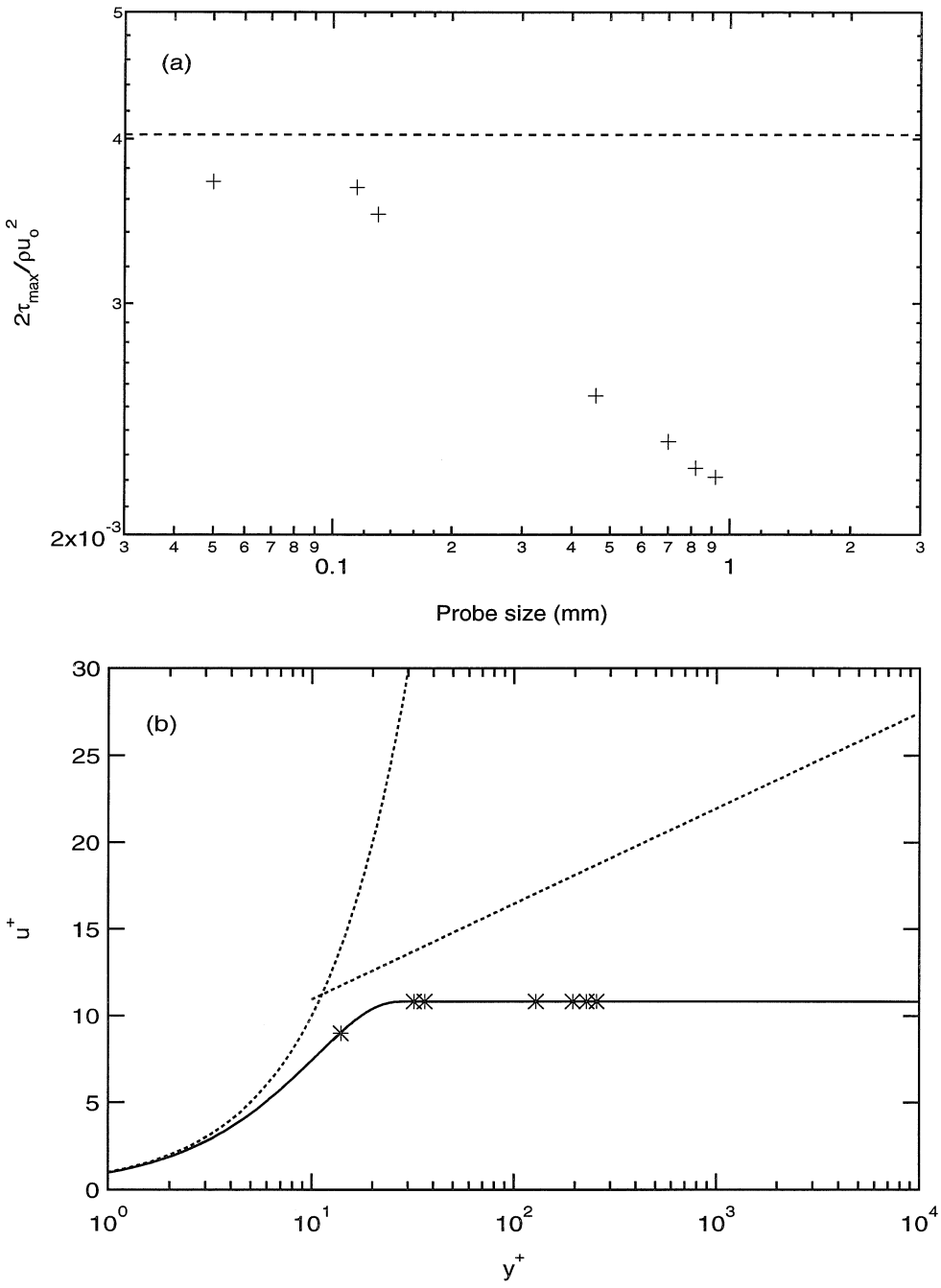

Figure 8.11: (a) Maximum shear stress under impinging plane jet ($H/D = 20.6$, $\mathrm{Re}_o = 6300$) measured by Tu & Wood (1996) ($\circ$) with various probe sizes compared with predicted laminar value (....), and (b) corresponding probe locations ($*$) in laminar boundary layer (_) compared with turbulent boundary layer (.....).

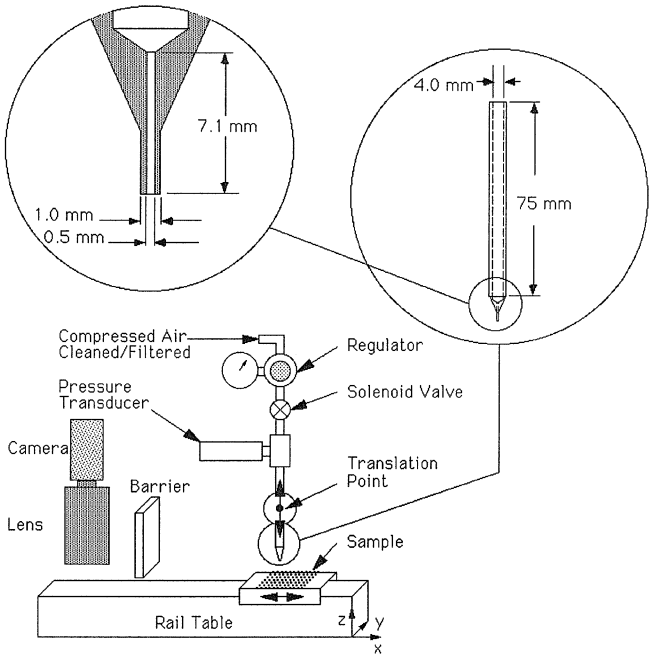

Figure 8.12: Translating gas jet experimental setup.

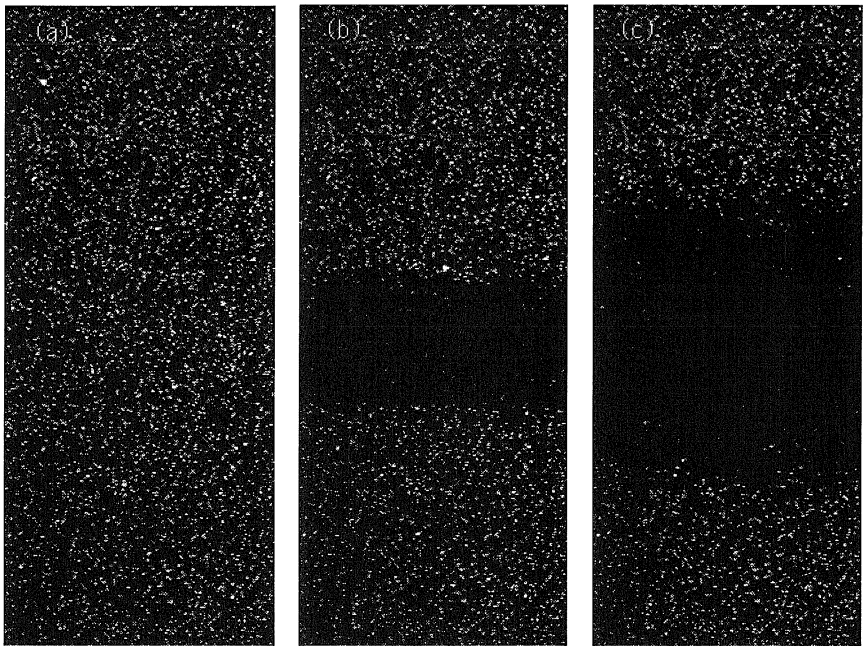

Figure 8.13: Images of Sample 10 recorded (a) before experiment, and after exposure to air jet; (b) $P_{jet}/P_{atm} = 2.02$, and (c) $P_{jet}/P_{atm} = 6.71$.

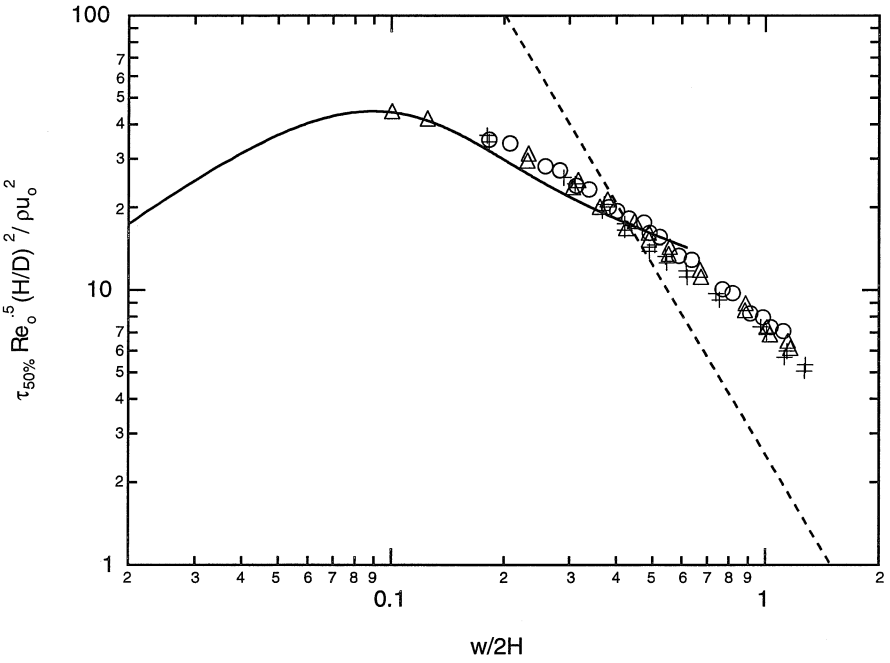

Figure 8.14: Observed $\tau_{50\%}$ shear stress locations for $V_{trans} = 1.8$ mm/s (+), $V_{trans} = 9.0$ mm/s (○), and $V_{trans} = 270.0$ mm/s (△) compared with impingement region model (_), and wall jet region expression (Eq. 8.21) (....).

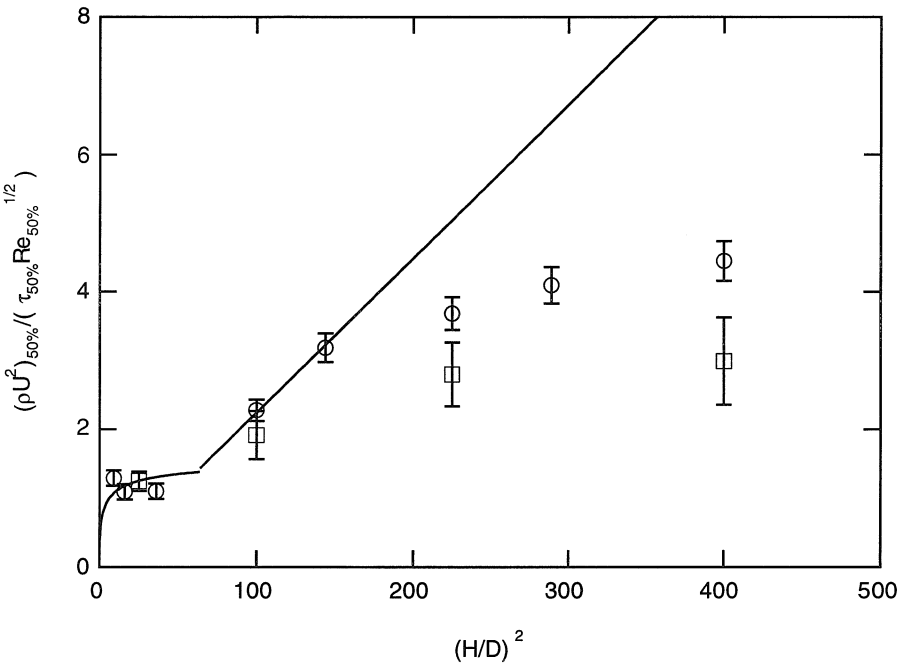

Figure 8.15: Comparison between measured threshold jet parameters (present experiment (○) and experiment of Smedley *et al.*, 1999 (□)) and incompressible theory (—).

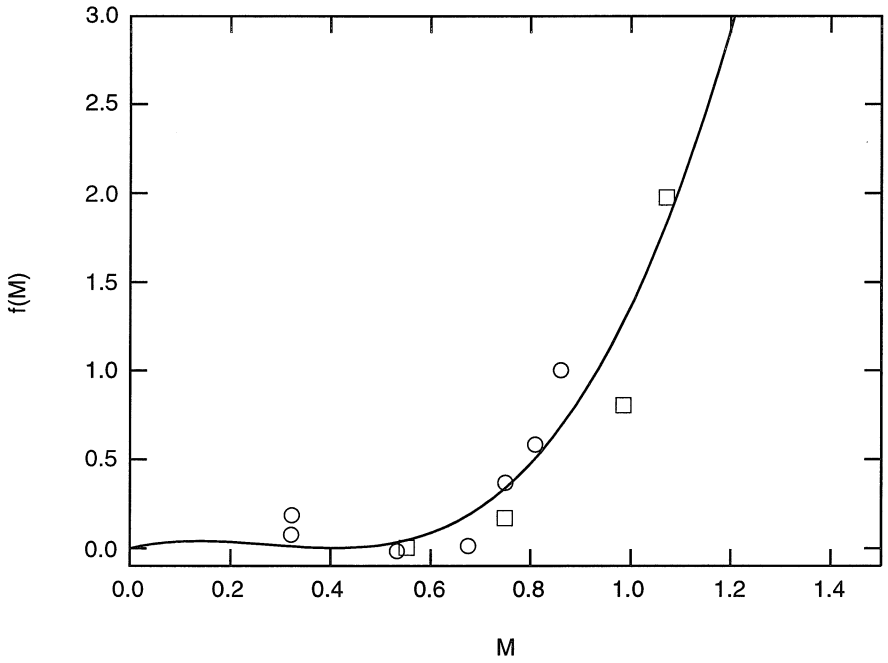

Figure 8.16: Measured Mach number correction function (present experiment (∘) and Smedley *et al.* (1999) (□)) with overlaid polynomial fit (Eq. 8.25) (_).

Chapter 9 Effect of Size and Material Properties on the Aerodynamic Entrainment of Microspheres

9.1 Abstract

An experimental study of the aerodynamic entrainment of monodisperse spheres from glass substrates is presented. The spheres were made of ammonium fluorescein and polystyrene standards (M_W=3,700, 18,700, and 114,200 amu). The use of monosized particles with carefully controlled properties leads to a narrow distribution of sphere-surface adhesion forces, facilitating the determination of the particle entrainment threshold. The spheres were exposed to well characterized shear stresses in two different flows, (i) laminar channel flow; and (ii) a normally impinging gas jet. Threshold shear stresses were found to be more sensitive to particle size than predicted by the existing resuspension theories, which are based on equilibrium adhesion models. Furthermore, resuspension was also found to be sensitive to the duration of the applied shear stress. This sensitivity depends upon the particle size and material properties. A kinetic model of particle detachment is presented to account for these observed trends.

9.2 Introduction

The entrainment of fine particles from surfaces in turbulent flows has been the focus of numerous theoretical [65, 14, 95, 96, 97] and experimental [14, 98, 99, 100] investigations, but the mechanism of particle detachment remains unclear. Both normal lift forces [65, 14, 98, 97] and tangential shear forces [95, 96, 100, 101] have

been proposed as the impetus for resuspension. Efforts to resolve the controversy have been hindered by the variability of the properties of the particles on surfaces that leads to ambiguous experimental observations. Only by studying the entrainment of particles with uniform properties, e.g., shape, size, mechanical properties, from a well characterized surface and with known interaction potentials can these questions be resolved. Noting that the experiments to date have involved a relatively broad distribution of particle/surface interactions and that the flows have been highly turbulent, theorists have developed statistical models aimed at predicting the probability of particle resuspension upon exposure to a series of random turbulent impulses. Although such models can be empirically related to observed resuspension rates in turbulent flows, neither the previous experiments nor the models are well suited to resolving the mechanics of flow-induced particle detachment.

Our goal in this study is to perform resuspension experiments in which the relationship between the flow and particle properties at the threshold to resuspension can be unambiguously determined in order to test particle detachment models. This can be achieved only if all of the following hold: (i) the particles are identical; (ii) the surface is uniform; and (iii) the flow field in the vicinity of the particles is well defined. It was shown in Chapter 8 that, when the first two criteria are met, particles can behave as quantized shear stress sensors. In that study, low density deposits 15.7 μm ammonium fluorescein spheres and 10.0 μm polystyrene ($M_w = 18,700$ Dalton) spheres on glass substrates were used to map the distribution of shear stress under normally impinging compressible and incompressible gas jets. The shear stress map inferred from particle entrainment measurements agrees well with previous measurements [91] of the shear stress distribution. The particles were uniformly resuspended when exposed to a particular shear stress that we shall label the threshold shear stress. The sharp onset of particle entrainment does not necessarily discount the theory that particle resuspension in the viscous sublayer results from turbulent bursting, nor does it resolve whether tangential forces causing rotation or sliding are more important than normal lift-off forces. To understand the resuspension event, the dependence of the threshold shear stress on particle size and mechanical properties must be resolved.

Fortunately, we now have a well defined flow field (or at least, a well defined shear stress distribution) in the normally impinging gas jet, allowing us to meet all three of the necessary criteria to perform such an investigation.

In order to clarify the importance of turbulent bursting in the viscous sublayer, we designed an experiment that would subject the same kind of particles used in the turbulent impinging jet experiments to a purely laminar flow. Differences between the average shear stress required for particle entrainment in the two experiments would reveal the significance of coherent structures on particle entrainment in the impinging jet flow.

9.3 Theory

9.3.1 Particle Adhesion

The adhesion of elastic particles to a flat surface is a complex combination of surface chemistry and solid mechanics that has long been a source of controversy. Many papers have focused on this topic so only key issues will be briefly summarized here.

The two most widely accepted elastic adhesion theories were devised by Johnson, Kendall, and Roberts (JKR) [102] and Derjaguin, Muller, and Toporov (DMT) [103]. The theories describe the detachment of spherical particles that are flattened due to attractive forces between the particle and a planar substrate, under the action of a normal force. Both theories predict a critical pull-off force that is proportional to the particle diameter, D_p, and the Dupré energy of adhesion, γ. In the DMT theory, the contact area gradually decreases to zero, leading to a detachment force of

$$F_{pull-off}^{DMT} = \pi \gamma D_p. \tag{9.1}$$

In the JKR theory, high tensile stresses are predicted along the outer edge of the contact area leading to crack propagation along the particle/surface interface under

the action of a critical force given by

$$F_{pull-off}^{JKR} = \frac{3}{4}\pi\gamma D_p. \tag{9.2}$$

Surprisingly, the JKR expression differs from the DMT expression by a factor of only $\frac{3}{4}$, even though the contact radius never approaches zero during detachment. Instead, the particle breaks off the surface from a finite contact radius, a_{cr}, equal to:

$$a_{cr} = \frac{a_o}{4^{\frac{1}{3}}} \tag{9.3}$$

where a_o is the contact radius at zero applied load and is dependent on the relevant elastic properties:

$$a_o = \left(\frac{3\gamma\pi D_p^2}{2K}\right)^{\frac{1}{3}} \tag{9.4}$$

$$K = \frac{4}{3}\left[\frac{1-\sigma^2_{\text{particle}}}{E_{\text{particle}}} + \frac{1-\sigma^2_{\text{surface}}}{E_{\text{surface}}}\right]^{-1} \tag{9.5}$$

E and σ are elastic modulus and Poisson ratio, respectively.

Several attempts have been made to reconcile the two approaches. Tabor [104] theorized that the JKR model applied to soft systems (low elastic moduli, high surface energies), while the DMT applied to hard systems (high elastic moduli, low surface energies). Muller, Yushchenko, and Derjaguin (MYD) [105] found that the pull-off force was dependent on a single dimensionless parameter, Φ, given by:

$$\Phi = \frac{32}{3\pi}\left[\frac{\gamma^2 D_p(1-\sigma^2)^2}{\pi E^2\epsilon^3}\right]^{\frac{1}{3}} \tag{9.6}$$

where ϵ is the distance of closest approach (typically 4 Å). It was found that the DMT model applies as Φ approaches zero, and the JKR model applies when $\Phi > 1$. This result supported Tabor's suggested trend.

The most surprising aspect of the JKR and DMT theories is that both predict no dependence of the particle pull-off force on the elastic moduli of the particle and surface. Intuitively, we might expect that, since the contact area is very dependent on

the elastic modulus of the particle material, then so would be the pull-off force. This issue was addressed by Tsai, Pui, and Liu (TPL) [106], who argued that as the elastic modulus of the material is decreased, the pull-off event should begin to resemble the separation of two flat surfaces.

The TPL method uses energy conservation and a force balance to derive a relationship between elastic flattening and the attractive van der Waals force. Like MYD, TPL found that the pull-off force could be expressed in terms of a single dimensionless parameter,

$$\Pi = \left(\frac{25\pi^2\gamma^2 D_p}{8\epsilon^3 K^2} \right)^{\frac{1}{3}}. \tag{9.7}$$

TPL approximated the pull-off force by:

$$F_{pull-off}^{TPL} = \frac{\gamma\pi D_p}{2}\left[\exp[0.124(\Pi - 0.05)^{0.439}] + 0.2\Pi\right] \tag{9.8}$$

Because of high stresses in the contact area between the particle and surface, the possibility of plastic deformation must be considered. This problem was addressed by Maugis and Pollock [107] who mapped the range of elasticity in terms the dimensionless quantity w^* given by:

$$w^* = \frac{2\gamma K^2}{D_p Y^3} \tag{9.9}$$

where Y is the yield strength of the material. For $w^* < 5.2$, deformations are fully elastic and JKR theory holds. For $w^* > 12000$, deformations are fully plastic and the contact radius, a, becomes proportional to $D_p^{\frac{1}{2}}$, rather than $D_p^{\frac{2}{3}}$, as predicted by JKR theory.

How a particle adheres to a surface represents only part of the overall problem. In fact, it is unclear how important equilibrium adhesion theories are in understanding the dynamics of particle resuspension, since the equilibrium model describes detachment when a normal force is applied infinitely slowly. Resuspension occurs suddenly, possibly too quickly to maintain the equilibrium. Nevertheless, equilibrium particle adhesion theories, at the very least, provide necessary information about the initial state of a particle-surface system.

9.3.2 Particle Resuspension

Inceptive motion

Wang [11] theorized three modes of inceptive motion leading to separation. These are:

1. Lift-off: When the normal component of a force applied to an adhered particle surpasses the pull-off force, the particle will be lifted off the surface.

2. Sliding: When the tangential component of an applied force surpasses the total normal force (including the sticking force) multiplied by a coefficient of static friction, the particle will begin to slide and thus be resuspended.

3. Rolling: When the total torque about a point on the edge of the contact circle (again, including the downward sticking force) is equal to zero, the particle will begin to roll around that point and thus off the surface. If the applied force is tangential to the surface and applied to the particle center (i.e., at a height of $\frac{D_p}{2}$ above the surface), then the removal force can be approximated by:

$$F_{rem}^{rotation} = \frac{2aF_{adhesion}}{D_p} \tag{9.10}$$

where a is the radius of the contact circle.

This resuspension analysis introduces the effect of an applied tangential force on an adhered particle. The JKR and DMT models describe the response of an adhered particle to an applied normal force. But since a small particle in a viscous sublayer experiences a tangential shear force, it is essential to understand this effect as well.

Using the JKR contact mechanics approach in incorporating the effect of a tangential force on a sphere in contact with a surface, Savkoor and Briggs [108] derived a critical tangential force of

$$T_c = 4\left[(PP_c + P_c^2)\frac{K}{\lambda}\right]^{\frac{1}{2}}, \tag{9.11}$$

where P is the applied normal force, $P_c = \frac{3}{4}\pi D_p \gamma$, and K and λ are elastic constants. This critical force represents the criterion for detachment induced by lateral displacement.

The effect of shear

To probe the validity of these models, the predicted threshold tangential force must be converted to a threshold shear stress. The drag force on a sphere in a linear shear flow at finite Reynolds number has been shown theoretically [109] and experimentally [110] to closely resemble the drag force on a sphere in a uniform flow, and can be estimated as [9]:

$$F_{\text{drag}} = \frac{\pi}{8} C_D \rho D_p^2 v^2, \tag{9.12}$$

where ρ is the density of the gas, and v is the gas velocity at the center plane of the sphere. The drag coefficient, C_D, is calculated from an empirical relation in terms of the particle Reynolds Number, Re_p, which is given by:

$$\text{Re}_\text{p} = \frac{\rho D_p v}{\mu}, \tag{9.13}$$

where μ is the dynamic viscosity of the gas. Equations (9.12) and (9.13) can be combined to determine a dimensionless drag force that is independent of the gas velocity, v. This parameter is called the Galileo number,

$$\text{Ga} = C_D \text{Re}_\text{p}^2 = \frac{8 F_{\text{drag}} \rho}{\pi \mu^2}. \tag{9.14}$$

Ga can be obtained directly from the predicted or measured threshold tangential force, allowing estimation of a critical particle Reynolds Number from the relationship between Ga and Re_p [9]. The threshold shear stress, τ, can then be calculated from the Reynolds number, e.g.,

$$\tau = \frac{2\mu^2 \text{Re}_\text{p}}{\rho D_p^2}. \tag{9.15}$$

Turbulent bursts

Particle resuspension by turbulent flows occurs over an extended period of time, rather than immediately after the flow rate exceeds an entrainment threshold. This was attributed to random turbulent bursts that expose particles within the viscous sublayer to the needed shear stress [13]. Estimates for bursting frequency and spatial

distribution were used to predict resuspension rates as a function of time in turbulent boundary layer flows.

9.4 Experimental

9.4.1 Sample Preparation

Particle generation

This experimental study requires smooth, spherical, and monodisperse particle samples on well characterized substrates. Previous studies of the resuspension of smooth monodisperse spheres employed commercially available particles, ranging from glass beads to PSL spheres. We employ a vibrating orifice aerosol generator (VOAG) that is compatible with organic solvents [45]. The VOAG is installed above a solution atomizer, a view region, a drying column, and a sampling region, as illustrated in Fig. 9.1. In the conventional VOAG, a capillary jet is excited by a piezoelectric device cemented to the orifice plate to induce formation of uniformly sized droplets. Because the piezoelectric is exposed to the solution, solvents that may attack the cement or the piezoelectric must be avoided. To avoid this complication, a bimorph piezoelectric device is cemented to the back of a piece of stainless steel shim stock with conductive epoxy. Only the stainless steel is exposed to the solution reservoir. When the crystal-shim assembly vibrates, the vibrations are carried acoustically through the solution creating a sufficient disturbance to force the breakup of the jet into monodisperse droplets. The size of the droplets, D_d, is easily calculated:

$$D_d = \left(\frac{6Q}{\pi f}\right)^{\frac{1}{3}}, \tag{9.16}$$

where Q is the solution flow rate, and f is the frequency of the applied disturbances.

A pressure feed system was used to force the solution through the orifice. The advantage of employing this method rather than the conventional syringe pump, is that an arbitrarily large solution reservoir can be used to ensure that particle samples

may be generated for an indefinite length of time under the same conditions. The disadvantage is that it is difficult to get an accurate measurement of the solution feed rate and thus the resulting droplet size. Fortunately, this is not critical, since particle sizes can be measured optically (see Section 9.4.4). A solution feed pressure of 138 kPa (20 psi) at the reservoir is typically necessary to start the jet through a 50 micron orifice. Once the jet is started, the pressure is then decreased to 28 kPa (4 psi) to sustain the jet. For this system, a jet sustaining pressure of 28 kPa corresponds to an approximate liquid feed rate of 1.4 ml/min.

The view region is used to verify that the droplets are monodisperse before they are collected as particles and observed under a microscope. This is achieved by introducing a gas jet perpendicular to the liquid jet and observing the deflection. Upon deflection, a monodisperse stream will remain a fine line, whereas a polydisperse stream will resemble a spray. Once the vibration frequency is adjusted so that monodispersivity is achieved, the deflection air is turned off, and the dispersion air is turned on. The dispersion air, applied to the jet just as it exits the orifice, helps to reduce coagulation of the droplets and thus should ideally minimize the presence of doublets in the final sample.

The droplets are carried into the drying column in a dilution flow of nitrogen. The dilution flow rate and column temperature are set specifically for each solvent used, since drying rate greatly affects the quality of the dry particles. The droplets must dry fast enough to evaporate all of the solvent and slow enough to maintain sphericity of the particles. For the polystyrene standards, toluene is the appropriate solvent. It was found that an internal column temperature of 80°C is sufficient to yield smooth, dry spheres for molecular weights under 200,000 amu. Above this molecular weight limit, the particle surfaces were very rough. The highest molecular weight used in this study was 114,200 amu. In each case, the temperature in the column was kept below the glass transition temperature of the polymer to avoid extra flattening of the spheres onto the substrate upon sedimentation. The ammonium fluorescein particles were prepared in a procedure similar to that described by Vanderpool and Rubow [5]. However, isopropanol, rather than water, and an internal temperature of over 100°C,

was found to yield high quality particles for this system. The dry particle diameter, D_p, is calculated from the initial droplet diameter:

$$D_p = D_d C^{\frac{1}{3}} \tag{9.17}$$

where C is the volumetric concentration of the solution.

After drying, the particles were allowed to settle on the appropriate substrate in the sampling region. The sampling region is located several inches below the heated region where it was kept close to room temperature to avoid any thermally induced alterations to the particles as they sit on the substrate. Deposition of particles for 5 to 15 minutes produced particle densities of tens to a few hundred per square mm. Once the substrates were coated, they were immediately placed in a dry, organic free environment for at least 18 hours before use in resuspension experiments.

For all of the experiments presented here, 1 x 3 inch glass slides were used as the substrates. The slides were subjected to a cleaning procedure that was found to greatly improve the uniformity of each substrate, as well as the repeatability of each experiment. The slides were first scrubbed with phosphate-free detergent and rinsed in distilled water. They were then washed in a 1:1 nitric acid bath and rinsed thoroughly in distilled water. Finally, they were baked at 300°C for one hour and allowed to cool in a dry box.

9.4.2 Translating Gas Jet Experiment

The experimental system used in the present study has been described in detail in Chapter 5. The apparatus, as illustrated in Figure 9.2, consists of a linear rail table with a vacuum-chuck sample holder mounted upon it. The jet nozzle is mounted on a y-z traverse. The nozzle was kept at a constant height of 5 mm above the substrate throughout this study. The removal efficiency was monitored with dark field microscopy and image analysis. A sample was mounted on the sample holder, and an initial picture was taken with a CCD camera and stored in a PC. The sample was then moved under the gas jet at a fixed speed of 1.8 mm/sec. Once the sample

moved completely past the jet, the jet was turned off and the sample moved back to its initial position where a final image was taken. By comparing the initial and final image, the particle removal efficiency was determined as a function of position in the imaged area. The particle density was monitored as scattered light intensity detected by the CCD camera.

After the sample was passed under the gas jet at a given pressure, a particle-free track was formed in the direction of slide motion. The width of the cleaned track increased with jet pressure. Each experiment involved passing the sample under the jet 12 times at successively greater jet pressure ratios. The range of jet pressures used was selected based on the size and material properties of the particles.

Figure 9.3 shows profiles of the mean pixel intensity across the track for a sequence of increasing jet pressure levels. The density of particles remaining in the deposit is proportional to the difference between that intensity and the minimum value observed for a clean substrate. At low jet pressures, a narrow track is partially cleared. Once the peak shear stress exceeds a threshold removal value, the center of the track is completely cleared of particles. At the edge of the track, the intensity quickly rises from this minimum value to its original value. The sharp rise in the removal efficiency at the edge of the track after a single pass of the jet at a given jet pressure ratio reveals that the spatial distribution of the shear stress across the jet impingement region does not vary with time, at least on the time scale of the jet passage, and that the shear stress required to remove the monodisperse, spherical particles is narrowly distributed. We define the threshold shear stress as that applied at the points where 50% of the particles are removed from the surface, and measure the corresponding track width from the intensity profiles.

9.4.3 Laminar Flow Cell Experiment

Apparatus

A rectangular flow channel was designed to produce surface shear stresses comparable to those generated by the impinging jet, while still maintaining laminar flow. The

Reynolds number, Re, of the channel is given by:

$$\mathrm{Re} = \frac{\rho \overline{u} h_c}{\mu}, \tag{9.18}$$

where h_c is the height of the channel, $\overline{u}$ is the mean gas velocity, and μ and ρ are the gas dynamic viscosity and density, respectively. To maintain low Re for high gas velocities, the channel height was fixed at 0.2 mm by clamping a piece of stainless steel shim stock, cut to the desired channel shape, between the glass substrate and aluminum base. The pressure drop in the channel was monitored by a series of pressure taps located along the center line of the channel. Flow through the cell was set by manual adjustment of the upstream pressure and computer control of a variable flow solenoid valve (MKS type 024BA). Flow rates were determined by measuring the pressure drop across a calibrated Meriam (Cleveland, OH) laminar flow element using an MKS type 223BD differential pressure transducer. Particles on the glass slide were illuminated using a HeNe laser sheet that was introduced into the flow cell from the flow outlet. A CCD camera with a telephoto lens was used to obtain images through a 19 mm diameter viewing port in the top plate. The experimental setup is illustrated in Fig. 9.4.

For laminar, incompressible flow through a wide channel, the pressure drop, G, in the channel increases linearly with flow rate, Q:

$$G = \frac{12 \mu Q}{h_c^3 w_c}, \tag{9.19}$$

where the width, w_c, of the channel was 1.27 mm. By comparing the measured pressure drop for various flow rates with this theoretical relation, we can determine when the turbulent transition begins. The data presented in Fig. 9.5 demonstrate that the operating range of the laminar flow cell is limited on the low end by the influence of the channel walls, and on the high end by the transition to turbulence, which occurs at a flow of close to 11 L/min. This corresponds roughly to a Reynolds Number of 1000. Within this flow range, the shear stress, τ_o, experienced by particles

on the glass slide is calculated from the measured flow through the channel as:

$$\tau_o = \frac{6\mu Q}{h^2 w_c}. \tag{9.20}$$

Saltation effects

In contrast to the turbulent jet experiment, saltation was found to play a dominant role in the resuspension of particles in the flow channel. When particles were present on the surface upstream of the viewing region and close to the channel inlet, particle removal in the viewing region occurred at significantly lower flow rates than when similar particles were deposited only in the viewing area. For this reason a slight modification was made to the particle generation procedure described in Section 9.4.1. Instead of putting the glass slides directly into the sampling port, the slides were masked to allow deposition to occur only in a narrow slit, 1.0 mm in width, located in the center of the viewing region, as in the resuspension experiments of Mudumala and Braaten [111]. With densities kept under 50 particles/mm^2, the effects of saltation were thus minimized.

Procedure

A glass slide that was masked during coating was clamped into the flow cell and an initial picture was recorded. Typically, one picture involved averaging 20 frames. Then the supply pressure was set with the manual pressure regulator and the flow rate was incremented, under computer control, using the variable solenoid valve. A picture was taken immediately following each incremental increase in the flow rate, and after a one minute exposure to the flow. The flow rate was calculated from the average of 1000 successive readings of the differential pressure across the laminar flow element over a 10 second period. The solenoid proportional control valve could only vary the flow rate over a range of 2.5 L/min at a given supply pressure, so it was necessary to ramp down the solenoid valve current and manually increase the supply

pressure four times in order to span the desired range of flow rates.

Each recorded image contained 640 x 480 pixels and 256 levels of grey and the area occupied by the particles was about 20 x 200 pixels at a scale factor of 19 pixels/mm. A measure of the particle density was determined for each picture by averaging the pixel intensity of this smaller specified area. For each image, the removal efficiency, η, was calculated from the average pixel intensity, I:

$$\eta(\%) = 100 \times \frac{I - I_{init}}{I_{clean} - I_{init}} \tag{9.21}$$

where I_{init} is the average pixel intensity obtained from the initial image, and I_{clean} is the average pixel intensity of a clean region of the slide, usually chosen from the last image of the series.

9.4.4 Particle Sizing

Particle size distributions were measured optically using an Olympus model BHA microscope equipped with a CCD Camera and NIH Image software. Usually, the particle laden slides used for particle sizing were specially coated with particles during the synthesis of samples for the experiment. However, due to the occasional lack of extra samples, sizing was sometimes performed using particles that remained outside the removal track on slides that had already been used in an experiment. For smaller particles (below 12 μm), 400x magnification (1.89 pixels/μm) was used, while 200x (.94 pixels/μm) was used for the larger particles. The focus was set manually to make the particle edges as sharp as possible. The unavoidable small variations in focus had little effect on the final size distributions.

Sizing a single particle involved locating the center of the particle using an NIH Image macro, and then calculating the average radial distribution of pixel values for 36 radial lines emanating isotropically from the particle center. This averaged curve possessed a near constant maximum within the particle (i.e., closer to the black level of 255) and then dipped down to the lighter background level. The edge of the particle was defined as the location of 75% of this decrease in pixel value. This percentage

was determined by calibrating the sizing technique with PSL spheres of known size.

Figure 9.6 displays a sample distribution obtained using this technique. A typical analysis involved sizing over 500 random particles on a sample. One notable feature in this distribution is the presence of doublets on the sample, revealed by the peak at 10.2 μm for this 8.1 μm sample. These were very difficult to eliminate completely in the particle generation process. Fortunately, the small number of doublets did not affect the threshold resuspension shear stress measurements.

9.5 Results

9.5.1 Translating Gas Jet Results

The two parameters measured in the jet experiment are the width, w, of the removal track and the removal efficiency, η, at the center of the track (see Section 9.4.2). For each experiment, these parameters were plotted against the strength of the impinging gas jet, expressed as the jet pressure ratio, P_{jet}/P_{atm}. Trackwidths are nondimensionalized with the jet exit diameter, D. The results from a series of experiments on three identical samples (8.0 μm polystyrene particles) are shown in Figs. 9.7 and 9.8. The results demonstrate very good repeatability. The width and efficiency data were averaged to yield the final plots used for analysis.

The averaged efficiency and width plots for a single molecular weight of polystyrene ($M_w = 18,700$ amu) are presented in Figs. 9.9 and 9.10 for several particle sizes. As expected, the plots show that it is more difficult to aerodynamically entrain smaller particles than larger ones, even though the pull-off force is linearly proportional to particle radius, as shown in Eqs. (9.1) and (9.2). Extracting threshold shear stresses from these data requires a knowledge of the shear stress distribution under a normally impinging jet. From the efficiency curve, we can interpolate to determine the jet pressure ratio that yields 50% removal directly under the jet. The threshold shear stress, $\tau_{50\%}$, is the maximum shear stress under a jet of this strength. The trackwidth data provides a threshold shear stress measurement for each jet pressure that yields

a width greater than zero, since the shear stress at that radial distance from the jet center is also the threshold shear stress for that particle sample.

It was found in a previous study [112] that the flow close to the stagnation point of an impinging jet is well described by laminar boundary layer theory. For fully developed jet impingement ($H/D > 8$), the maximum shear stress is located within this region, at a radial distance, r_{max}, given by

$$r_{max} = 0.09H, \tag{9.22}$$

where H is the jet height above the surface. The maximum shear stress, τ_{max}, is calculated in terms of the jet exit parameters, e.g.,

$$\tau_{max} = 44.6(\rho U^2)\mathrm{Re}_o^{-\frac{1}{2}} \left(\frac{H}{D}\right)^{-2} [1 + f(M)], \tag{9.23}$$

where D is the jet exit diameter, Re_o is the jet Reynolds number, M is the Mach number at the jet exit, and ρU^2 is the dynamic pressure at the jet exit, which is calculated directly from the jet pressure ratio [21]. The empirical function, $f(M)$, of the Mach number was found to be [112]:

$$f(M) = 0.66M - 3.2M^2 + 3.9M^3$$

for an air jet. Figure 9.11 displays the shape of the shear stress distribution as predicted by laminar boundary layer theory [112].

The transition to a turbulent boundary layer at some distance beyond r_{max} signifies the beginning of the wall jet region of the flow. It was observed [112] that particle entrainment in the wall jet region does not scale with the mean shear stress, but rather, with some percentage of the amplitude of the shear stress fluctuations. Therefore, only efficiency measurements made close to the stagnation point were used to determine the threshold jet parameters. The threshold jet parameters from the translating jet experiments are listed in Table 9.1 along with the threshold shear stresses, $\tau_{50\%}$, which were calculated using Eq. (9.23).

9.5.2 Laminar Flow Cell Results

Removal efficiency curves, obtained from the laminar channel flow experiment, are presented in Fig. 9.12 for two sizes of ammonium fluorescein particles. The data are noisier than the jet data, since the total number of particles under observation is smaller. However, repeatability is still very good, and the shift in removal threshold for the different particle sizes is clear.

Figure 9.13 compares removal efficiency data obtained from a translating gas jet experiment and a laminar channel flow experiment performed on identical particle samples (20.6 μm ammonium fluorescein particles). Since the lowest jet pressure ratio used in the jet experiment ($P_{jet}/P_{atm} = 1.056$) produced 100% removal directly beneath the jet, the removal efficiency curve portrayed in Fig. 9.13 was obtained directly from the average pixel intensity profile (as in Fig. 9.3) from the first jet pass. The shear stress distribution under a jet of strength $P_{jet}/P_{atm} = 1.056$ was calculated using the laminar boundary model presented in the previous study [112]. The error bars in the jet data shown in Fig. 9.13 represent the accuracy limits of the pressure transducer. The relative proximity of the two efficiency curves suggests that the same resuspension mechanism occurs in both the translating gas jet and the laminar flow cell experiments. However, the shift in the measured shear stress may be related to the kinetics of detachment, since the exposure of the particles to the shear stress is much longer in the laminar flow cell than in the translating jet experiments. The kinetics issue will be discussed in more detail in Section 9.7. The threshold shear stresses, $\tau_{50\%}$, obtained from the channel flow experiments are presented in Table 9.2.

9.6 Comparison with Equilibrium Theories

The results presented in Section 9.5 provide very strong evidence that the force responsible for particle resuspension is tangential to the surface. Similar observations were made by Braaten, Shaw, and Paw U (1993) [100], who attributed 85% of 62 individual resuspension events to coherent structures within the viscous sublayer - usually ejection-sweep (E-S) patterns which are characterized by a sudden rise in the

shear stress experienced by the particle. Since the present observations were made in burst-free environments, we are able to pinpoint threshold shear stresses for various particle sizes and materials, and thus compare our data to theories describing the mechanics of the resuspension of a single particle.

A list of the relevant material parameters is provided in Table 9.3. Assuming that the Dupré energy of adhesion is double the geometric mean of the surface energies of the particle and surface [113], we can use MYD theory to decide whether JKR or DMT theory is more appropriate to this system. The smallest value of Φ calculated from Eq. (9.6) (i.e., smallest particle size, elastic modulus of glass) is 10. This is well within the JKR regime. So, if adhesion induced deformations are purely elastic, JKR theory applies.

Using Eq. (9.9) and the yield strength of polystyrene, we find that $w^* = 0.6$ for a 6.6 μm particle. This indicates that the deformation within the contact area is fully elastic. However, Rimai *et al.* [114] found using scanning electron microscope imaging that the contact area between polystyrene spheres and silicon substrates is proportional to the particle diameter, as would be expected for fully plastic deformation. Because of this ambiguity, we compare our data to the predicted resuspension thresholds assuming fully elastic JKR adhesion as well as fully plastic adhesion.

Figure 9.14 shows the threshold shear stress data plotted against particle size for all of the materials used from both the gas jet and the laminar flow cell experiments. There is good agreement in the magnitude of the shear stress with the predictions of the various theories, but none of the models predict as strong a dependence on the particle diameter as observed for each material. There exists at least an inverse cube dependence of the shear stress on the particle diameter for all of the materials used. The lowest molecular weight of polystyrene (open squares) exhibits an even stronger dependence on the particle diameter, probably due to viscoelastic effects that become more important as the molecular weight of the polymer is reduced.

9.7 Kinetics of Particle Detachment

The failure of resuspension models based on equilibrium adhesion theories to accurately describe the size dependence of the threshold shear stress suggests that resuspension dynamics cannot be ignored. Modeling particle resuspension as a dynamic process requires some insight concerning the effect on the resuspension threshold of the duration of the applied force. All of the results presented from the jet experiment so far were obtained using a constant sample translation speed of $V_{trans} = 1.8$ mm/s, thereby exposing all particles to the same force duration. Additional experiments were conducted with ammonium fluorescein and polystyrene particle samples to explore the influence of translation speed. The observed threshold shear stresses from these experiments are presented in Table 9.4. The increase in the threshold shear stress with translation speed indicates that higher forces are necessary to induce resuspension for short exposures than for longer ones. Fig. 9.15 displays the time history of the shear stress experienced by a single particle at a threshold location (i.e., at the edge of the removal track) for three translation speeds ($V_{trans} = 1.8$, 9.0, and 270 mm/s), where $t = 0$ is defined when the particle experiences the maximum shear stress.

Maugis (1992) [115] showed that the pull-off force predicted by JKR theory follows directly from application of the Griffith criteria for crack propagation along the particle/surface interface, e.g.,

$$G = \gamma, \tag{9.24}$$

where G is the released elastic energy per unit of crack area. This is the minimum energy required to initiate crack propagation through a solid. Describing particle detachment with the solid fracture analogy is justified because of the tensile stress singularities at the edge of the contact region predicted by JKR theory, resembling the stress singularities surrounding a crack tip in a solid. Therefore, a dynamic model of particle detachment based on the kinetics of crack propagation through a solid is developed to explain the observed dependence on threshold force on force duration.

The crack propagation velocity, v_{crack}, can be related to the excess elastic energy

surrounding the crack by the expression [116]:

$$\frac{G-\gamma}{\gamma} = \mathcal{F}(v_{crack}), \tag{9.25}$$

where $\mathcal{F}(v_{crack})$ depends on energy loss rates due to friction or viscoelastic effects at the crack tip. Unloading experiments of glass spheres and punches in contact with polyurethane substrates were used to quantify viscoelastic losses yielding the relation [116]

$$\mathcal{F} \sim (\alpha v_{crack})^{\frac{3}{5}}, \tag{9.26}$$

where α is the WLF shift factor [116]. Since energy loss mechanisms have not been quantified for the high molecular polymer or ammonium fluorescein dye particles used in the present experiments, we will assume the expression

$$\mathcal{F} = C v_{crack}^{1/n}, \tag{9.27}$$

where C and n are related to energy losses at the crack tip (i.e., the periphery of the contact region). It is reasonable to assume that these parameters depend on material properties, but also on particle diameter since the compressive stress gradient within the contact region increases with decreasing particle size.

The elastic energy release rate, G, for an elastic sphere in contact with a surface is calculated from JKR theory to be [115]

$$G = \frac{\left(2a^3K + D_p F_N\right)^2}{6\pi D_p a^3 K}, \tag{9.28}$$

where F_N is the upward normal force applied to the particle. Since the time scale for detachment in the jet experiments is on the order of hundreths of a second (see Fig. 9.15) and the time scale for contact radius equilibration during unloading is several minutes [116], it is reasonable to assume that the contact radius, a, in Eq. (9.28) is unchanged from the equilibrium value under zero applied load given by Eq. (9.4). The applied normal force, F_N, is related to the applied shear stress depending

on the resuspension mechanism. The results of the laminar flow cell experiments, in which particles are exposed to at least one minute of shear stress per pressure increment, suggest that the JKR rotation mechanism is correct (see Fig. 9.14), and thus

$$F_N = \left(\frac{D_p}{2a} - \frac{\delta}{a}\right) F_{drag}, \tag{9.29}$$

where the distance, δ, that the particle center approaches the surface during adhesion is easily calculated from JKR theory [102], and F_{drag} is calculated as described in Section 9.3.2.

Since the crack propagates at a finite velocity, detachment cannot occur unless the crack has traveled the full length of the contact interface. Since an applied normal force causes the crack to propagate from the contact periphery inward, the crack propagation distance is equal to the contact radius, a. However, this creates the contradiction that the point of rotation located on the contact periphery must maintain contact with the surface until detachment is complete, as required by Wang's [11] rolling mechanism. For the present model we assume that a crack is allowed to propagate from the periphery, except from a very small region surrounding the point of rotation, which maintains contact with the surface. The effects of further deformation to the sphere associated with this mechanism are neglected.

It is clear from Fig. 9.15 that particles passing underneath the impinging gas jet are exposed to a quickly varying shear stress, and thus, the crack velocity must vary during detachment as well. Once the applied shear stress surpasses the equilibrium value determined by the Griffith criteria (i.e., the equilibrium threshold), the crack will begin to propagate and continue until the shear stress falls below the equilibrium value. The threshold detachment condition is obtained from Eqs. (9.25) and (9.27) and can be written in terms of the sample translation speed, v_{trans}, e.g.,

$$\int_{-x_o}^{x_o} \left(\frac{G-\gamma}{\gamma}\right)^n dx = C' a v_{trans}, \tag{9.30}$$

where x_o is the distance between the maximum shear stress location and the equilibrium threshold shear stress location, and $C' = C^n$.

Since Eq. (9.30) cannot be written explicitly for G, determination of the threshold shear stress was performed through an iterative process. Figures 9.16 and 9.17 compare the results of these calculations with the observed effect of translation speed and particle size, respectively, for ammonium fluorescein particles. Note the good agreement between the laminar shear cell data and the equilibrium JKR rolling model. The parameters, n and C', were chosen to fit the data for both plots (Figs. 9.16 and 9.17). The size dependence of the exponent, n, was estimated to be

$$n = C'' D_p^{1.5}, \tag{9.31}$$

where D_p is in microns. The remaining parameters were assigned the values

$$C' = 10^{15}$$

$$C'' = 0.14.$$

Decreasing values of n implies more energy losses at the crack tip and, thus, lower crack propagation speeds. Qualitatively, n should be larger than the measured value of 5/3 for viscoelastic materials, as observed for this size range.

Since the same particle size effect is observed for the polystyrene particles, the same size dependence on the exponent, n, is assumed. However, the constant C' was decreased to 1.7×10^{14}, presumably to account for differences in material properties. Figures 9.19 and 9.18 compare these calculations with the experimental data for polystyrene. Agreement is good for the 18,700 amu polystyrene, but a further decrease in C' is required to fit the 114,200 amu polystyrene. This suggests a strong dependence of C' on elastic modulus, since the surface energies of the two molecular weights of polystyrene are within a few percent [117].

Qualitatively, the stronger size sensitivity of the low molecular weight (3,700 amu) polystyrene particles (see Fig. 9.14) is expected within the context of the model, as viscoelastic losses at the crack tip would greatly affect the value of n and, thus, the size

dependence of the crack propagation speed. The exact dependence was not attainable with the present experiments due to the excessively high shear stresses necessary to entrain the smaller low molecular weight polystyrene particles.

9.8 Summary

A translating gas jet and a laminar channel flow were used to determine critical resuspension parameters for various particle sizes and materials. Particle generation and substrate preparation techniques were perfected in order to ensure uniformity and repeatability in the results. Threshold shear stresses were extracted from removal patterns and plotted as a function of particle diameter, D_p. It was found that the threshold shear stress is more sensitive to particle size than predicted by equilibrium models. A dynamic resuspension model, based on crack propagation kinetics, is presented. The model qualitatively explains the deviations from equilibrium resuspension; however, more information concerning energy loss mechanisms at the contact region periphery is needed in order to quantify the dynamic resuspension process. The present work demonstrates the importance of kinetics to particle resuspension.

Table 9.1: Threshold shear stress measurements from normal jet experiment.

Material	D_p (μm)	$(P_{jet}/Patm)_{50\%}$	$(\rho U^2)_{50\%}$ (kPa)	$\mathrm{Re}_{50\%}$	$M_{50\%}$	$\tau_{50\%}$ (Pa)
PS(M_W=114,200)	6.6	1.81	130	13300	.959	1080
	8.3	1.41	72.9	9130	.717	431
	9.7	1.31	56.6	7840	.632	321
PS(M_W=18,700)	6.6	2.10	157	15300	1.09	1670
	8.0	1.64	108	11700	.874	773
	8.1	1.48	83.4	9930	.767	517
	12.9	1.18	35.0	5940	.497	206
	13.5	1.13	25.6	5010	.425	162
PS(M_W=3,700)	9.5	1.87	139	13800	.989	1210
	13.1	1.17	31.8	5640	.474	191
Ammonium Fluorescein	8.4	1.79	128	13100	.952	1050
	10.4	1.47	82.9	9890	.765	513
	15.7	1.16	29.8	5440	.459	181

Table 9.2: Threshold shear stress measurements from channel flow experiment.

Material	Particle Size (μm)	$\tau_{50\%}$ (Pascals)
Ammonium Fluorescein	18.2	43.4 $\pm$ 1.3
	20.6	30.8 $\pm$ 1.6
	21.2	34.7 $\pm$ 5.0

Table 9.3: Relevant material properties.

$E_{\text{polystyrene}}$	2.8×10^9 Pa
$\sigma_{\text{polystyrene}}$	.33
$\gamma_{\text{polystyrene}}$	4.62×10^{-2} $\frac{J}{m^2}$
$Y_{\text{polystyrene}}$	7.6×10^7 Pa
$E_{\text{amm.fl.}}$	1.2×10^9 Pa
$\sigma_{\text{amm.fl.}}$	.33
$\gamma_{\text{ammfl.}}$	$\sim 4.62 \times 10^{-2}$ $\frac{J}{m^2}$
E_{glass}	6.9×10^{10} Pa
σ_{glass}	.20
γ_{glass}	1.41×10^{-2} $\frac{J}{m^2}$
μ_{air}	1.81×10^{-5} $\frac{kg}{m-s}$
ρ_{air}	1.17 $\frac{kg}{m^3}$

Table 9.4: Average threshold shear stress for various translation speeds.

Material	Particle Size (μm)	Translation Speed (mm/s)	$(\tau_{50\%})_{ave}$ (Pa)
Ammonium Fluorescein	8.4	1.8	1050
	8.4	9.0	1190
	8.4	270	2360
	15.7	1.8	181
	15.7	9.0	223
	15.7	270	259
PS(M_W=18,700)	7.8	1.8	784
	7.8	9.0	1316
	7.8	270	2710

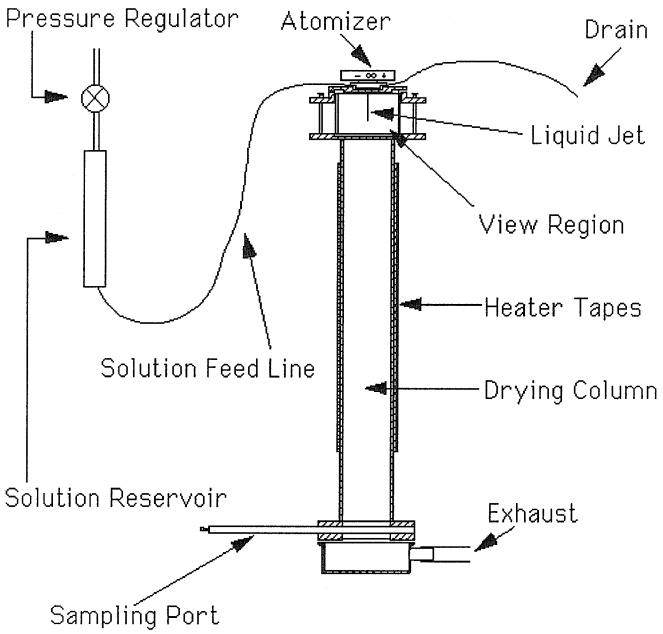

Figure 9.1: Schematic of particle synthesis apparatus.

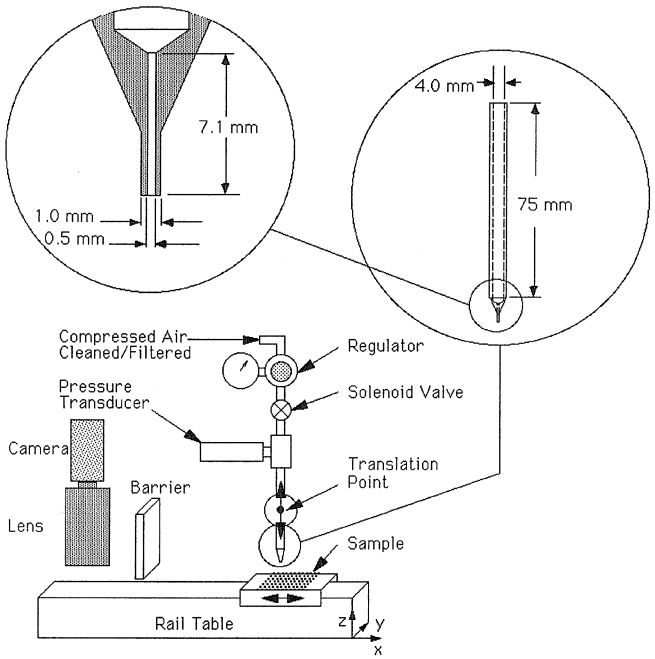

Figure 9.2: Translating gas jet experimental setup.

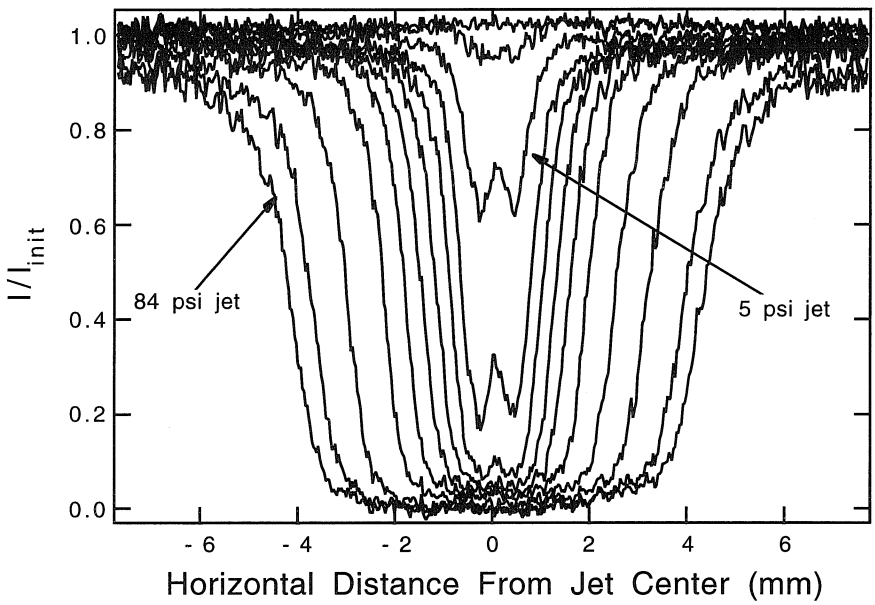

Figure 9.3: Particle removal profiles for various jet pressures.

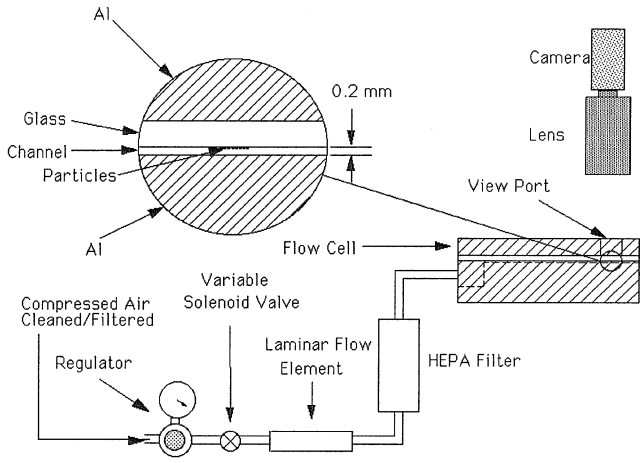

Figure 9.4: Laminar flow cell experimental setup.

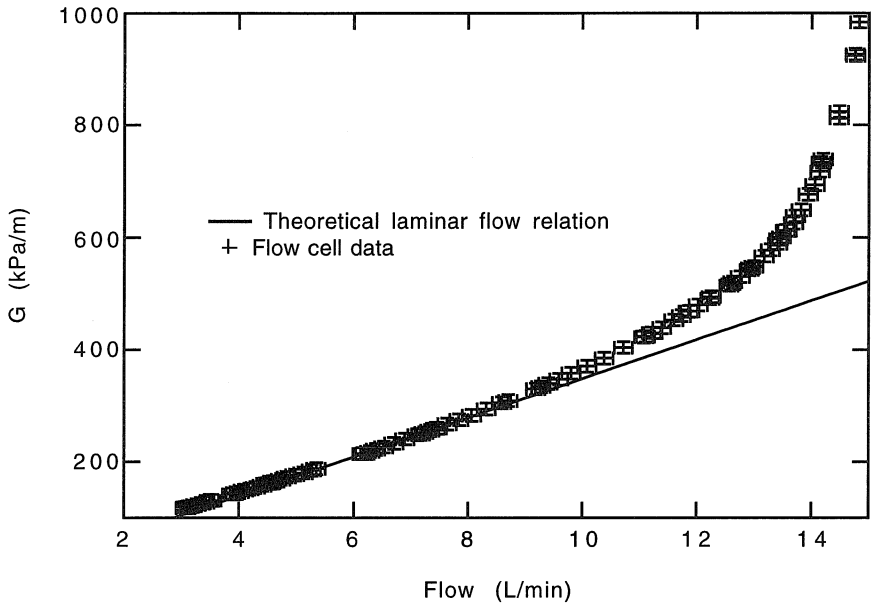

Figure 9.5: Measured pressure drop in flow channel compared to laminar flow results.

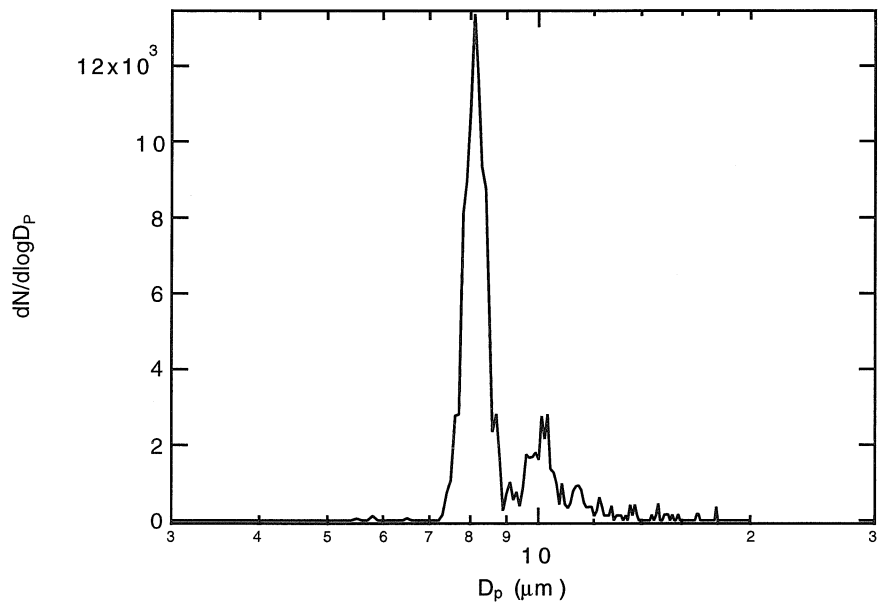

Figure 9.6: Particle size distribution for nominally 8.1 μm polystyrene particles.

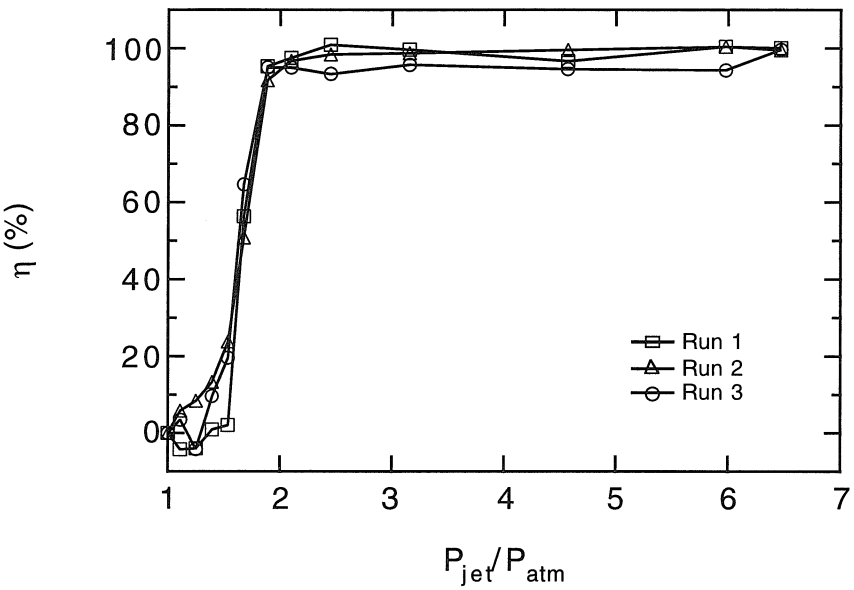

Figure 9.7: Repeatability in removal efficiency curve.

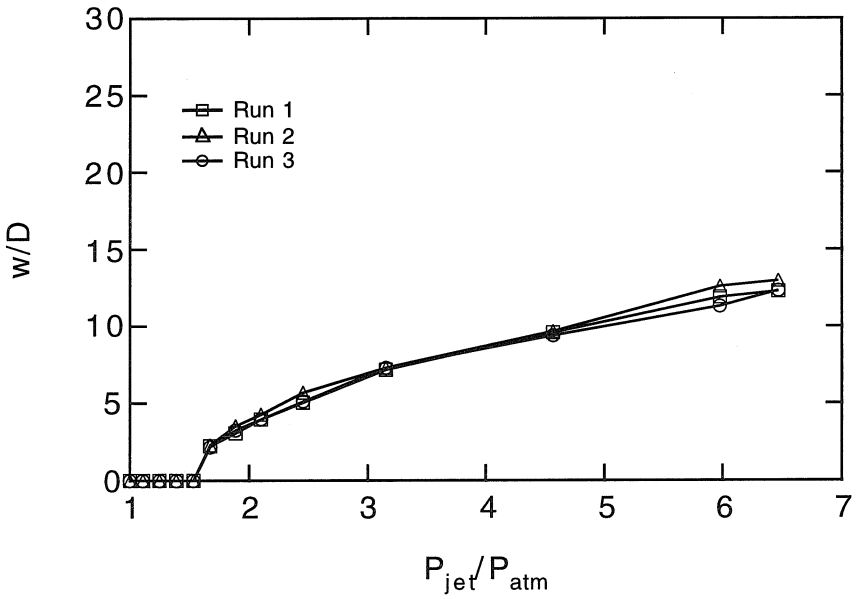

Figure 9.8: Repeatability in width curve.

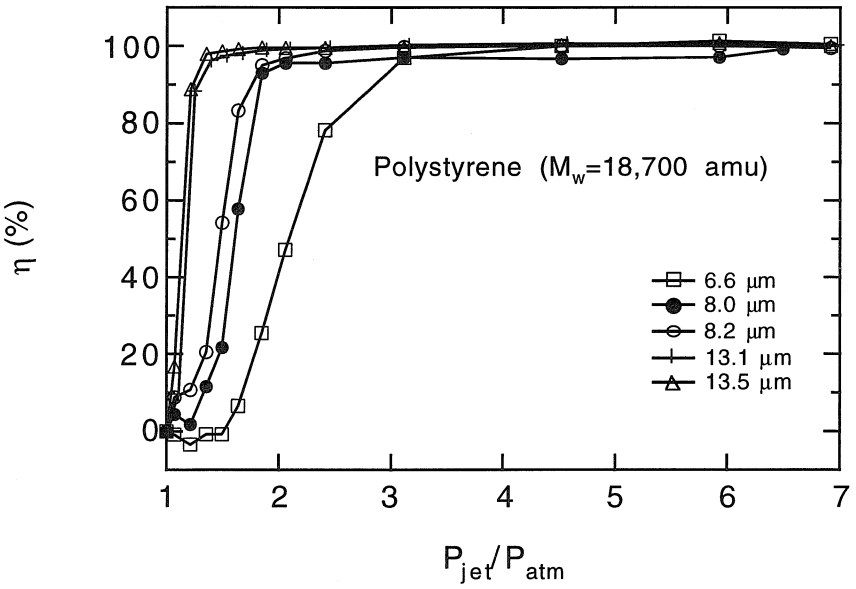

Figure 9.9: Removal efficiency curves for medium molecular weight polystyrene.

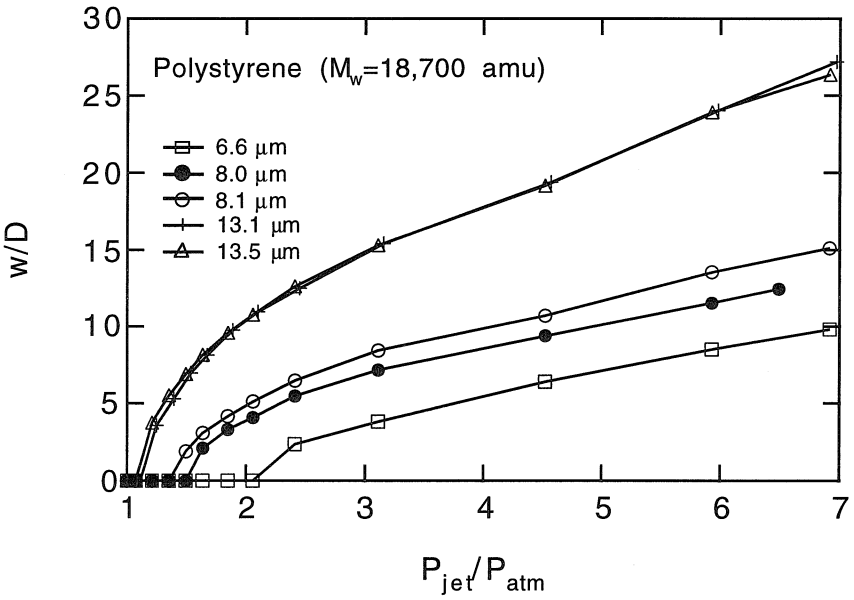

Figure 9.10: Width curves for medium molecular weight polystyrene.

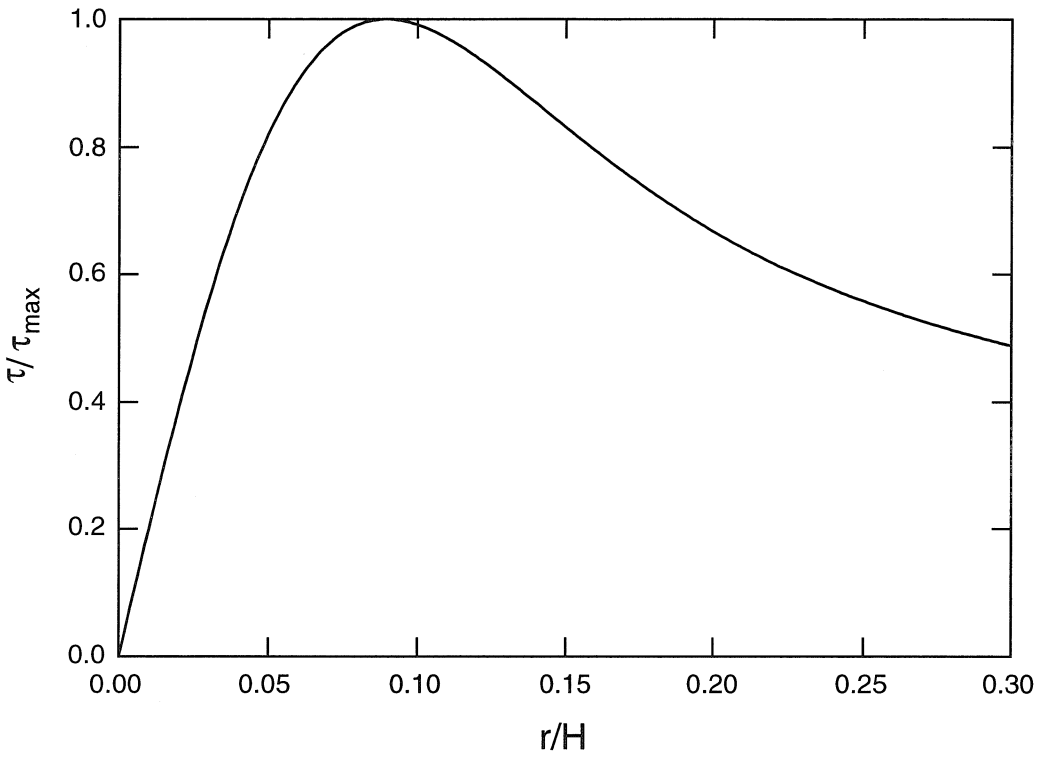

Figure 9.11: Wall shear stress distribution under impinging jet predicted from laminar boundary layer theory.

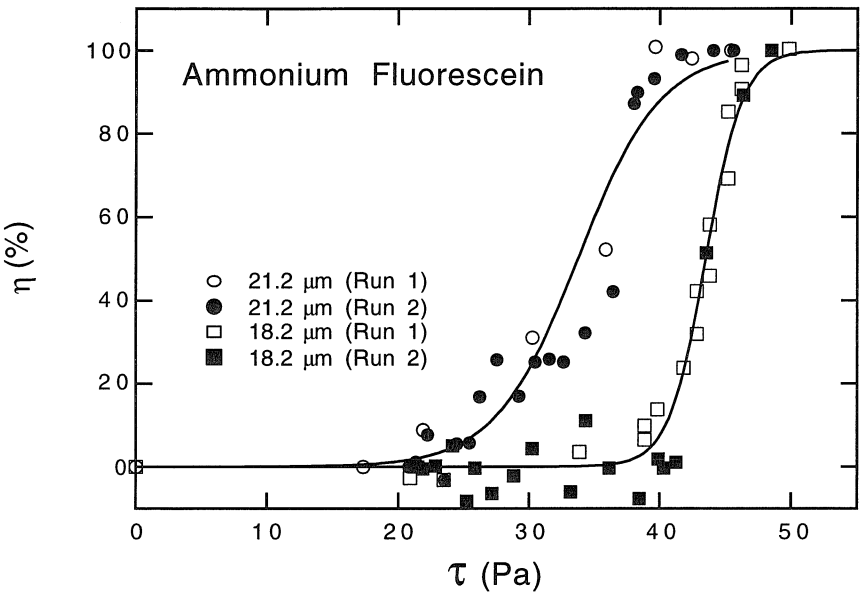

Figure 9.12: Removal efficiency curves obtained from laminar channel experiment for 18.2 and 21.2 μm ammonium fluorescein particles.

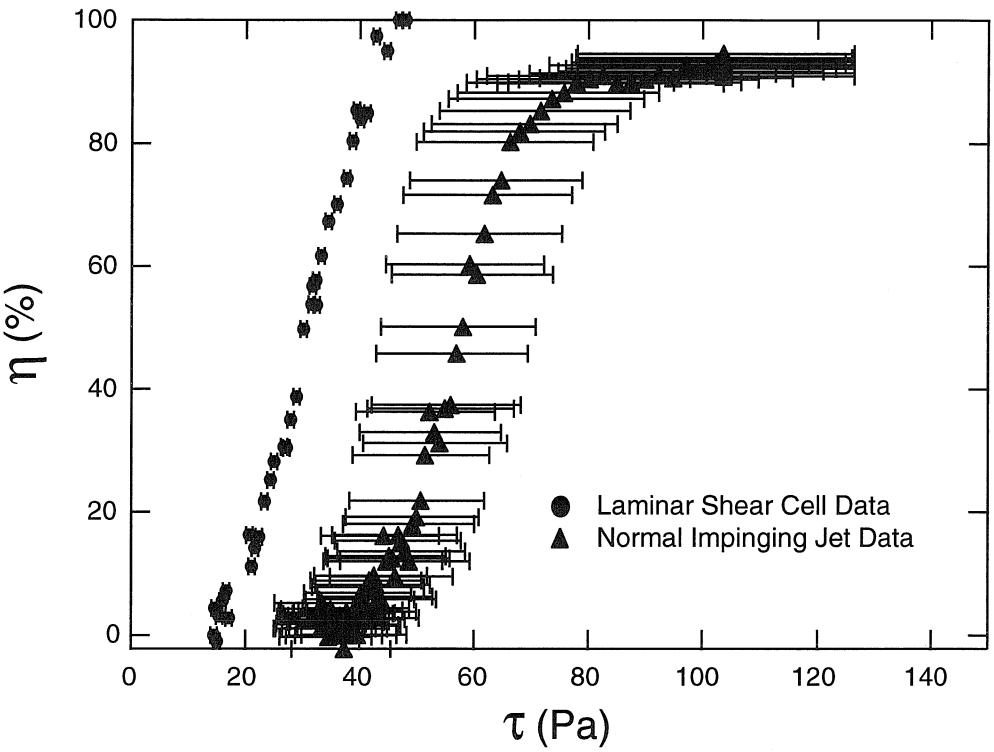

Figure 9.13: Comparison between laminar flow and translating jet results obtained for identical particle samples and 20.6 μm ammonium fluorescein particles.

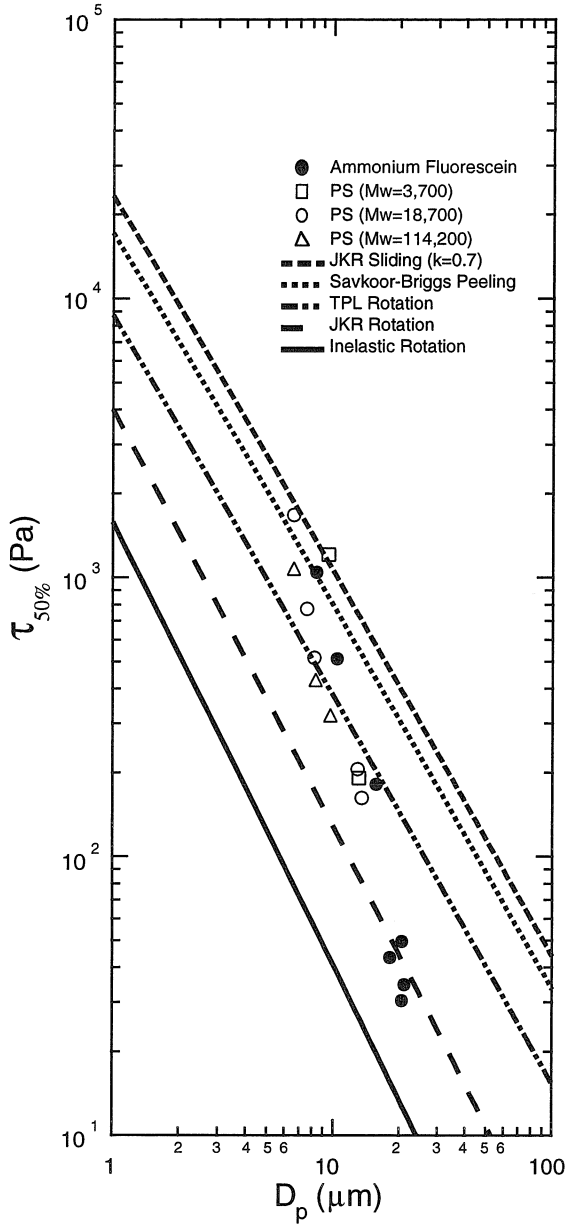

Figure 9.14: Threshold shear stress data compared with predictions for polystyrene from various equilibrium adhesion theories.

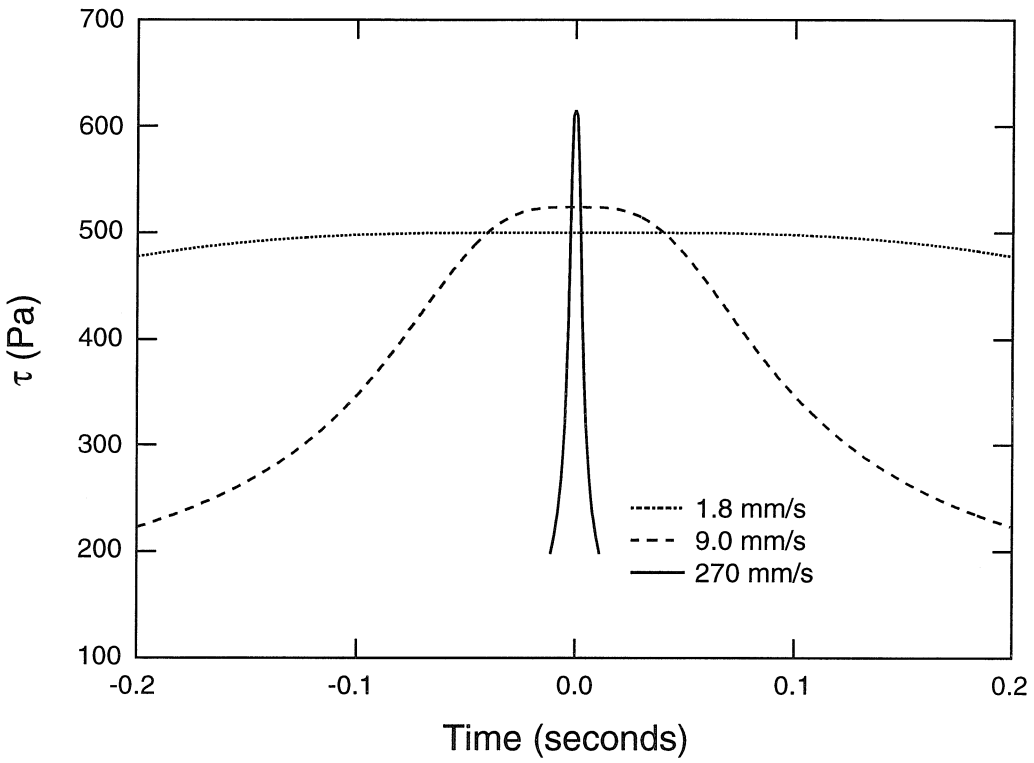

Figure 9.15: Shear stress history at threshold for 8.4 μm polystyrene particle (V_{trans} = 1.8, 9.0, 270 mm/s).

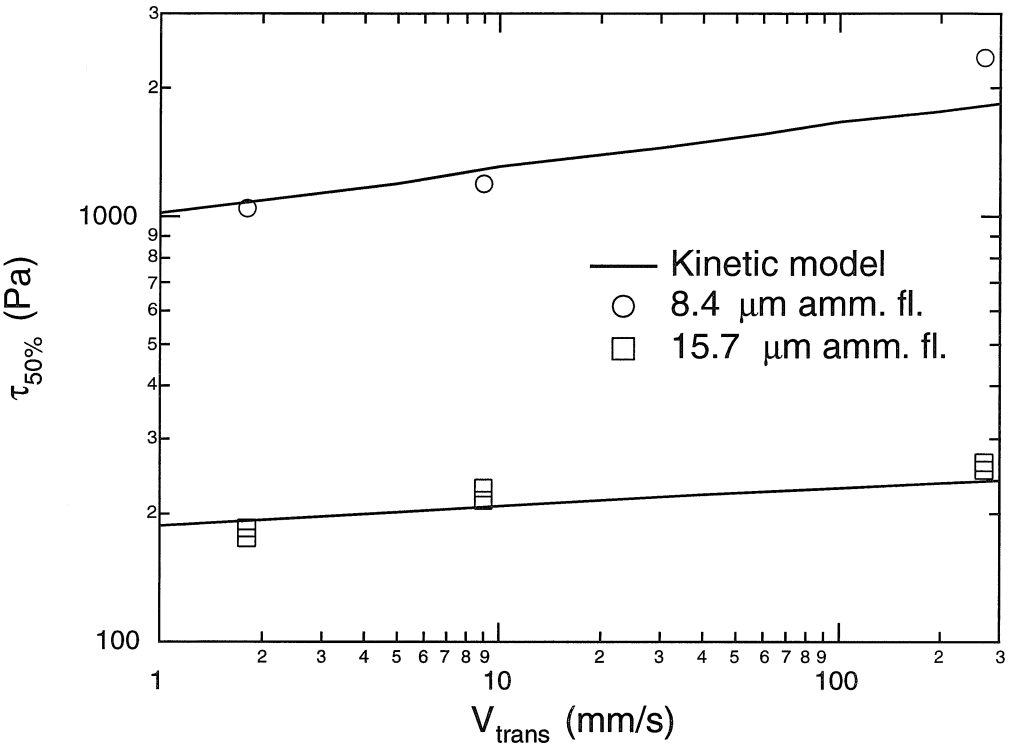

Figure 9.16: Observed and predicted effect of translation speed on threshold shear stress for ammonium fluorescein.

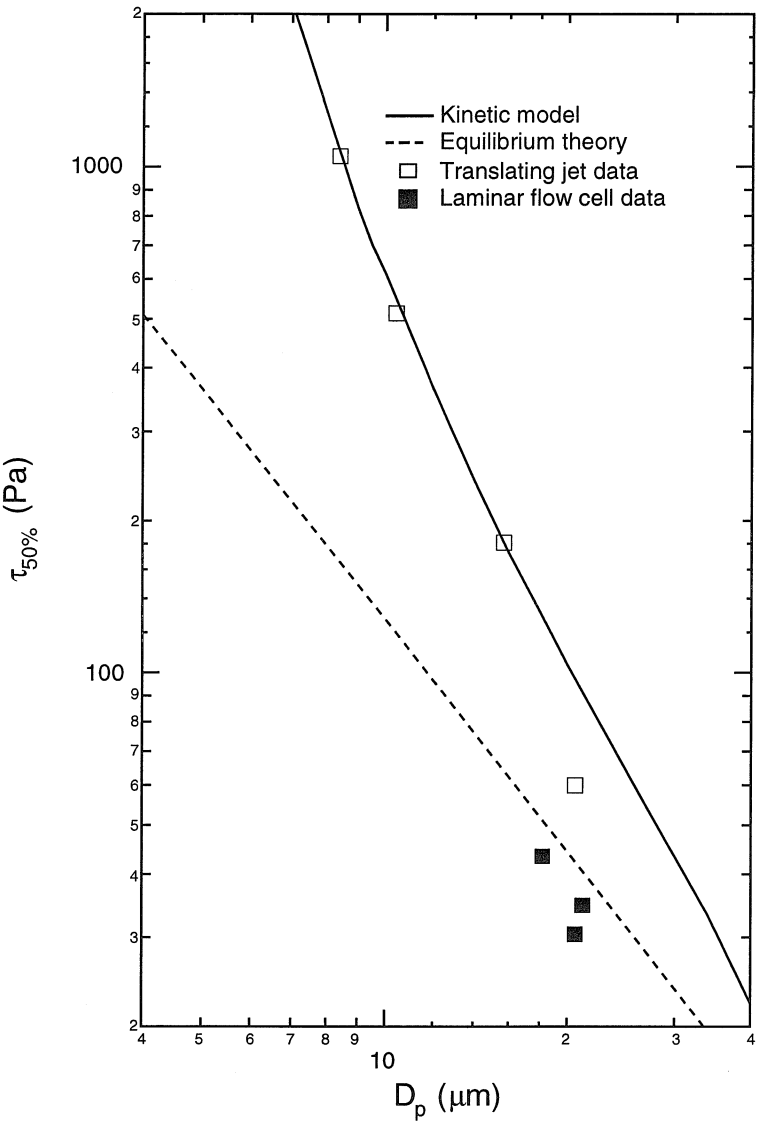

Figure 9.17: Observed and predicted effect of particle size on threshold shear stress for ammonium fluorescein.

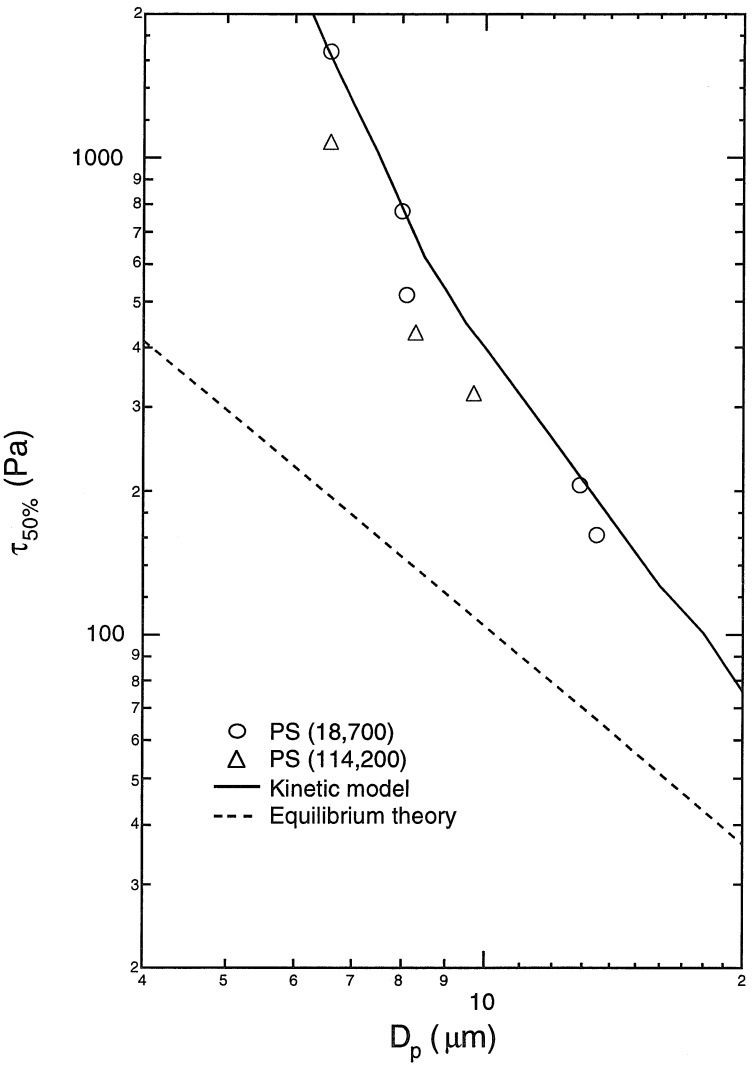

Figure 9.18: Observed and predicted effect of translation speed on threshold shear stress for polystyrene.

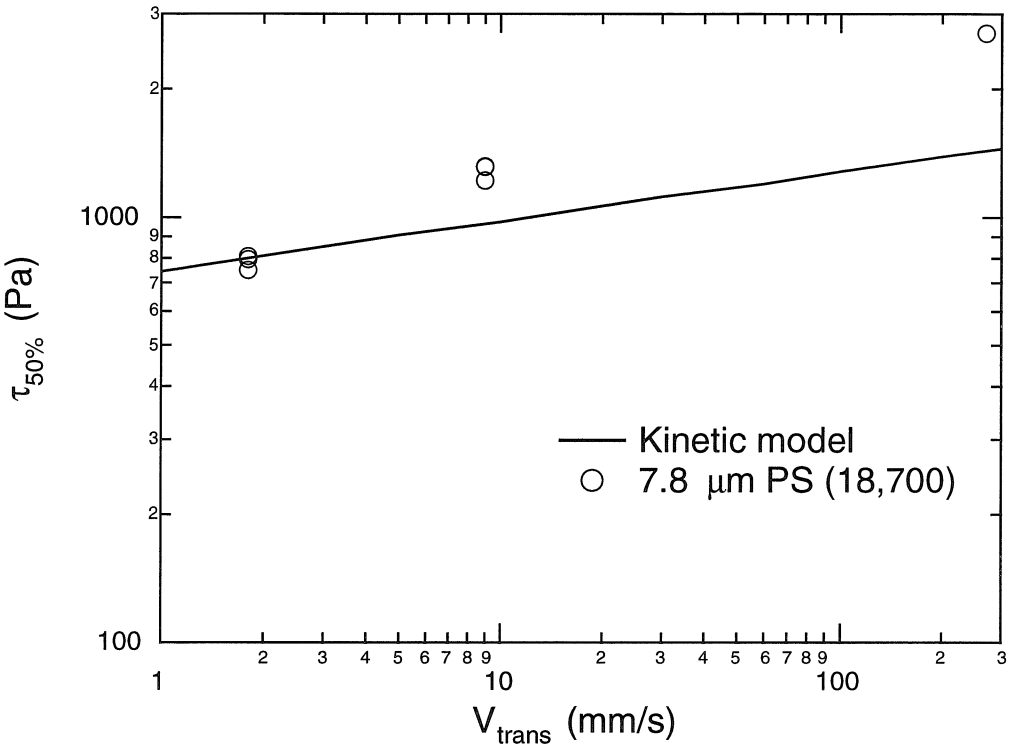

Figure 9.19: Observed and predicted effect of translation speed on threshold shear stress for polystyrene.

Chapter 10 Method for Characterization of Adhesion Properties of Trace Explosives in Fingerprints and Fingerprint Simulations

10.1 Abstract

The near inevitable transfer of explosive particulate matter through fingerprints makes it possible to detect concealed explosives through surface sampling. Repeatable and well-characterized fingerprint simulation facilitates quantitative comparison between particulate sampling methods for subsequent detection of trace explosive residues. This study employs a simple, but reproducible sampling system to determine the accuracy of a fingerprint simulation. The sampling system uses a gas jet to entrain particles from a substrate and the resulting airborne particles are then aspirated onto a Teflon filter. A calibrated Barringer IonScan 400 ion mobility spectrometer was used to determine the mass of explosive material collected on the filter. The IonScan 400 was calibrated with known masses of 2,4,6-trinitrotoluene (TNT). The resulting calibration curve is in good agreement with that obtained by Garofolo *et al.* (1994) [118] for an earlier model of the instrument. The collection efficiency of the sampling system was measured for three particle sizes (8.0, 10.0, and 13.0 μm) using spherical polystyrene particles laced with known quantities of TNT. Collection efficiency ranged from less than 1% for the larger particles to 5% for the smaller particles. Particle entrainment from the surface was monitored with dark field imaging of the remaining particles. The sampling system was then applied to two C4 test samples - a fingerprint transfer and a dry Teflon transfer. Over 100 ng of RDX was collected from the dry

transfer sample, while less than 1 ng was collected from the fingerprint transfer. Possible explanations for this large difference are presented based on the system calibration.

10.2 Introduction

Efforts to detect hidden explosives have taken two approaches: advanced imaging technologies that seek to detect the bulk material, and direct chemical identification of trace explosives on a person, package or luggage. A number of trace explosive detectors have been developed, and several are now in use for screening luggage and cargo at airports. Gas chromatography with chemiluminescent detection of the NO produced by pyrolysis of nitrate explosives, and ion mobility spectrometry are being used at many airports. Mass spectrometry systems for trace explosives detection during security screening are under development, as are a variety of other sensor technologies. All of these methods detect vapor-phase explosives.

Most modern explosives have very low vapor pressures at room temperature. Because of that low volatility, small particles of explosive materials that are inadvertently deposited on surfaces remain accessible for long times, but, although high sensitivities have been achieved with many of these instruments, direct detection by gas sampling alone remains extremely difficult. The effectiveness of trace explosives detection can be greatly enhanced by combining the analytical instrument with a sampling system that delivers the particles from the suspect surface directly to the analyzer. Sampling methods include air sampling or vacuuming a surface, blowing air jets onto a surface to dislodge particles or dust, fibers, or skin flakes to which the explosive may be bound, and wiping the surface. Once particles are collected they can be heated to enhance the vaporization of the trace explosives and the *system* sensitivity.

The efficiency of a system for physical sampling of trace particles on surfaces depends on the nature of the particles and the substrate, the forces that bind the particle to the surface, and the way that the extraction forces are applied to the

particles. The crystalline explosive is generally present in a soft, polymeric matrix, making small particles of the explosive quite sticky. They may be bound to a smooth solid surface, or on fibers or skin, both of which may readily release small fragments that may carry the explosive particles to the analyzer. The particle may be deposited directly on the substrate, or it may be bound to the surfaces with oils in fingerprints or other materials. Removal forces may be applied by an air flow or mechanically by wiping with a tissue, brush, or swab. Once a particle is detached from the surface, it may be transferred to the analytical system, either by sampling the air in which an airborne particle is entrained or by physical transfer of the wipe, or it may be lost or may deposit on surfaces that are not subject to direct analysis, possibly including the original surface.

To understand the efficacy of a sampling method, it must be challenged with samples with well-known properties. Ideally, such samples should reproduce the essential features of the trace explosives likely to be encountered in security applications. A major mode of transfer of particulate explosives is in fingerprints, so there has been considerable effort to develop a synthetic fingerprint. It has been noted that the nature of fingerprints produced after handling an explosive varies as successive fingerprints are made, but variations with applied force, humidity, and from one person to another remain substantial.

Fox *et al.* [119] developed a method for producing highly reproducible challenge samples of explosives of interest by applying known quantities of a suspension of the explosive to a substrate. The suspension is made by dispersing the explosive material into the suspension, so crystals of the explosive are incorporated with the size distribution likely to be encountered in real fingerprints produced after contact with the material. Our preliminary investigations of the adhesion of the particles deposited by the prescribed method to glass plates using the aerodynamic extraction procedure described below revealed that the particles were more tightly bound to the surface than particles in fingerprint samples. This enhanced binding may be caused by the film of polymer that is deposited along with the particles. Samples deposited on fibers produced a similar anomaly as the liquid soaked into the fibers [120]. To

develop a standard deposit on fibrous substrates, Chamberlain [120] developed a modified procedure wherein the suspension is first transferred to Teflon and allowed to dry. The dried deposit is then pressed onto the substrate to be tested, mechanically transferring the sample without the associated liquid.

These standard samples represent an important advance toward quantification of trace explosive sampling systems and procedures. The question remains, however, of how well these reproducible samples simulate fingerprints. In this chapter, a method is described that can be used to probe one important aspect of this question: What force, or more precisely, what shear stress is required to detach explosive particles from surfaces? A new technique that employs the well-characterized flow of a gas jet impinging normal to a surface [90, 112] to entrain particles from that surface has been adapted to measure the gas-phase shear stress required to detach particles from the surface. The previous experiments in which this system was used to entrain uniformly sized spherical particles have shown that the shear stress is a strong and well-defined function of the particle size. The particle entrainment apparatus has been augmented by the addition of a sampling system to collect the airborne particles. The particle extraction and collection efficiencies are separately measured using monosized, spherical, TNT-labeled polystyrene particles. The system is then used to examine the entrainment thresholds for particles in fingerprints and dry-transfer samples on glass slides. We begin with a brief discussion of particle adhesion and the approaches to measuring the forces involved.

10.3 Particle Adhesion

A quantitative description of the adhesion of a small particle to a surface must account for a complex combination of molecular interactions and mechanical stresses that deform both the particle and the surface to increase the area of contact. Even the simplest case of a spherical elastic particle at equilibrium with a flat, rigid surface has been the source of considerable controversy [102, 103, 104, 105, 106] that has only recently approached resolution. Debate about the magnitude of the force that

must be applied to detach the particle from the surface and the extent of deformation near the interface has delayed consideration of important complicating factors such as surface roughness. The classical theories of particle adhesion describe equilibrium between the particle and the substrate, and provide estimates of the force required to detach the particle infinitely slowly. The relevance of the equilibrium theories to detachment of viscoelastic particulate or substrate materials has received little attention. It is, therefore, not surprising that little is known about the adhesion of the ill-characterized and nonuniform particulate deposits in fingerprints.

Direct measurement of the adhesion force between a single particle and a substrate is now possible with scanning probe microscopy techniques, but the question of sampling of such particles from a substrate requires examination of how much material is extracted from an ensemble of particles with a range of particle sizes and shapes and, likely, of quantities of fingerprint oils and other materials that will influence the "stickiness" of the particles. To design and validate a standard sample for calibration and evaluation of security systems, one would like to simulate the mechanisms involved in sampling, but to do so quantitatively. The various sampling approaches can be divided into two classes based on the way the forces are applied to the particles: (*i*) mechanical forces applied by brushing or wiping; and (*ii*) aerodynamic shear forces produced by a gas flow along the surface. The former forces will involve a complex interaction between the particles, substrate, wipe material, applied pressure, and wipe velocity. The latter are more amenable to quantification and will be employed here.

The velocity of a gas flowing along a surface varies from a relatively high value far from the surface to zero at the surface due to viscous dissipation. A particle on a surface only senses the gas motion within the distance that the particle extends from the surface, i.e., for a spherical particle to a distance of one diameter from the surface. For the micron-sized particles of interest here, it is not the absolute velocity of the gas that determines the force applied to the particle, but rather the shear stress,

$$\tau = -\mu \frac{dU}{dz}, \tag{10.1}$$

where μ is the gas viscosity, and U and z are the gas velocity and distance from the surface, respectively. Similar applications of shear stress to particles should yield similar detachment behavior for those particles.

The shear stress delivered to a surface by a steady flow, and hence to particles on that surface, decreases with distance in the flow direction as the thickness of the boundary layer in which viscous dissipation occurs increases. Small particles on large objects are small compared to the boundary layer thickness. On this scale, the velocity increases linearly with distance from the surface (see Fig. 10.1). The shear stress experienced by particles on the surface is related to the rate of increase through Eq. (10.1). The steep velocity gradients (and thus high shear stresses) necessary to entrain small particles are most readily applied by keeping the thickness of the boundary layer small. Historically, the aerodynamic entrainment of dust particles from surfaces has been investigated using turbulent flows [1, 12, 14, 99, 100]. This approach is valuable, since, in most practical situations, dust entrainment occurs within turbulent boundary layers. The particles are generally confined to the viscous sublayer, a thin region near the surface in which viscous dissipation dominates. The mean shear rate within this sublayer is, however, thought to be too small to account for the observed entrainment [14]. The surface shear rate fluctuates dramatically due to the unsteady nature of the turbulent flow. Energetic turbulent bursts lead to brief high shear events that dominate entrainment in large-scale turbulent flows [1, 12, 14, 99, 100]. The random nature of these bursts makes it very difficult to quantify the entrainment process, so we seek an alternative approach that will more predictably yield the necessary high shear stress.

Smedley *et al.* [21] and Phares *et al.* [46] have recently demonstrated that micron-sized particles can be effectively entrained by an impinging gas jet and that, by careful design of the experiment to minimize start-up transients, the threshold for particle detachment can be determined quantitatively. Phares *et al.* [90, 112] have extended that work to quantify the shear stresses applied by the impinging gas jet. In the present work, we shall use extraction of particles from a surface by an impinging gas jet to infer relative adhesion forces.

The shear stress applied to a surface by a gas jet impinging normally to a surface is zero at the stagnation point (on the center line of the jet), rises to a maximum with increasing radius, and then falls as the boundary layer grows. This behavior is illustrated in Fig. 10.2 which depicts the radial distribution of the shear stress created by the normal impingement of a circular jet located a height, H, from the surface. Not only is the velocity gradient close to the surface sufficient to entrain small particles from the surface, but the shear stress can be unambiguously determined at each radial location.

Several conclusions were drawn from the experiments of Smedley *et al.* [21] and Phares *et al.* [46] that are relevant to the sampling of explosive residues from surfaces. First, the shear stress required to induce particle entrainment was found to have at least an inverse cube dependence on particle size. This sensitivity to size is much stronger than predicted by equilibium adhesion theory. Polystyrene spheres smaller than 4 μm in diameter were left untouched by the impinging jet, whereas particles over 12 μm were completely removed from the surface with much smaller jet pressures. Second, they observed that particle detachment is time dependent. The kinetics of particle detachment was found to closely resemble the kinetics of crack propagation through a solid [46], with detachment occurring more rapidly as the imposed force is increased. A consequence of the detachment kinetics is that a larger impulsive force, such as that imposed by an impinging shock wave [121] or an impacting particle (see Chapter 3), is required to detach a particle than would be needed under steady application of the force. Moreover, viscous dissipation at the contact interface during separation slows the detachment of viscoelastic materials, increasing the sensitivity to particle size over that of purely elastic materials.

10.4 Experimental

10.4.1 Translating Gas Jet Apparatus

The impinging jet apparatus used to study particle sampling in this study is shown in Fig. 10.3. The system consists of a computer controlled high speed rail table, a vacuum chuck sample holder designed to secure a 25 x 75 mm rectangular substrate, a circular jet nozzle mounted on a rotation stage, and a glass suction tube. The jet nozzle and suction tube are located within a sampling region that is shielded from the laboratory with lucite barriers. The jet pressure is adjusted using a regulator and measured with a Lucas P4100 pressure transducer. Suction is drawn through a glass tube (1.9 cm inside diameter) by a diaphragm pump at a constant flow rate of 40 L/min. A Teflon filter, designed for analysis by the IonScan 400 ion mobility spectrometer, is at the end of the tube 13.5 cm from the suction tube inlet and sealed on both sides with o-rings. The suction tube inlet is flattened into a half circle so that the tube inlet could be lowered close to the jet stagnation zone where particle entrainment occurs. A HeNe laser sheet provides glancing angle illumination of the particles on the substrate, allowing dark field images to be recorded using a CCD camera equipped with a telephoto lens and connected to a Macintosh computer using a Scion LG3 frame grabber card.

10.4.2 Composite Calibration Particle Generation

Monosized spheres made of a polystyrene and TNT mixture were produced in a vibrating orifice aerosol generator (VOAG), specially designed to work with organic solvents [45]. A solution of toluene and equal mass amounts of polystyrene and TNT is forced through a small circular orifice, 50 μm in diameter, resulting in fine liquid jet. Breakup of the jet into monosized droplets is induced by sinusoidal vibrations produced by a piezoelectric crystal and transferred acoustically to the orifice through the solution reservoir behind the orifice. The droplets are aerodynamically dispersed and carried in a dry nitrogen sheath flow through a warm drying column, where

the droplets dry into smooth, solid spheres of equal size as illustrated in Fig. 10.4. Attempts to make pure TNT particles from a solution of toluene and TNT resulted in rough and non-spherical particles; so polystyrene was added to the solution to maintain particle sphericity. The final particle size is adjusted by varying the liquid flow rate through the orifice, the solution concentration, and the excitation frequency. The dry spheres are uniformly deposited on cleaned substrates at the bottom of the drying column and subsequently stored in a dry, organic-free environment until use. Three particle sizes were fabricated for this study: 8.0, 10.0, and 13.0 μm. The total mass of TNT in the 8.0, 10.0, and 13.0 μm composite particles was estimated to be 0.17, 0.30, and 0.70 ng, respectively.

The substrates used were 25 x 75 mm glass microscope slides. Prior to deposition, the glass slides were thoroughly cleaned with phosphate-free detergent and rinsed with distilled, deionized water. Uniform particle deposits with surface densities of approximately 25 particles/mm^2 were used for the experiments.

10.4.3 Ion Mobility Spectrometer

Chemical detection of the entrained particles was performed by ion mobility spectrometry (IMS). In this technique, atmospheric pressure chemical ionization produces ions from vapor phase analyte molecules. The ions are introduced into a drift tube in a brief pulse. The current detected at a Faraday plate at the end of the drift tube yields the spectrum of ion mobilites.

The IMS used in this study is a Barringer IonScan 400 which has been designed for detection of trace quantities of explosives or contraband in security applications. To quantify the measurements, several modifications to the instrument were required. In normal IonScan 400 operation, mobility analysis is triggered by movement of the filter holder assembly, which is located on a manual translation stage, into the instrument housing. Once the filter is in place inside the instrument, the filter is sealed, the desorber heater turned on, and the drift tube entrance gate pulsed at a frequency of 42 times a second for 20 seconds. The currents measured within predetermined

intervals associated with a peak of interest are added to provide an estimate of the peak area. Thus mobility spectra are being acquired as soon as the desorber heater is turned on. Since all ion detection in the drift tube contributes to the total mass measurement of the initial sample, even the initial spectra acquired while the desorber heater is still heating up are valuable.

In the present study, the movement of the filter assembly was used to trigger the collection of all 840 spectra during the full 20 seconds of analysis time. Spectra were digitized and stored in a Macintosh computer that was interfaced to the IonScan using a Data Translation Lab NB data acquisition card. To improve the time resolution and peak area determination, the currents from the Faraday plate detector were recorded using an analog-to-digital conversion card on an external Macintosh computer. The peaks were identified and the peak areas above the instrument baseline were measured using the recorded mobility spectra.

10.4.4 Procedure

A clean Teflon filter was analyzed in the IMS, and the explosive peak location was monitored. The cumulative peak area obtained for the clean filter provided the baseline reading for that filter. The filter was then clamped to the end the suction tube, and a test substrate was placed flush with the surface of the translation stage and secured using the vacuum chuck. The stage was moved underneath the CCD camera. A set of images, arranged to cover the entire sampling area, was obtained both before and after the sampling experiment. The size of the sampling area depended on the test sample used. For the uniform particle deposits generated with the VOAG, a set of three images, spanning 58 mm of the substrate length and 15 mm of the substrate width, was necessary to observe the full extent of entrainment. The remaining 23 mm of the substrate length was not exposed to the jet due to size limitations of the rail table. For the fingerprint and dry transfer C4 deposits, only one image was needed to view the entire deposit which was located near the center of the substrate. Each recorded image contained 640 x 480 pixels with 256 levels of grey and was integrated

on the CCD chip for a total of 12 frames (0.4 s) to enhance the signal-to-noise ratio. Although the level of magnification (32 μm/pixel) in these images is not sufficient to resolve individual particles, the average pixel intensity of an imaged region is proportional to the particle density within the region.

Once the initial images were recorded, the air jet with a pressure ratio P_{jet}/P_{atm} was started, the suction through the filter was turned on at a flow rate of 40 L/min, and the jet was translated at a constant velocity of 1.8 mm/s under the air jet. Once the sampling region had moved past the air jet, the suction was turned off, and the substrate was returned to the camera location to record the remaining particles on the substrate. Figure 10.5 displays two close up views of the same area within the sampling region before and after a sampling experiment of 10.0 μm composite particles. The image analysis necessary to determine the number of removed particles is presented in Section 10.4.5.

Immediately after a sampling experiment, the Teflon filter was removed from the suction tube assembly and placed in the IMS for explosive mass determination. The peak locations for the two types of explosives, TNT and C4, used in this study were determined before the sampling experiments from direct filter deposits of the explosives. This allowed peak area measurements to be performed during analysis of the filter. Nevertheless, all of the obtained mobility spectra were stored in the computer during each filter analysis. In each case, all of the explosive material vaporized from the filter after the first analysis run, and any further analysis yielded baseline level peak areas. Figure 10.6 displays mobility spectra obtained before and after a sampling experiment on composite particles. Collection of composite particulate material by the Teflon filter is evidenced by the presence of a peak between 12 and 13 ms, corresponding to the mobility of the TNT anions formed in the reaction region of the instrument. Extracting mass information from the spectra requires the calibration presented in Section 10.5.

After each sampling experiment the suction tube was wiped with acetone prior to insertion of a new filter. The translation stage was also wiped with acetone whenever the test sample was changed. A total of 8 test samples were analyzed, including

one 8.0 μm, two 10.0 μm, and three 13.0 μm composite particle samples, one C4 fingerprint, and one C4 Teflon transfer sample.

The jet diameter was 5 mm, and the jet height, H, measured along the centerline of the jet from the jet exit to the sample surface was held constant at 10 jet diameters. Several jet pressure ratios, P_{jet}/P_{atm}, and jet incidence angles, θ, were used in the experiments. Table 10.1 summarizes the experimental parameters used for each sample.

In order to maximize the number of sampling experiments given the number of test samples, most of the samples were used for multiple sampling experiments. Since samples would be exposed to the jet more than once, multiple experiments were run such that the jet pressure ratio was increased for successive experiments, causing additional particle removal. Calculation of removal efficiency (see Section 10.4.5) incorporated the number of particles that were already removed in previous runs. Redeposition of particles on the test substrate was observed to be infrequent, and was ignored in the analysis.

10.4.5 Image Analysis

For each sampling experiment, one initial and one final set of images were recorded for further analysis. A comparison between the two image sets provides information about the number of particles that were entrained during the experiment. The initial images of the polystyrene/TNT composite particles contained a nearly uniform distribution of monodisperse particles. During a sampling experiment, particles that pass within a distance of $.09H$ from the jet stagnation point experience the maximum shear stress imposed by the gas jet [21]; and a percentage of these are subsequently removed from the substrate. This causes a decrease in the pixel intensity mainly concentrated in a path of width $.09H$. Since particle removal is constant along the translation axis of the substrate, the pixel intensity, I, was averaged for each row of pixels spanning the entire length of the sampling region, yielding one initial and one final average pixel intensity profile. In order to calculate the removal efficiency, the

average pixel intensity measured for a clean particle-free glass slide was taken to be the clean pixel intensity, I_0, corresponding to 100% removal. The removal efficiency, η, corresponding to a row of pixels is calculated from the initial and final average pixel intensities from the equation

$$\eta = \frac{I_{final} - I_{initial}}{I_0 - I_{initial}}, \tag{10.2}$$

where a black pixel has a value of 255 and a white pixel has a value of 0. The same value of the clean pixel intensity, I_0, was used for each sample, as repeated measurements for clean slides yielded variations in pixel intensity of less than 1%. The removal efficiency profile after a single sampling experiment on Sample 2 (13 μm particles, 90° jet incidence, $P_{jet}/P_{atm} = 1.49$) is plotted in Fig. 10.7 against the closest radial distance, r, from the jet stagnation point. The vertical lines denote the boundaries within which particles are exposed to the maximum shear stress imposed by the jet. Note that almost all particle removal occurs in this region. In this particular case, about 30% of the particles present in the high shear stress region before the experiment were removed.

Conversion of removal efficiency to the total number of entrained particles requires a measure of the total number of particles present within the imaged region. Initial particle densities were measured optically to be close to 25 particles/mm^2 and the size of the imaged area is 870 mm^2, yielding 21,750 particles initially in the imaged area. The average removal efficiency, η_{ave}, is calculated from the efficiency profiles (see Fig. 10.7) and the total number, N_e, of entrained particles is thus given by $N_e = 21,750\eta_{ave}$.

Due to the wide range of particle sizes and roughness present in the C4 deposits, particle removal is randomly distributed throughout the deposit. Average pixel intensity is no longer proportional to particle surface densities, since the deposited particles do not scatter light uniformly as do monosized spheres. Therefore, quantitative information about particle removal is not attainable from the raw images; only chemical analysis provides quantitative measurements of removal. However,

qualitative differences between the two types of deposits may be derived from the images and will be discussed later.

10.5 IonScan 400 Calibration

The IMS was calibrated for quantitative mass determination with known mass amounts of TNT by the method described by Garofolo *et al.* [118], with some slight modifications. TNT (obtained from Chem Service, West Chester, PA) containing a minimum of 30% water by weight (quoted 99% pure by the manufacturer) was dehydrated by recrystallization in acetone. HPLC/GC-grade acetonitrile was used to dissolve the TNT in preparing stock solutions. A stock solution with a concentration of 200 ng/μL was prepared, from which subsequent dilutions were used to yield concentrations of 100, 66.7, 33.3, 16.7, 8.33, 4.17, 2.08, 1.04, and 0.52 ng/μL. Further dilution of the 0.52 ng/μL solution as a stock solution yielded concentrations of 0.26, 0.13, and 0.013 ng/μL. These last three solutions are below the range investigated for the previous calibration [118]. All of the solutions were made using two Eppendorf 2000 tip ejector pipettes; one was reported to have an accuracy of 1.6% of full scale with a range of 100 to 1000 μL, and the other was reported to have an accuracy of 2.5% of full scale with a range of 10 to 100 μL.

Care was taken to ensure that the same IMS operating parameters were used as in the previous study [118], including the shutter grid pulse width, scan period, delay time, and drift tube temperature. The IMS was placed in *bake-out* mode for 8 hours, prior to the calibration runs to ensure the absence of any contaminants. A standard solution of 1 μL was placed on a clean Teflon filter and allowed to dry for 20 to 30 seconds before analysis. Typically, 5 to 10 analysis runs were performed for the same concentration, with approximately 1 minute between runs to allow the filter to cool to minimize sample vaporization prior to analysis. During a 20 second analysis run, 840 mobility spectra were acquired and sent to a computer through a data acquisition board for analysis of the TNT peak, which was found to lie between 12.34 and 13.06 ms. The peak amplitude, which is given in digital units (1 du = 2.44 mV) by the IMS,

was monitored and the cumulative peak area between these limits was determined for all 840 spectra. A clean filter was also analyzed and the cumulative peak area between the same limits was determined and taken to be the baseline value. The baseline was subtracted from cumulative peak areas obtained for all of the analysis runs. The corrected cumulative peak areas and corresponding TNT mass quantities are provided in Table 10.2.

Figure 10.8 displays the results of the present calibration compared with the results from the previous study [118], where the x-error bars in the present measurements represent the standard deviation determined from repeatability for each solution, and the y-error bars were calculated from uncertainties in the solution concentrations. Results from the previous study were reported as average peak areas and were converted to cumulative peak areas for comparison here. Even though the two studies used different models of the IonScan, there is good agreement in the response of the IMS to sample mass between the two studies. One particularly noteworthy feature is that both calibrations exhibit a cusp in the IonScan response at around 5 ng of TNT. This is probably an artifact caused by a gain change within the instrument. Two separate exponential fits, also displayed in Fig. 10.8, were made to describe both sides of the cusp.

The calibration in Fig. 10.8 allows a calculation of the mass of TNT present on the filter. Determining the number of collected particles from this mass requires knowledge of the mass of TNT in each composite particle. Since baseline levels were achieved after one analysis run of the composite particles, it was assumed that all of the TNT present in the composite particles was desorbed during analysis. The results presented in Section 10.6.1 are based on the assumption that exactly half of the particle mass is TNT (see Section 10.4.2). Although further chemical analysis of the composite particles is required to confirm this assumption, the results obtained provide a measure of the collection efficiency, and are therefore sufficient to demonstrate the effect of parametric variation on collection efficiency.

10.6 Results

10.6.1 Composite Particles

One disadvantage to performing resuspension and collection experiments with a deposit of monosized particles is that, since there is a strong size dependence on adhesive as well as aerodynamic forces experienced by a particle, removal and collection efficiencies will be either very high or very low. The particle sizes considered in these experiments exhibit very low removal and collection efficiencies, as calculated from image analysis and ion mobility analysis. However, the results obtained for the monosized composite particles, which are summarized in Table 10.3, exhibit variation with particle size in both removal and collection efficiency.

The effect of particle size on removal efficiency is displayed in Fig. 10.9. The plot clearly shows that aerodynamic entrainment of smaller particles becomes increasingly difficult, as previous investigations [16, 46] have shown. This result is expected, since smaller particles reside deeper within the viscous sublayer of the boundary layer where fluid velocities are small, and the drag experienced by a particle decreases with its surface area. A hyperbolic tangent is fit to the data in Fig. 10.9 to emphasize that removal efficiency would increase dramatically for particle sizes larger than 13.0 μm.

In contrast, the collection efficiency increases with decreasing particle size due to inertial effects as shown in Fig. 10. Small particles follow the changes of direction of the gas flow more readily than do larger ones. Even though the sampling flow rate (40 L/min) is much greater than the maximum jet flow rate ($\sim$ 1 L/min), inertia limits the entrainment of the larger particles into the sample flow. Larger particles are, therefore, more likely to collide with the suction tube walls or to escape collection entirely.

Figure 10.11 displays the effect of jet impingement angle on collection efficiency. An important feature of this plot is the low collection efficiency observed for $\theta = 30°$. The length of the region from which particles are entrained doubles as the incidence angle is decreased from $\theta = 90°$ to $\theta = 30°$, so it should be possible to collect more material at low incidence angles, but the system will have to be optimized to take

advantage of the increased entrainment. Since maximum collection efficiency in the present experiments was observed at $\theta = 60°$, this impingement angle was used for subsequent experiments on the C4 deposits.

10.6.2 C4 Deposits

Figures 10.12 and 10.13 display the raw images of the dry Teflon transfer and the fingerprint transfer, respectively. Significant differences are apparent in the size and concentration of the particles present on each substrate. The dry transfer deposit appears to contain smaller numbers of particles than does the fingerprint, but the particles appear to be smaller in the latter deposit. The results of the sampling experiments on the C4 deposits are summarized in Table 10.4. For both applied jet pressures, the cumulative peak area obtained from the sampling of the dry transfer deposit is one order of magnitude greater than that obtained from the fingerprint deposit. Although the IMS calibration obtained in Section 10.5 is not expected to hold exactly for C4 due to the difference in molecular weight between TNT and the RDX present in C4, the calibration curve is applied to estimate the relative masses of C4 obtained from both deposits. These results indicate that two to three orders of magnitude more C4 was collected from the dry transfer deposit. Removal images of the dry transfer and fingerprint deposits are displayed in Figs. 10.14 and 10.15, respectively, as differences between the final and initial images. Black spots are particles that were removed, while white spots indicate particles that were deposited during sampling, likely redeposition of that had been entrained elsewhere on the sample. In light of the removal efficiencies exhibited by the composite particles, it is not surprising that many of the larger particles from both deposits were entrained.

Even though the fingerprint appeared to contain more particles than were present in the dry transfer deposit, more particulate mass was entrained from the latter sample. Since both deposits were exposed to the same aerodynamic shear stress, this result suggests that the particles in the fingerprint adhere to the substrate more strongly than do those in the dry transfer deposit. This is not surprising since capillary

forces due to the oils in the fingerprint can significantly increase particle adhesion. It should be noted, however, that although the present results demonstrate the ability to compare particle adhesion in terms of the shear stress required for entrainment of particles from different samples, no quantitative conclusions about the adhesion forces in the two deposit types are possible from just two samples.

10.7 Concluding Remarks

The present work has demonstrated a system that is capable of subjecting particulate deposits to known aerodynamic shear stresses to study the forces binding micron sized particles of explosives to surfaces. Systematic trends in both the particle removal efficiency and the sample collection efficiency with particle size have been observed for samples consisting of uniformly sized, TNT-laced polystryrene particles. Particle entrainment under the action of steady or long duration shear increases with increasing particle size, as expected given the increase of the applied aerodynamic forces relative to particle adhesion with particle size. In contrast, the aerodynamic sampling decreases in efficiency with increasing particle size as particle inertia impairs the ability of the particle to follow the gas motion into and through the sampling system.

Two different samples of C4 were also examined: a C4-laden fingerprint, and a sample produced by a new dry transfer technique, both on clean glass slides. Although more particles were present on the former sample, more were entrained from the latter. Quantitative evaluation of the shear stress required for particle entrainment will require analysis of additional samples in combination with data on the absolute quantities of the explosive in each of the samples. Nonetheless, the two order of magnitude differences between two masses entrained from the two samples demonstrates the feasibility of using aerodynamic entrainment to probe the properties of standard samples. Coupled with direct microscopy-based measurements of the sizes of the particles involved, aerodynamic entrainment could also provide estimates of the actual adhesion forces involved.

The present results also illustrate the possibility of using aerodynamic forces to sample particles from surfaces directly. A small impinging jet imparts much greater shear stresses to a surface than can be achieved with larger air flows that would probe the entire surface of an object that is being screened. The range of particle sizes that is amenable to aerodynamic sampling is limited, however. Previous work has shown that use of transient flows can extend the range of aerodynamic sampling to smaller particle sizes.

Although the present results indicate that the approach of aerodynamic extraction and sampling has merit, there remains considerable room for improvement at larger particle sizes where inertial effects limit the collection efficiency. The sampling system has not been optimized to improve the efficiency of collection of the extracted particles. The observation of low collection efficiency at low jet impingement angles where entrainment is the most efficient clearly indicates that the optimal design of the sampling system is directly related to the approach taken to particle entrainment. The sampling system must be designed to minimize inertial impaction or gravitational deposition of the largest particles to be sampled. An alternate approach would be to ensure that any surfaces on which particles might deposit are hot enough to ensure evaporation so that the material of interest can be delivered to the analyzer.

The present studies were performed using one of the instruments that has been approved by the FAA for security screening in airports. The Barringer IonScan is designed to analyze discrete samples for periods up to 20 s. The detection limit of the instrument is sufficiently low that a small number of micron-sized particles can be detected. A more flexible instrument that allows continuous monitoring of sampled gases could be interfaced to a continuous sampling system to provide a real-time analytical capability.

Table 10.1: Experimental parameters for test samples.

Sample	Deposit	θ (degrees)	P_{jet}/P_{atm}
1	13.0 μm composite	90	1.49, 1.84
2	13.0 μm composite	90	1.49, 1.84
3	10.0 μm composite	90	1.49, 1.84
4	8.0 μm composite	90	3.80
5	10.0 μm composite	30	1.49, 1.84, 3.80
6	13.0 μm composite	30, 60	1.49, 1.84, 3.80
7	C4 fingerprint	60	1.84, 3.80
8	C4 dry transfer	60	1.84, 3.80

Table 10.2: Calibration results for IonScan 400.

TNT mass (ng)	Cumulative Peak Area (du-ms)
0.013	7661
0.13	10130
0.26	10436
0.52	27496
1.04	28342
2.08	44292
4.17	93894
8.33	100834
16.7	112890
33.3	132454
66.7	151532
100	174128
200	196006

Table 10.3: Experimental results for removal and collection of composite particle test samples.

Experiment	Sample	Particle size (μm)	θ (degrees)	P_{jet}/P_{atm}	Number Entrained	Number Collected	Collection Efficiency (%)
1	1	13.0	90	1.49	1108	3	.28
2			90	1.84	640	2	.32
3	2	13.0	90	1.49	817	2	.36
4			90	1.84	1178	3	.36
5	3	10.0	90	1.49	704	4	.56
6			90	1.84	163	2	1.3
7	4	8.0	90	3.80	80	4	5.0
8	5	10.0	30	1.49	134	0	0
9			30	1.84	699	0	0
10			30	3.80	1189	1	.08
11	6	13.0	30	1.49	786	1	.12
12			30	1.84	258	0	0
13			60	1.84	147	2	1.4

Table 10.4: Experimental results for removal and collection of C4 deposit test samples.

Sample	Type	P_{jet}/P_{atm}	Cumulative Peak Area (du-ms)	Estimated RDX Mass (ng)
7	Dry transfer deposit	1.84	1.31×10^5	34
		3.80	1.78×10^5	105
8	Fingerprint deposit	1.84	2.00×10^4	0.4
		3.80	1.30×10^4	0.3

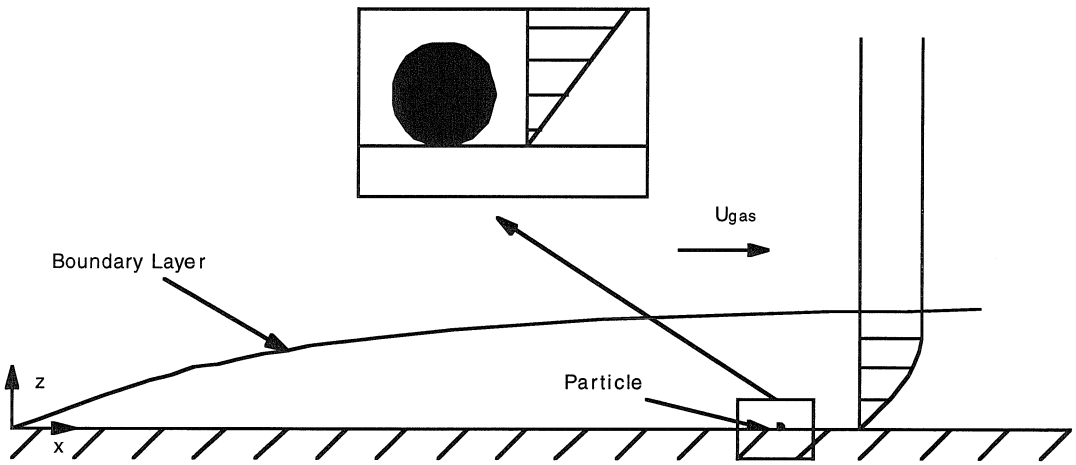

Figure 10.1: Particle within a boundary layer produced by a uniform flow over a flat surface.

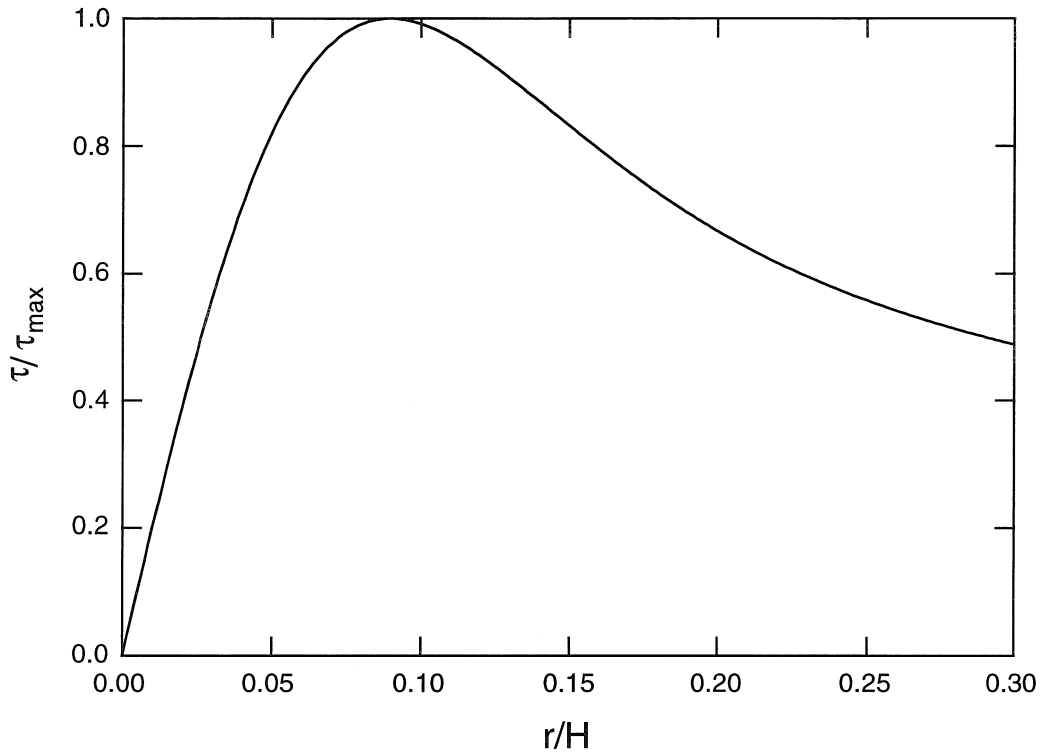

Figure 10.2: Relative shear stress distribution caused by the impingement of a circular jet onto a flat surface.

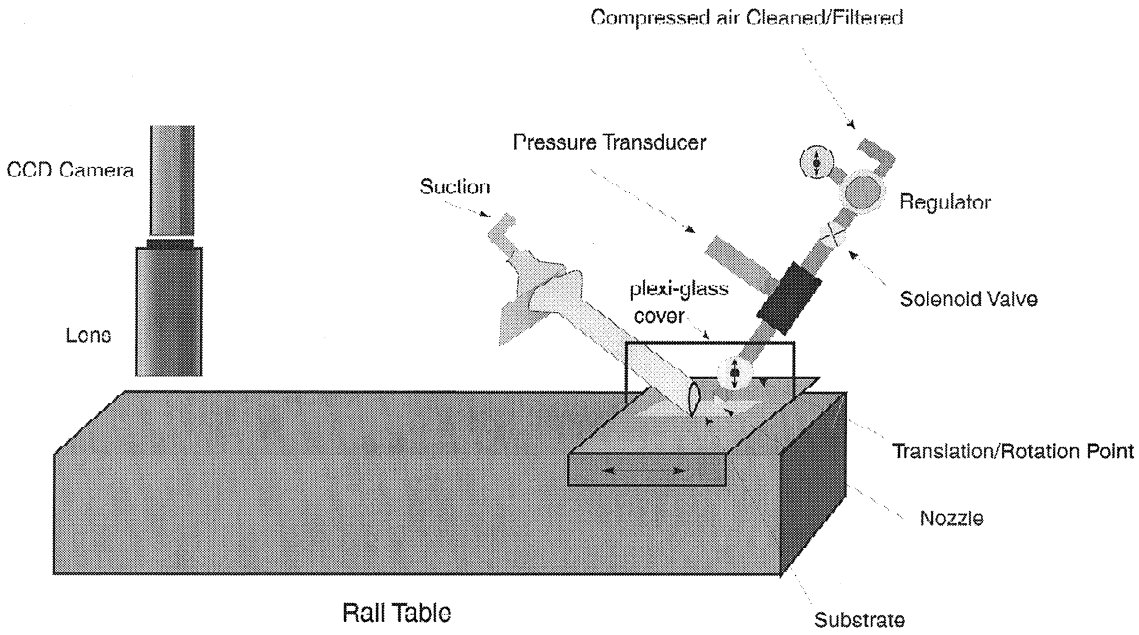

Figure 10.3: Translating gas jet apparatus.

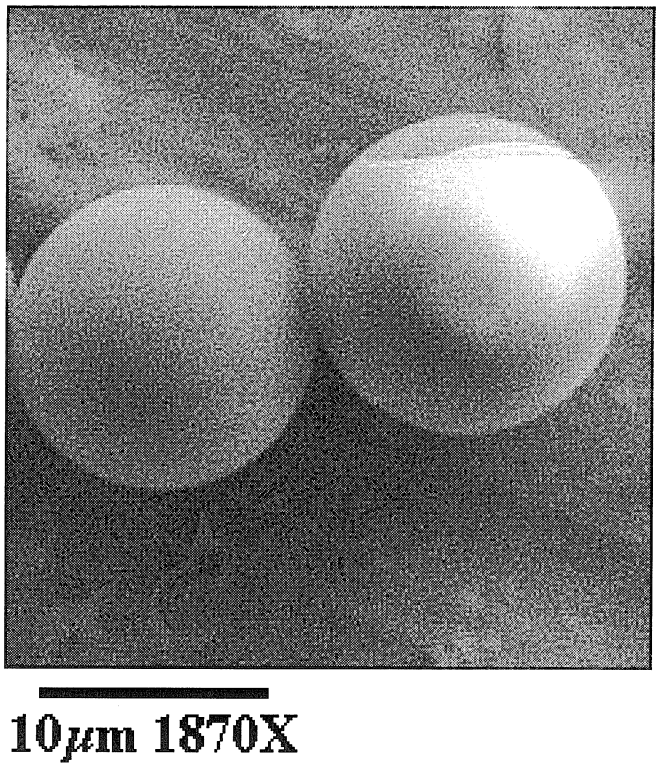

Figure 10.4: Scanning electron microscope image of composite polystyrene/TNT particles at 1870x magnification.

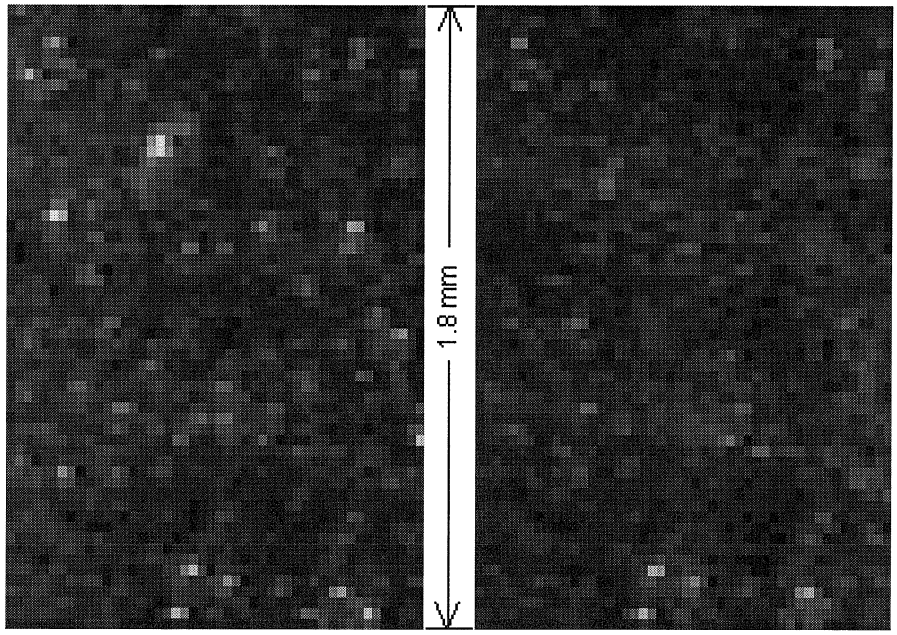

Figure 10.5: Raw images before and after sampling experiment that show removal of 10 μm composite particles.

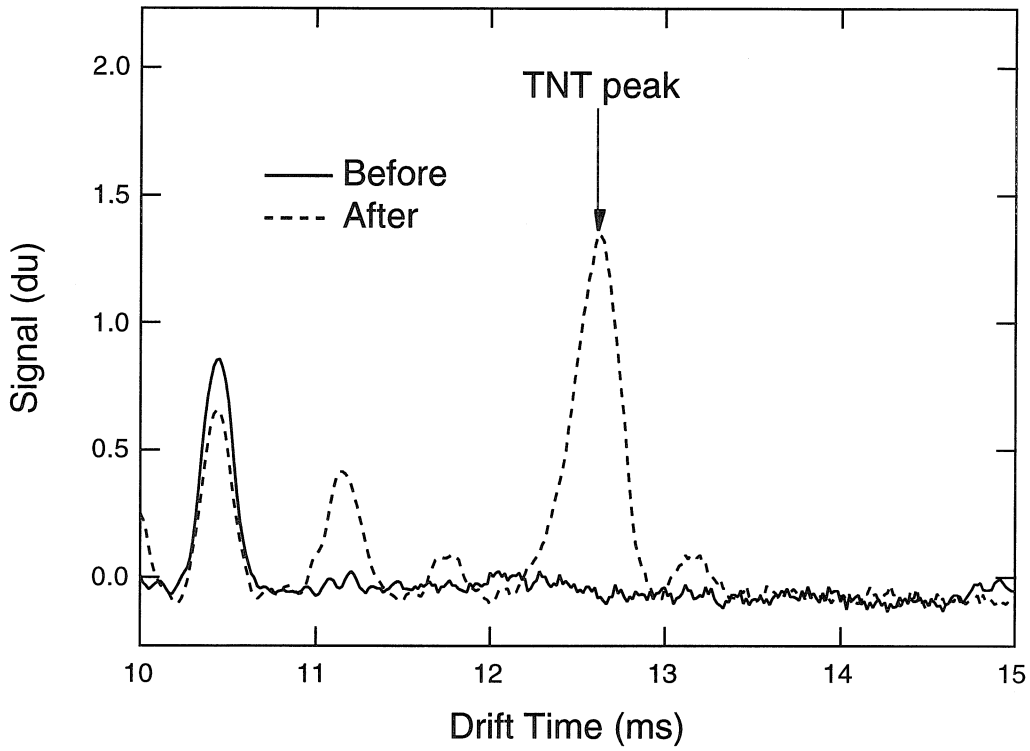

Figure 10.6: Sample mobility spectra obtained from analysis on filter before and after a TNT sampling experiment (1 du = 2.44 mV).

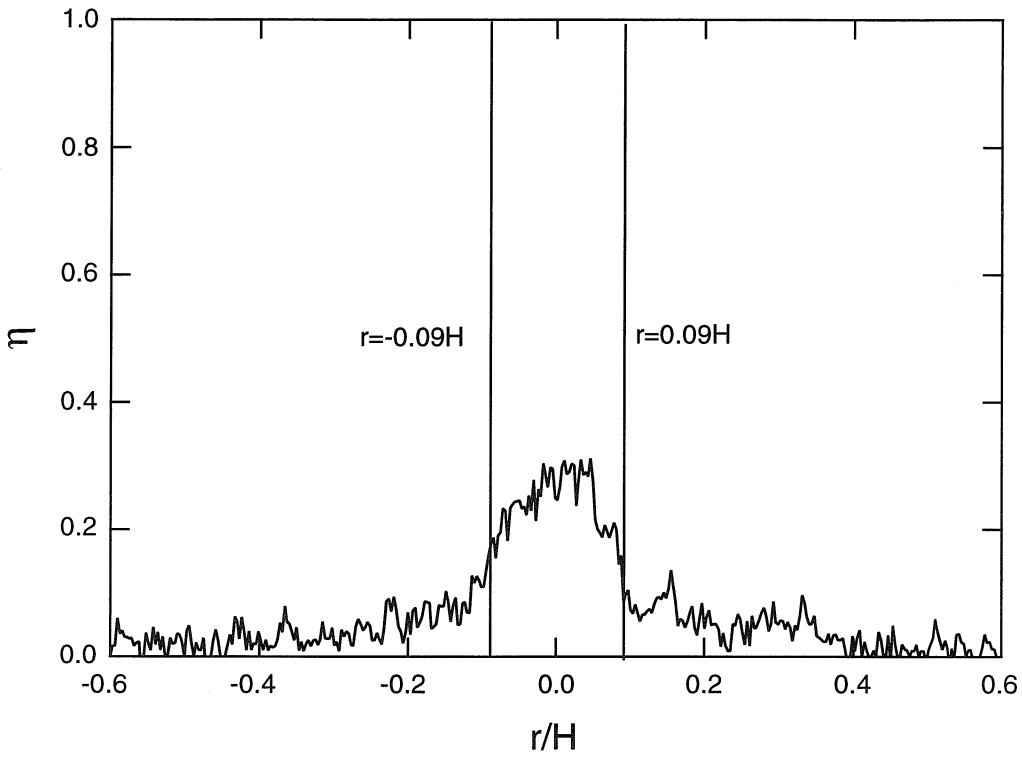

Figure 10.7: Removal efficiency profile from sampling experiment on Sample 2. The vertical lines represent the maximum shear stress boundaries.

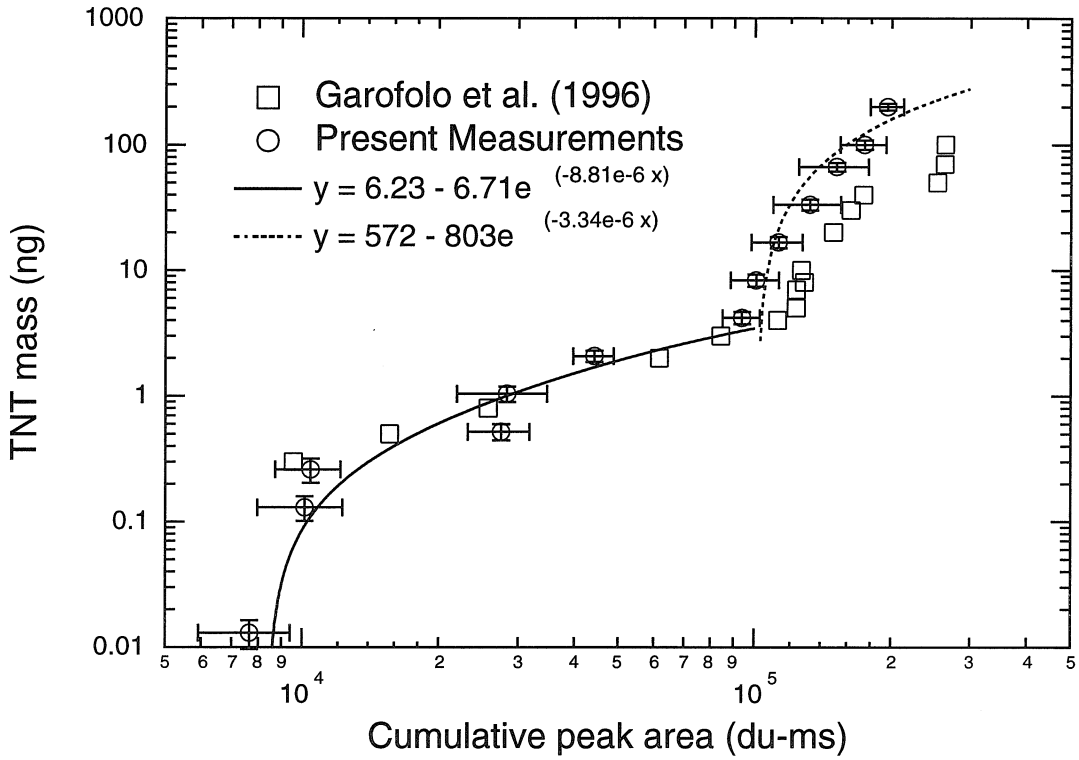

Figure 10.8: TNT mass calibration for two IonScan models.

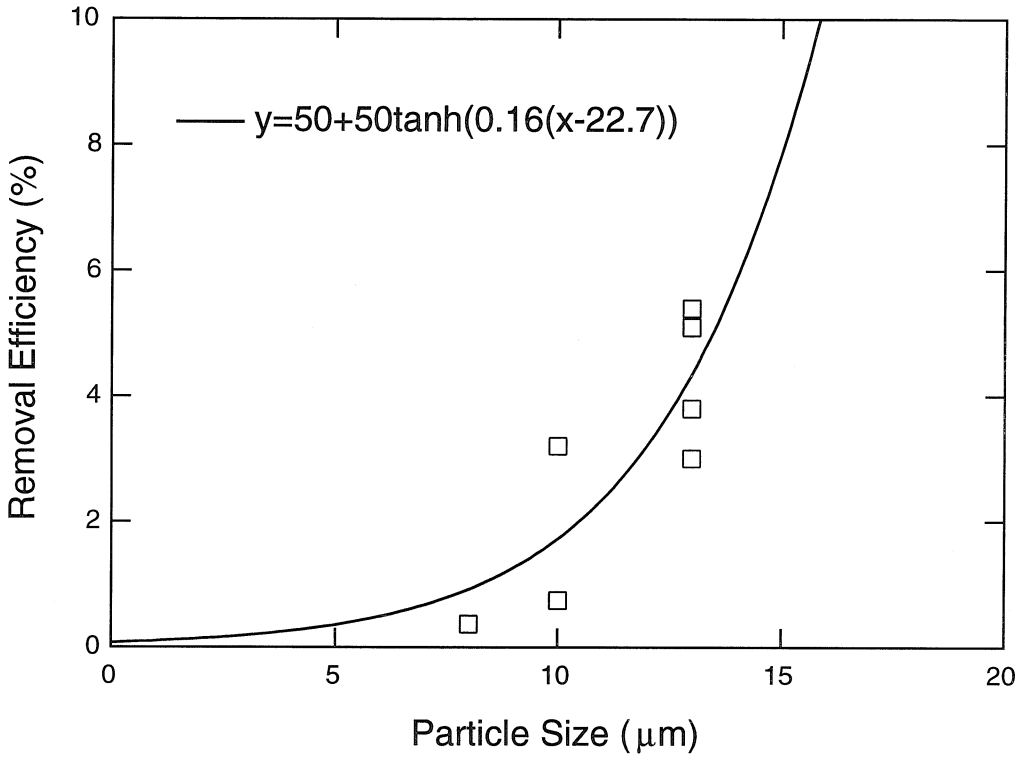

Figure 10.9: Effect of particle size on removal efficiency of composite particles for $\theta = 90°$.

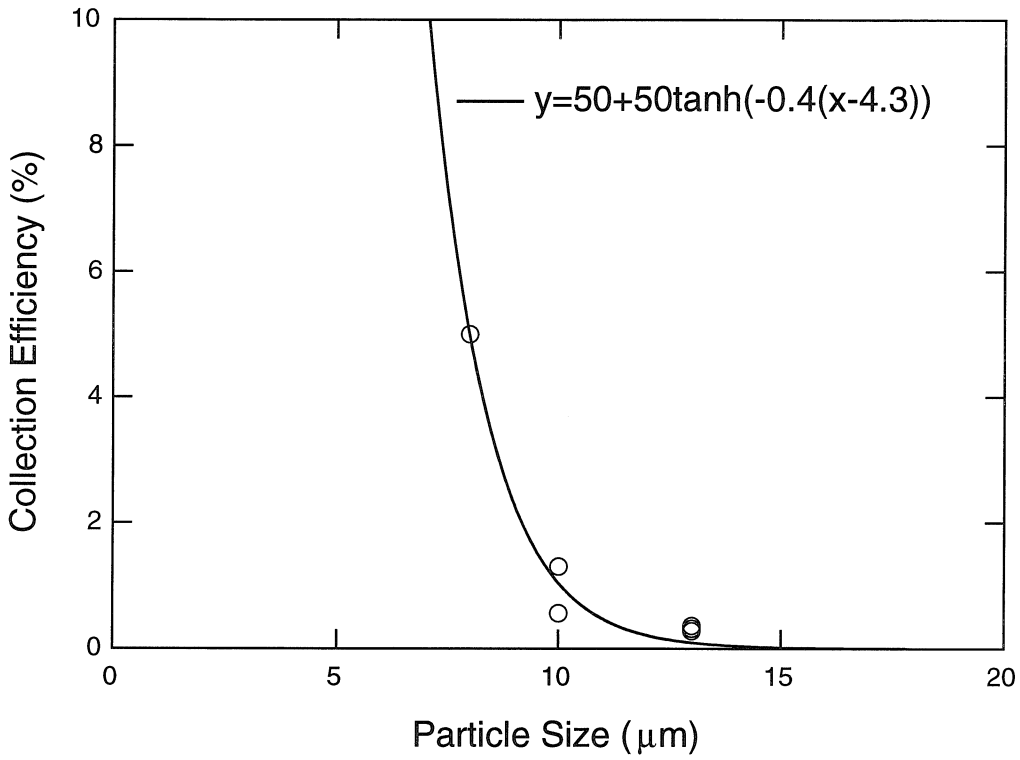

Figure 10.10: Effect of particle size on collection efficiency of composite particles for $\theta = 90°$.

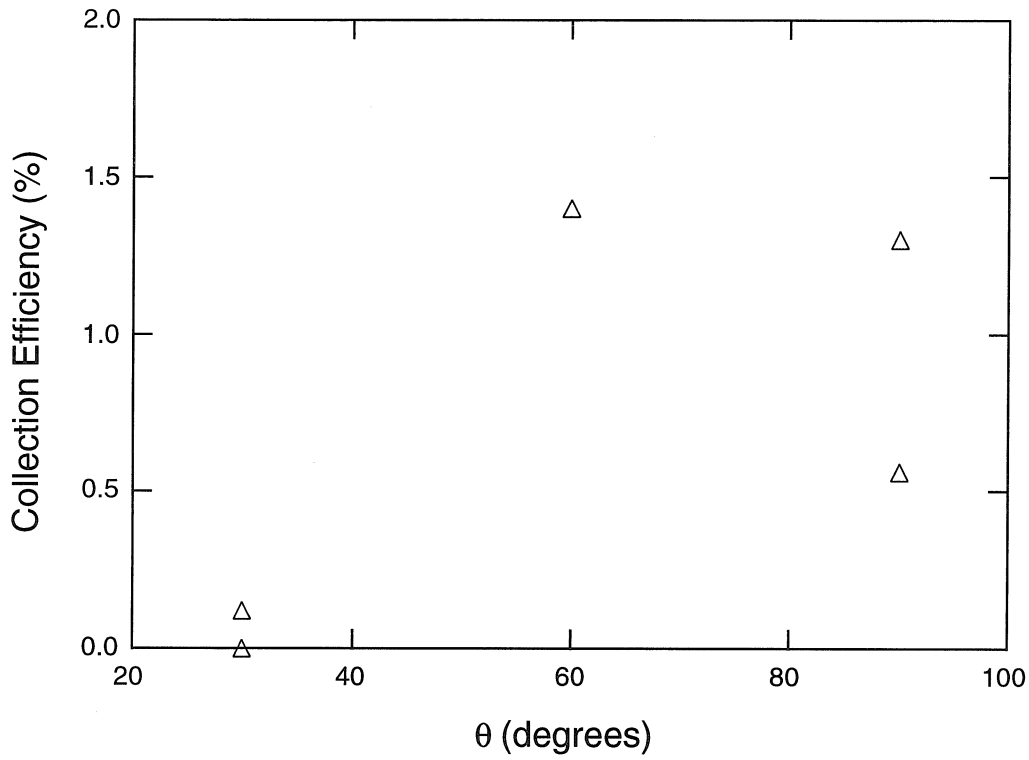

Figure 10.11: Effect of jet impingement angle, θ, on collection efficiency of composite particles for 10.0 μm particles.

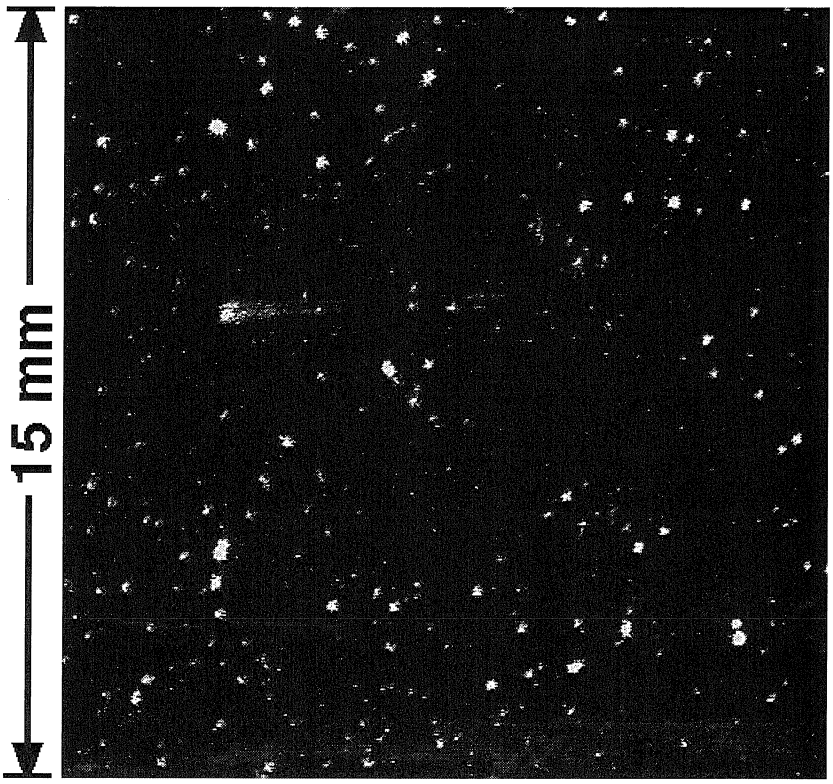

Figure 10.12: Initial raw image of C4 dry Teflon transfer deposit.

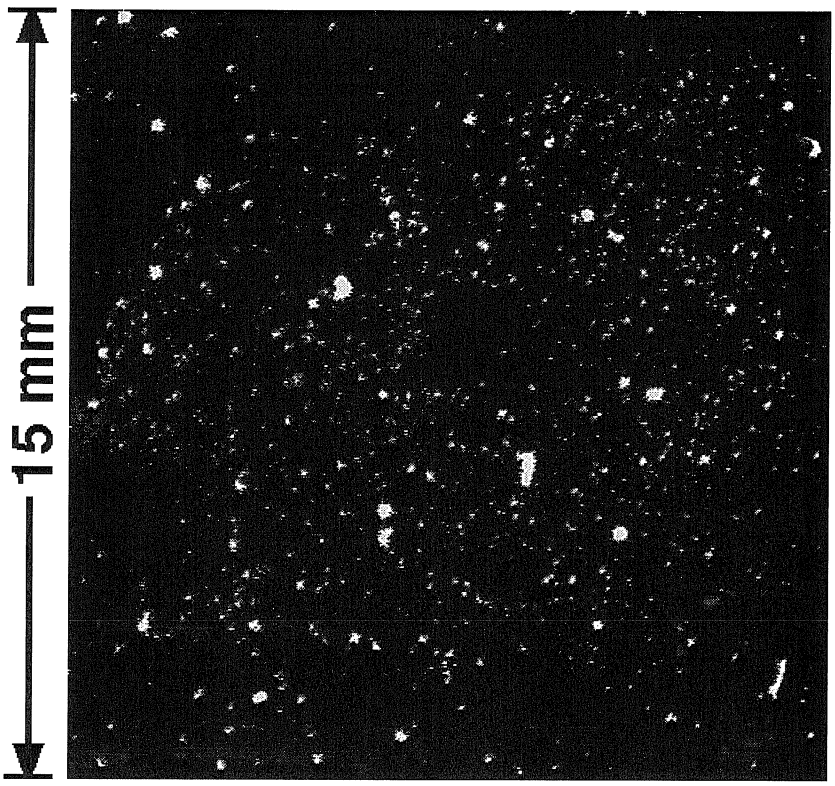

Figure 10.13: Initial raw image of C4 fingerprint deposit.

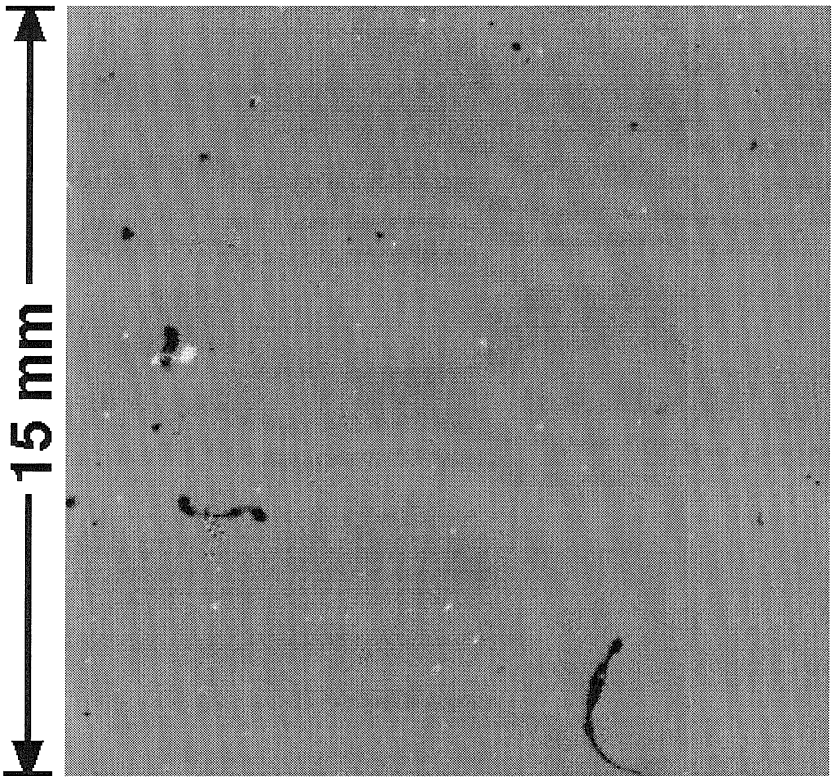

Figure 10.14: Difference between final and initial images of dry transfer deposit.

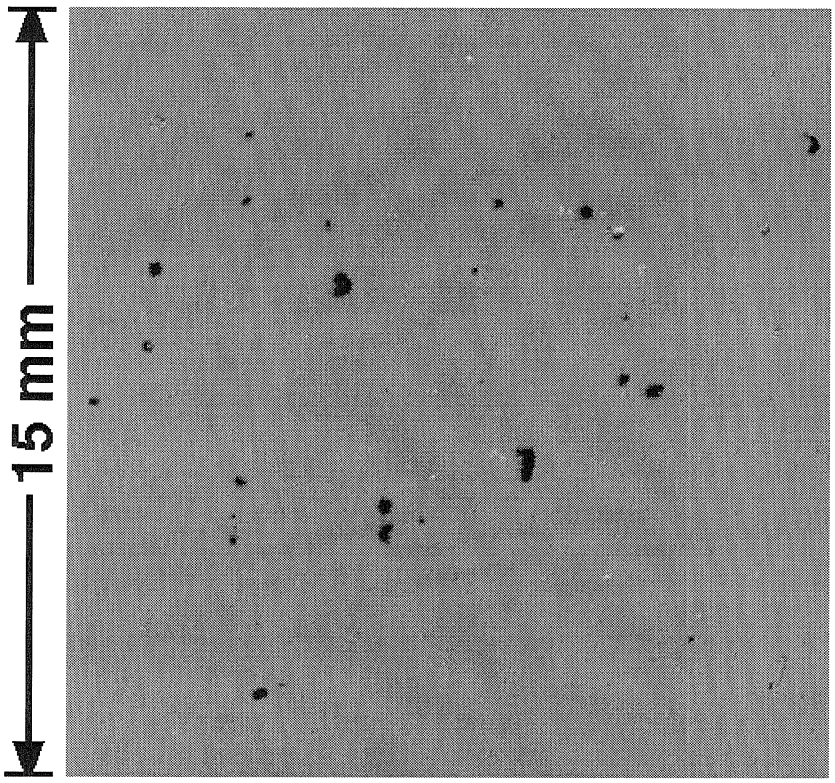

Figure 10.15: Difference between final and initial images of fingerprint deposit.

Chapter 11 Conclusions and Future Considerations

Well-characterized spherical particles were exposed to impulsive forces induced by particle impaction and shock impingement as well as to the steady shear of a laminar flow. Removal was monitored optically using dark-field microscopy or an optical particle counter. The conditions associated with the threshold to resuspension were determined from the removal data. It was found that the threshold was evidenced by reproducible and abrupt changes in the removal of monosized spheres for each type of imposed force.

Describing the mechanics of particle resuspension involves combining the kinetics of an applied force with the molecular interactions and mechanical stresses associated with particle adhesion. The results of the experiments were used to quantify the threshold to resuspension for various applied forces facilitating the development of models describing the resuspension mechanism. It was found through fluid mechanical modeling and experimentation that impinging gas jets not only provide the shear stresses necessary to aerodynamically entrain micron sized particles, but also provide the well-characterized and reproducible flow field required for quantification of the resuspension threshold.

Using monosized spherical particles to verify the shear stress distribution under an impinging gas jet predicted by laminar boundary layer theory and to determine the effects on the shear stress distribution of compressibility facilitated the use of impinging jets to quantify the effect on threshold resuspension of particle size, material, and force duration. It was found that the detachment process does not occur instantaneously, but rather over a length of time determined by the magnitude of the applied force. The kinetics of particle detachment was likened to the kinetics of subcritical crack propagation through a solid. A kinetic detachment model based on

crack propagation through a viscoelastic solid explained the large sensitivity of the resuspension threshold to particle size.

Physically, the presented kinetic detachment model inherently assumes large energy losses at the contact region periphery during detachment. Modeling and quantifying the energy loss mechanisms is beyond the scope of the present work, as such a task would involve direct observation of a single detaching particle, rather than a statistical ensemble. This might be accomplished using atomic force microscopy (AFM) and carefully observing the loading and unloading force-displacement curves of various spheres adhered to the cantilever tip. Similar experiments using lateral force microscopy (LFM) to directly measure the force required to displace a sphere tangentially along a surface could aid in confirming the resuspension mechanisms (i.e., rolling or sliding) that have been predicted from the observed threshold conditions in this study. Ultimately, the microsphere resuspension model can be applied to the resuspension of rough and nonspherical particles from surfaces. Approximating rough particles as an agglomerate of spherical particles is not a new concept, but the absence of an accurate microsphere resuspension model has hindered testing the validity of the approximation for rough particle adhesion and resuspension.

The practical application of the present work to explosive detection presented in Chapter 10 demonstrates the importance of understanding the resuspension process. The development of effective particulate sampling technologies has generally lacked the focus of the scientific community, as physical chemists rose to the challenge of lowering explosive vapor detection limits to the picogram level. We are currently in a position that detecting concealed explosives is hindered by the inability to transfer particulate residues from a surface to the vapor analyzer. The present work has provided some important insight into the nature of an efficient particle sampler. First the sampler must impose two separate forces to a particle laden substrate: (i) a steady shear force to entrain larger particles, and (ii) an impulsive force that can act well within the viscous sublayer (i.e., an impinging shock wave or particle) to entrain the smaller particles that are left untouched by even very high shear stresses. And second, large particles must be vaporized immediately after entrainment to prevent inertial

impaction with the sampler walls prior to collection.

The natural extension of the presented model experiments using monosized spheres is to investigate the resuspension of particles from various types of surfaces. The resuspension of particles from well-characterized fibers or fabrics can be used to probe the effectiveness of particulate sampling from clothing. Etched silicon substrates could be used to determine the conditions required for maximum contaminant removal from semiconductor surfaces. Investigating particle entrainment from a bed of well-characterized spheres could provide insight into the initiation of dust storms by wind. In each of these cases, the experimental techniques and theoretical models presented in this thesis could be applied to increase understanding of the particle resuspension inherent in all of these processes.

Bibliography

[1] J.H. Vincent and W. Humphries. The collection of airborne dusts by bluff bodies. *Chem. Eng. Sci.*, 33:1147–1155, 1978.

[2] D.M. Scheafer, M. Carpenter, B. Gady, R. Reifenberger, L.P. Demejo, and D.S. Rimai. Surface-roughness and its influence on particle adhesion using atomic-force techniques. *J. Adhesion Sci. Tech.*, 9(8):1049–1062, 1995.

[3] R.N. Berglund and B.Y.H. Liu. Generation of monodisperse aerosol standards. *Env. Sci. Tech.*, 7:147–153, 1973.

[4] Y. Levendis. *A fundamental study of char oxidation kinetics using model materials.* PhD dissertation, California Institute of Technology, 1988.

[5] R.W. Vanderpool and K.L. Rubow. Generation of large, solid, monodisperse calibration aerosols. *Aerosol Science and Technology*, 9:65–69, 1988.

[6] L. Layden and D. Wadlow. High velocity carbon dioxide snow for cleaning vacuum system surfaces. *J. Vac Sci. Technol.*, 8:3881–3883, 1990.

[7] R. Sherman, J. Grob, and W. Whitlock. Dry surface cleaning using co2 snow. *J. Vac Sci. Technol.*, 9:1970–1977, 1991.

[8] W. John and V. Sethi. Threshold for resuspension by particle impaction. *Aerosol Science and Technology*, 19:69–79, 1993.

[9] R.C. Flagan and J.H. Seinfeld. *Fundamentals of Air Pollution Engineering.* Prentice Hall, Englewood Cliifs, N.J., 1988.

[10] L.D. Landau and E.M. Lifshits. *Theory of Elasticity.* Moskow, 1970.

[11] H.C. Wang. Effects of inceptive motion on particle detachment from surfaces. *Aerosol Science and Technology*, 13(1):386–393, 1990.

[12] M. Corn and F. Stein. Re-entrainment of particles from a plane surface. *Am. Ind. Hyg. Assoc. J.*, 26:225–236, 1965.

[13] J.W. Cleaver and B. Yates. Mechanism of detachment of colloidal particles from a flat substrate in a turbulent flow. *J. Col. Int. Sci.*, 44:464–473, 1973.

[14] H.Y. Wen and G. Kasper. On the kinetics of particle reentrainment from surfaces. *J. Aerosol Sci.*, 20(4):483–498, 1989.

[15] G.A. Sehmel. Complexities of particle deposition and re-entrainment in turbulent pipe flow. *J. Aerosol Sci.*, 2:63–72, 1971.

[16] B.Y.H. Liu, S.H. Yoo, J.P. Davies, G. Gresham, and S.F. Hallowell. Development of particle standards for testing explosive detection systems: characterization of the adhesion forces between composition 4 particles and polyethylene. *SPIE Cargo Inspection Technologies*, 2276:45–55, 1994.

[17] K. Gotoh, S. Takebe, H. Masuda, and Y. Banba. The effect of humidity on the removal of fine particles on a solid surface using a high-speed air-jet. *Kagaku Kogaku Ronbunshu*, 20(2):205–212, 1994.

[18] K. Gotoh, S. Takebe, and H. Masuda. Effect of surface material on particle removal using high speed air jet. *Kagaku Kogaku Ronbunshu*, 20(5):685–692, 1994.

[19] K. Gotoh, M. Kida, and H. Masuda. Effect of particle diameter on removal of surface particles using high speed air jet. *Kagaku Kogaku Ronbunshu*, 20(5):693–700, 1994.

[20] K. Gotoh, M. Tagaya, and H. Masuda. Mechanism of air jet removal of particles. *Kagaku Kogaku Ronbunshu*, 21(4):723–731, 1995.

[21] G.T. Smedley, D.J. Phares, and R.C. Flagan. Entrainment of fine particles from surfaces by gas jets impinging at normal incidence. *in press, Experiments in Fluids.*

[22] Y. Otani, H. Emi, T. Morizane, and J. Mori. Removal of fine particles from wafer surface by pulse air jets. *Kagaku Kogaku Ronbunshu*, 19:114–119, 1993.

[23] H. Masuda, K. Gotoh, H. Fudkada, and Y. Banba. The removal of particles from flat surfaces using a high-speed air jet. *Advanced Powder Tech.*, 5(2):205–217, 1994.

[24] Y. Otani, N. Namiki, and H. Emi. Removal of fine particles from smooth flat surfaces by consecutive pulse air jets. *Aerosol Sci. and Tech.*, 23(4):665–673, 1995.

[25] K. Gotoh, K. Karube, H. Masuda, and Y. Banba. High-efficiency removal of fine particles deposited on a solid surface. *J. Soc. Powder Tech. Jpn*, 31(10):726–733, 1994.

[26] K.W. Montz and J.K. Beddow. Adhesion and removal of particulate contaminants in a high-decibel acoustic field. *Powder Tech.*, 55:133–140, 1988.

[27] L.B. Emmons and W.B. Pennebaker. An investigation of dust pickup and transport in a shock tube. Bachelor's project, Lehigh University, 1957.

[28] B. Fletcher. The interaction of a shock with a dust deposit. *J. Phys. D*, 9:197–202, 1976.

[29] C.C. Hwang. Initial stages of the interaction of a shock wave with a dust deposit. *Int. J. Multiphase flow*, 12(4):655–666, 1986.

[30] O. Igra and K. Takayama. Shock tube study of the drag coefficient of a sphere in a non-stationary flow. *Proc. Roy. Soc. Lond. A*, 4442:231–247, 1993.

[31] G. Ben-Dor. Dust entrainment by means of a planar shock induced vortex over loose dust layers. *Sock Waves*, 4:285–288, 1995.

[32] T. Suzuki, Y. Sakamura, T. Adachi, and S. Kobayashi. An experimental study on the initial mechanism of particle liftup by a shock passage. *Trans. Jpn Soc. Aero. Space Sci.*, 38(121):243–250, 1995.

[33] K. Hanjalic and I. Smajevic. Detonation-wave technique for on-load deposit removal from surfaces exposed to fouling: part i - experimental investigation and development of the method. *J. of Engineering for Gas Turbines and Power*, 116:223–230, 1994.

[34] K. Hanjalic and I. Smajevic. Detonation-wave technique for on-load deposit removal from surfaces exposed to fouling: part i - full scale application. *J. of Engineering for Gas Turbines and Power*, 116:231–236, 1994.

[35] Y.W. Kim. A new, diaphragmless, flexible, luminous shock tube. In *Proc. 13th International Symposium on Shock Tubes and Waves*, pages 89–97, 1981.

[36] Y.I. Chutov, V.N. Podolski, and D.A. Braion. Electromechanical shock tube. *Instruments and Experimental Techniques*, 35(2):680–682, 1992.

[37] S.M. Hurst and S.H. Bauer. A piston-actuated shock-tube, with laser schlieren diagnostics. *Rev. Sci. Instrum.*, 64(5):1342–1346, 1994.

[38] I.S. Shpigel. A quick-acting electrodynamic vacuum valve. *Instr. and Meas. Eng. USSR*, 1:156, 1959.

[39] B. Gorowitz, K. Moses, and P. Gloersen. Magnetically driven fast-acting valve for gas injection into high vacua. *Rev. Sci. Instr.*, 31(2):146–148, 1960.

[40] D. Wetstone. Fast-acting gas valve. *Rev. Sci. Instr.*, 32(11):1209–1211, 1961.

[41] R.S. Lowder and F.C. Hoh. Fast gas valve for plasma research. *Rev. Sci. Instr.*, 33(11):1236–1238, 1962.

[42] G. Kuswa, C. Stallings, and A. Stamm. Improved fast opening gas puff valve. *Rev. Sci. Instr.*, 41:1362–1363, 1970.

[43] V.V. Prut and S.A. Shibaev. An injector of solid hydrogen pellets. *Instruments and Experimental Techniques*, 37(2):195–199, 1994.

[44] P.K. Loewenhardt, M.R. Brown, J. Yee, and P.M. Bellan. Performance characterization of the caltech compact torus injector. *Rev. Sci. Instr.*, 66(2):1050–1055, 1995.

[45] Y.A. Levendis and R.C. Flagan. Synthesis, formation, and characterization of micron-sized glassy-carbon spheres of controlled pore structure. *Carbon*, 27(2):265–283, 1989.

[46] D.J. Phares, G.T. Smedley, and R.C. Flagan. Aerodynamic entrainment of microspheres of various size and material. *submitted to J. Aerosol Sci.*, 1999.

[47] H.W. Liepmann and A. Roshko. *Elements of Gasdynamics.* Wiley, New York, 1957.

[48] P.A. Thompson. *Compressible-Fluid Dynamics.* The Maple Press Company, 1984.

[49] J.J. Quirk. *An adaptive mesh refinement algorithm for computational shock hydrodynamics.* PhD dissertation, Cranfield Institute of Technology, U.K., College of Aeronautics, June-August 1991.

[50] K. Takayama, A. Sasoh, O. Onodera, and R. Kaneko. Experimental investigation on tunnel sonic-boom. *Shock Waves*, 5(3):127–138, 1995.

[51] A. Galkowski. Reflection of a strong spherical shock wave in gas action on an indeformable perfectly smooth plane. *J. of Tech. Phys.*, 28(4):415–430, 1987.

[52] A. Galkowski. The transition from regular reflection to mach reflection in the problem of a strong spherical shock wave acting on an indeformable perfectly smooth plane. *J. of Tech. Phys.*, 28(2):163–171, 1987.

[53] A. Galkowski. Some remarks on the theory of irregular reflection of a shock wave from a surface. *Arch. Mech.*, 41(6):837–855, 1989.

[54] H.G. Hornung, H. Oertel, and R.I. Sandeman. Transition to mach reflection of shock waves in steady and pseudosteady flow with and without relaxation. *J. Fluid Mech.*, 90:541–560, 1979.

[55] R.A. Bowling. An analysis of particle adhesion on semiconductor surfaces. *J. Electrochem. Soc.*, 132(9):2208–2214, 1985.

[56] G. Ziskind, M. Fichman, and C. Gutfinger. Resuspension of particulates from surfaces to turbulent flows – review and analysis. *J. Aerosol Sci.*, 26(4):613–644, 1995.

[57] G.A. Sehmel. Particle resuspension: a review. *Environ. Int.*, 4:107–127, 1980.

[58] M.W. Reeks and D. Hall. Deposition and resuspension of gas-borne particles in recirculating turbulent flows. *J. Fluids Enana*, 110(4):165–171, 1988.

[59] A. Fromentin. Time dependent particle resuspension from a multi-layer deposit by turbulent flow. *J. Aerosol Sci.*, 20:911–914, 1989.

[60] S. Beltaos and N. Rajaratnam. Plane turbulent impinging jets. *J. Hydr. Res.*, 11(1):29–59, 1973.

[61] S. Beltaos and N. Rajaratnam. Circular turbulent impinging jets. *J. of Hyd. Div., Proc. ASCE*, 100(HY10):1313–1328, 1974.

[62] P. Bradshaw and E.M. Love. The normal impingement of a circular air jet over a flat surface. R & M 3205, Aero Research Council, England, 1961.

[63] C.D. Donaldson and R.S. Snedeker. A study of free jet impingement. part 1. mean properties of free and impinging jets. *J. Fluid Mech.*, 45:281–319, 1971.

[64] P.R. Bevington. *Data Reduction and Error Analysis for the Physical Sciences.* McGraw-Hill, New York, 1969.

[65] M.W. Reeks, J. Reed, and D. Hall. On the resuspension of small particles by a turbulent flow. *J. Phys. D*, 21:574–589, 1988.

[66] S. Beltaos. Oblique impingement of circular turbulent jets. *J. Hydr. Res.*, 14(1):17–36, 1976.

[67] C.V. Tu and D.H. Wood. Wall shear stress measurements beneath an impinging jet. *Exp. Therm. and Fluid Sci.*, 13:364–373, 1996.

[68] T. Strand. On the theory of normal ground impingement of axisymmetric jets in inviscid incompressible flow. Paper 64-424, AIAA, New York, 1964.

[69] M.T. Scholtz and O. Trass. Mass transfer in a nonuniform impinging jet. *AIChE J.*, 16(1):82–90, 1970.

[70] V. Parameswaran. Study of reattaching wall jets. Ph.d. thesis, Dept. Mech. Eng. University of Waterloo, Ontario, Canada, 1973.

[71] A. Rubel. Computations of jet impingement on a flat surface. *AIAA J.*, 18(2):168–175, 1980.

[72] A. Rubel. Inviscid axisymmetric jet impingement with recirculating stagnation regions. *AIAA J.*, 21(3):351–357, 1983.

[73] J.M. Kuhlman and W.M. Cavage. Jet ground vortex formation by annular jets. *J. Aircraft*, 31(4):794–801, 1994.

[74] J.J. Schauer and R.H. Eustis. The flow development and heat transfer characteristics of plane turbulent impinging jets. Tech Report 3, Dept. Mech. Eng. Stanford University, Stanford, CA, 1963.

[75] M. Kumada and I. Mabuchi. Studies on the heat transfer of impinging jet. *Bull. JSME*, 13(55):77–85, 1970.

[76] H. Schlichting. *Boundary Layer Theory.* McGraw-Hill, New York, 1960.

[77] A.M. Kuethe. Investigations of the turbulent mixing regions formed by jets. *J. Appl. Mech.*, 2:A87–A95, 1935.

[78] F. Giralt, C. Chia, and O. Trass. Characterization of the impingement region in an axisymmetric turbulent jet. *Ind. Eng. Chem. Fundam.*, 16(1):21–28, 1977.

[79] L.J.S. Bradbury. The impact of an axisymmetric jet onto a normal ground. *Aero. Quarterly*, 23:141–147, 1972.

[80] H.J. Sheen, W.J. Chen, and S.Y. Jeng. Recirculation zones of unconfined and confined annular swirling jets. *AIAA J.*, 34(3):572–579, 1996.

[81] M.D. Deshpande and R.N. Vaishnav. Submerged laminar jet impingement on a plane. *J. Fluid Mech.*, 114:213–236, 1982.

[82] M. Bouainouche, N. Bourabaa, and B. Desmet. Numerical study of the wall shear stress produced by the impingement of a plane turbulent jet on a plate. *Int. J. of Num. Meth. for Heat and Fluid Flow*, 7:548–564, 1997.

[83] M.K. Looney and J.J. Walsh. Mean-flow and turbulent characteristics of free and impinging jet flows. *J. Fluid Mech.*, 147:397–429, 1984.

[84] M.B. Glauert. The wall jet. *J. Fluid Mech.*, 1:625–643, 1956.

[85] M. Poreh, Y.G. Tsuei, and J.E. Cermak. Investigation of a turbulent radial wall jet. *J. Applied Mech.*, 34:457–463, 1967.

[86] B.E. Launder and W. Rodi. The turbulent wall jet - measurements and modeling. *Ann. Rev. Fluid Mech.*, 15:429–459, 1983.

[87] K. Kataoka and T. Mizushina. Local enhancement of the rate of heat transfer in an impinging round jet by free-stream turbulence. In *Proc. 5th International Heat Transfer Conference*, page FC8.3, 1974.

[88] G.N. Abramovich. *The Theory of Turbulent Jets.* The MIT Press, Cambridge, MA, 1963.

[89] T.F. Wall, V. Subramanian, and P. Howley. An experimental study of the geometry, mixing and entrainment of particle-laden jets up to ten diameters from the nozzle. *Trans. Inst. Chem. Eng.*, 60:65–69, 1982.

[90] D.J. Phares, G.T. Smedley, and R.C. Flagan. Inviscid jet impingement. *submitted to Phys. Fluids*, 1999.

[91] K. Kataoka, Y. Kamiyama, S. Hashimoto, and T. Komai. Mass transfer betweeen a plane surface and an impinging turbulent jet: the influence of surface-pressure fluctuations. *J. Fluid Mech.*, 119:91–105, 1982.

[92] S. V. Alekseenko and D.M. Markovich. Electrodiffusion diagnostics of wall shear stresses in impinging jets. *J. Applied Electrochemistry*, 24:626–631, 1994.

[93] V.C. Patel. Calibration of the preston tube and limitations on its use in pressure gradients. *J. Fluid Mech.*, 23:185–208, 1965.

[94] W.D. Baines and J.F. Keffer. Shear stress and heat transfer at a stagnation point. *J.Heat Mass Transfer*, 19:21–26, 1976.

[95] M. Soltani and G. Ahmadi. On particle adhesion and removal mechanisms in turbulent flows. *J. Adhesion Sci. Technol.*, 8(7):763–785, 1994.

[96] P. Vainstein, G. Ziskind, M. Fichman, and C. Gutfinger. Kinetic model of particle resuspension by drag force. *Phys. Rev. Letters*, 78(3):551–554, 1997.

[97] M. Lazaridis, Y. Drossinos, and G. Georgopoulos. Turbulent resuspension of small nondeformable particles. *J. Coll. Int. Sci.*, 204(1):24–32, 1998.

[98] Ker-Ching Hsieh. *Studies of particle reentrainment/detachment from flat surface.* PhD dissertation, University of Minnesota, 1991.

[99] M. Taheri and G.M. Bragg. A study of particle resuspension in a turbulent flow using a preston tube. *Aerosol Science and Technology*, 16:15–20, 1992.

[100] D.A. Braaten, R.H. Shaw, and K.T. Paw U. Boundary-layer flow structures associated with particle reentrainment. *Boundary-Layer Meteorology*, 65:255–272, 1993.

[101] D.B. Ingham and B. Yan. Reentrainment of particles on the outer of a cylindrical blunt sampler. *J. Aerosol Sci.*, 25(2):327–340, 1994.

[102] K.L. Johnson, K. Kendall, and A.D. Roberts. Surface energy and the contact of elastic solids. *Proc. R. Soc. Lond. A.*, 324:301–313, 1971.

[103] B.V. Derjaguin, V.M. Muller, and Y.P. Toporov. Effect of contact deformations on the adhesion of particles. *J. of Colloids and Interface Science*, 53(2):314–326, 1975.

[104] D. Tabor. Surface forces and surface interactions. *J. of Colloids and Interface Science*, 58(1):2–13, 1977.

[105] V.M. Muller, V.S. Yushchenko, and B.V. Derjaguin. On the influence of molecular forces on the deformation of an elastic sphere and its sticking to a rigid plane. *J. Colloid Interface Sci.*, 77:91–101, 1980.

[106] C. Tsai, D.Y.H. Pui, and B.Y.H. Liu. Elastic flattening and particle adhesion. *Aerosol Science and Technology*, 15:239–255, 1991.

[107] D. Maugis and H.M. Pollock. Surface forces, deformations and adherence at metal microcontacts. *Acta Metall.*, 32(9):1323–1334, 1984.

[108] A.R. Savkoor and G.A.D. Briggs. The effect of a tangential force on the contact of elastic solids in adhesion. *Proc. R. Soc. Lond. A.*, 356:103–114, 1977.

[109] D.S. Dandy and H.A. Dwyer. A sphere in shear flow at finite reynolds number: effect of shear on particle lift, drag, and heat transfer. *J. Fluid Mech.*, 216:381–410, 1990.

[110] F. Yamamoto, M. Koukawa, H. Monya, A. Teranishi, and H. Miyamoto. An experimental study for simulation of pneumatic conveying. *JSME B*, 36(2):294–299, 1993.

[111] K. Mudumala and D.A. Braaten. The role of gravity in the reentrainment-deposition trajectories of large particles. In *AAAR '97 Abstracts Sixteenth Annual Conference*, page 479, 1997.

[112] D.J. Phares, G.T. Smedley, and R.C. Flagan. The wall shear stress produced by the normal impingement of a jet on a flat surface. *submitted to J. Fluid Mech.*

[113] F.M. Fowkes. Attractive forces at interfaces. *Ind. Eng. Chem.*, 56(12):40–52, 1964.

[114] D.S. Rimai, L.P. Demejo, R. Bowen, and J.D. Morris. Particles on surfaces: adhesion induced deformations. In *Particles on Surfaces: Detection, Adhesion, and Removal*, pages 1–31, 1995.

[115] D. Maugis. Adhesion of spheres: the jkr-dmt transition using a dugdale model. *J. Coll. Int. Sci.*, 150(1):243–269, 1992.

[116] D. Maugis. Subcritical crack growth, surface energy, fracture toughness, stick-slip and embrittlement. *J. Materials Sci.*, 20:3041–3073, 1985.

[117] J. Brandrup and E.H. Immergut. *Polymer Handbook.* Wiley-Interscience, New York, 1989.

[118] F. Garofolo, F. Marziali, V. Migliozzi, and A. Stama. Rapid quantitative determination of 2,4,6-trinitrotoluene by ion mobility spectrometry. *Rap. Comm in Mass Spectrom.*, 10:1321–1326, 1996.

[119] F.T. Fox, S. Sisk, R. DiBartolo, D.A. Green, and J.F. Miller. Preparation and characterization of plastic explosive suspensions as analogs of fingerprint derived contaminants for use in certification of explosives detection systems. 1995.

[120] T. Chamberlain. Unpublished.

[121] G.T. Smedley, D.J. Phares, and R.C. Flagan. Entrainment of fine particles from surfaces by impinging shock waves. *Experiments in Fluids*, 26(1-2):116–125, 1999.

[122] H. Hertz. *Gesammelte werke*. Liepzig, 1895.

Appendix A Equilibrium particle adhesion

When an uncharged spherical particle comes into contact with a surface, it will experience two forces. Instantaneous Coulombic interactions between the molecules in the sphere and surface result in a net attractive force known as the van der Waals force. This force causes the particle to approach the surface, deforming both the particle and surface and increasing the area of contact. This deformation leads to a repulsive elastic force. At equilibrium, the magnitudes of the two forces are equal. The critical force necessary to pull a particle from its equilibrium position to separation from the surface is called the pull-off force. In order to determine this force, we need to investigate the equilibrium condition from the point of view of macroscopic elasticity theory in the presence of intermolecular adhesion.

A.1 Hertz Elasticity Theory

In the case of two solids being pushed together, the elastic deformation and pressure distribution can be calculated by solving the equation of elastic equilibrium [10]:

$$\nabla(\nabla \cdot \vec{u}) + (1 - 2\sigma)\nabla^2 \vec{u} = 0 \tag{A.1}$$

where $\vec{u}$ is the deformation vector of one of the solids, and σ is the Poisson ratio of the same solid. Hertz solved this equation for the case of two spheres being pushed together with a force, F, and obtained the deformation of a sphere at a point located a distance, r, from the symmetry axis of the two spheres [122]:

$$u_z(r) = \frac{1 - \sigma^2}{\pi E} \iint \frac{P_z(x, y)}{r}\, dx\, dy, \tag{A.2}$$

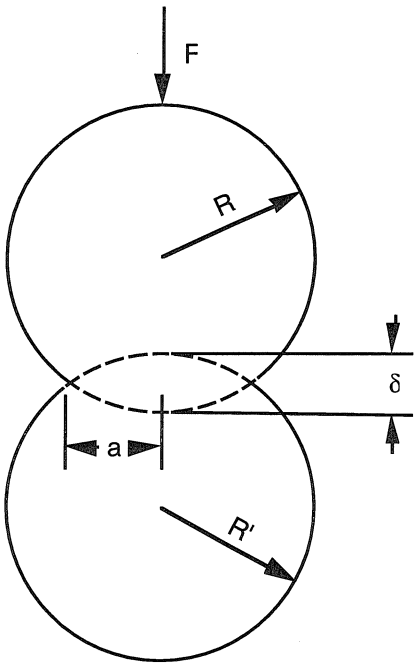

Figure A.1: Hertz problem of two spheres in contact.

where E is the Young's Modulus of one of the spheres, and P_z is the spatial pressure distribution at the solid interface due to the applied force, F. From Fig. A.1, it is apparent that F causes the centers of the spheres to approach each other from the initial contact by a distance, δ, resulting in a contact circle of radius, a. For the case of two spheres, Hertz calculated that P_z is parabolic within the contact zone, and from Eq. A.2, obtained the following relations:

$$a^3 = KRF, \tag{A.3}$$

$$a^2 = R\delta, \tag{A.4}$$

where R is the reduced radius, and K depends on the elastic constants of both spheres (labeled 1 and 2):

$$K = \frac{4}{3}\left[\frac{1-\sigma_1^2}{E_1} + \frac{1-\sigma_2^2}{E_2}\right]^{-1} \tag{A.5}$$

These results form the basis for future theories describing the adhesion of particles to surfaces.

A.2 Derjaguin, Muller, Toporov Theory (DMT)

In finding the van der Waals attraction between a sphere and a surface, Derjaguin *et al.* (1975) split the force into two parts [103]: (i) the force on the contact area, F_s', and (ii) the force on the annulus just outside the contact radius, F_s''. The rigorous

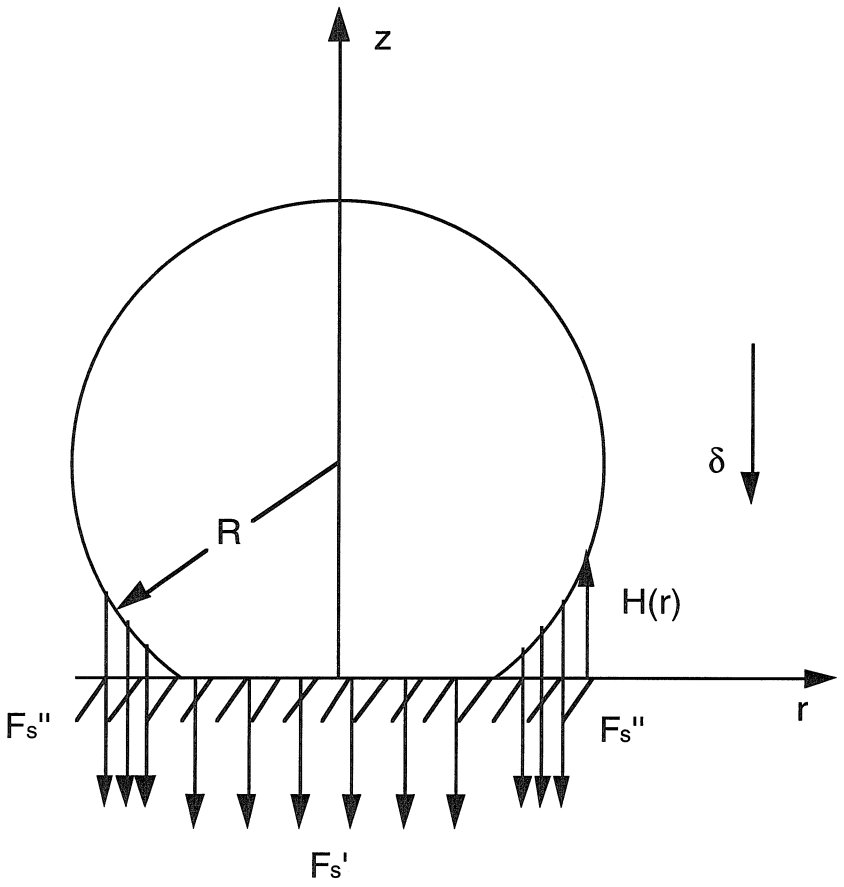

Figure A.2: The DMT particle adhesion model.

calculation of the force on the outer annulus requires knowledge of its exact shape, i.e., its deformation from a perfect sphere. This was provided by the Hertzian theory:

$$u_z(r) = \frac{3KF}{8a^3}[2a(r^2-a^2)^{\frac{1}{2}} + (2a^2-r^2)\arccos(1-\frac{2a^2}{r^2})] \tag{A.6}$$

leading to the equation of the surface just outside the contact zone:

$$H(r) = \frac{1}{\pi R}[a(r^2-a^2)^{\frac{1}{2}} + (r^2-2a^2)\arctan(\frac{\sqrt{r^2-a^2}}{a})] + \epsilon \tag{A.7}$$

where ϵ is the distance of closest approach (typically 4 to 6 $\mathring{A}$). The non-contact van der Waals potential is:

$$W_s'' = 2\pi \int_a^\infty \Phi[H(r)]rdr \tag{A.8}$$

where Φ is the interaction energy per unit surface area. Correspondingly, in the contact region:

$$W_s' = \int_0^a \Phi(\epsilon)2\pi rdr = \pi a^2 \Phi(\epsilon) \tag{A.9}$$

Using Equation A.3 from Hertz theory, and differentiating the potential with respect to the distance of approach, δ, the attractive force exerted on the contact region of the sphere is found to be:

$$F_s' = \pi R\Phi(\epsilon) \tag{A.10}$$

From Equations A.7 and A.8, it can be shown that the maximum attractive force on the non-contact annulus occurs at point contact ($a = 0$), where it is equal to:

$$F_s'' = \pi R\Phi(\epsilon) \tag{A.11}$$

Furthermore, the repulsive force is zero at point contact and only grows with increasing deformation. Hence, we can conclude that the maximum sticking force, and thus the critical force needed to separate the sphere from the surface, occurs at point contact, and is exactly equal to:

$$F_{pull-off} = F_s' + F_s'' - F_{rep} = 2\pi R\Phi(\epsilon) \tag{A.12}$$

Application of an upward force to a particle sitting on a surface will cause the contact area to decrease. If the applied force approaches the pull-off force, the contact area will approach zero, and the particle will separate from the surface.

One very important drawback to the DMT theory is that all deformations are assumed to be Hertzian. More specifically, we would expect that, if half of the attractive force is concentrated on the annulus outside the contact area, then that area of the sphere would experience a greater deformation than what is predicted

by Equation A.6. DMT theory is, therefore, applicable when these deformations are negligible, which is the case for very rigid solids or very small interaction energies. Otherwise we must approach the problem from a contact mechanics point of view.

A.3 Johnson, Kendall, Roberts Theory (JKR)

Suppose we now assume that the annulus deformation is so great that a significant portion of the sphere around the original contact area will be drawn into contact with the surface. The attractive force is then dominated by the contact region and the short-range force, F_s'', can be neglected. The resulting particle profile resembles a neck (see Figure A.3) . The stresses within this new contact area remain compressive towards the center, but become infinitely tensile towards the edge. The stress

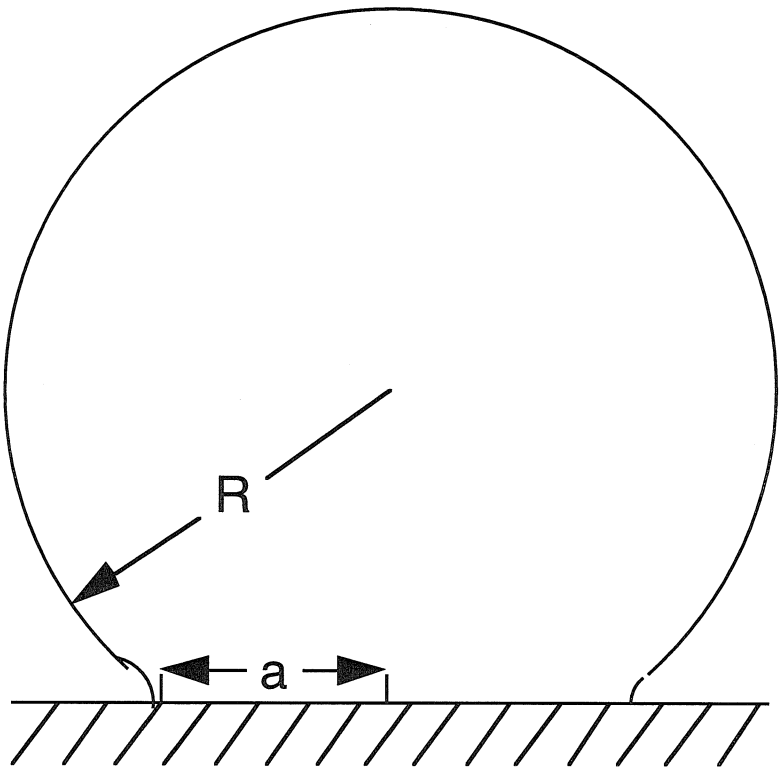

Figure A.3: The JKR particle adhesion model.

distribution at the edge quantitatively resembles that surrounding a crack in a solid,

allowing us to deduce that a certain critical upward force exists such that a crack between the particle can propagate radially inward from the neck edge. This force is the pull-off force.

Johnson, Kendall, and Roberts (1971) calculated this critical force using an energy minimization approach common in fracture mechanics [102] - seeking the conditions that lead to:

$$\frac{dU_{total}}{d\delta} = 0 \tag{A.13}$$

where

$$U_{total} = U_{elastic} + U_{mechanical} + U_{surface} \tag{A.14}$$

The surface and mechanical energy contributions are given by:

$$U_{surface} = -2\pi a^2 \Phi(\epsilon) \equiv -2\pi a^2 \gamma \tag{A.15}$$

$$U_{mechanical} = -F\delta \tag{A.16}$$

where γ is defined as the interaction energy per unit area at the distance of closest approach, ϵ. To determine the elastic energy contributions, we consider a sphere pressed onto a surface with a force, F. Hertz would predict a resulting contact radius, a_o. In the presence of intermolecular attraction, however, the actual contact radius is $a > a_o$. In calculating the elastic energy stored in the sphere, JKR suggested taking the Hertzian energy required to achieve a contact radius, a, with a force, $F_1 > F$, and subtracting from that the energy released when the force is relaxed to F keeping a constant. The result is:

$$U_{elastic} = \frac{1}{K^{\frac{2}{3}} R^{\frac{1}{3}}} [\frac{1}{15} F_1^{\frac{5}{3}} + \frac{1}{3} F^2 F_1^{-\frac{1}{3}}] \tag{A.17}$$

K is the same elastic constant as in Equation A.3. From Equations A.13 - A.17, we obtain:

$$a^3 = \frac{R}{K}(F + 3\gamma\pi R + \sqrt{6\pi\gamma RF + (3\pi\gamma R)^2}) \tag{A.18}$$

This is an expression for the equilibrium contact radius when a force, F, is being

applied normally to the sphere. If F is negative, the force acts upward, directed away from the surface. As can be seen from Eq. (A.18), the contact radius will only be real if the expression under the square root is positive. The critical force occurs when that expression is zero, leading to:

$$F_{pull-off} = \frac{3}{2}\pi R\gamma \equiv \frac{3}{2}\pi R\Phi(\epsilon) \tag{A.19}$$

Surprisingly, the JKR expression differs from the DMT expression by only a factor of $\frac{3}{4}$. However, in the JKR model, the contact radius never approaches zero. Instead, the particle breaks off the surface from a finite contact radius.

A.4 Generalizing the DMT and JKR Approaches

Both the DMT and JKR theories have often been criticized in the literature because of the respective shortcomings of each approach. The DMT model fails to take into account the response of the non-contact annulus to the short range van der Waals interaction with the surface. The JKR model does not even consider the existence of a short range force affecting any region of the sphere that is not in contact with the surface. However, it is more useful to think of these as approximations rather than flaws. In this way, we can take advantage of the fantastic simplicity offered by the results of both approaches, provided that the approximations hold. Tabor (1978) theorized that the JKR model applied to soft systems (low elastic moduli, high surface energies), while the DMT applied to hard systems (high elastic moduli, low surface energies) [104]. Muller, Yushchenko, and Derjaguin (MYD)(1980) devised a way to quantitatively assign regions of applicability by numerically solving Equation A.2 assuming that the Lennard-Jones potential describes the attractive and repulsive interactions of the molecules in the sphere and surface [105]. Instead of integrating a Hertzian parabolic pressure distribution, MYD used the appropriate Lennard-Jones induced pressure:

$$P_z(h(x,y)) = \frac{A}{6\pi\epsilon^3}[(\frac{\epsilon}{h})^9 - (\frac{\epsilon}{h})^3] \tag{A.20}$$

where h is the distance between a point on the sphere and the surface, and A is the Hamaker constant. MYD found that the pull-off force was dependent on a single dimensionless parameter, μ, where:

$$\mu = \frac{32}{3\pi}[\frac{\gamma^2 R(1-\sigma^2)^2}{2\pi E^2 \epsilon^3}]^{\frac{1}{3}} \tag{A.21}$$

Furthermore, it was found that the DMT model applies as μ approaches zero, and the JKR model applies when $\mu > 1$. This result supported Tabor's suggested trend.

A.5 Effect of Elastic Properties on Equilibrium Particle Adhesion - TPL Theory

The most surprising aspect of the JKR and DMT theories is that both predict absolutely no dependence of the particle pull-off force on the elastic moduli of the particle and surface. Intuitively, we might imagine that, since the contact area is very dependent on the hardness of the particle material, then so would be the pull-off force. This issue was addressed by Tsai, Pui, and Liu (TPL) (1991) [106], who argued that as the hardness of the material is decreased, the pull-off event should begin to resemble the separation of two flat surfaces the size of the contact area between the particle and surface. This argument essentially forces the pull-off force to have as strong a dependence on material elastic properties as the size of the contact area.

The TPL method [106] involves using energy conservation and force balance to achieve a relationship between elastic flattening and the attractive van der Waals force. Similar to MYD, TPL discovered that the pull-off force was dependent on a single dimensionless parameter analogous to μ. However, the reverse trend is predicted: for small μ the pull-off force is half that predicted by DMT theory, and for large μ the pull-off force increases with contact area as if two flat surfaces were being pulled apart.

TPL theory is generally not cited by the seemingly tight circle of researchers studying particles on surfaces. Perhaps the result is too drastically different from

the adhesion theories accepted for the last twenty years. The advantage of the theory, though, is that it provides an explanation for an observation we have already made in the lab: soft polyethylene spheres are more difficult to remove from a glass surface than hard polyethylene spheres. On the other hand, how a particle adheres to a surface represents only part of the overall problem. In fact, it is unclear how important equilibrium adhesion theories are in understanding the dynamics of particle resuspension. Certainly the manner in which the pull-off force is applied will affect the appropriateness of considering these models (i.e., a continuously applied force, as opposed to a very quick impulse). Nevertheless, particle adhesion theories will, at the very least, provide necessary information about the initial state of a particle-surface system.

Appendix B Direct application of adhesion theories to resuspension

B.1 Incipient Motion

Wang (1990) theorized three modes of incipient motion leading to separation [11].

1. Lift-off: When the normal component of a force applied to an adhered particle surpasses the pull-off force, the particle will be lifted off the surface.

2. Sliding: When the tangential component of an applied force surpasses the total normal force (including the sticking force, which Wang erroneously equates to the pull-off force) multiplied by a coefficient of static friction, the particle will begin to slide and thus be resuspended.

3. Rolling: When the total torque about a point on the edge of the contact circle (again, including the downward sticking force) is equal to zero, the particle will begin to roll around that point and thus off the surface.

This resuspension theory is fairly simplistic, but it does introduce a concept that all the equilibrium adhesion theories fail to mention - the effect of an applied tangential force on an adhered particle. We know that under an applied upward force, JKR predicts a crack propagation through the interface; and DMT predicts a gradual release of the particle from the surface. But since it is much easier to apply a tangential force to a fine particle, it is essential to understand this effect as well.

B.2 Savkoor-Briggs Theory

Fortunately, since the JKR theory is an energy minimization theory, simply incorporating another energy term is not a problem. The mechanical energy associated with

displacing a sphere tangentially a short distance α with a force T is $-\frac{1}{2}T\alpha$ [108]. Incorporating this term in the JKR calculations, Savkoor and Briggs (1979) derived a critical tangential force:

$$T_c = 4[(PP_c + P_c^2)\frac{K}{\lambda}]^{\frac{1}{2}} \tag{B.1}$$

where P is the applied normal force, $P_c = \frac{3}{2}\pi R\gamma$, and K and λ are elastic constants given by

$$K = \frac{4}{3}\left[\frac{1-\sigma_p^2}{E_p} + \frac{1-\sigma_s^2}{E_s}\right]^{-1} \tag{B.2}$$

and

$$\lambda = \frac{2-\sigma_p}{G_p} + \frac{2-\sigma_s}{G_s}, \tag{B.3}$$

where σ is the Poisson ratio, E is the elastic modulus, G is the shear modulus, and the subscripts p and s refer to the particle and surface, respectively. This critical force represents the criterion for a lateral crack to propagate between the adhered surfaces.